

Copyright

by

Molly Elizabeth Kent

2011

**The Thesis Committee for Molly Elizabeth Kent
Certifies that this is the approved version of the following thesis:**

**Examining Supercritical CO₂ Dissolution Kinetics during Carbon
Sequestration through Column Experiments**

**APPROVED BY
SUPERVISING COMMITTEE:**

Supervisor:

Phil Bennett

Meinhard Bayani Cardenas

Katherine Romanak

**Examining Supercritical CO₂ Dissolution Kinetics during Carbon
Sequestration through Column Experiments**

by

Molly Elizabeth Kent, B.A.

Thesis

Presented to the Faculty of the Graduate School of

The University of Texas at Austin

in Partial Fulfillment

of the Requirements

for the Degree of

Master of Science in Geological Sciences

The University of Texas at Austin

August 2011

Acknowledgements

Many thanks to my advisor, Phil Bennett, and my committee members, Bayani Cardenas and Katherine Romanak, for all their help making this thesis a reality. I am also grateful to Will Wolfe, Kuldeep Chaudhary, Kim Gilbert, Jay Santillan, and everyone involved with the CFSES program. Thanks to the Bennett lab group, especially the ever-patient Kim Myers, for all their editing help. Thanks to my friends and roommates for putting up with me while I wrote this, and lastly, thank you to my family.

May 6, 2011

Abstract

Examining Supercritical CO₂ Dissolution Kinetics during Carbon Sequestration through Column Experiments

Molly Elizabeth Kent, MSGeoSci
The University of Texas at Austin, 2011

Supervisor: Phil Bennett

Carbon sequestration is a method of capturing and storing excess anthropogenic CO₂ in the subsurface. When CO₂ is injected, the temperature and pressure at depth turn it into a supercritical (SC) fluid, where density is that of a liquid, but viscosity and compressibility resemble a gas. Ultimately the SC CO₂ is trapped at depth either by low permeability sealing layers, by reactions with minerals, or by dissolving into fluids. The injected CO₂ is buoyant and initially exists as a non-aqueous hydrophobic layer floating on top of the subsurface brine, up against the upper sealing formation, but over time it will dissolve into the brine and potentially react with minerals. The details of that initial dissolution reaction, however, are only poorly understood, and I address three basic questions for this research: What is the fundamental kinetics of SC CO₂ dissolution into water? How fast does dissolved CO₂ diffuse away from the source point? And what geochemical conditions influence the dissolution rate?

To answer these questions I employed a high pressure flow-through approach using a column packed with coarse quartz sand. The system was both pressure and temperature controlled to have either liquid or SC CO₂ present, and was typically run at 100 Bar, 0.5 to 2.5 mls/min, and 28-60°C. After establishing the hydraulic parameters for the column using two conservative tracers (Br, As), injections (5 and 20 µl) were made either as aqueous solutions equilibrated to high pressure CO₂, or as pure liquid or SC CO₂ into 0.1 mmol NaOH. For all experiments the pH of the system was monitored, and [CO₂] over time was calculated from those data.

For injections of brine with dissolved CO₂, transport was conservative and was nearly identical to the conservative tracers. The CO₂ quickly mixes in the column and does not react with the quartz. The liquid and SC CO₂ injections, however, do not act conservatively, and have a very long tailing breakthrough curve that extends to tens of pore volumes. I hypothesize that the SC CO₂ is becoming trapped as a droplet or many droplets in the pore spaces, and the long breakthrough tail is related either to the rate of dissolution into the aqueous phase, the diffusion of dissolved CO₂ away from the phase boundary, or the reaction with the NaOH, limited to the narrow contact zones in the pore throats. Because of the speed at which acid-base reactions occur (nanosecond kinetics), I infer that the rate limiting step is either surface dissolution or diffusion. From plots of $\ln[CO_2]$ v. *time* I obtained values for k , the specific rate of the dissolution reaction

$R = -k[CO_2]$. No trend for k was seen with respect to changes in temperature, but k did show a trend with respect to changing flow rate. k increased from an average value of 3.05×10^{-3} at 0.5 ml/min to an average value of 3.38×10^{-3} at 1.6 ml/min, and then held constant at the higher flow rates, up to 2.5 ml/min. I interpret these data to show that at low flow rates, the reaction is diffusion limited; the fluid nearest the contact zone becomes saturated with dissolved CO_2 . At higher flow rates, the fluid is moving fast enough that saturation cannot occur, and the kinetics of the dissolution reaction dominate.

Simple geometric models indicate that the CO_2 /water interface is shaped like a spherical cap, indicating that the snapped-off CO_2 is forming a meniscus in the pore throat, limiting the surface area across which dissolution can occur.

Table of Contents

List of Tables	ix
List of Figures	x
Introduction.....	1
CO ₂ and Climate Change	1
Properties of CO ₂	4
Methods.....	8
General Approach	8
Aqueous Injections.....	9
Liquid and SC CO ₂ Injections.....	11
CO ₂ Dissolution Kinetics	13
Dissolved CO ₂ Injections	14
Results.....	16
Aqueous injections.....	16
Liquid and SC CO ₂ injections	16
CO ₂ Dissolution Kinetics	19
Dissolved CO ₂ Injections	20
Discussion	21
Conclusions.....	26
Tables	28
Figures.....	37
Appendix I: curves for all aqueous injections.....	55
0.6 mmol KH ₂ AsO ₄	55
0.7 mmol KH ₂ AsO ₄	59
0.8 mmol KH ₂ AsO ₄	63
0.9 mmol KH ₂ AsO ₄	67

<i>1.0 mmol KH₂AsO₄</i>	71
<i>3.0 mmol KH₂AsO₄</i>	75
<i>0.5 mmol NaBr</i>	77
<i>1.0 mmol NaBr</i>	79
<i>2.0 mmol NaBr</i>	81
<i>Dissolved CO₂ in 0.1 N CaCl₂</i>	83
Appendix II: curves for all liquid and SC CO ₂ injections.....	84
<i>Liquid CO₂ (28.5°C), 5 μL injections</i>	84
<i>Liquid CO₂ (28.5°C), 20 μL injections</i>	88
<i>Supercritical CO₂ (35°C), 5 μL injections</i>	97
<i>Supercritical CO₂ (35°C), 20 μL injections</i>	100
<i>Supercritical CO₂ (45°C), 5 μL injections</i>	107
<i>Supercritical CO₂ (45°C), 20 μL injections</i>	111
<i>Supercritical CO₂ (60°C), 5 μL injections</i>	119
<i>Supercritical CO₂ (60°C), 20 μL injections</i>	124
Appendix III: sample spreadsheet.....	132
References.....	146
Vita	148

List of Tables

Table 1: t of peak, vol. required for recovery, D_L and α for 200 μL injections of KH_2AsO_4 .	29
Table 2: t of peak, vol. required for recovery, D_L and α for 200 μL injections of NaBr .	30
Table 3: Time of min. pH, ΔpH , and vol. required for recovery for liquid CO_2 injections (28.5°C).	30
Table 4a: $C_{T_{\text{CO}_2}}$ as calculated from pH, injection loop volume, and carbon analyzer for all 5 μL liquid and SC CO_2 injections.	31
Table 4b: $C_{T_{\text{CO}_2}}$ as calculated from pH data and injection loop volume for all 20 μL liquid and SC CO_2 injections.	32
Table 5a: $\frac{C_{T_{\text{CO}_2}} \text{ (from pH)}}{C_{T_{\text{CO}_2}} \text{ (from loop vol.)}}$ as a percentage for all 5 μL CO_2 injections.	33
Table 5b: $\frac{C_{T_{\text{CO}_2}} \text{ (from pH)}}{C_{T_{\text{CO}_2}} \text{ (from loop vol.)}}$ as a percentage for all 20 μL CO_2 injections.	33
Table 6: Time of min. pH, ΔpH , and vol. required for recovery for supercritical CO_2 injections (35, 45, 60°C).	34
Table 7: k values for liquid and supercritical CO_2 injection experiments.	35
Table 8: Percent of measured CO_2 recovered by droplet shape models.	35
Table 9: Time of min. pH, ΔpH , vol. required for recovery, D_L and α for dissolved CO_2 injections.	36

List of Figures

Figure 1: Phase diagram for CO ₂ (17).	37
Figure 2: General flow-through setup.....	38
Figure 3: The CO ₂ -scrubbing apparatus used for all dissolved, liquid, and supercritical CO ₂ experiments.	38
Figure 4: CO ₂ droplet shape models.	39
Figure 5: Schematic of traveling valve used to transfer a sample of brine containing dissolved CO ₂	40
Figure 6a: A typical absorbance curve for a 200 μL aqueous injection of KH ₂ AsO ₄	41
Figure 6b: A typical absorbance curve for a 200 μL aqueous injection of NaBr.	41
Figure 7: A typical pH curve for a 20 μL injection of liquid CO ₂ (28.5°C).....	42
Figure 8: Mass balances for all liquid and CO ₂ injections.....	43
Figure 9: A typical pH curve for a 20 μL injection of supercritical CO ₂ (60°C).	45
Figure 10: Incremental [DIC] and pH over time.	45
Figure 11: A plot of $\ln[CO_2]$ v. time.....	47
Figure 12: A typical pH curve for a 20 μL injection of dissolved CO ₂	47
Figure 13: Example: time of maximum absorbance v. flow rate for KH ₂ AsO ₄ injections	48
Figure 14a: Absorbance peaks become narrower and sharper as flow rate is increased and dispersion decreases (KH ₂ AsO ₄).	48
Figure 14b: Absorbance peaks become narrower and sharper as flow rate is increased and dispersion decreases (NaBr).....	49

Figure 15: Comparison of a typical aqueous absorption (top) and dissolved CO₂ pH (bottom) curve.....50

Figure 16: Comparison of typical liquid and supercritical pH curves to a dissolved CO₂ injection.....51

Figure 17: Conceptual model: CO₂ snap-off and limited CO₂ surface area.52

Figure 18: the behavior of *k* in relation to flow rate for 5 μL injections.52

Figure 19: the behavior of *k* in relation to flow rate for 20 μL injections.53

Figure 20: Diffusion controls the reaction rate at low flow rates.53

Figure 21: Surface dissolution kinetics controls the reaction rate at higher flow rates.54

Introduction

CO₂ AND CLIMATE CHANGE

It is generally accepted that the global climate is changing, and the leading theory on the cause is anthropogenic greenhouse gases (1) enhancing the Earth's natural greenhouse effect. The natural greenhouse effect is part of the Earth's system (2), and it keeps the planet's temperature warm and stable (3). Many gases qualify as "greenhouse gases," including water vapor, CO₂, methane, and others (2, 3, 4).

A greenhouse gas works the same way that glass does in a greenhouse, hence the name (2). Sunlight can pass through most gases because it is shortwave radiation (5). After passing through the atmosphere, the sunlight hits the earth's surface and ~47% of it is absorbed (5). The earth's surface then radiates that energy back as longwave radiation, but greenhouse gases in the atmosphere block 95% of it, creating a warming effect (5).

CO₂ is not the most powerful greenhouse gas, but compared to water, which is (3), CO₂ has a long residence time (3, 4). Water vapor cycles in and out of the atmosphere on a daily or even hourly basis (5), whereas CO₂ can linger in the atmosphere for years (1, 3). In addition, CO₂ is abundant (3, 6), and becoming more so (1).

Since 1959, the average concentration of CO₂ in the atmosphere has increased from 315.98 ppm to 389.78 ppm (7), and annual mean global temperature has increased nearly 0.5°C in the same timespan (3). CO₂ is one of the byproducts of fossil fuel burning, and 86% of the world's energy comes from fossil fuels (1). In 2000, global emissions totaled 23.5 gigatons of CO₂, mostly from power plants and other large point sources (1). Reducing this number is a critical step in slowing global climate change. If the CO₂ could be collected and stored, its influence on the global carbon cycle and

climate could be mitigated. Carbon capture and sequestration (CCS) is one suggested solution to this problem.

CCS has become an important area of research because while there is a recognized need to shift away from fossil fuels, the national energy infrastructure is almost entirely dependent upon them (8). There will necessarily be a long transition period from fossil fuels to other resources, during which the effects of continued fossil fuel use will need to be mitigated (9), and CCS would fill this need.

Carbon capture and sequestration is the process of removing CO₂ from the atmosphere and storing it somewhere. CO₂ capture technologies are already in use today, most often utilized as a purification method for other industrial gases (1). CO₂ is also extracted for use in enhanced oil recovery (EOR), a common, proven practice (10). CO₂ produced as a byproduct of oil and gas is captured and used on site (10). CO₂ is pumped back into the subsurface, where it mixes with remaining hydrocarbons, creating a fluid that is easier to extract than hydrocarbon alone (10). The additional hydrocarbons recovered using this technique offset the cost of the CO₂ capture and pumping, and depending on the price of oil and gas, may even increase net profit (1). This use, however, does not qualify as sequestration, because the CO₂ used in EOR is not captured from the atmosphere; it is extracted from the subsurface (9). EOR does prove, however, that carbon capture technologies are robust.

There are many potential storage options, once CO₂ has been captured. CO₂ reservoirs include soils, vegetation, sediments and rocks, the atmosphere, the top layer of the ocean, and the deep ocean (5). The two largest reservoirs are sediments and rocks (6.6×10⁷ gigatons), and the deep ocean (3.8×10⁴ gigatons) (5). In comparison, soil and vegetation together (the biosphere) only contain 2,170 gigatons (5). The deep ocean and rock reservoirs have the lowest exchange rates with the global carbon cycle; the deep

ocean exchanges 37 gigatons per year, while sediments and rocks only exchange 0.2 gigatons per year (5). Because of their size and their residence times, the deep ocean and rock reservoirs are the best options for carbon sequestration.

Because the ocean is potentially a huge reservoir for excess CO₂, deep-ocean injections of CO₂ have begun on a small-scale test basis (1). The CO₂ is injected at 1,000 meters or deeper, so that it is below the well-mixed surface layer and remains in the liquid phase (1). The residence time for such injections is predicted to be “at least several hundreds of years” (1).

Injecting CO₂ into the oceans also changes the pH of the surrounding waters, and although the long-term effects of these pH changes on the ocean ecosystem have not been studied (1), changes in the surface layer of the ocean have already been seen (11). The pH of ocean surface waters has dropped by 0.1 (1), simply because the ocean is naturally taking up more CO₂ as it accumulates in the atmosphere (11). Experiments have been conducted with organisms that live near the ocean’s surface, exposing them to elevated CO₂ levels. These organisms showed “reduced rates of calcification, reproduction, growth, circulatory oxygen supply and mobility” (1). Given that the annual trade in seafood is worth \$55 billion (12), the oceans are a critical resource, and until we know more about how CO₂ sequestration will affect them, geological storage presents an excellent alternative.

Geological storage of CO₂ is potentially the best option for several reasons; the technologies required to implement it exist, it can often be done at a location near the CO₂ source, the storage capacity is large, and the residence times are long (1, 9). EOR is an excellent example of extant technologies that could easily be adapted for use in large-scale carbon capture, transport and sequestration. The technologies would simply have to

be scaled up and applied to the most effective capture locations, namely large point sources of CO₂, such as coal-burning power plants (1, 8).

Potential geologic storage sites are widespread, existing in such diverse formations as carbonates, sedimentary basins, basalts, saline aquifers, and depleted hydrocarbon reservoirs (8). While transport of CO₂ is already an established technology (10), the ability to sequester CO₂ near its point of production would be very valuable. It would eliminate transport costs, and reduce the chance of leakage (10). The final step of CO₂ sequestration involves pumping equipment, similar to or the same as that already in use in oil fields around the world (1). Because most, if not all, of the technologies exist, geologic storage is also less expensive than other potential methods. According to the Intergovernmental Panel on Climate Change, it would cost between 0.5 and 8.0 US\$ per ton of CO₂ stored. If the benefits of EOR are factored in, even with an outdated assumed price of 15-20 US\$ per barrel of oil, each ton of CO₂ earns 10-16 \$US (1).

Recognizing the need to develop CCS technologies, in 2009 the US Department of Energy created 46 Energy Frontier Research Centers (EFRCs), designed to “harness the most basic and advanced discovery research in a concerted effort to establish the scientific foundation for a fundamentally new U.S. energy economy” (13). The Center for Frontiers of Subsurface Energy Security (CFSES) at UT is one of these EFRCs, focused on subsurface energy. The Center is tasked with investigating “the transport of native and injected fluids, particularly carbon dioxide, in geological systems” at the sub-pore to pore scale (14).

PROPERTIES OF CO₂

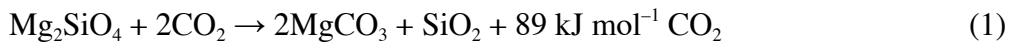
To investigate this problem, it is critical to understand what happens to CO₂ during sequestration. Once the CO₂ has been captured, it must be compressed into a

liquid so that it can be transported and pumped. CO₂ only becomes a liquid at temperatures above -56.6°C and pressures greater than 75.13 psi (15).

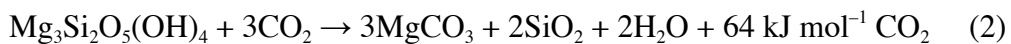
When it is pumped into the subsurface, the higher temperature at depth causes the CO₂ to become a supercritical fluid (16). Supercritical fluids are neither liquid nor gas, but display properties of both; density is similar to a liquid, but viscosity and compressibility are like a gas. CO₂ becomes a supercritical fluid above 30.85°C and 1069 psi, conditions that exist in many carbon sequestration sites (16). Small changes in temperature and/or pressure can cause large changes in the behavior and properties of a supercritical fluid (Figure 1)(17). Supercritical (SC) CO₂ is a non-wetting, non-aqueous fluid that is less dense than water, so there are three main mechanisms for trapping it in the subsurface (16). Firstly, the CO₂ can form a hydrophobic layer that floats on top of the groundwater, up against an impermeable sealing formation (16). This is the least secure situation for the CO₂, as the buoyant fluid will naturally exploit any fractures in the rock, migrating upwards towards the surface, and escape back into the atmosphere (10).

The second method of trapping the CO₂ is through dissolution into the water along the CO₂/water contact (16). Once the CO₂ has dissolved, it is no longer buoyant. It can also react with the surrounding minerals (8, 16), in a similar reaction to classic silicate weathering (1). Metal oxides react naturally with CO₂, and the following are the most thermodynamically favored (1):

Olivine:



Serpentine:



Wollastonite:



By strategically injecting CO₂ into silicate-rich formations or alkaline aquifers, these reactions can be exploited (1). If such a reaction occurs, the CO₂ will be incorporated into a solid, the third and most secure form of sequestration (16).

These trapping mechanisms are the accepted conceptual models (1), but they have not been thoroughly tested or investigated. The dissolution of CO₂ into water is a key step in the carbon sequestration process; how quickly the dissolution occurs and what controls it will dictate how long the CO₂ resides in the subsurface as a separate phase.

The rate at which injected CO₂ dissolves and moves into an injection site will affect the overall efficiency of the sequestration process: if the CO₂ remains concentrated around the injection well, then it will delay the injection of more CO₂. Conversely, if the CO₂ quickly dissolves into the subsurface fluids and is transported throughout the injection site, then pumping can proceed at a faster pace (14).

The kinetics of the initial dissolution reaction, while assumed to be fast, have not been measured. According to Berner (18), dissolution rates of minerals can be controlled by the rate of transport of ions away from the dissolving surface, the rate at which ions or molecules detach from the surface, or a combination of the two. Berner (18) states that “increased renewal of water, or flushing, accelerates the dissolution of minerals ... only up to a limiting flushing rate beyond which flushing has virtually no effect and dissolution is controlled solely by mineral reactivity.”

The purpose of this research was to investigate the dissolution of liquid and supercritical CO₂ into water, to determine the controls on dissolution rate, and I proposed the following questions: 1. What is the fundamental kinetics of SC CO₂ dissolution into water? 2. How fast does dissolved CO₂ diffuse away from the source point? 3. What geochemical conditions influence the dissolution rate?

If we can answer these questions we will be a step closer to understanding exactly how carbon sequestration works, because we will have a better grasp of the underlying physics that dictate how long CO₂ will linger in the subsurface, and how long it will influence the local geochemistry.

Methods

GENERAL APPROACH

Flow-through column experiments were done using a stainless steel column (1 cm diameter, and 25 cm height) packed with quartz sand (590-640 μm) and flushed with 3 mmol NaCl as an analog for a CO_2 injection site. Column porosity and average pore size were determined using a CT scan of a Peek column packed with the same sand (19). Porosity was also determined by dividing the weight of the sand by the density of quartz (20) to determine the volume of the sand:

$$\frac{\text{grams } \text{SiO}_2}{2.65 \text{ (g/cm}^3\text{)}} = \text{sediment vol.} \quad (4)$$

$$\left(1 - \frac{\text{sediment vol.}}{\text{column vol.}}\right) * 100 = \% \text{ porosity} \quad (5)$$

The column was oriented vertically inside a Brinkmann column heater, with flow from bottom to top. Continuous measurements were recorded by a tunable UV absorbance detector and a flow-through pH electrode downstream of the column (Figure 2). Bromide and arsenate tracer tests were run to characterize the hydraulic behavior of the column. An injection loop at the inflow end of the column could be adjusted for volume (5-200 μL), and to accept the three required injection types: a supercritical fluid, a self-contained pressurized coil, or syringe injections of aqueous tracer solutions.

CO_2 injections were done at four temperatures and seven flow rates, with the NaCl solution buffered to pH 10 with 0.1 N NaOH. To prevent atmospheric CO_2 from entering the system, the mobile phase reservoir headspace was isolated using a CO_2 -

scrubber (Figure 3). For CO₂ injections into 1.5 ml/min flow, the outflow was collected 10 mls at a time in glass syringes attached directly to a 3-way Luer Lock valve. Two syringes were attached to the valve at all times so that new syringes could be switched into the flow with no loss of pressure. Each incremental sample was analyzed immediately in an Apollo 9000 Combustion TOC Analyzer for dissolved inorganic carbon (DIC).

The DIC data for each sample were reported in ppm, and converted to moles as follows:

$$\frac{\text{ppm}}{12 \text{ mg/mmol} / 1000 \text{ mg}} = \text{moles C} \quad (6)$$

Total DIC measured in this way was compared to total DIC calculated from the pH measurements (see Liquid and SC CO₂ Injections section below). The data matched well, and pH data alone were collected for the remainder of the CO₂ experiments.

AQUEOUS INJECTIONS

Injections of dissolved salts were the first experiments run on the apparatus. These injections served to characterize the hydraulic behavior of the column. All injections were 200 μL, and the two tracers used were NaBr and KH₂AsO₄.

Experiments were run for Br⁻ concentrations of 0.5, 1.0 and 2.0 mmol, at flow rates of 0.5, 1.0, 1.5, 2.0 and 2.5 mls/min. Experiments were run for AsO₄³⁻ concentrations of 0.6, 0.7, 0.8, 0.9 and 1.0 mmol, at flow rates of 0.5 to 1.5 mls/min, at intervals of 0.1 ml/min. One set of injections was run with 3.0 mmol AsO₄³⁻, at flow rates of 0.5, 1.0, 1.5, 2.0 and 2.5 mls/min. Data were recorded using a PC running the PeakSimple software Peak3.56, which recorded absorbance from the UV spectrophotometer at 1 Hz for the length of the run.

The collected data were exported into Excel. Time of breakthrough and time of recovery were chosen by hand off a plotted curve of the data, as the baseline absorption values fluctuated due to the sensitivity of the detector, and made a single baseline value difficult to calculate. Time of maximum absorption was calculated using the MAX function in Excel.

The dispersion coefficient (D_L) for each run was calculated as follows (21):

$$D_L = \left(\frac{V_x L}{8} \right) * (J_{0.84} - J_{0.16})^2 \quad (7)$$

$$V_x = \frac{\text{flow rate}_{(ml/s)}}{(\text{cross - sectional area} * \text{porosity})} \quad (8)$$

L = length ,

$$J_{0.84} = \frac{(U - 1)}{U^{1/2}}, \text{ when } C/C_{\max} = 0.84 \quad (9)$$

$$J_{0.16} = \frac{(U - 1)}{U^{1/2}}, \text{ when } C/C_{\max} = 0.16 \quad (10)$$

$$\text{pore volumes } U = \frac{\left(\frac{\text{flow rate}_{(ml/min)}}{60} \right) * \text{time of recovery}}{\text{porosity}} \quad (11)$$

C = solute concentration

Dispersivity (α_L) was calculated as follows (21):

$$\alpha_L = \frac{D_L - D^*}{V_x} \quad (12)$$

$$\text{effective diffusion coefficient } D^* = D_d * \omega \quad (13)$$

$$D_d = 2.01 \times 10^{-9} \text{ m}^2 / \text{s} \quad (21) \quad (14)$$

$$\omega = 0.7 \quad (21) \quad (15)$$

LIQUID AND SC CO₂ INJECTIONS

Injections of liquid CO₂ were performed with the column and injection loop temperature set to 28.5°C. At flow rates of 0.1, 0.5, 1.0 and 1.5 mls/min, the injections were 5 µL in volume; at flow rates of 1.0, 1.5, 1.6, 1.7, 2.0 and 2.5 mls/min, the injection volume was 20 µL. The injection loop was connected directly to a supercritical fluids pump running at a set pressure of 1,500 psi (Figure 2).

For each injection, the supercritical fluids pump pressure (psi), column temperature (°C) and room temperature (°C) were recorded at the beginning of the run. Data for pH were recorded by a PC running DataStudio, which recorded a measurement from the pH electrode every 15 seconds, starting at the moment of injection.

Injections of supercritical CO₂ were performed with the column and injection loop temperature set to 35, 45 and 60°C, using the same procedure as the liquid CO₂ injections.

For both liquid and SC CO₂ injections, because the mobile phase was buffered to pH 10 with NaOH, the CO₂ dissolution reactions are:



Therefore, pH was converted to [CO₂] as follows:

At all pH,

$$[Na^+] = 10^{-(14-pH_i)} \quad (16)$$

$$[H^+] = 10^{-pH} \quad (17)$$

$$[OH^-] = \frac{K_w}{[H^+]} \quad (18)$$

At $pH \leq 8.3$, it was assumed that $[CO_3^{2-}]$ was negligible (22). Therefore, for each data point with $pH \leq 8.3$:

$$[HCO_3^-] = [Na^+] + [H^+] - [OH^-] \quad (19)$$

$$[H_2CO_3] = \frac{[HCO_3^-][H^+]}{K_{a1}} \quad (20)$$

$$C_{TCO_2} = [H_2CO_3] + [HCO_3^-] \quad (21)$$

For data points with $pH \geq 8.4$, it was assumed that $[H_2CO_3]$ was negligible (22). Therefore, for each data point with $pH \geq 8.4$:

$$C_{TCO_2} = [Na^+] + [H^+] - [OH^-] \quad (22)$$

The C_{TCO_2} measurements for each injection were summed for the total calculated number of moles CO_2 . For each experiment the number of moles CO_2 injected was determined as follows, under the assumption that the injection loop volume was accurate:

$$\rho_{(g/\mu l)} * inj. \text{ loop vol}_{(\mu l)} = \text{grams } CO_2 \quad (23)$$

$$\frac{\text{grams } CO_2}{44_{(g/mol)}} = \text{moles } CO_2 \quad (24)$$

Density was calculated using the MIT online CO_2 properties calculator (23) and the temperature and pressure recorded at the time of injection.

A mass balance calculation was performed for each liquid and SC CO_2 injection, comparing the injected number of moles to the measured number of moles:

$$\frac{\text{measured moles } CO_2}{\text{injected moles } CO_2} * 100 = \text{percent } CO_2 \text{ recovered} \quad (25)$$

CO₂ DISSOLUTION KINETICS

The overall dissolution reaction rate is $R = -k[CO_2]^n$. If the reaction rate is proportional to $[CO_2]$, then $n=1$, $R = -k[CO_2]$, and the reaction is 1st-order. If the reaction is 1st-order, a plot of $\ln[CO_2]$ v. *time* will be linear, and the slope of the line will equal $-k$. A k value was determined for each CO₂ injection by fitting a trendline in Excel to the longest linear section of the $\ln[CO_2]$ v. *time* plot.

Because the dissolution of liquid or SC CO₂ into water is a surface dissolution reaction, the units of $[CO_2]$ are cm²/unit volume. The unit volume was dependent on the flow rate and the measurement interval, and was easily calculated:

$$\frac{\text{flow rate}_{(\text{mls}/\text{min})}}{15/60} = \text{mls}/\text{data point} \quad (26)$$

The surface area of the CO₂, however, was more difficult to constrain. If, for example, the CO₂ in the column was a spherical droplet, then the $[CO_2]$ at a given measurement could be used calculate the radius, and thus the volume, of the CO₂ droplet at that moment:

$$r_{\text{sphere}} = \sqrt{\frac{[CO_2]}{4\pi}} \quad (27)$$

$$V_{\text{sphere}} = \frac{4}{3}\pi r^3 \quad (28)$$

By calculating the volume of the sphere for each data point and summing those volumes, a total injected volume of CO₂ was determined. After converting the total volume to moles CO₂ using the density provided by the MIT calculator, the model result

was compared to the measured DIC. If the two results matched, then the theoretical shape was accepted as a good model for the actual shape and surface area of the CO₂ droplet(s).

Other theoretical models tested included a cube, a hemisphere and a spherical cap with the radius set to 0.05 cm (Figure 4). Volumes were determined as follows:

$$s_{cube} = \sqrt{\frac{[CO_2]}{6}} \quad (29)$$

$$V_{cube} = s^6 \quad (30)$$

$$r_{hemisphere} = \sqrt{\frac{[CO_2]}{2\pi}} \quad (31)$$

$$V_{hemisphere} = \frac{4}{6} \pi r^3 \quad (32)$$

$$h_{sph. cap} = \frac{[CO_2]}{2\pi r} \quad (r = 0.05) \quad (33)$$

$$V_{sph. cap} = \frac{\pi h}{6} (3r^2 + h^2) \quad (34)$$

DISSOLVED CO₂ INJECTIONS

Injections of an aqueous fluid equilibrated to high-pressure gaseous CO₂ were conducted to act as a control for the liquid and SC CO₂ injections. Because the CO₂ in these injections was already dissolved, the possible influence of dissolution kinetics was eliminated.

Brine and high-pressure gaseous CO₂ were allowed to equilibrate, and then an isolated loop was used to transfer a 20 μL sample of the brine to the column without a loss of pressure (Figure 5). Data were recorded by a PC running the DataStudio software, which recorded a measurement from the pH electrode every 15 seconds for the length of the run.

pH was converted to [CO₂] as for the liquid and SC CO₂ injections, while D_L and α were determined as for the aqueous tracer injections.

Results

AQUEOUS INJECTIONS

All successful injections resulted in near-symmetrical, bell-shaped absorption curves (Figure 6a, 6b). Column porosity was 0.4 according to the CT scan and 0.52 according to the bulk density calculations, although a large void had formed at the top of the column, so the bulk density value is likely high. Average pore size was 0.125 μL ($\pm 50\%$), with a total pore volume of 8 ml, according to the CT scan.

Time of maximum absorption for the AsO_4^{3-} injections decreased with flow rate, from an average of 1,188 seconds at 0.5 mls/min to an average of 409 seconds at 1.5 mls/min. The number of pore volumes required to return to initial conditions varied from 0.60 to 0.41, but did not show a clear trend in relation to flow rate. Dispersivity values for the arsenate injections ranged from an average of 7.04 cm at 0.5 mls/min to an average of 8.33 cm at 1.5 mls/min, showing an increase in dispersivity with increasing flow rate (Table 1).

The time of maximum absorption for the NaBr injections decreased with flow rate, from an average of 1,722 seconds at 0.5 mls/min to an average of 271 seconds at 2.5 mls/min. The number of pore volumes required to return to initial conditions varied from 1.25 to 1.55, but did not show a clear trend in relation to flow rate. Dispersivity values for the bromide injections ranged from an average of 2.18 cm at 0.5 mls/min to an average of 9.18 cm at 2.5 mls/min, increasing with flow rate (Table 2).

LIQUID AND SC CO_2 INJECTIONS

All liquid CO_2 injections produced a precipitous drop in pH, followed by a gradual recovery back to the initial pH (Figure 7). The average change in pH was 5.6.

If CO₂ dissolution is assumed to be very fast and not rate limiting, the dispersivity values for the CO₂ injections were much higher than for the aqueous tracer injections: at 1.0 ml/min, $\alpha = 1.23 \times 10^9$ cm for the liquid CO₂ versus an average of 9.93 cm for arsenate, and an average of 3.51 cm for bromide. However, dissolution kinetics do play a role, so these values are only “apparent dispersivity” and are not useful as a comparison.

[CO₂], as calculated from the pH data, rose abruptly after injection and returned gradually to baseline values. The number of pore volumes required to return to baseline values averaged 17.61 for the 5 μ L injections, and 50.82 for the 20 μ L injections (Table 3).

Results for $C_{T_{CO_2}}$ as calculated from the pH data varied widely (Table 4a, 4b). For the 5 μ L injections, the minimum $C_{T_{CO_2}}$ was 2.88×10^{-5} moles (at 1.0 ml/min) while the maximum was 9.05×10^{-5} moles (at 1.5 mls/min). For the 20 μ L injections, the minimum $C_{T_{CO_2}}$ was 7.42×10^{-5} moles (at 1.0 mls/min) while the maximum was 6.64×10^{-4} moles (at 1.7 mls/min). Assuming the injection loop size was accurate, average injected $C_{T_{CO_2}}$ would be 9.04×10^{-5} moles for the 5 μ L injections and 3.61×10^{-4} moles for the 20 μ L injections, with small variances due to the slight differences in CO₂ density between injections (Table 4a, 4b).

Mass balance calculations showed very inconsistent values for the percent CO₂ recovered during each injection (Table 5a, 5b, Figure 8). The minimum CO₂ recovered was 20.62%, from a 20 μ L injection into 1.0 ml/min flow. The maximum was 214.08%, from a 20 μ L injection into 1.7 mls/min flow. Only two injections were within 10% of 100% recovery: 5 μ L into 1.5 mls/min flow and 20 μ L into 2.0 mls/min flow.

All SC CO₂ injections produced a precipitous drop in pH, followed by a gradual recovery back to the initial pH (Figure 9). The average change in pH was 5.7. Apparent dispersivity was again much higher than the aqueous tracer injections: $\alpha = 1.23 \times 10^9$ cm,

4.08×10^4 cm and 2.37×10^9 cm at 1.0 ml/min for the SC CO₂ at 35, 45 and 60°C respectively, versus an average of 9.93 cm for arsenate, and an average of 3.51 cm for bromide.

[CO₂] rose abruptly and returned gradually to baseline values. The number of pore volumes required to return to baseline averaged 41.77 for the 5 μL injections, and 52.35 for the 20 μL injections at 35°C; 15.70 for the 5 μL injections, and 43.93 for the 20 μL injections at 45°C; and 17.71 for the 5 μL injections, and 55.97 for the 20 μL injections at 60°C (Table 6).

$C_{T_{CO_2}}$ as calculated from the pH data varied widely (Table 4a, 4b). For the 5 μL injections, the minimum $C_{T_{CO_2}}$ was 7.33×10^{-5} moles at 35°C (at 1.5 mls/min), 5.72×10^{-5} moles at 45°C (at 0.5 mls/min) and 8.49×10^{-5} moles at 60°C (at 1.0 ml/min). The maximum $C_{T_{CO_2}}$ was 1.21×10^{-4} moles at 35°C (at 0.5 mls/min), 9.24×10^{-5} moles at 45°C (at 1.5 mls/min) and 1.63×10^{-4} moles at 60°C (at 0.5 mls/min)..

For the 20 μL injections, the minimum $C_{T_{CO_2}}$ was 7.66×10^{-5} moles at 35°C (at 1.0 ml/min), 1.01×10^{-4} moles at 45°C (at 1.0 ml/min) and 6.87×10^{-5} moles at 60°C (at 1.0 ml/min). The maximum $C_{T_{CO_2}}$ was 5.92×10^{-4} moles at 35°C (at 1.6 mls/min), 5.62×10^{-4} moles at 45°C (at 1.6 mls/min) and 5.81×10^{-4} moles at 60°C (at 2.5 mls/min).

Assuming the injection loop size was accurate, average injected $C_{T_{CO_2}}$ would be 8.29×10^{-5} moles for the 5 μL injections and 3.31×10^{-4} moles for the 20 μL injections at 35°C; 6.31×10^{-5} moles for the 5 μL injections and 2.49×10^{-4} moles for the 20 μL injections at 45°C; and 3.56×10^{-5} moles for the 5 μL injections and 1.46×10^{-4} moles for the 20 μL injections at 60°C (Table 4a, 4b). Small variances were due to the slight differences in CO₂ density between injections.

Mass balance calculations showed very inconsistent values for the percent CO₂ recovered during each injection (Table 5a, 5b, Figure 8). The minimum CO₂ recovered at

35°C was 23.19%, from a 20 µL injection into 1.0 ml/min flow. The maximum was 179.34%, from a 20 µL injection into 1.6 mls/min flow. The minimum CO₂ recovered at 45°C was 39.93%, from a 20 µL injection into 1.0 ml/min flow. The maximum was 220.75%, from a 20 µL injection into 1.6 mls/min flow. The minimum CO₂ recovered at 60°C was 47.10%, from a 20 µL injection into 1.0 ml/min flow. The maximum was 455.68%, from a 5 µL injection into 0.5 mls/min flow. Across all three temperatures, only three injections were within 10% of 100% recovery: 5 µL into 0.5 mls/min flow, 5 µL into 1.0 ml/min flow and 20 µL into 1.5 mls/min flow, all at 45°C.

$C_{T_{CO_2}}$ as calculated from pH matched $C_{T_{CO_2}}$ as measured by the carbon analyzer to within an average of 151.2% (Table 4a, 4b, Figure 10), indicating that the $C_{T_{CO_2}}$ values as calculated from pH were more accurate than the $C_{T_{CO_2}}$ values given by the injection loop. Bubbles and/or void space in the injection apparatus, may have caused the inaccuracies, or changes in pump pressure near the time of injection could have caused large changes in the CO₂ density.

CO₂ DISSOLUTION KINETICS

Plots of $\ln[CO_2]$ v. *time* always showed a linear section in the part of the graph where pH was returning to baseline (Figure 11). The rate of the reaction in these sections was independent of [CO₂]. Values of k (Table 7) ranged from 1.6×10^{-3} (28.5°C, 20 µL, 1.0 ml/min) to 6.6×10^{-3} (35°C, 5 µL, 1.5 mls/min). In cases where the graph shows more than one linear section, the k value was determined using the longest linear section. The multiple sections are most likely the result of snapped-off CO₂ remobilizing as dissolution causes the CO₂ droplet to shrink until it is small enough to move with the bulk fluid.

The spherical cap model for CO₂ droplet shape was the best fit, consistently producing the closest volume to the actual injected volume of CO₂ (Table 8). The best result, 116.21% of the actual volume, was for a 5 µL injection at 45°C into 0.5 mls/min flow. The cube model was consistently the worst, with its best result only accounting for 7.29% of a 5 µL injection at 60°C into 1.5 mls/min flow.

DISSOLVED CO₂ INJECTIONS

All dissolved CO₂ injections produced a near-symmetrical, bell-shaped pH curve (Figure 12). The average change in pH was 3.9. Dispersivity values were much higher than those calculated for the aqueous tracer injections at equivalent flow rates: $\alpha = 2.34 \times 10^{10}$ cm at 1.0 ml/min for the dissolved CO₂ versus an average of 9.93 cm for arsenate, and an average of 3.51 cm for bromide (Table 9). The average number of pore volumes required to return to initial conditions was 7.9.

Discussion

The contrast between the quick recovery of the conservative tracer tests and the delayed recovery to baseline of the liquid and SC CO₂ experiments indicates that something besides dispersivity is affecting the behavior of the injected CO₂. The behavior of the conservative tracers was as expected: breakthrough occurred at one column volume, calculated using a 40% porosity value of 8 ml (Figure 6a, 6b, Appendix I); the height of the absorption peak was dependent on concentration, and the time the peak occurred was dependent on flow rate (Figure 13). Transport is conservative for both Br⁻ and AsO₄³⁻. The dispersion coefficient (D_L) and dispersivity (α) values seen in the aqueous injections indicate a decrease in dispersion with an increase in flow rate (Table 8). In other words, the higher the flow rate, the earlier the peak occurs, and the sharper, taller and narrower it becomes (Figure 14a, 14b, Appendix I). These behaviors indicate that higher flow rates lead to a faster return to initial conditions, as expected.

The CO₂ tests were also expected to show conservative behavior, and the dissolved CO₂ pH curves matched closely with the aqueous injection curves (Figure 15, Appendix I), displaying a near-symmetrical bell shape. Thus, transport of CO₂ dissolved in water is conservative. The liquid and SC CO₂ injections, however, behaved differently. The current conceptual model of CO₂ dissolution dictates that dissolution is nearly instantaneous, and thus the CO₂ will behave as a conservative tracer would. However, these experiments show that the pH curves were not bell-shaped, and the recovery time was always long, sometimes ten times as long as for the conservative tracer tests (Figure 16, Appendix II).

At all temperatures and flow rates, and for both injection sizes, all the CO₂ injections generated long, trailing breakthrough curves (Appendix II). The long recovery

times were hypothesized to be a result of the CO₂ separating into droplets immediately after injection, and those droplets becoming trapped in the sediment (Figure 17). The average pore size was only 0.125 μL (±50%) (19), while the smallest injection size was 5 μL, so multiple pores must have been filled. Once the CO₂ had snapped off in the pores, it became immobile and could only dissolve into the bulk fluid across the limited surface area where CO₂ and fluid were in direct contact with one another (Figure 17). The CO₂ was thus trapped in the column, and delayed the pH recovery. Calculating the dispersivity for the liquid and SC CO₂ injections was not useful, as snap-off and dissolution kinetics interfered with dispersion and made comparisons impossible.

The mass balance calculations implied that there was little consistency in injection size for the liquid and SC CO₂ injections. For the fourteen liquid CO₂ experiments, only two injections were within 10% of 100% recovery: 5 μL into 1.5 mls/min flow and 20 μL into 2.0 mls/min flow. This indicates some problem with the injection apparatus, and the results of the SC CO₂ experiments show that it was worse at higher temperatures: out of thirty-seven SC CO₂ experiments, only three injections were within 10% of 100% recovery: 5 μL into 0.5 mls/min flow, 5 μL into 1.0 ml/min flow and 20 μL into 1.5 mls/min flow, all at 45°C.

When total CO₂ as measured by the carbon analyzer was compared to total CO₂ as calculated from pH, the data matched to within 151.2%. The mass balance calculations comparing total CO₂ as calculated from pH to total CO₂ injected were done under the assumption that the injection loop volumes were accurate and consistent. However, the physical properties of SC CO₂, especially density, change rapidly with changes in temperature and pressure, and a slight difference in either of these parameters from injection to injection could cause large differences in injection volume. In addition, experiments run on similar equipment by Gilbert and Wolfe (24) showed that tiny

bubbles in the CO₂ lines are almost impossible to avoid, and can have a huge effect on the calculated volume. Thus, the size of the injection loop could not be used as an accurate measure for the actual amount of injected CO₂, and the inaccuracy of the mass balances could be dismissed.

From the linear nature of the $\ln[CO_2]$ v. *time* plots (Figure 11), we know that the CO₂ dissolution reaction is 1st-order. The k values generated from the $\ln[CO_2]$ plots showed an increasing trend with increasing flow rates. For all temperatures, the 5 μ l injections (0.5-1.5 ml/min) showed an increase in k with an increase in flow rate (Table 7, Figure 18). The same trend is visible in the 20 μ l injections at the lower flow rates (1.0-1.5 ml/min), but k stops increasing at flow rates higher than 1.5 ml/min (Table 7, Figure 19). In general, k increased from an average value of 3.05×10^{-3} at 0.5 ml/min to an average value of 5.7×10^{-3} at 1.5 ml/min, and then held constant at the higher flow rates, up to 2.5 ml/min. This behavior was present across all temperatures, for both liquid and SC CO₂ injections, implying that the density of the CO₂ does not affect the dissolution reaction.

The relationship between diffusion and surface dissolution explains the trend in the k values. At low flow rates, the bulk fluid nearest the CO₂ surface becomes saturated with CO₂ and the available OH⁻ is reacted. If the fluid nearest the CO₂ surface is in equilibrium with CO₂, no more dissolution will occur until diffusion dilutes the CO₂ into the bulk fluid (Figure 20). Thus, diffusion is the limiting factor. As flow rate increases, however, diffusion increases as the fluid nearest the CO₂ begins to get flushed away and replaced with unsaturated fluid. Eventually, the flow rate is high enough to outpace diffusion altogether, and k ceases to increase. The fluid nearest the CO₂ surface is moved away before it can become saturated (Figure 21), and the surface dissolution reaction becomes the rate-limiting step. This is very similar to the model presented by Berner

(18), with the only difference being that instead of a mineral surface, it is being applied to a fluid/fluid interface.

The shape of the CO₂/water contact also influences reaction rate, simply because if there is more surface area for the reaction to occur across, then the reaction will progress at a faster rate. The spherical cap model provides the best fit to the data, indicating that the trapped CO₂ is forming a meniscus in the pore throat. Whether the meniscus is convex or not would have no effect on reaction rate, as the shape of the surface would remain the same either way. The depth of the meniscus, however, would affect reaction rate; a parabolic model would allow for more surface area than the spherical cap model analyzed here.

The physical properties of the CO₂ could also affect the droplet shape – the meniscus formed by liquid CO₂ will have a different curvature than one formed by SC CO₂. Because small changes in temperature and pressure can result in large changes in the physical properties of SC CO₂, the shape of the CO₂/fluid contact is likely to change with temperature and pressure as well. This variability in physical properties makes it very difficult to characterize the behavior of SC CO₂ in an aquifer where the temperature and pressure will vary with time and location. Modeling the behavior of CO₂ in the subsurface is a major goal of the EFRC, and the ability to constrain CO₂ dissolution rates will be a critical tool in achieving this goal, as will the ongoing work by Chaudhary (19) with CT scanning.

The relationship between diffusion and surface dissolution, and the shape of the CO₂/water contact will impact the results seen during carbon sequestration. The flow rates used in these experiments are very high compared to those found in actual injection sites; a typical hydraulic conductivity for a good aquifer is 15 m/day (25). At these slower flow rates, diffusion will control the rate of CO₂ dissolution. The amount of CO₂

that can go into solution is thus limited, and if the CO₂ cannot dissolve quickly, it will linger in the subsurface as a supercritical fluid or in its liquid phase.

If the CO₂ lingers for longer than expected, it may cause more mineral dissolution than planned, or a wider zone of decreased pH than anticipated. Future work will address this issue, as the inert quartz sand in the column will be replaced with more realistic mineral assemblages. Determining how the CO₂ affects the minerals and how the minerals affect the snap-off and movement of the CO₂ is the next step in answering some of the questions this research has raised.

The rate at which the injected CO₂ dissolves and disperses throughout an injection site will affect the overall efficiency of the sequestration process. If the CO₂ remains as an immiscible fluid concentrated around the injection well, then the injection of more CO₂ will be delayed. Conversely, if the CO₂ immediately dissolves into the subsurface fluids and is quickly transported throughout the injection site, then pumping can proceed at a faster pace (14). Future experiments examining how clay minerals, for instance, are affected by the injection of CO₂, will help solve this problem.

Even if the permeability of the injection site is somehow unaffected, this research indicates that the dissolution of SC CO₂ into water is slower than expected. This in turn means that the residence time of injected CO₂ is likely to be longer than first thought. Other considerations aside, longer residence times will simply increase the benefit gained through carbon sequestration..

Conclusions

The kinetics of supercritical CO₂ dissolution into water are complex when the two fluids are interacting within porous media. The snap-off of the CO₂ will effectively cause SC CO₂ to be trapped in the pores, increasing the length of time over which it can influence the subsurface geochemistry. Once dissolved, the transport of CO₂ is conservative, but the dissolution process is not as straightforward, nor as rapid, as assumed under present conceptual models.

The dissolution of liquid and SC CO₂ into water is controlled by diffusion at low flow rates, and surface dissolution kinetics at higher flow rates. At low flow rates, the fluid nearest the CO₂ surface becomes saturated with CO₂. Once the fluid nearest the CO₂ surface is in equilibrium with CO₂, no more dissolution will occur until diffusion can dilute the CO₂ into the fluid. Thus, diffusion is the limiting factor.

As flow increases, k increases as well, as diffusion and flow both dilute the CO₂-saturated zone. As flow continues to increase, the fluid near the CO₂ is flushed away before it can become saturated, and dissolution kinetics control the dissolution rate. The limiting step transitions from diffusion to surface dissolution kinetics at a flow rate of approximately 1.5 ml/min. At flow rates higher than 1.5, $k = 0.0025$ (28.5°C), $= 0.0047$ (35°C), $= 0.0042$ (45°C), $= 0.003$ (60°C).

The shape of the CO₂ droplet also influences the rate of CO₂ dissolution, because if there is more surface area, there will be more dissolution. The best model for the shape of the CO₂/water contact was a spherical cap, implying that the snapped-off CO₂ forms a meniscus in the pore throat. More work is needed to determine the exact shape, as the curvature of the meniscus may change with temperature and pressure, and CT scanning holds great promise for solving this problem.

Further investigation of the CO₂ dissolution process is needed; the column and sediment used in this experiment were designed to be as unreactive as possible, and any injection site chosen for carbon sequestration in the field will certainly not be inert. Future work using a more realistic mineral assemblage is likely to yield more complex, but more realistic results.

Tables

Aqueous injections of 200 μL KH_2AsO_4 at 28.5° C					
[KH_2AsO_4]=0.6 mmol	Flow rate (ml/min)	t of max. abs. (sec)	col. volumes to recover (40% porosity)	D (cm^2/sec)	α (cm)
	0.5	xx	xx	xx	xx
	0.6	993	0.6	1.4E-04	7.5
	0.7	852	0.6	1.7E-04	7.6
	0.8	748	0.5	2.0E-04	8.0
	0.9	668	0.4	2.3E-04	7.0
	1.0	607	0.6	2.6E-04	8.2
	1.1	554	0.6	2.8E-04	8.1
	1.2	507	0.5	3.0E-04	8.0
	1.3	470	0.6	3.5E-04	8.4
	1.4	439	0.6	3.7E-04	8.2
1.5	409	0.7	3.8E-04	8.0	
[KH_2AsO_4]=0.7 mmol	Flow rate (ml/min)	t of max. abs. (sec)	col. volumes to recover (40% porosity)	D (cm^2/sec)	α (cm)
	0.5	1190	0.6	1.1E-04	7.2
	0.6	990	0.5	1.4E-04	7.6
	0.7	852	0.7	1.7E-04	7.7
	0.8	750	0.5	2.0E-04	7.9
	0.9	667	0.6	2.3E-04	8.1
	1.0	607	0.6	2.5E-04	8.0
	1.1	550	0.4	2.7E-04	7.8
	1.2	509	0.6	3.0E-04	8.0
	1.3	469	0.6	3.3E-04	8.0
	1.4	437	0.5	3.7E-04	8.2
1.5	408	0.0	3.9E-04	8.1	
[KH_2AsO_4]=0.8 mmol	Flow rate (ml/min)	t of max. abs. (sec)	col. volumes to recover (40% porosity)	D (cm^2/sec)	α (cm)
	0.5	1186	0.5	1.1E-04	7.1
	0.6	988	0.4	1.3E-04	6.8
	0.7	856	0.4	1.6E-04	7.0
	0.8	747	0.4	1.8E-04	7.0
	0.9	666	0.4	2.0E-04	7.1
	1.0	606	0.4	6.3E-04	19.9
	1.1	553	0.5	2.9E-04	8.1
	1.2	507	0.5	3.2E-04	8.4
	1.3	470	0.5	3.3E-04	8.0
	1.4	438	0.5	3.5E-04	7.8
1.5	409	0.5	3.9E-04	8.1	

[KH ₂ AsO ₄]=0.9 mmol	Flow rate (ml/min)	t of max. abs. (sec)	col. volumes to recover (40% porosity)	D (cm ² /sec)	α (cm)
	0.5	1188	0.5	1.1E-04	7.1
	0.6	988	0.5	1.4E-04	7.2
	0.7	851	0.6	1.7E-04	7.7
	0.8	745	0.6	1.9E-04	7.6
	0.9	664	0.6	2.2E-04	7.8
	1.0	605	0.7	2.5E-04	7.9
	1.1	553	0.6	2.7E-04	7.8
	1.2	506	0.6	3.0E-04	8.0
	1.3	470	0.7	3.3E-04	8.0
	1.4	438	0.6	3.7E-04	8.3
	1.5	410	0.7	4.2E-04	8.8
[KH ₂ AsO ₄]=1.0 mmol	Flow rate (ml/min)	t of max. abs. (sec)	col. volumes to recover (40% porosity)	D (cm ² /sec)	α (cm)
	0.5	1189	0.5	1.1E-04	6.6
	0.6	991	0.5	1.3E-04	7.0
	0.7	849	0.5	1.7E-04	7.6
	0.8	743	0.6	2.0E-04	8.0
	0.9	661	0.6	2.3E-04	7.9
	1.0	602	0.6	2.5E-04	7.8
	1.1	549	0.5	2.8E-04	8.1
	1.2	508	0.6	3.1E-04	8.0
	1.3	469	0.6	3.3E-04	8.1
	1.4	438	0.7	3.7E-04	8.4
	1.5	408	0.6	4.1E-04	8.6
[KH ₂ AsO ₄]=3 mmol	Flow rate (ml/min)	t of max. abs. (sec)	col. volumes to recover (40% porosity)	D (cm ² /sec)	α (cm)
	0.5	1674	2.9	8.2E-05	5.2
	1.0	701	2.0	2.5E-04	7.8
	1.5	447	2.5	4.2E-04	8.8
	2.0	337	2.0	5.4E-04	8.6
	2.5	272	2.2	6.7E-04	8.4

Table 1: *t* of peak, vol. required for recovery, D_L and α for 200 μ L injections of KH₂AsO₄.

Aqueous injections of 200 μ L NaBr at 28.5° C					
[NaBr]=0.5 mmol	Flow rate (ml/min)	t of max. abs. (sec)	col. volumes to recover (40% porosity)	D (cm ² /sec)	α (cm)
	0.5	1669	1.4	3.8E-05	2.4
	1.0	770	1.3	1.3E-04	4.0
	1.5	446	1.4	3.0E-04	6.3
	2.0	338	1.5	2.1E-03	32.8
	2.5	271	1.4	5.2E-04	6.5
[NaBr]=1.0 mmol	Flow rate (ml/min)	t of max. abs. (sec)	col. volumes to recover (40% porosity)	D (cm ² /sec)	α (cm)
	0.5	1801	1.6	-8.8E-05	-8.8E-05
	1.0	809	1.3	-4.4E-05	-4.4E-05
	1.5	468	1.2	-2.9E-05	-2.9E-05
	2.0	342	1.2	-2.1E-05	-2.1E-05
	2.5	272	1.2	-1.7E-05	-1.7E-05
[NaBr]=2.0 mmol	Flow rate (ml/min)	t of max. abs. (sec)	col. volumes to recover (40% porosity)	D (cm ² /sec)	α (cm)
	0.5	1697	1.6	6.5E-05	4.1
	1.0	670	1.3	2.1E-04	6.5
	1.5	453	1.2	2.8E-04	5.8
	2.0	338	1.2	4.7E-04	7.3
	2.5	271	1.6	1.7E-03	21.0

Table 2: t of peak, vol. required for recovery, D_L and α for 200 μ L injections of NaBr.

Liquid CO ₂ injections into 0.1 mmol NaOH at 28.5° C					
Flow rate (ml/min)	injection vol (μ L)	t of min. pH (sec)	Δ pH	col. volumes to recover (40% porosity)	
0.5	5	1515	5.4	19.3	
1.0	5	930	4.9	14.6	
1.5	5	615	4.8	23.0	
1.0	20	1155	5.2	43.0	
1.5	20	510	6.3	66.0	
1.6	20	465	6.3	48.3	
1.7	20	495	6.7	34.3	
2.0	20	510	5.6	51.1	
2.5	20	495	5.2	62.3	

Table 3: Time of min. pH, Δ pH, and vol. required for recovery for liquid CO₂ injections (28.5°C).

temp (°C)		28.5°C	
flow rate (mls/min)	0.5	1.0	1.5
CT _{CO2} (moles) from pH data	7.3E-05	3.2E-05	9.7E-05
loop vol	9.0E-05	9.0E-05	9.0E-05
analyzer	xx	xx	8.9E-05
temp (°C)		35°C	
flow rate (mls/min)	0.5	1.0	1.5
CT _{CO2} (moles) from pH data	1.2E-04	7.4E-05	7.3E-05
loop vol	8.3E-05	8.3E-05	8.3E-05
analyzer	xx	xx	xx
temp (°C)		45°C	
flow rate (mls/min)	0.5	1.0	1.5
CT _{CO2} (moles) from pH data	5.7E-05	6.2E-05	9.2E-05
loop vol	6.2E-05	6.3E-05	6.4E-05
analyzer	xx	xx	7.9E-05
temp (°C)		60°C	
flow rate (mls/min)	0.5	1.0	1.5
CT _{CO2} (moles) from pH data	1.6E-04	8.5E-05	9.5E-05
loop vol	3.6E-05	3.6E-05	3.5E-05
analyzer	xx	xx	8.2E-05

Table 4a: $C_{T_{CO_2}}$ as calculated from pH, injection loop volume, and carbon analyzer for all 5 μ L liquid and SC CO₂ injections.

temp (°C)	28.5°C					
flow rate (mls/min)	1.0	1.5	1.6	1.7	2.0	2.5
CT _{CO2} (moles) from						
pH data	8.4E-05	7.7E-04	4.8E-04	9.0E-04	4.0E-04	3.2E-04
loop vol	3.6E-04	3.6E-04	3.6E-04	3.6E-04	3.6E-04	3.6E-04
temp (°C)	35°C					
flow rate (mls/min)	1.0	1.5	1.6	1.7	2.0	2.5
CT _{CO2} (moles) from						
pH data	7.7E-05	4.8E-04	5.9E-04	5.3E-04	4.7E-04	5.1E-04
loop vol	3.3E-04	3.3E-04	3.3E-04	3.3E-04	3.3E-04	3.3E-04
temp (°C)	45°C					
flow rate (mls/min)	1.0	1.5	1.6	1.7	2.0	2.5
CT _{CO2} (moles) from						
pH data	1.0E-04	2.4E-04	5.6E-04	3.8E-04	5.5E-04	2.7E-04
loop vol	2.5E-04	2.5E-04	2.5E-04	2.5E-04	2.5E-04	2.4E-04
temp (°C)	60°C					
flow rate (mls/min)	1.0	1.5	1.6	1.7	2.0	2.5
CT _{CO2} (moles) from						
pH data	6.9E-05	2.5E-04	1.9E-04	2.9E-04	4.1E-04	5.8E-04
loop vol	1.5E-04	1.5E-04	1.4E-04	1.4E-04	1.5E-04	1.5E-04

Table 4b: $C_{T_{CO_2}}$ as calculated from pH data and injection loop volume for all 20 μ L liquid and SC CO₂ injections.

temp (°C)	28.5°C		
flow rate (mls/min)	0.5	1.0	1.5
pH C _T /loop C _T	72.6%	31.9%	100.0%
temp (°C)	35°C		
flow rate (mls/min)	0.5	1.0	1.5
pH C _T /loop C _T	145.2%	89.3%	88.5%
temp (°C)	45°C		
flow rate (mls/min)	0.5	1.0	1.5
pH C _T /loop C _T	91.5%	98.6%	144.3%
temp (°C)	60°C		
flow rate (mls/min)	0.5	1.0	1.5
pH C _T /loop C _T	455.7%	236.8%	269.9%

Table 5a: $\frac{C_{T_{CO_2}} \text{ (from pH)}}{C_{T_{CO_2}} \text{ (from loop vol.)}}$ as a percentage for all 5 μL CO₂ injections.

temp (°C)	28.5°C					
flow rate (mls/min)	1.0	1.5	1.6	1.7	2.0	2.5
pH C _T /loop C _T	20.6%	175.0%	115.7%	214.1%	99.8%	82.3%
temp (°C)	35°C					
flow rate (mls/min)	1.0	1.5	1.6	1.7	2.0	2.5
pH C _T /loop C _T	23.2%	145.0%	179.3%	161.6%	141.4%	154.9%
temp (°C)	45°C					
flow rate (mls/min)	1.0	1.5	1.6	1.7	2.0	2.5
pH C _T /loop C _T	39.9%	98.2%	220.8%	150.2%	220.0%	116.5%
temp (°C)	60°C					
flow rate (mls/min)	1.0	1.5	1.6	1.7	2.0	2.5
pH C _T /loop C _T	47.1%	174.1%	135.3%	201.3%	279.0%	393.6%

Table 5b: $\frac{C_{T_{CO_2}} \text{ (from pH)}}{C_{T_{CO_2}} \text{ (from loop vol.)}}$ as a percentage for all 20 μL CO₂ injections.

Supercritical CO₂ injections into 0.1 mmol NaOH at 35° C					
35° C	Flow rate (ml/min)	injection vol (μL)	<i>t of min. pH (sec)</i>	ΔpH	col. volumes to recover (40% porosity)
	0.5	5	2025	5.2	22.8
	1.0	5	1335	5	15.6
	1.5	5	750	4.9	86.9
	1.0	20	1035	5.2	28.4
	1.5	20	465	6.3	64.0
	1.6	20	465	6.5	55.4
	1.7	20	450	6.2	26.7
	2.0	20	390	6.3	88.3
2.5	20	480	6.1	51.2	
45° C	Flow rate (ml/min)	injection vol (μL)	<i>t of min. pH (sec)</i>	ΔpH	col. volumes to recover (40% porosity)
	0.5	5	2040	5.3	14.6
	1.0	5	1110	4.7	19.0
	1.5	5	585	4.6	22.6
	1.0	20	1050	5.3	31.9
	1.5	20	510	6.7	41.1
	1.6	20	465	6.6	45.8
	1.7	20	555	6.1	40.6
	2.0	20	450	6.6	44.8
2.5	20	390	5.7	59.3	
60° C	Flow rate (ml/min)	injection vol (μL)	<i>t of min. pH (sec)</i>	ΔpH	col. volumes to recover (40% porosity)
	0.5	5	2100	5.8	17.7
	1.0	5	1275	5.3	19.0
	1.5	5	810	5.7	14.0
	1.0	20	1110	5.1	32.8
	1.5	20	855	5.6	61.9
	1.6	20	780	5.6	59.1
	1.7	20	810	5.7	87.4
	2.0	20	660	5.9	49.3
2.5	20	525	6.2	45.2	

Table 6: Time of min. pH, ΔpH, and vol. required for recovery for supercritical CO₂ injections (35, 45, 60°C).

5 μL	Flow Rate (ml/min)			mean k value
temp ($^{\circ}\text{C}$)	0.5	1.0	1.5	
28.5	0.003	0.0038	0.0064	0.0044
35	0.0025	0.0031	0.0066	0.0041
45	0.0041	0.0047	0.0052	0.0047
60	0.0026	0.0025	0.0047	0.0033

20 μL	Flow Rate (ml/min)						mean k value
temp ($^{\circ}\text{C}$)	1.0	1.5	1.6	1.7	2.0	2.5	
28.5	0.0016	0.0023	0.0043	0.0023	0.0026	0.0027	0.0026
35	0.0025	0.0032	0.0043	0.0045	0.0048	0.0051	0.0041
45	0.0024	0.0029	0.0041	0.0042	0.0042	0.0026	0.0034
60	0.0023	0.0028	0.0028	0.0028	0.003	0.0031	0.0028

Table 7: k values for liquid and supercritical CO_2 injection experiments.

temperature	28.5 $^{\circ}\text{C}$		28.5 $^{\circ}\text{C}$		45 $^{\circ}\text{C}$		45 $^{\circ}\text{C}$	
	flow rate	injected volume	flow rate	injected volume	flow rate	injected volume	flow rate	injected volume
	1.5 mls/min	4.9 μL	2.0 mls/min	20.0 μL	0.5 mls/min	5.0 μL	1.0 mls/min	5.0 μL
	5.E-03 cm	5.E-03 cm	2.E-02 cm	2.E-02 cm	5.E-03 cm	5.E-03 cm	5.E-03 cm	5.E-03 cm
	model volume	% of injected	model volume	% of actual	model volume	% of actual	model volume	% of actual
sphere	9.1E-04	18.4%	4.4E-03	22.1%	2.0E-03	41.0%	1.4E-03	28.7%
cube	6.6E-04	13.3%	3.2E-03	16.0%	1.5E-03	29.7%	1.0E-03	20.8%
hemisphere	1.3E-03	26.0%	6.2E-03	31.3%	2.9E-03	58.0%	2.0E-03	40.6%
spherical cap	3.0E-03	61.7%	9.5E-03	47.6%	5.8E-03	116.2%	3.2E-03	64.3%

temperature	45 $^{\circ}\text{C}$		45 $^{\circ}\text{C}$		60 $^{\circ}\text{C}$	
	flow rate	injected volume	flow rate	injected volume	flow rate	injected volume
	1.5 mls/min	6.2 μL	1.5 mls/min	20.0 μL	1.5 mls/min	11.6 μL
	6.E-03 cm	6.E-03 cm	2.E-02 cm	2.E-02 cm	1.E-02 cm	1.E-02 cm
	model volume	% of actual	model volume	% of actual	model volume	% of actual
sphere	1.4E-03	22.8%	4.6E-03	23.1%	1.2E-03	10.1%
cube	1.0E-03	16.5%	3.3E-03	16.7%	8.4E-04	7.3%
hemisphere	2.0E-03	32.2%	6.5E-03	32.7%	1.6E-03	14.2%
spherical cap	3.2E-03	52.0%	8.8E-03	44.3%	3.2E-03	27.8%

Table 8: Percent of measured CO_2 recovered by droplet shape models.

Dissolved CO₂ injections into 0.1 M CaCl₂ at 28.5° C						
Flow rate (ml/min)	injection vol (μL)	<i>t</i> of min. pH (sec)	ΔpH	col. volumes to recover (40% porosity)	<i>D</i> (cm ² /sec)	<i>a</i> (cm)
1.0	20	1530	4.1	6.2	6.4E-04	2.3E+10
2.0	20	1020	3.6	9.5	7.0E-04	3.4E+10

Table 9: Time of min. pH, ΔpH, vol. required for recovery, D_L and α for dissolved CO₂ injections.

Figures

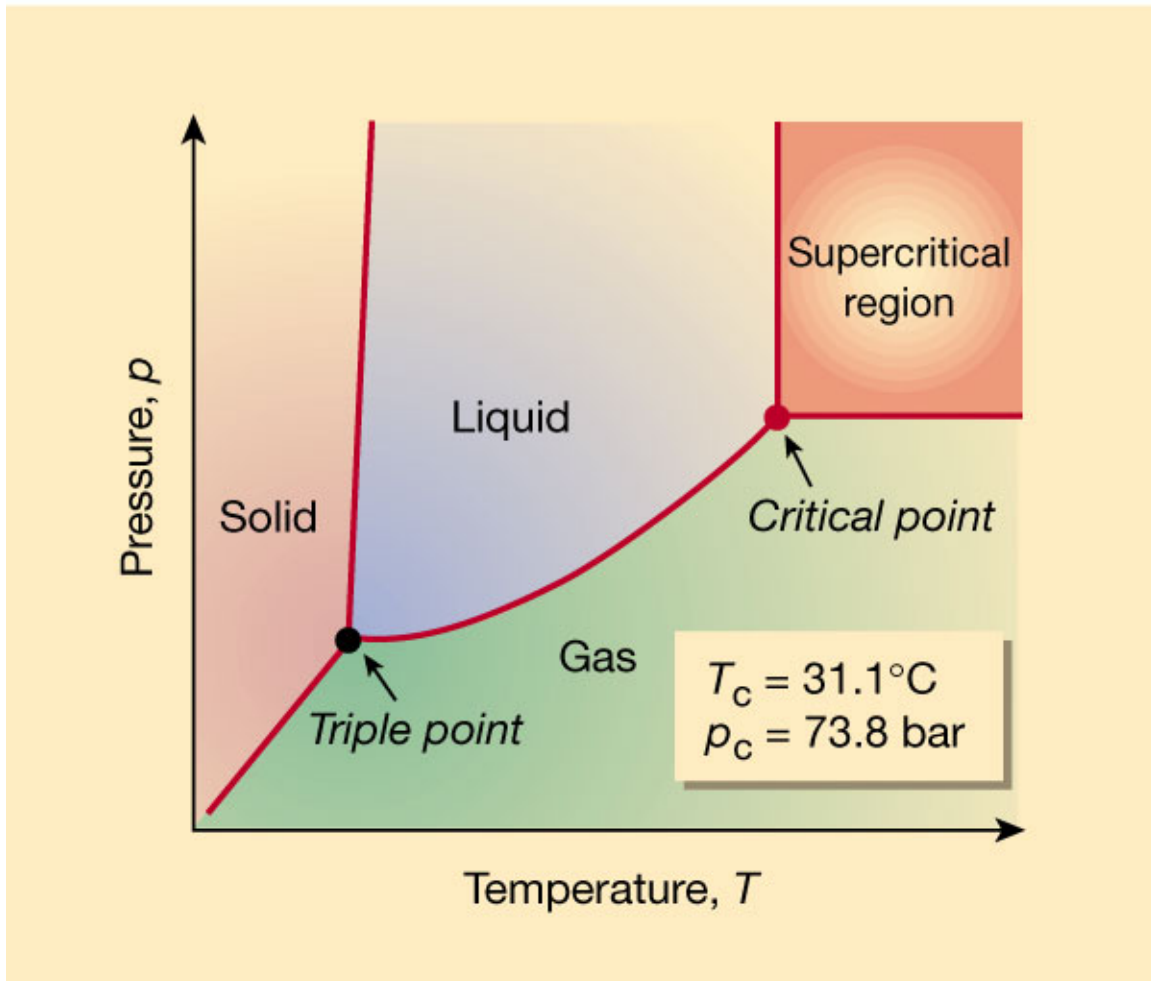


Figure 1: Phase diagram for CO₂ (17).

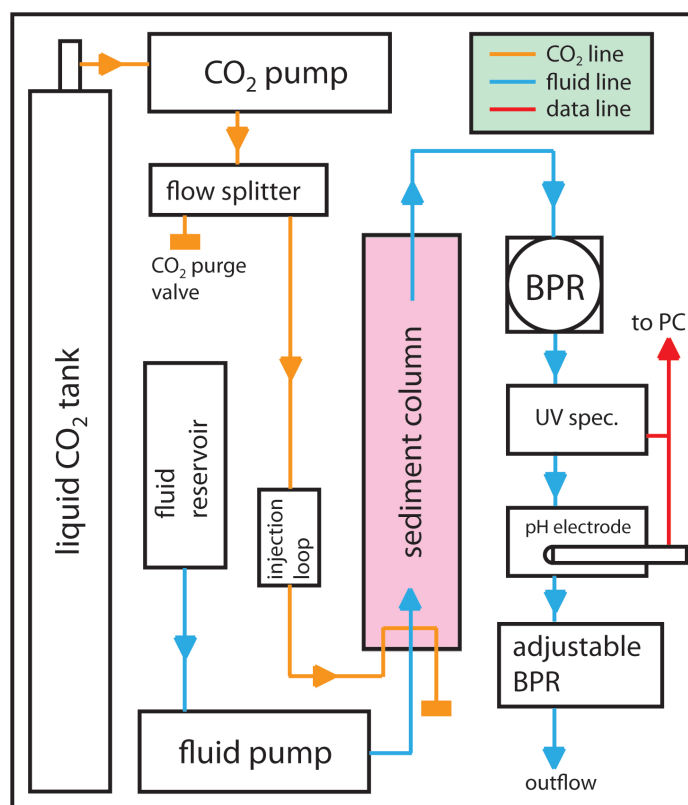


Figure 2: General flow-through setup.

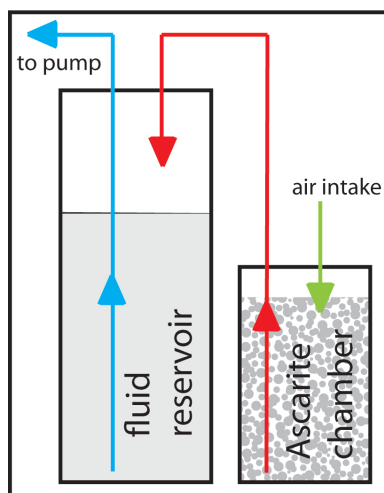


Figure 3: The CO₂-scrubbing apparatus used for all dissolved, liquid, and supercritical CO₂ experiments.

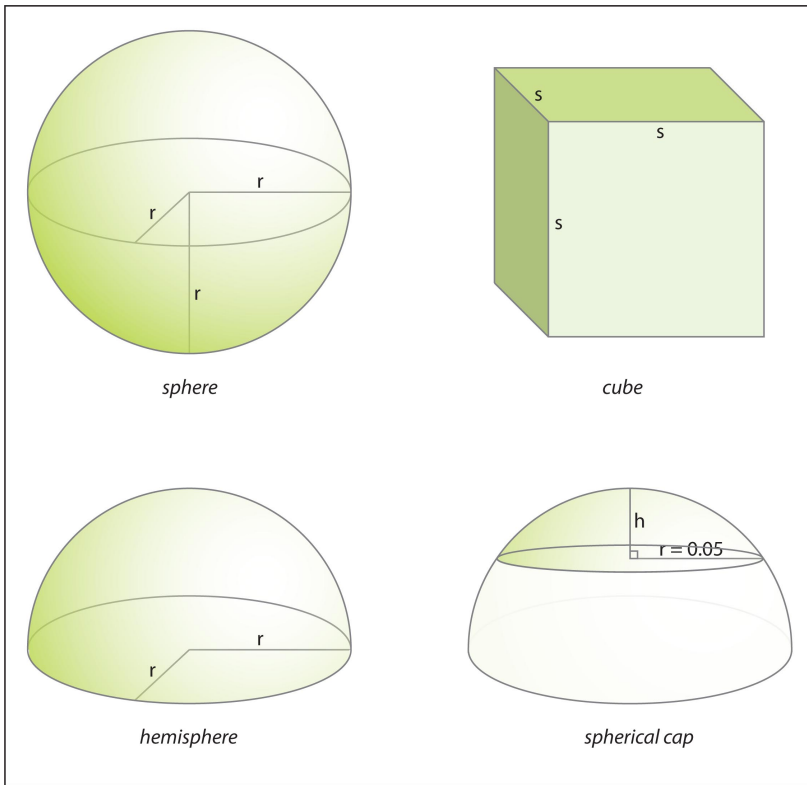


Figure 4: CO₂ droplet shape models.

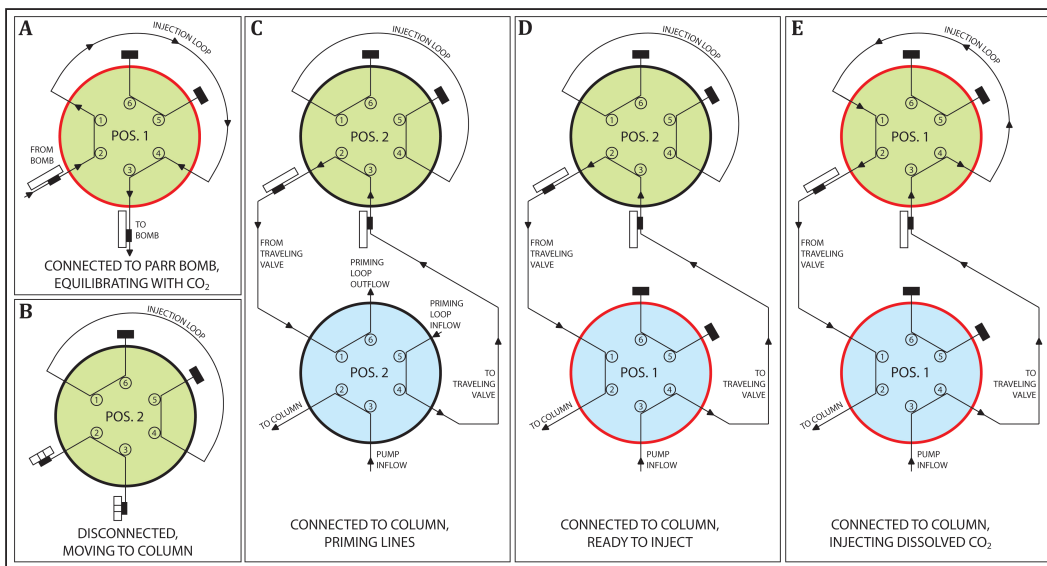


Figure 5: Schematic of traveling valve used to transfer a sample of brine containing dissolved CO_2 .

A: injection loop is left overnight to equilibrate with pressurized brine and CO_2 . **B:** Traveling valve is disconnected, isolating the injection loop at pressure. **C:** Traveling valve is connected to column injection valve, and lines are primed with brine. **D:** Column injection valve is set to include traveling valve in active flow. **E:** Injection of sample loop into active flow. **Green** = traveling valve, **blue** = column injection valve. **Red border** = valve in position 1, **black border** = valve in position 2.

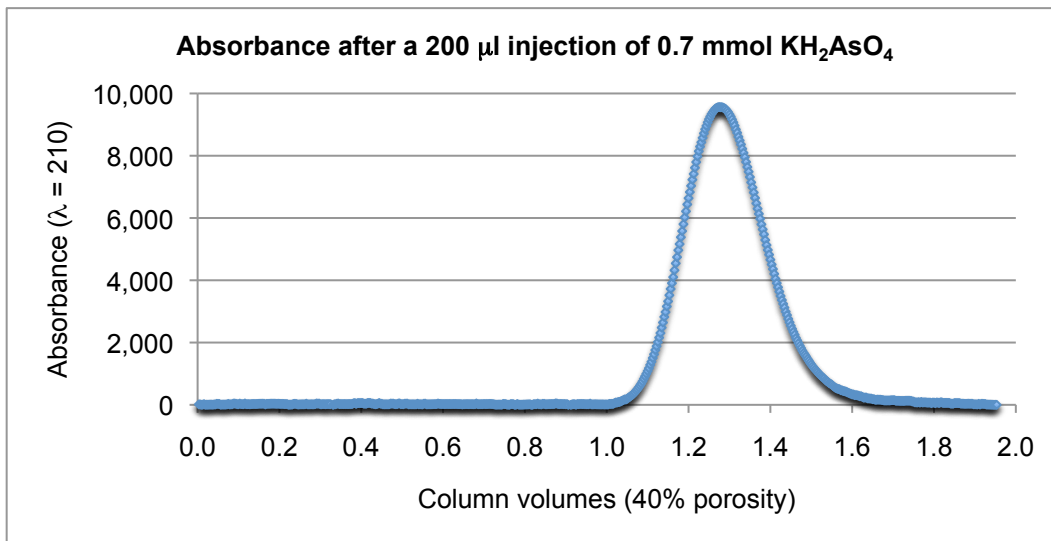


Figure 6a: A typical absorbance curve for a 200 µL aqueous injection of KH_2AsO_4 .

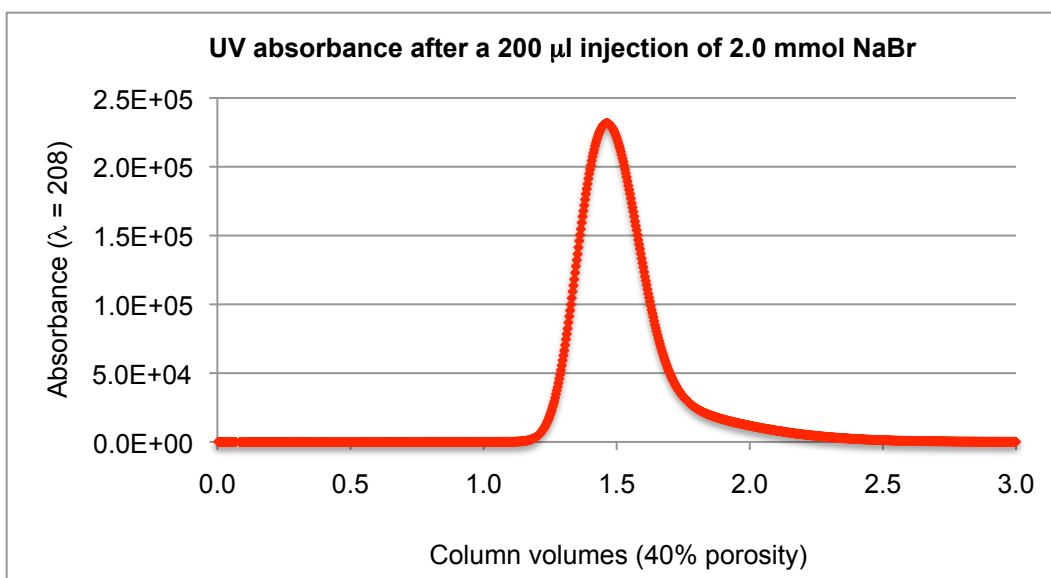


Figure 6b: A typical absorbance curve for a 200 µL aqueous injection of NaBr .

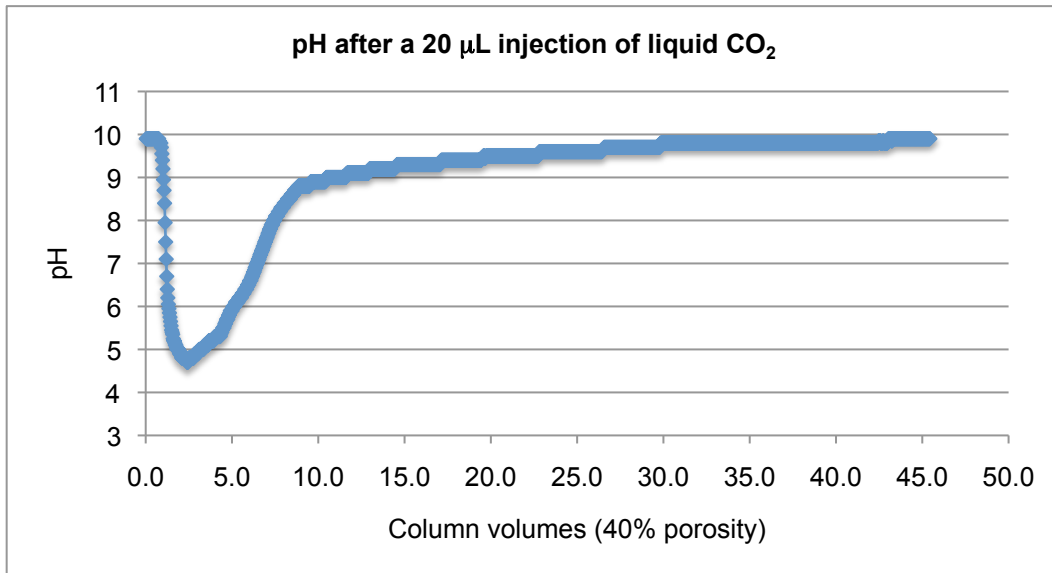


Figure 7: A typical pH curve for a 20 μL injection of liquid CO₂ (28.5°C).

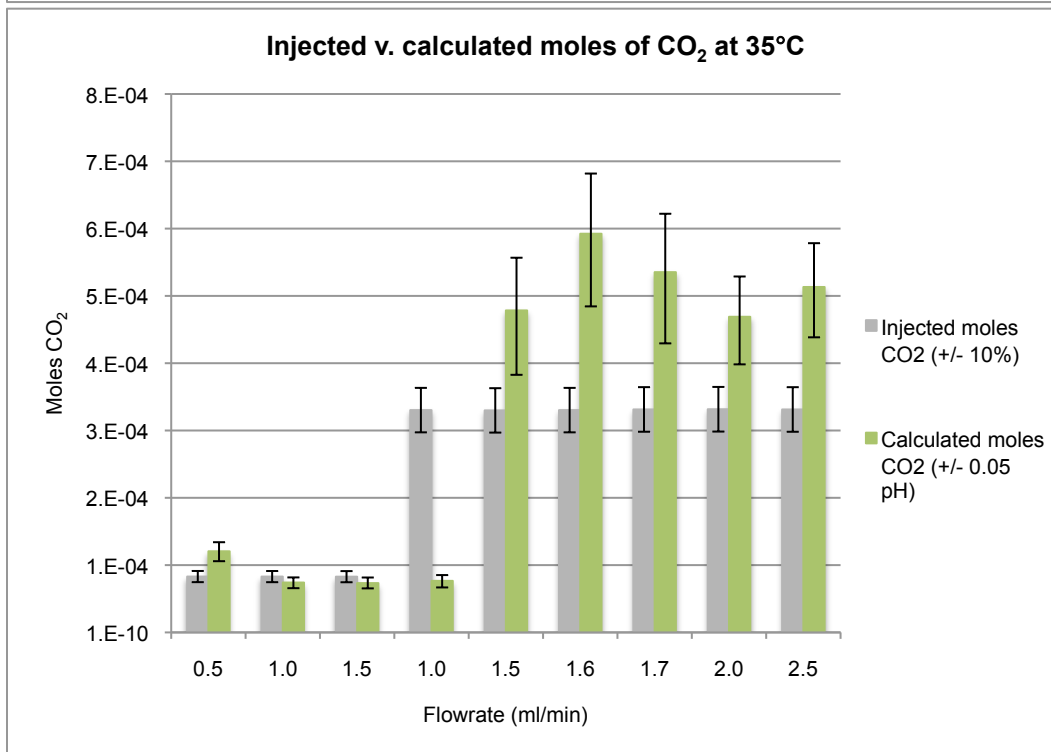
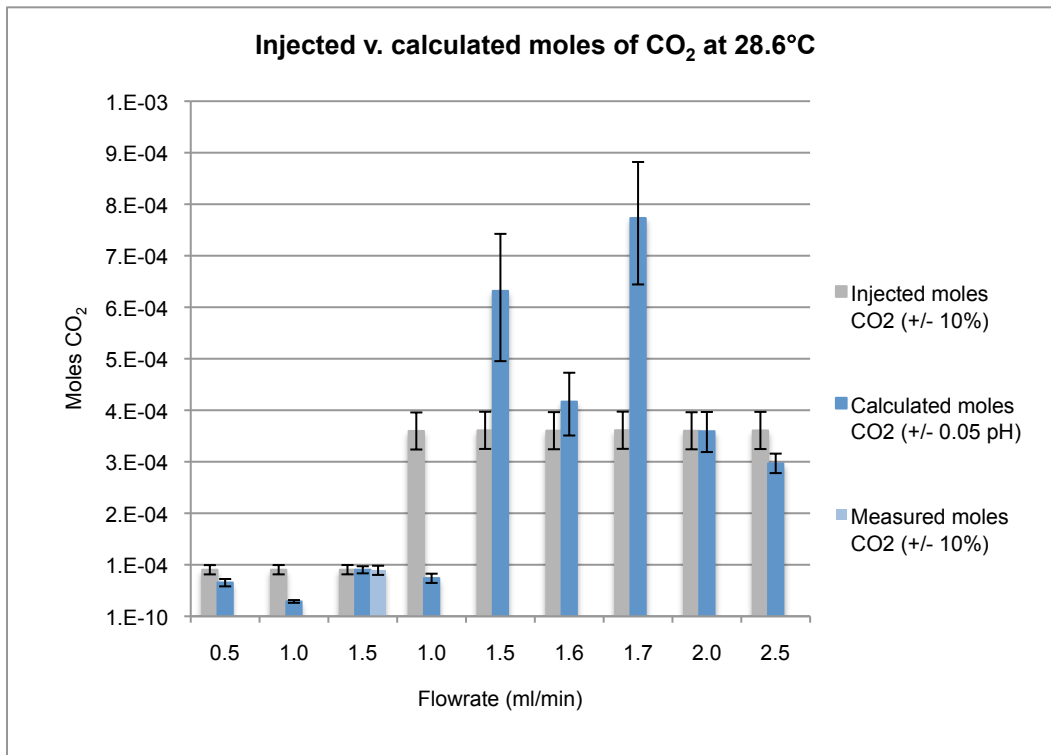


Figure 8: Mass balances for all liquid and CO₂ injections.

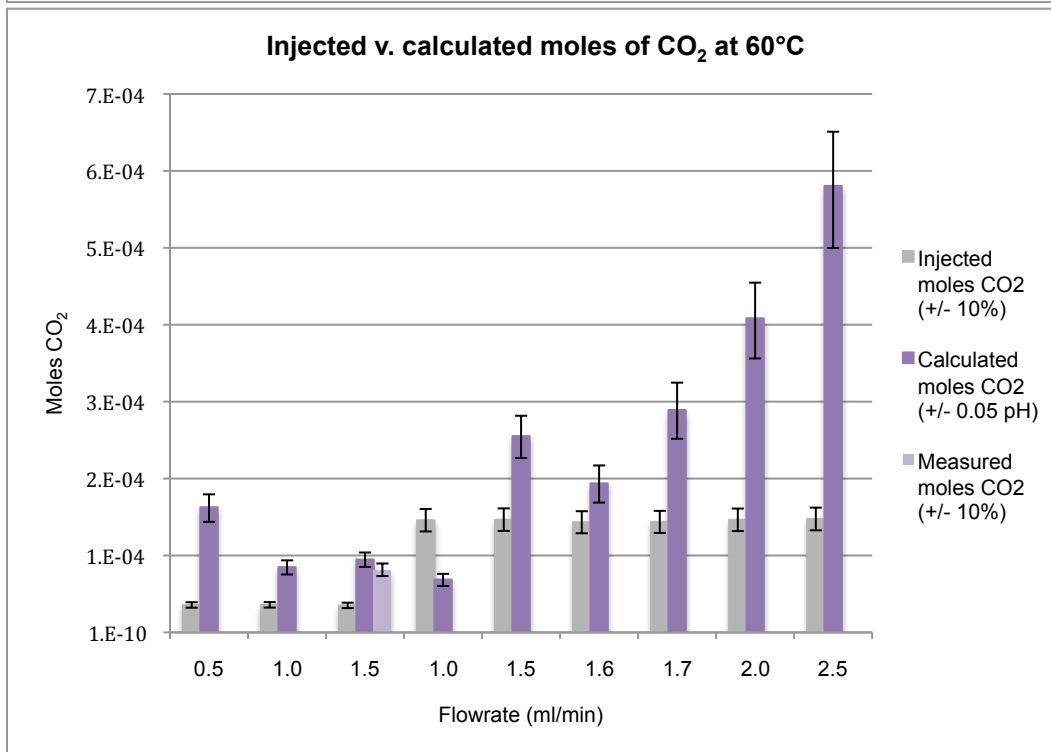
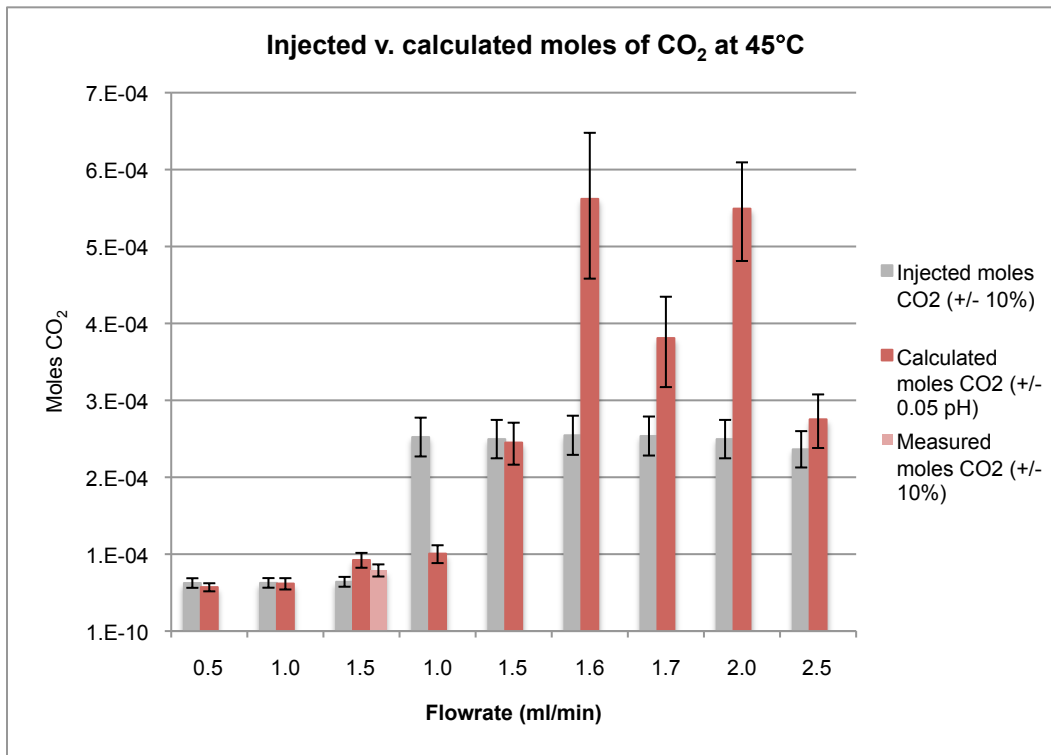


Figure 8 cont: Mass balances for all liquid and CO₂ injections.

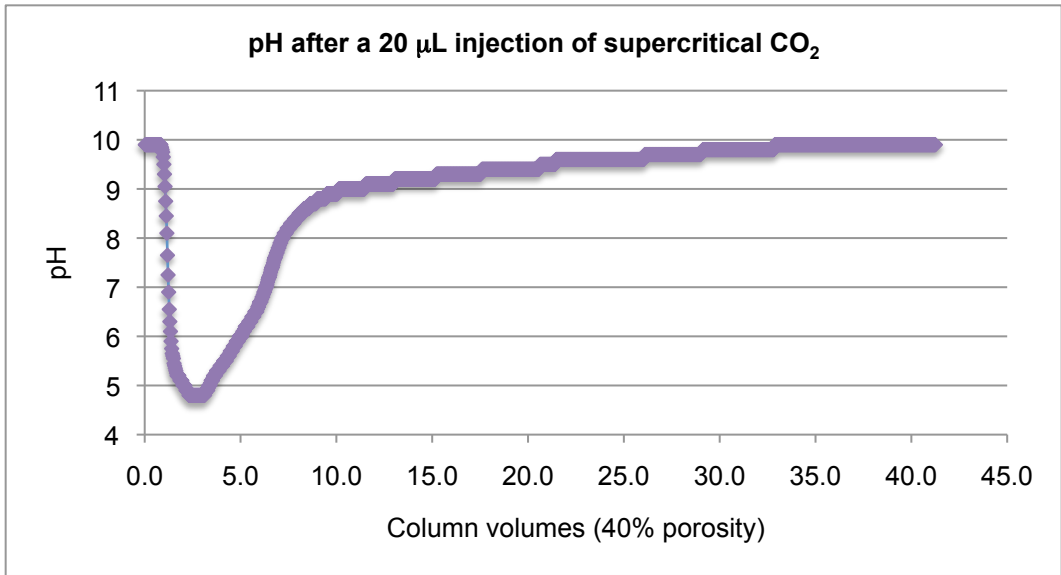


Figure 9: A typical pH curve for a 20 μL injection of supercritical CO_2 (60°C).

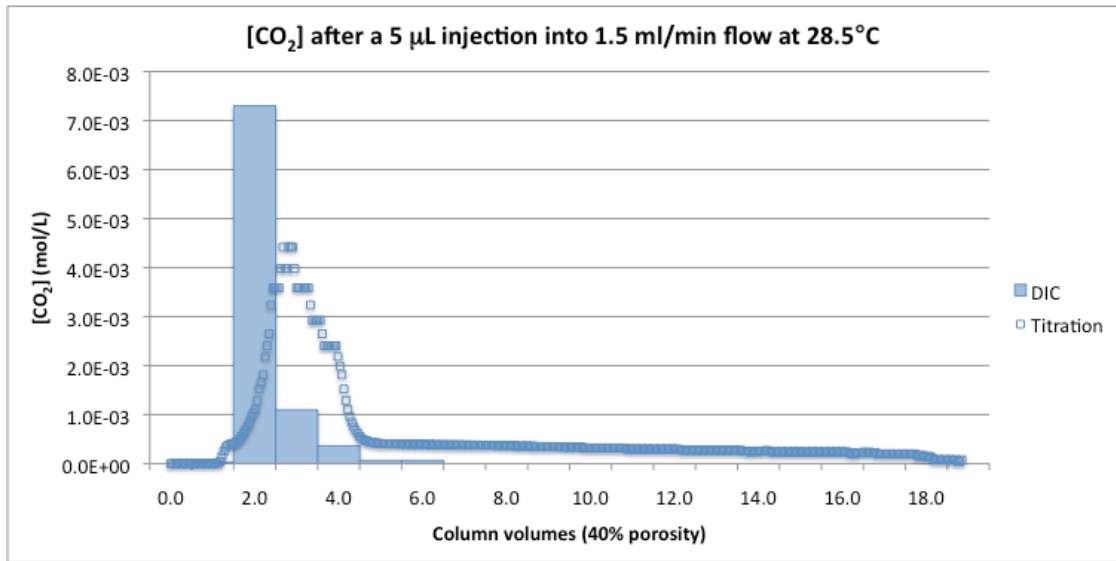


Figure 10: Incremental [DIC] and pH over time.

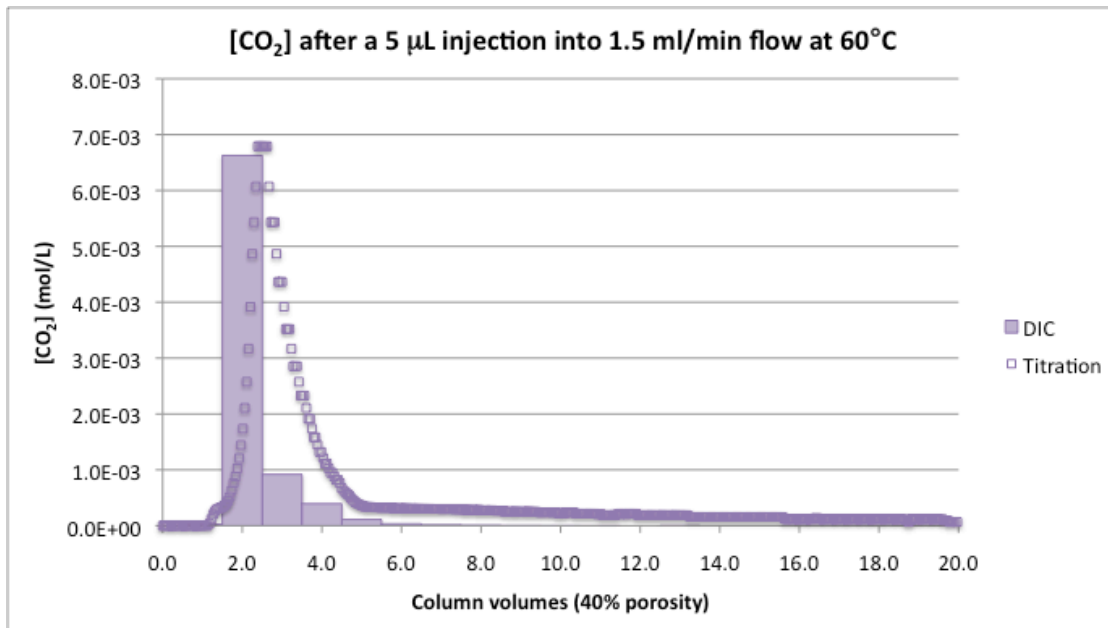
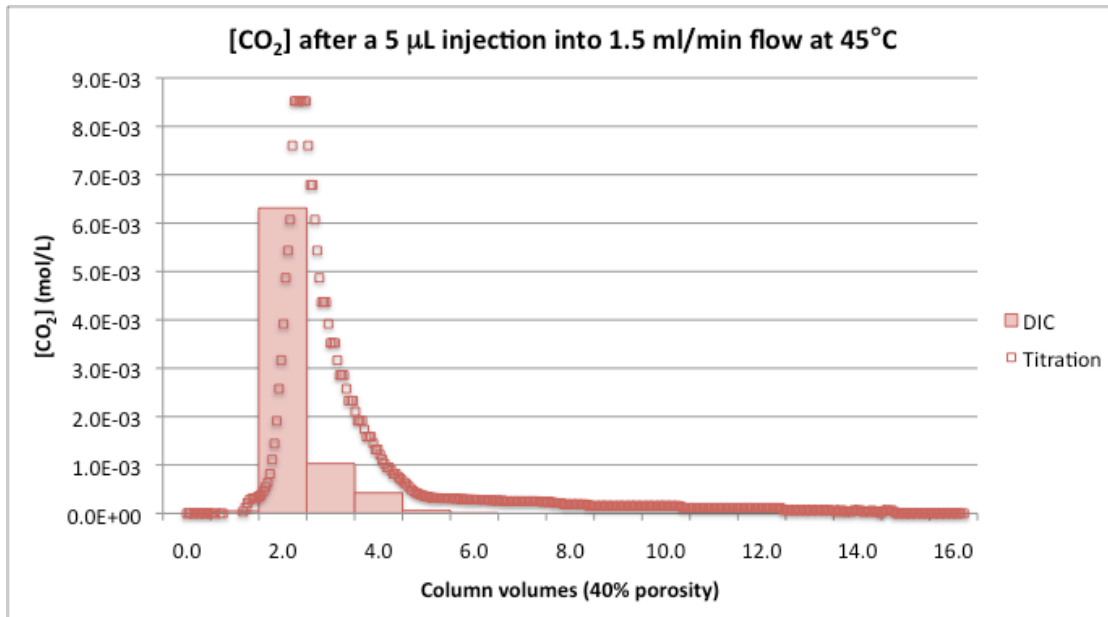


Figure 10 cont: Incremental [DIC] and pH over time.

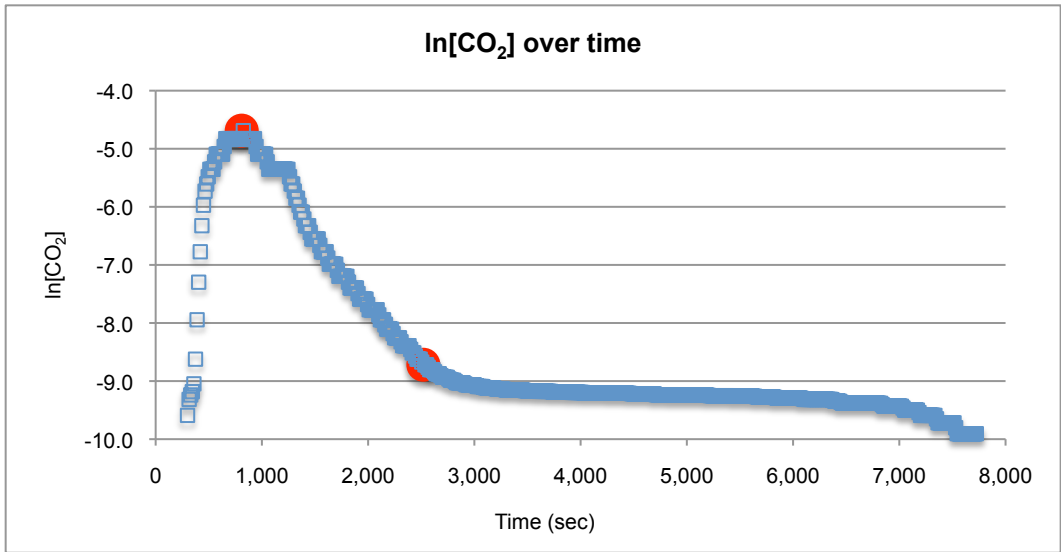


Figure 11: A plot of $\ln[CO_2]$ v. time.

Between the red dots, $y = -0.0025x - 2.6151$ ($R^2 = 0.98227$), therefore, $k = 0.0025$.

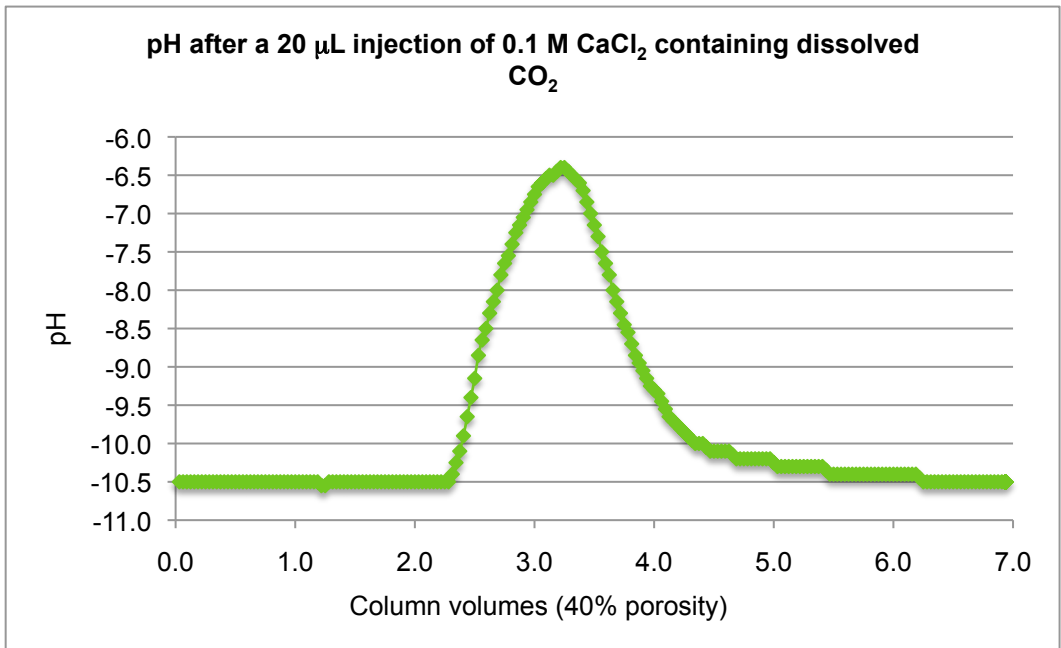


Figure 12: A typical pH curve for a 20 μL injection of dissolved CO_2 .

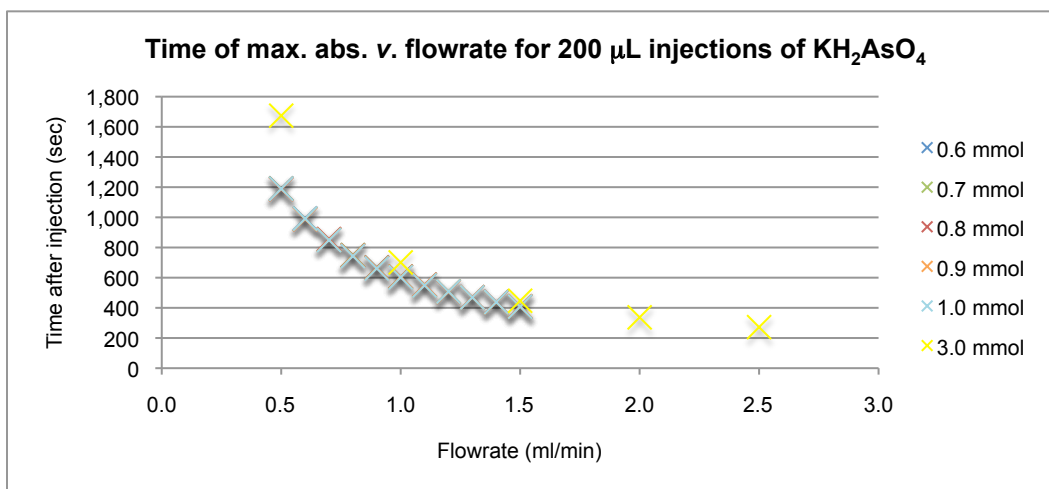


Figure 13: Example: time of maximum absorbance v. flow rate for KH_2AsO_4 injections

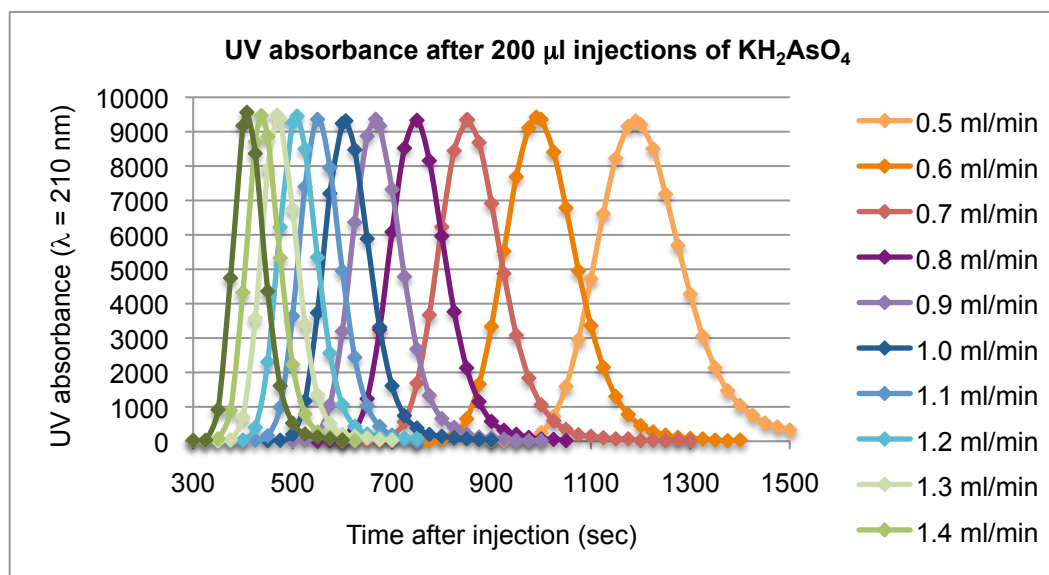


Figure 14a: Absorbance peaks become narrower and sharper as flow rate is increased and dispersion decreases (KH_2AsO_4).

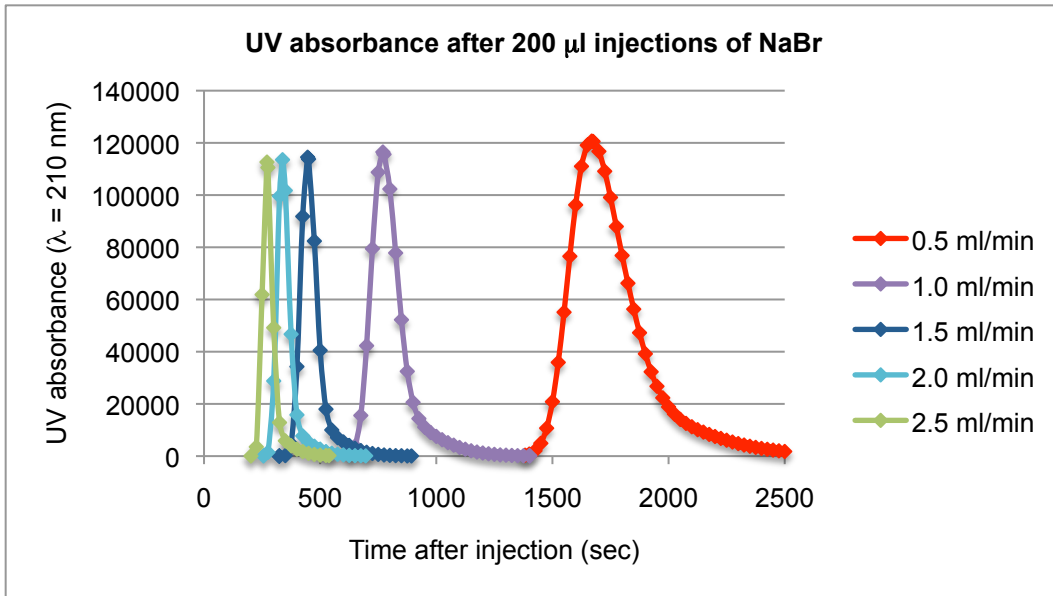


Figure 14b: Absorbance peaks become narrower and sharper as flow rate is increased and dispersion decreases (NaBr).

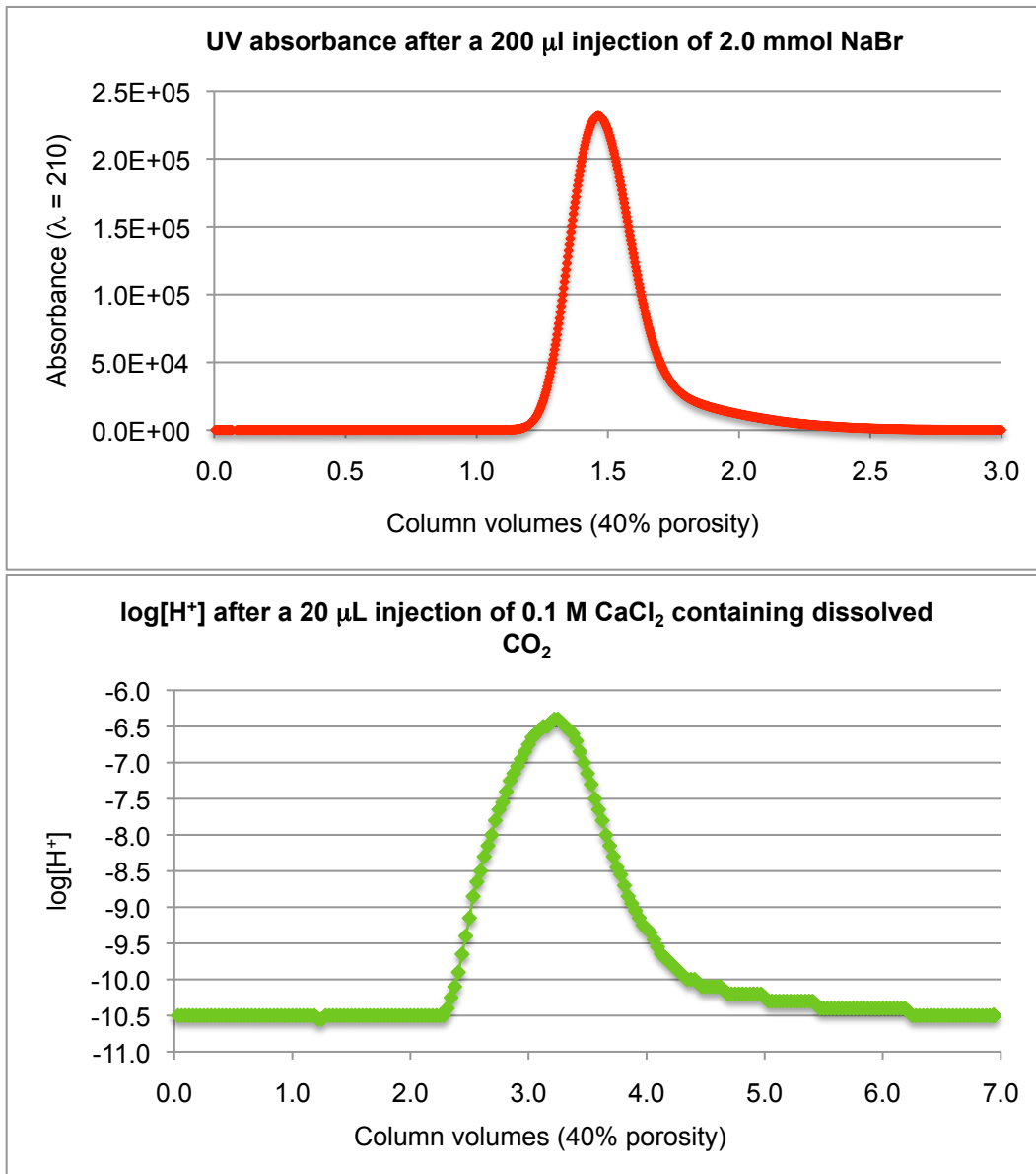


Figure 15: Comparison of a typical aqueous absorption (top) and dissolved CO_2 pH (bottom) curve.

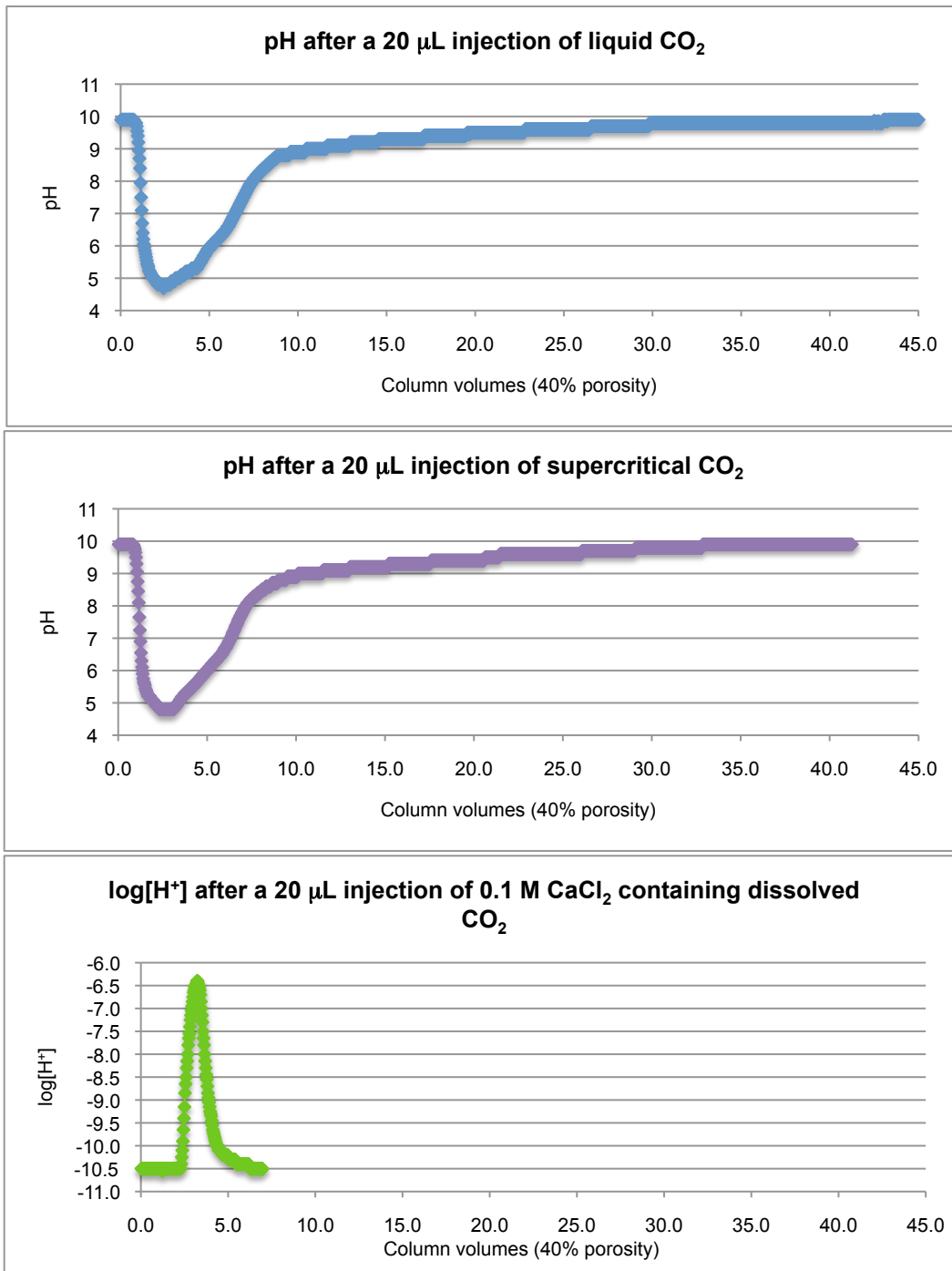


Figure 16: Comparison of typical liquid and supercritical pH curves to a dissolved CO_2 injection.

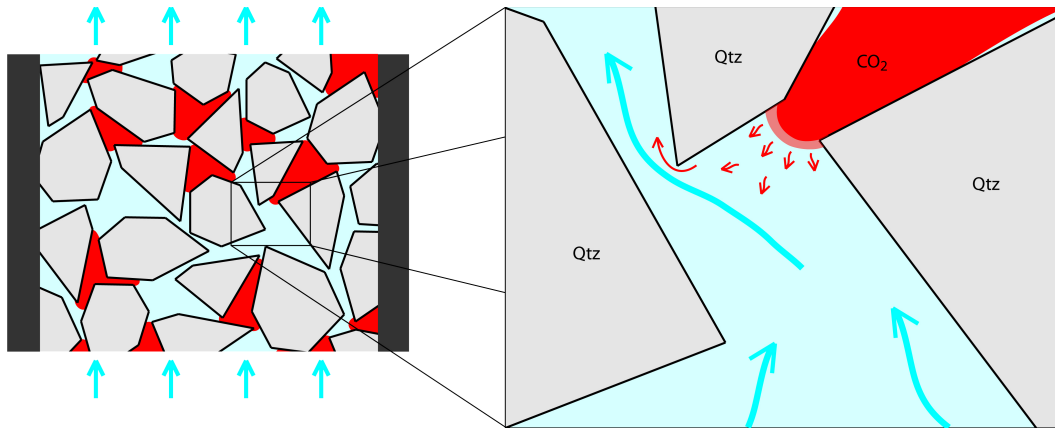


Figure 17: Conceptual model: CO₂ snap-off and limited CO₂ surface area.

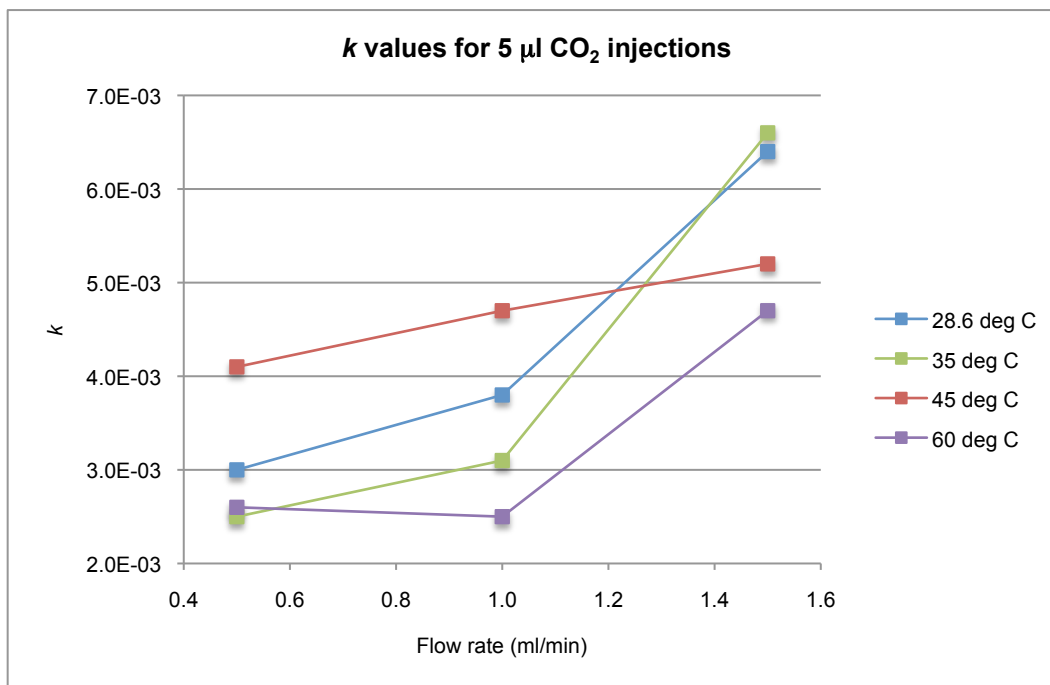


Figure 18: the behavior of k in relation to flow rate for 5 μ L injections.

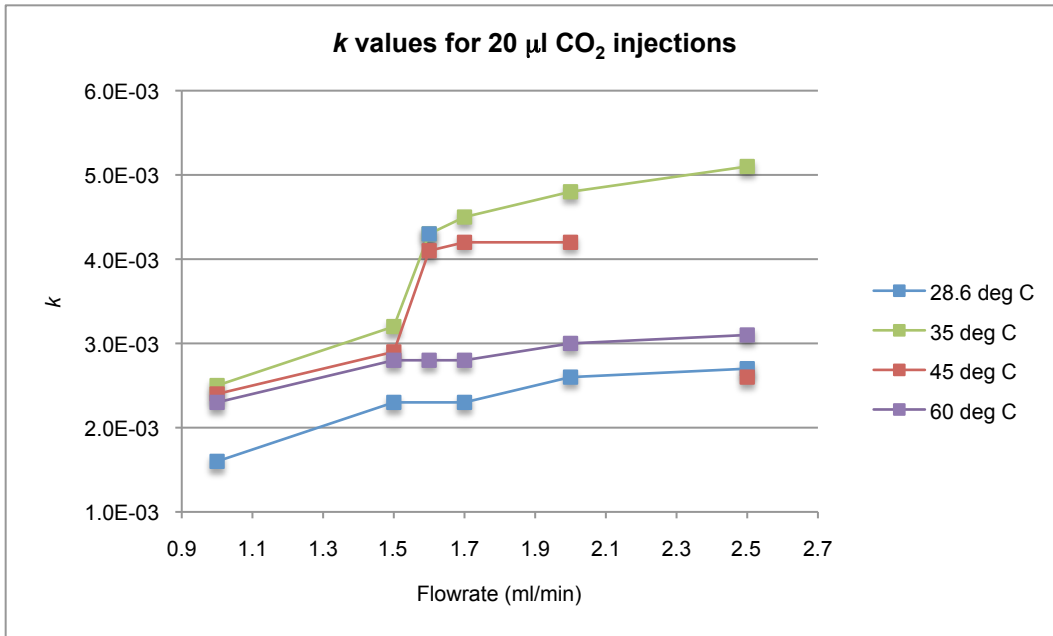


Figure 19: the behavior of k in relation to flow rate for 20 μL injections.

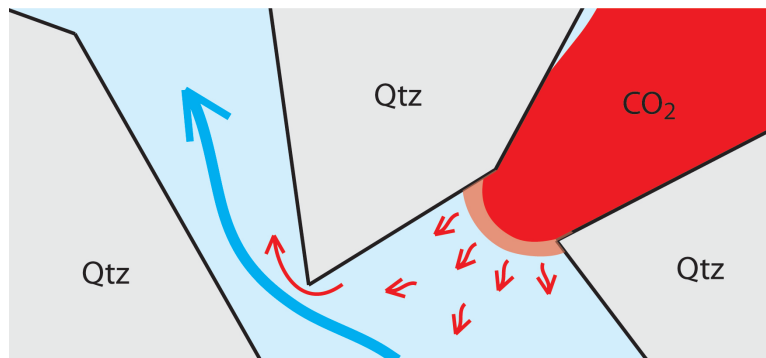


Figure 20: Diffusion controls the reaction rate at low flow rates.

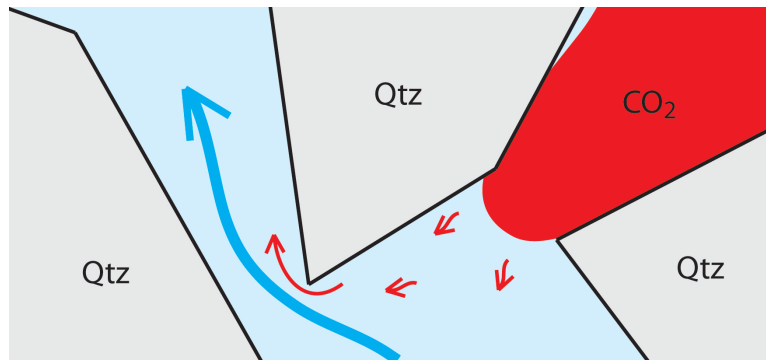
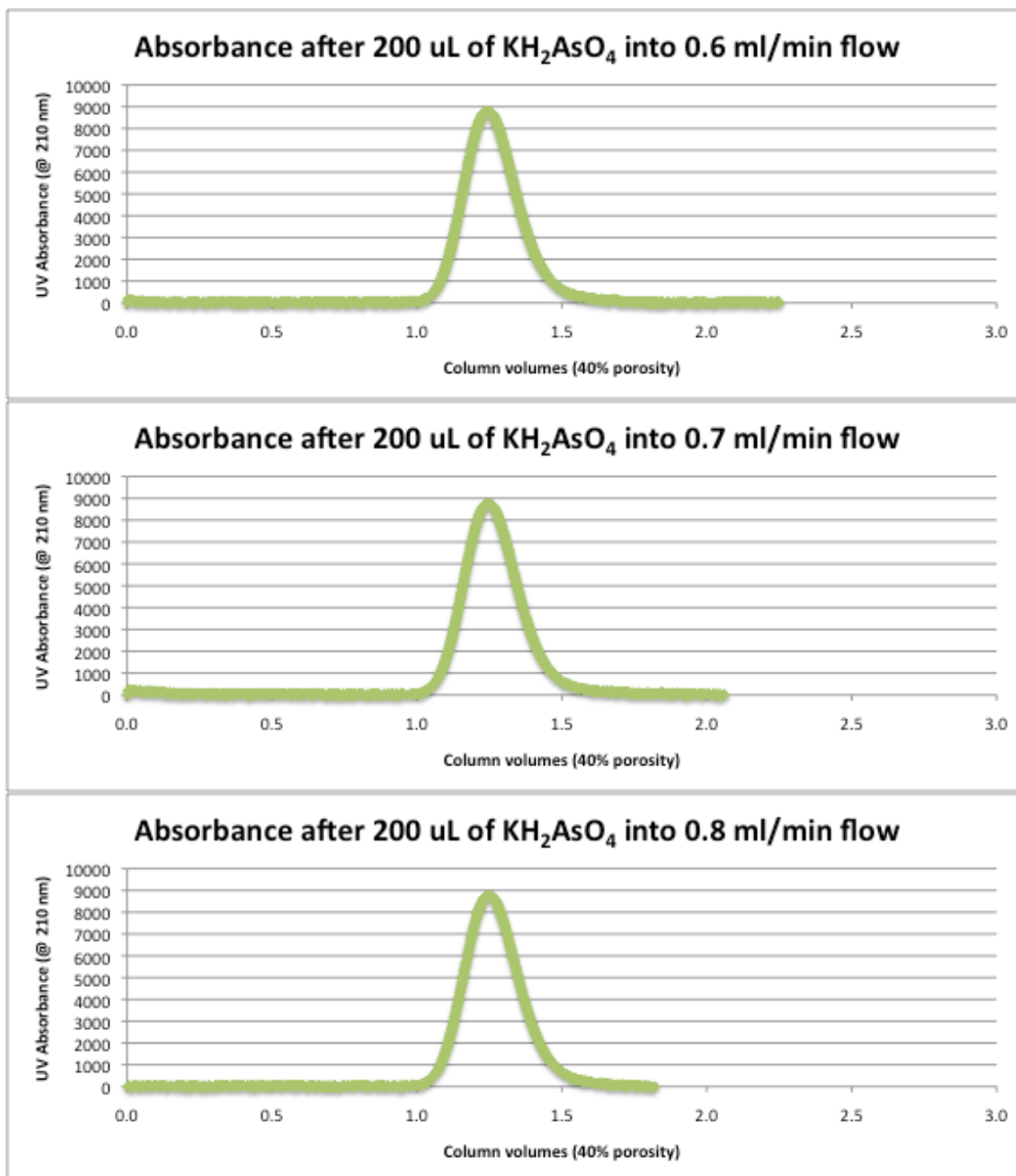


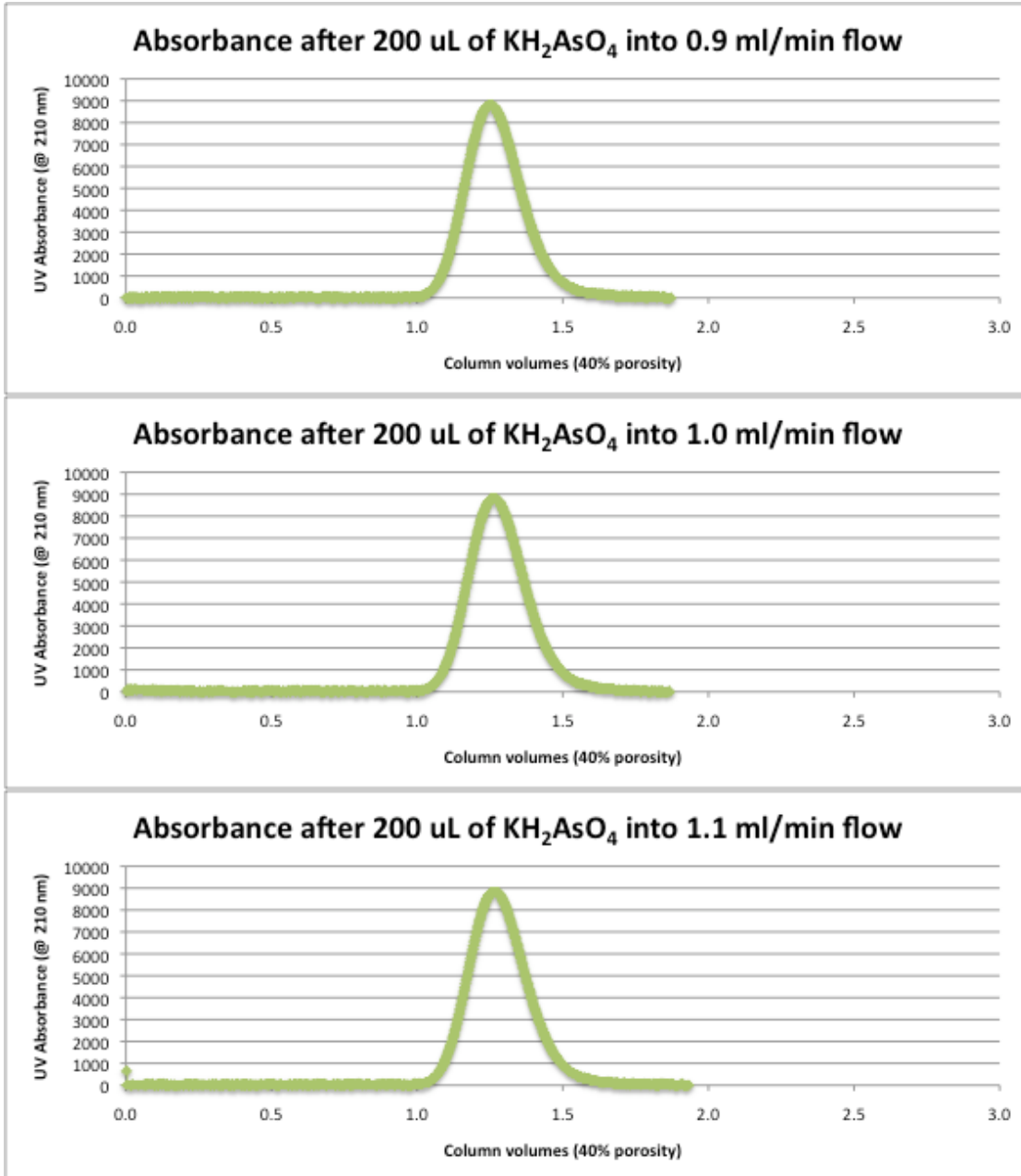
Figure 21: Surface dissolution kinetics controls the reaction rate at higher flow rates.

Appendix I: curves for all aqueous injections

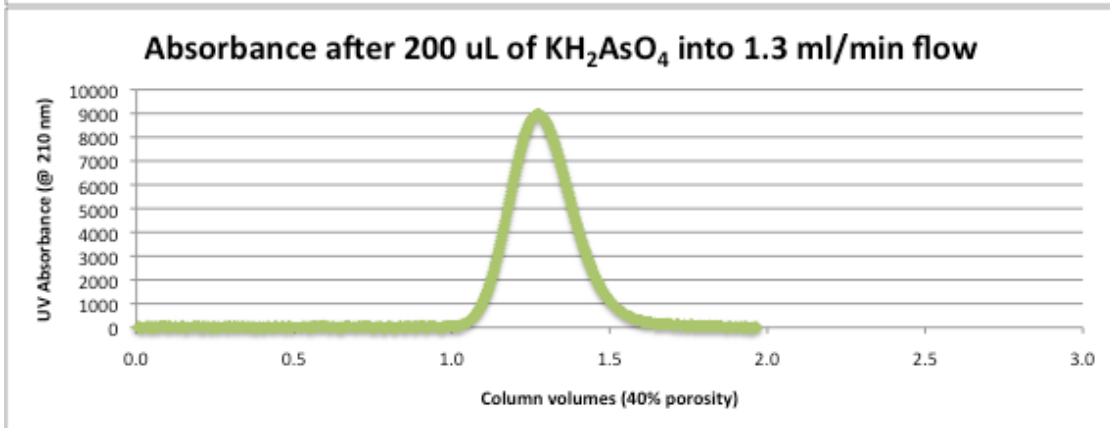
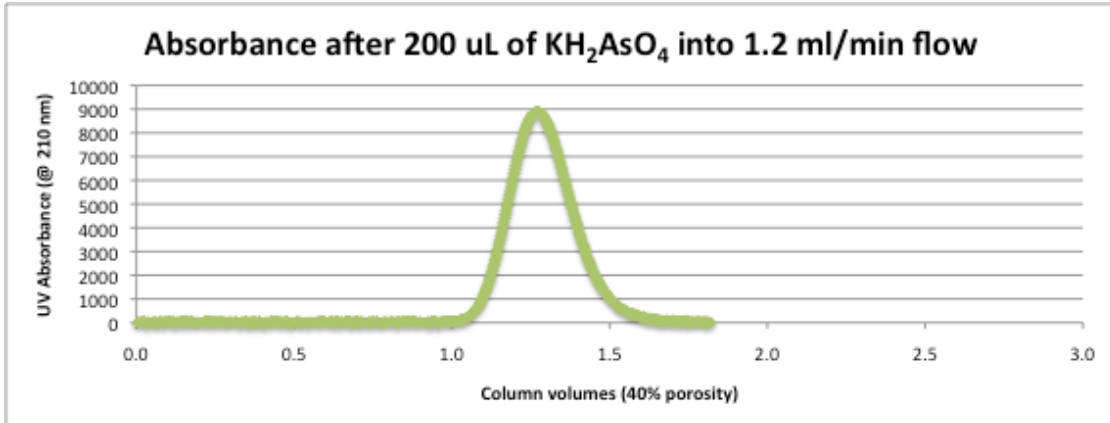
0.6 mmol KH₂AsO₄



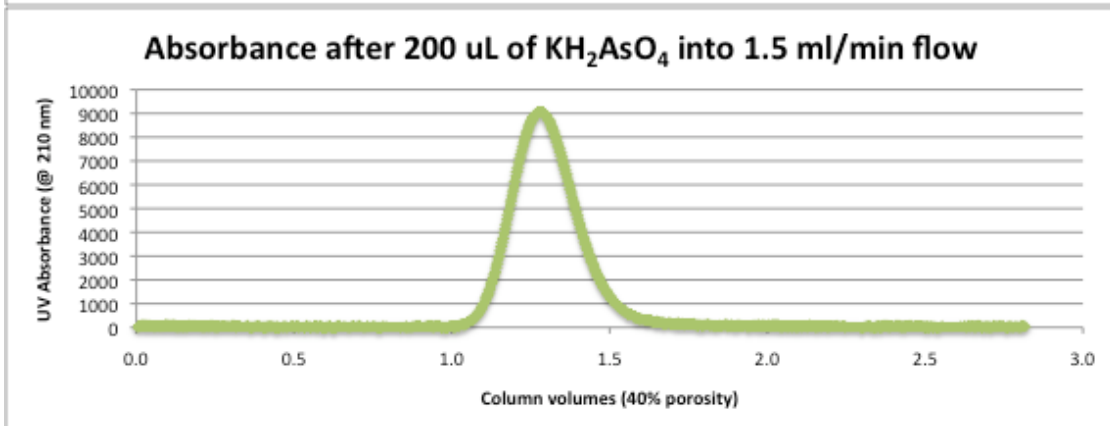
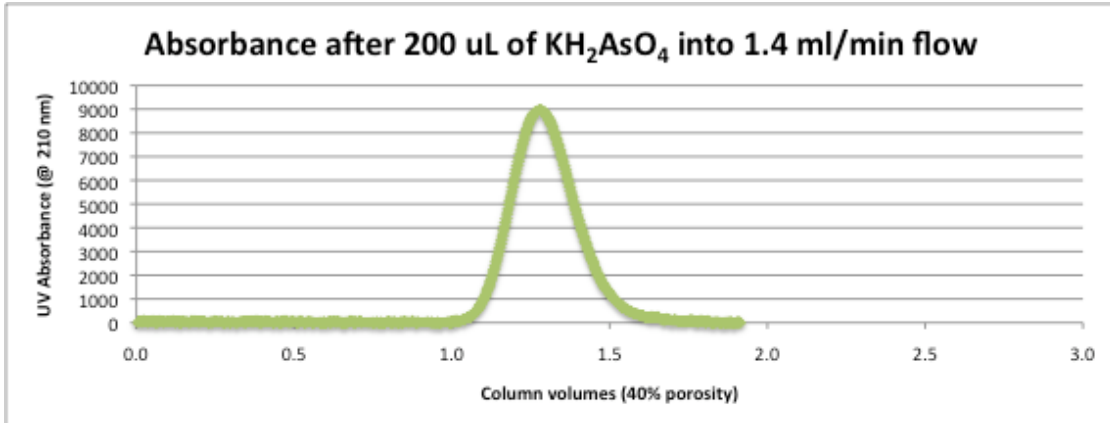
0.6 mmol KH₂AsO₄



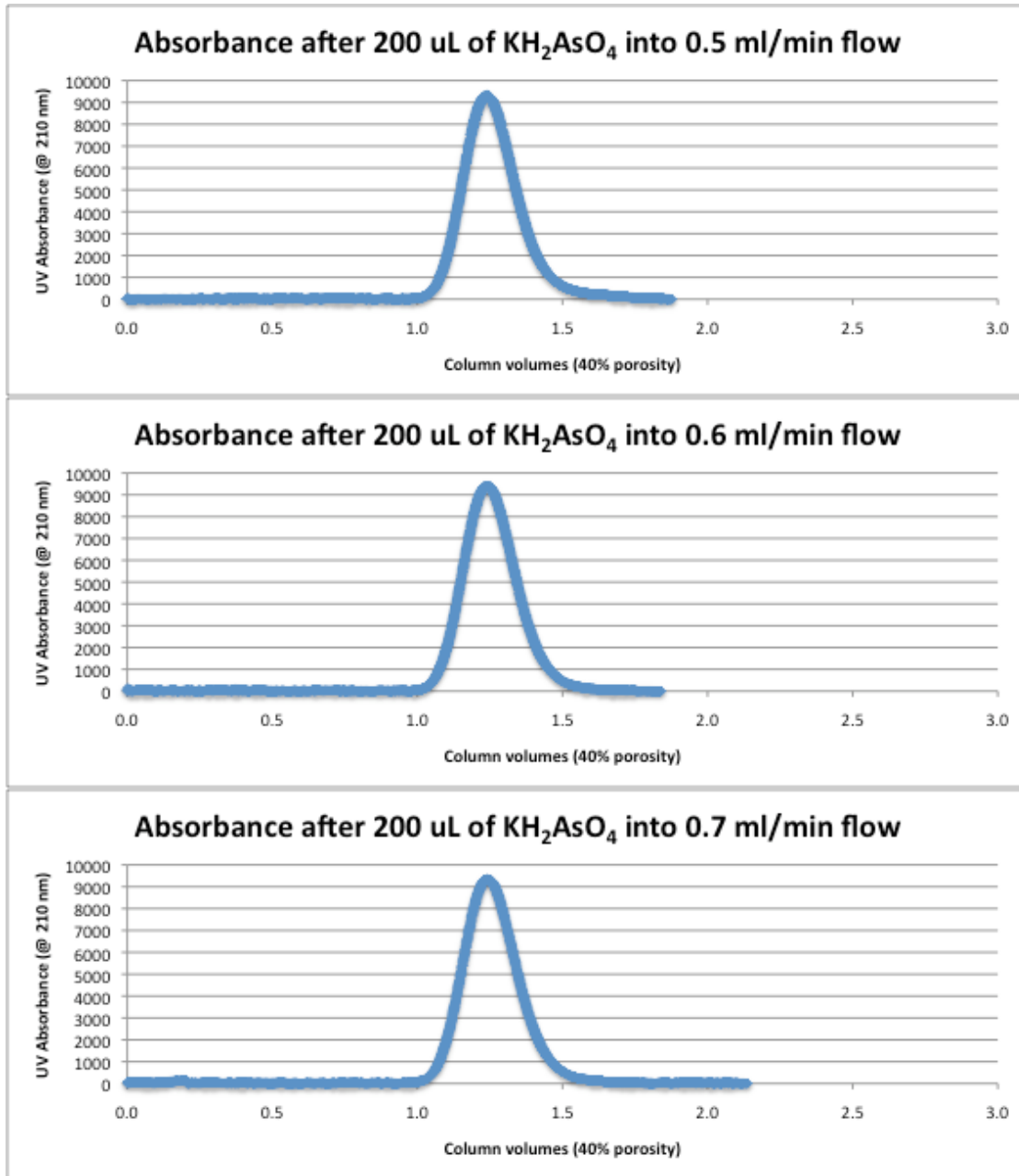
0.6 mmol KH₂AsO₄



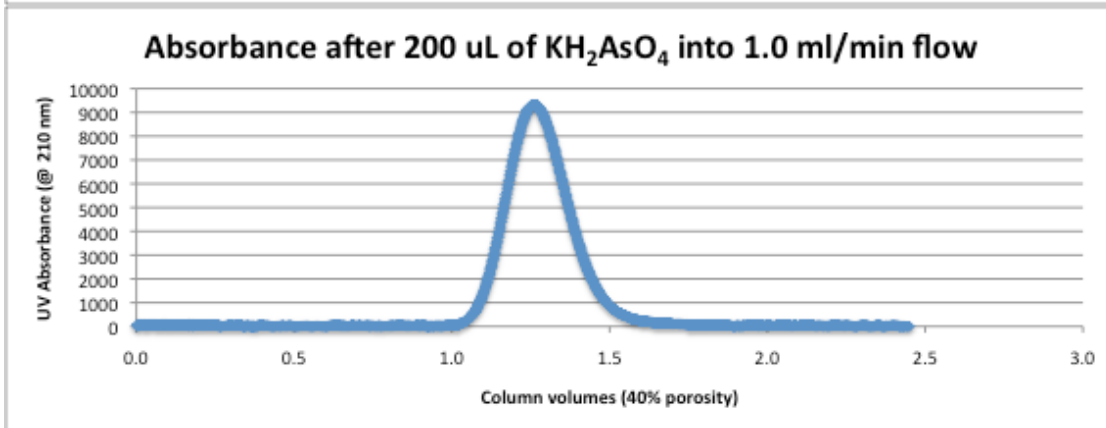
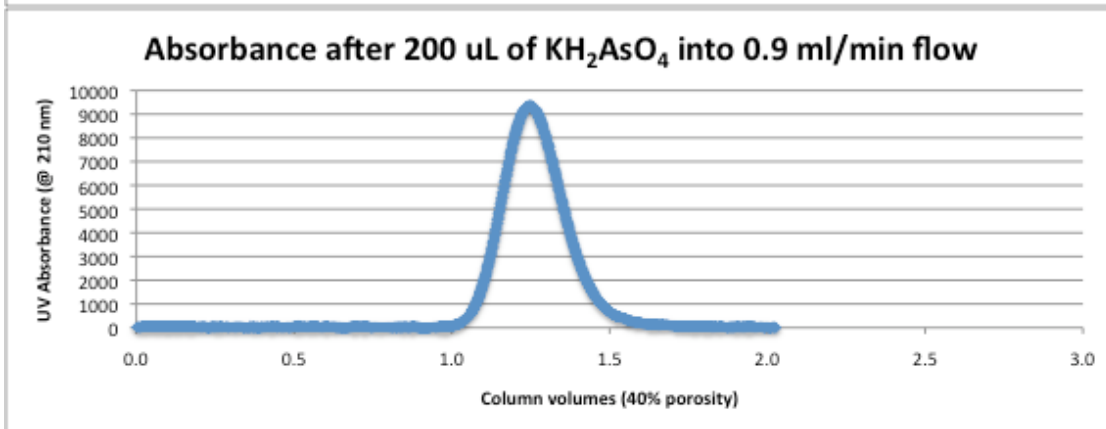
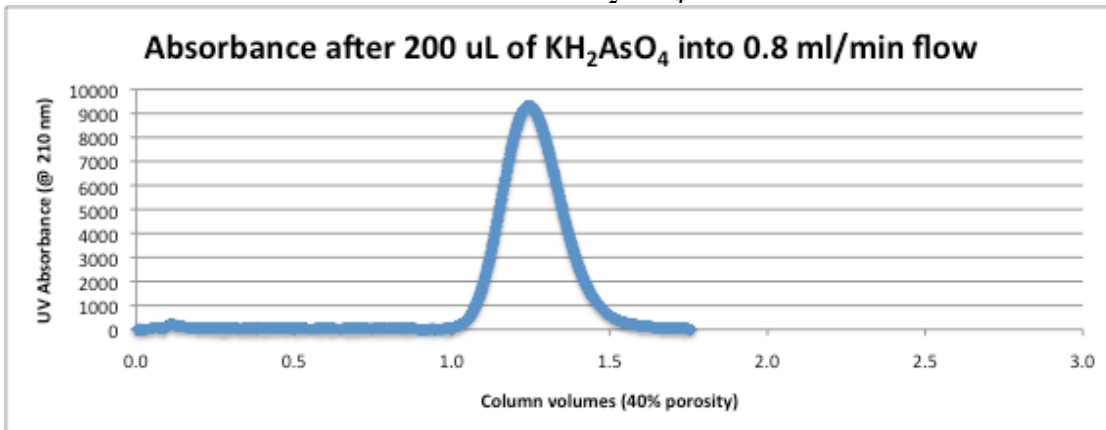
0.6 mmol KH₂AsO₄



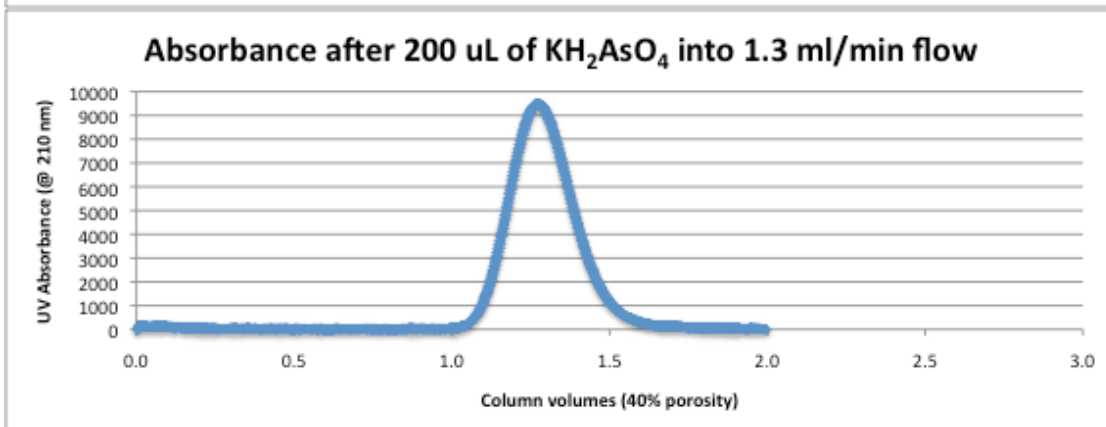
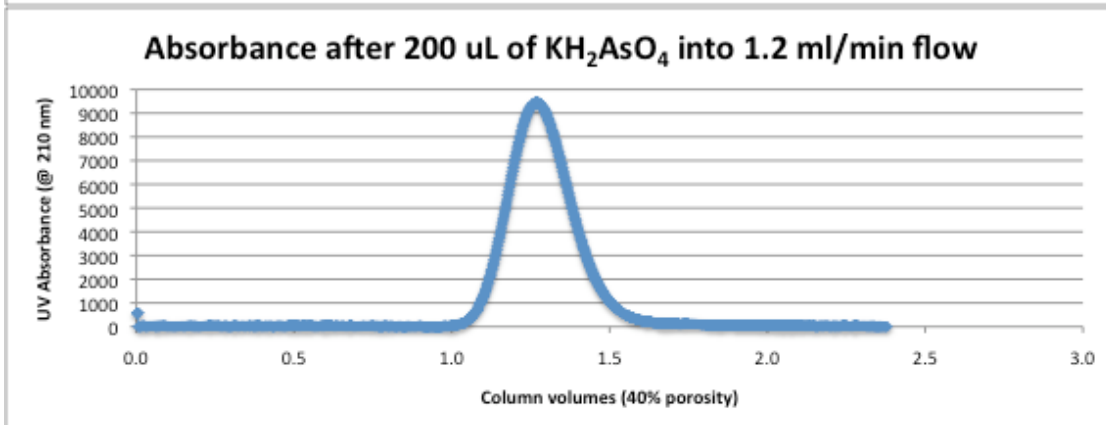
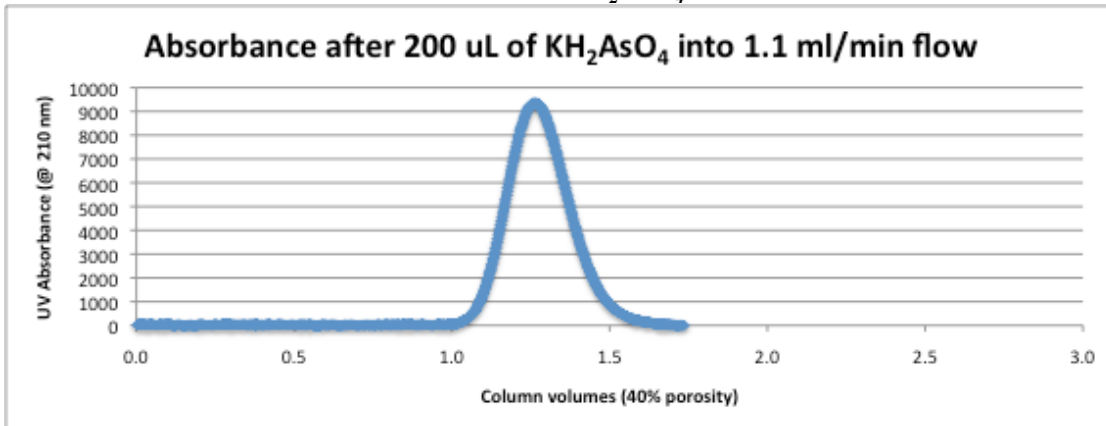
0.7 mmol KH₂AsO₄



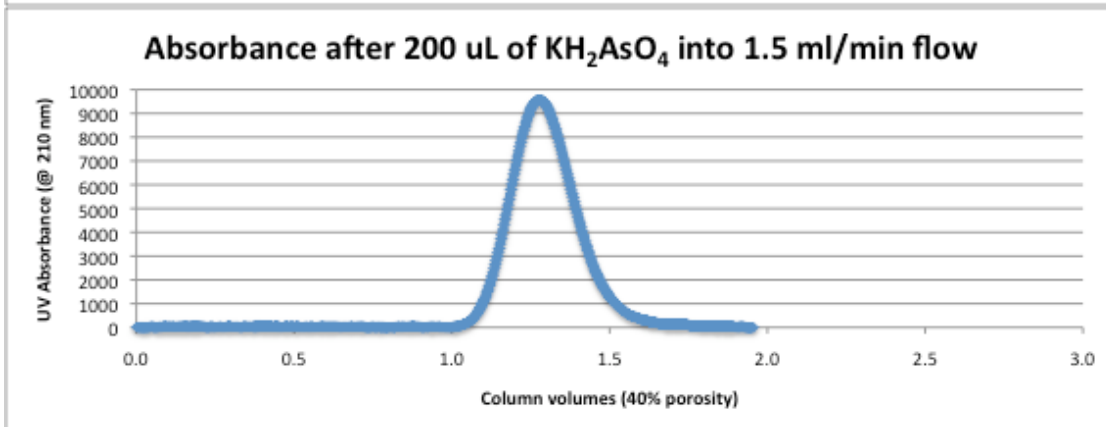
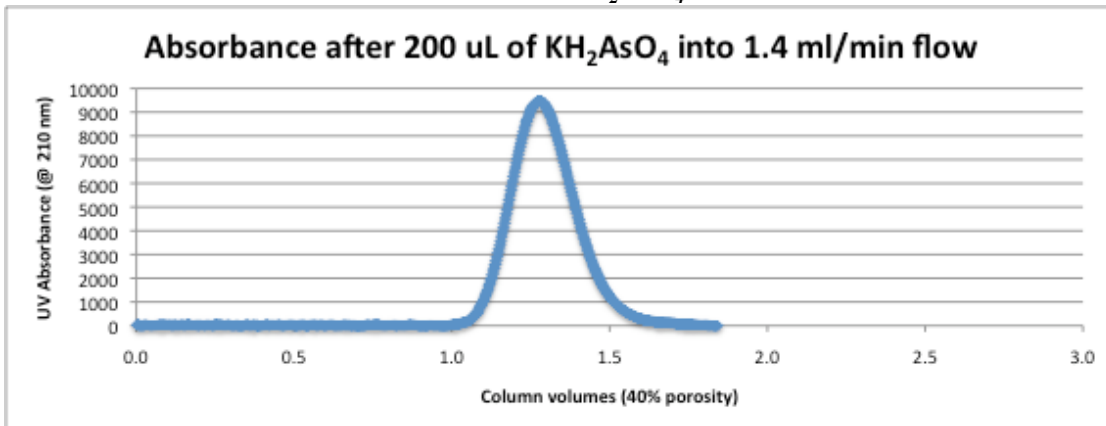
0.7 mmol KH₂AsO₄



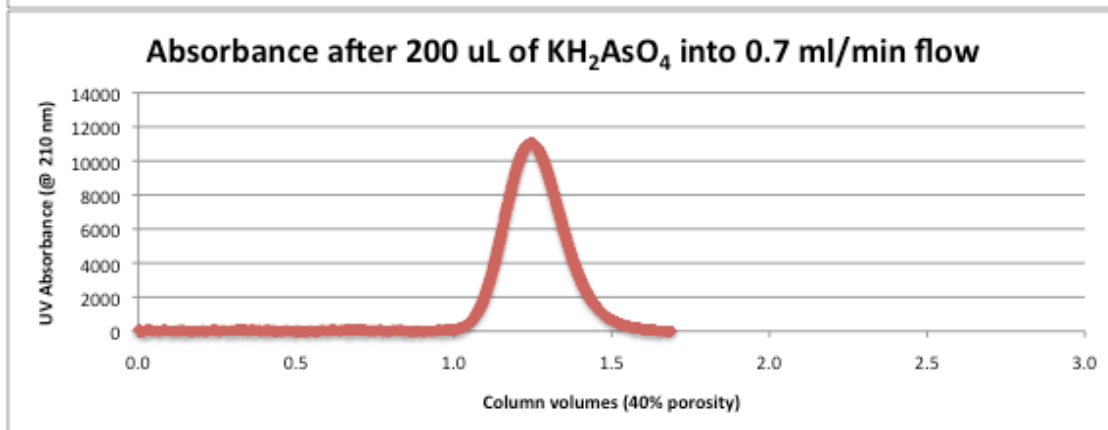
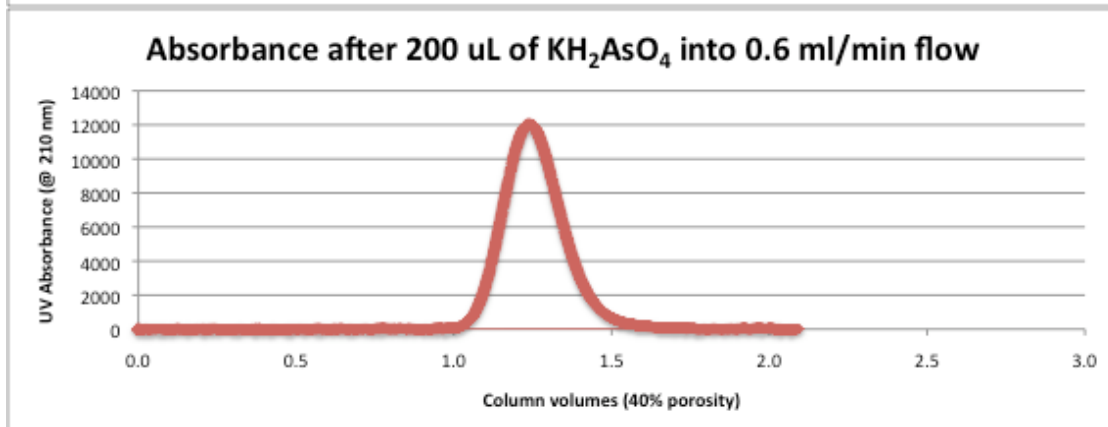
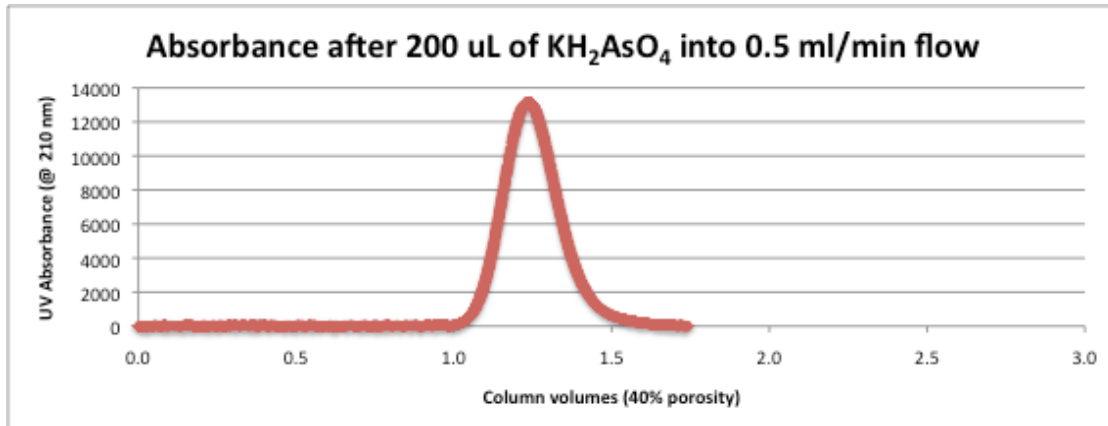
0.7 mmol KH₂AsO₄



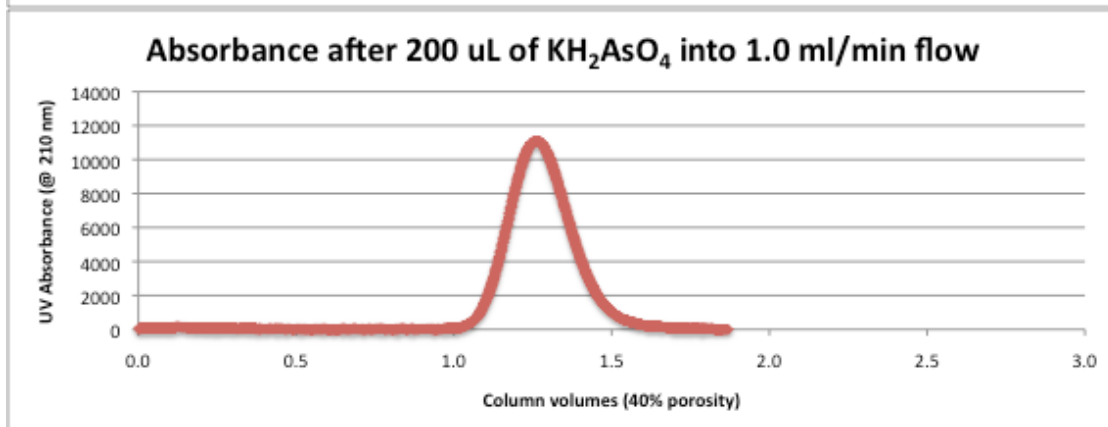
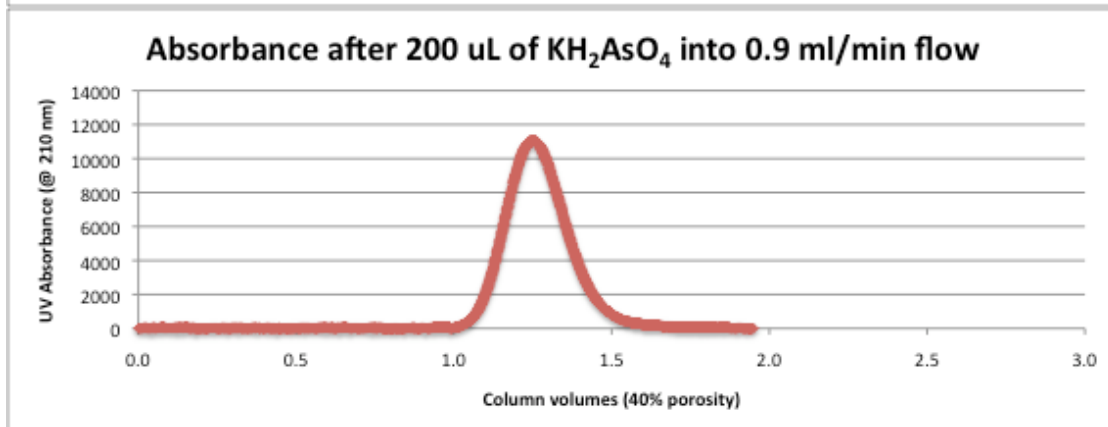
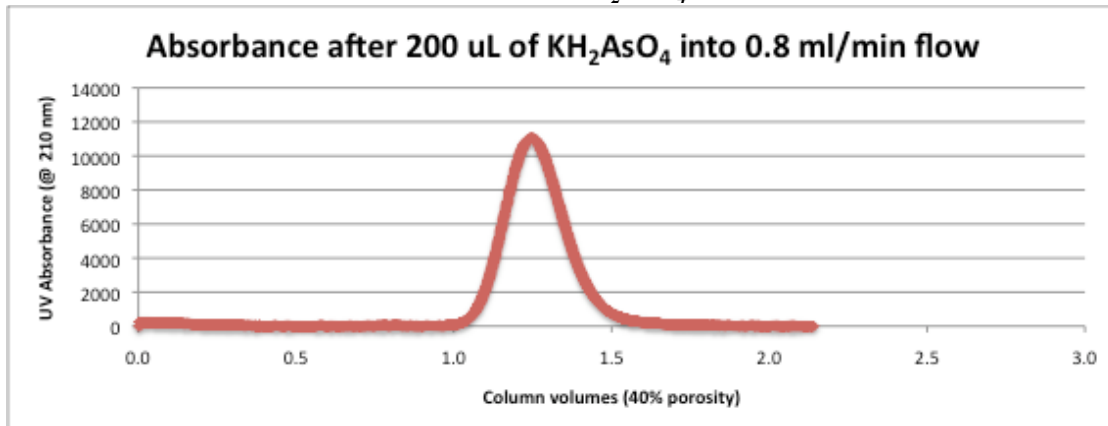
0.7 mmol KH₂AsO₄



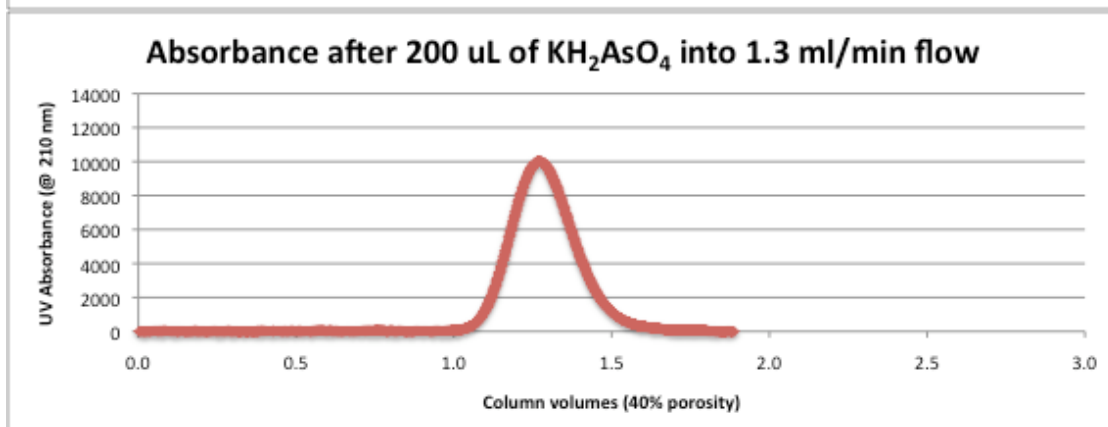
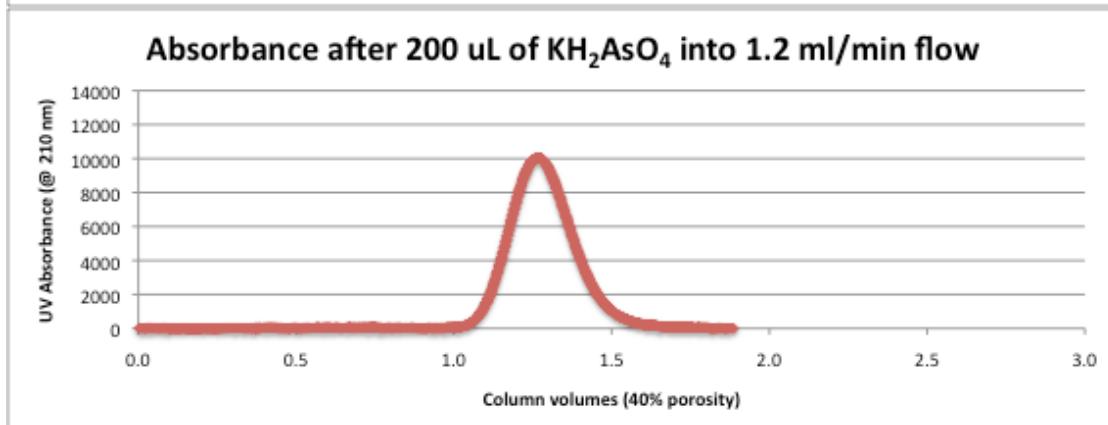
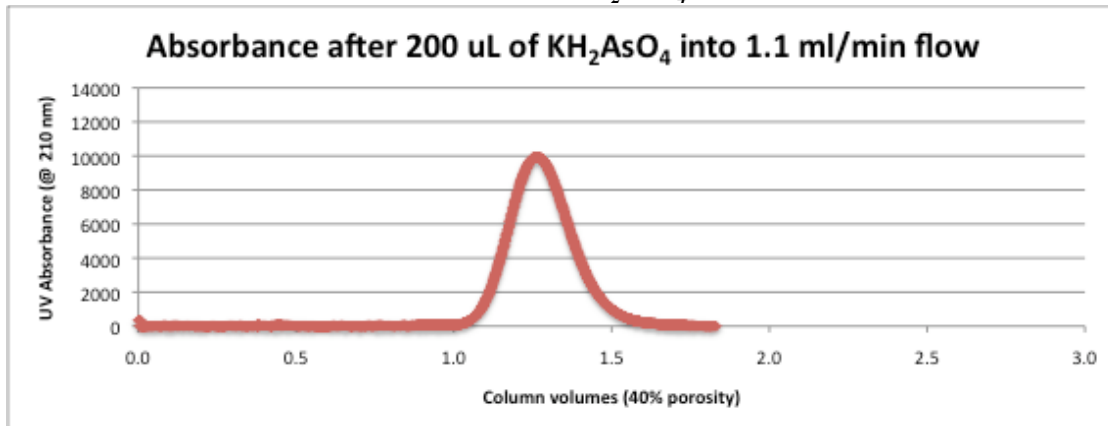
0.8 mmol KH₂AsO₄



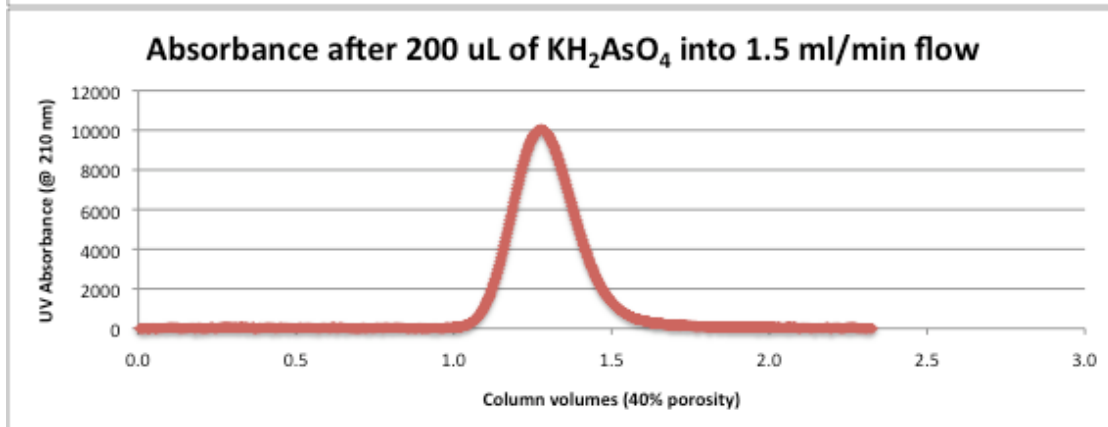
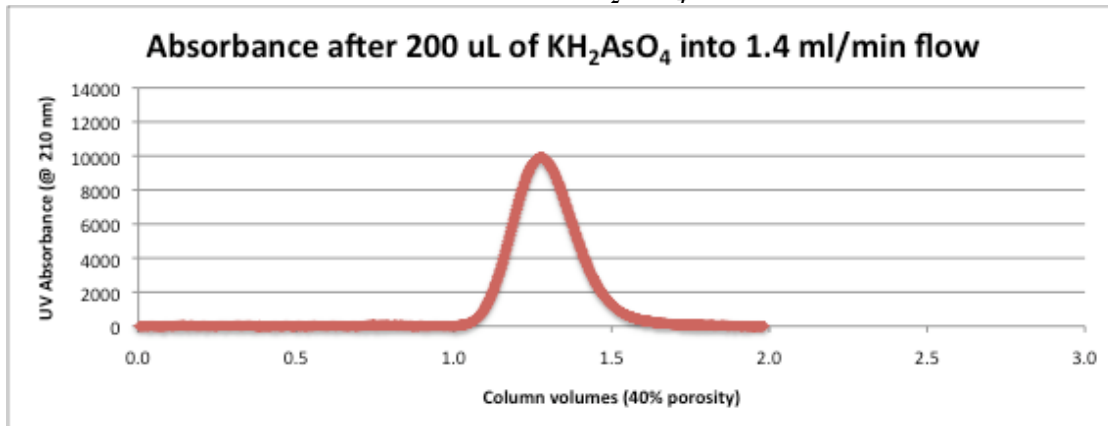
0.8 mmol KH₂AsO₄



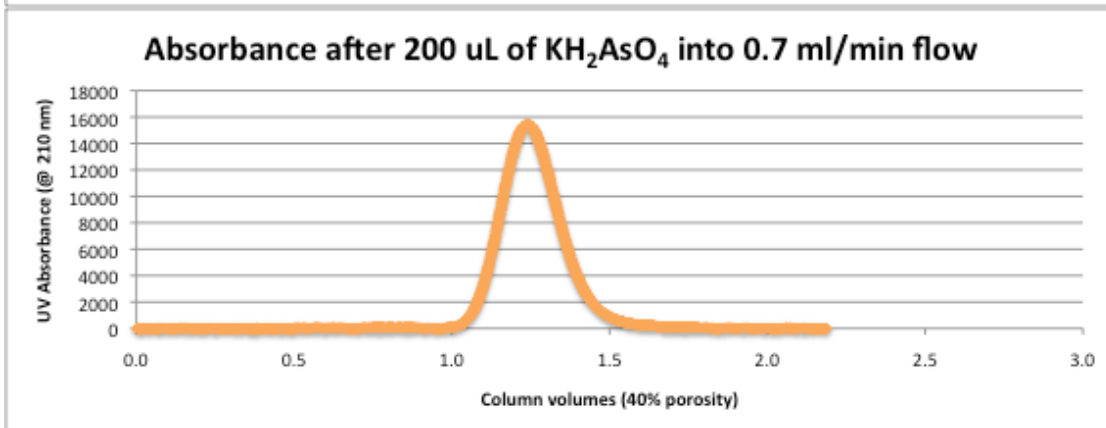
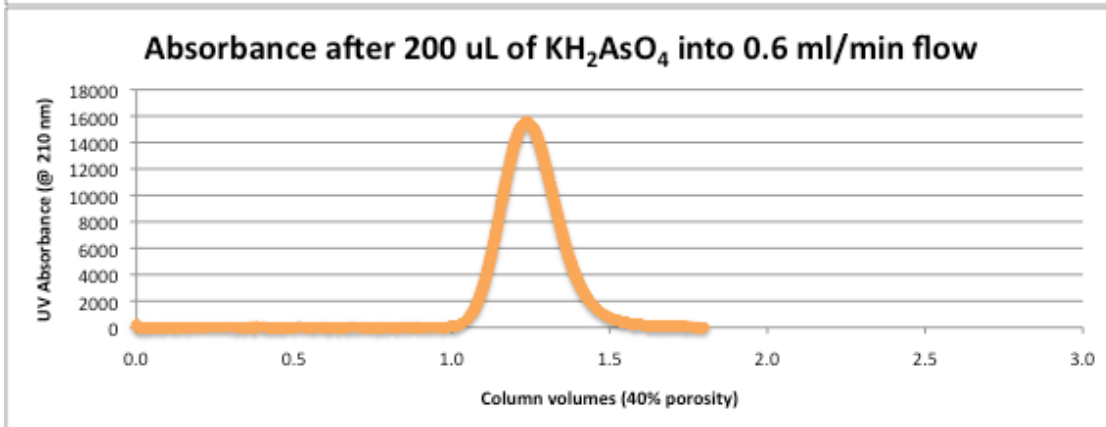
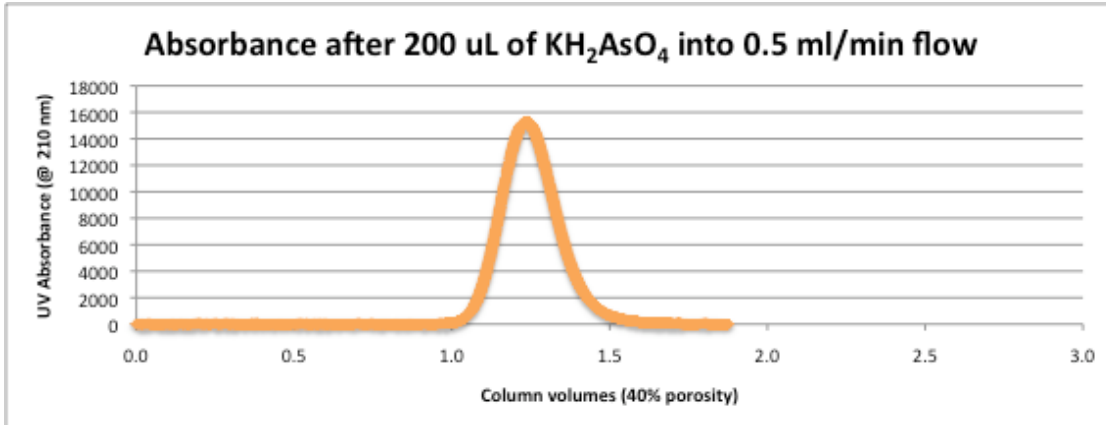
0.8 mmol KH₂AsO₄



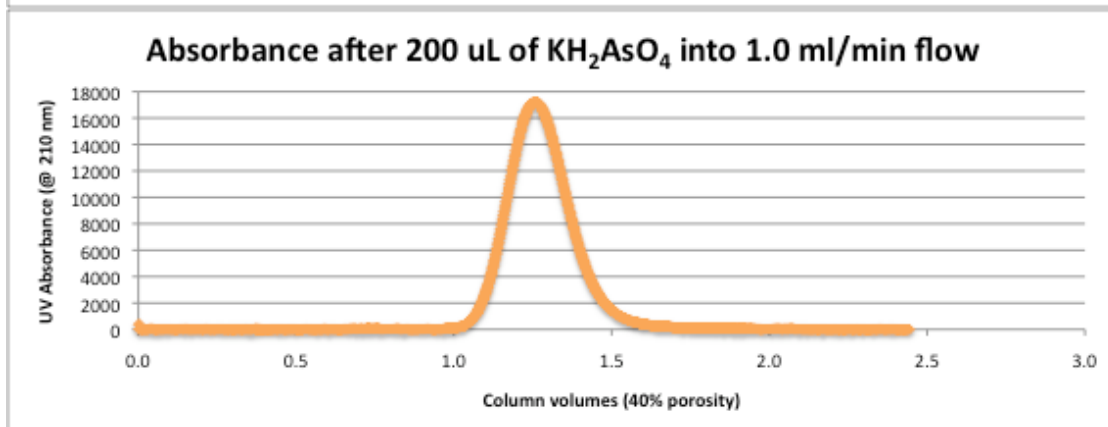
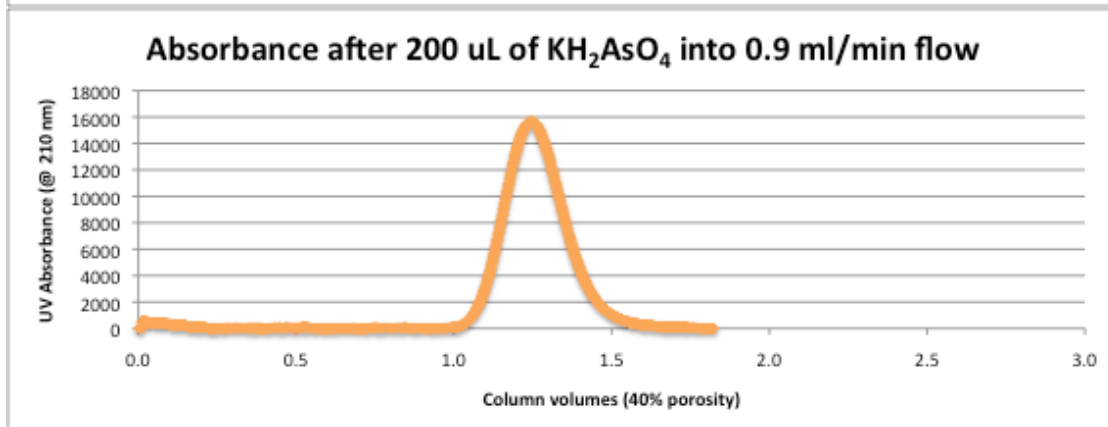
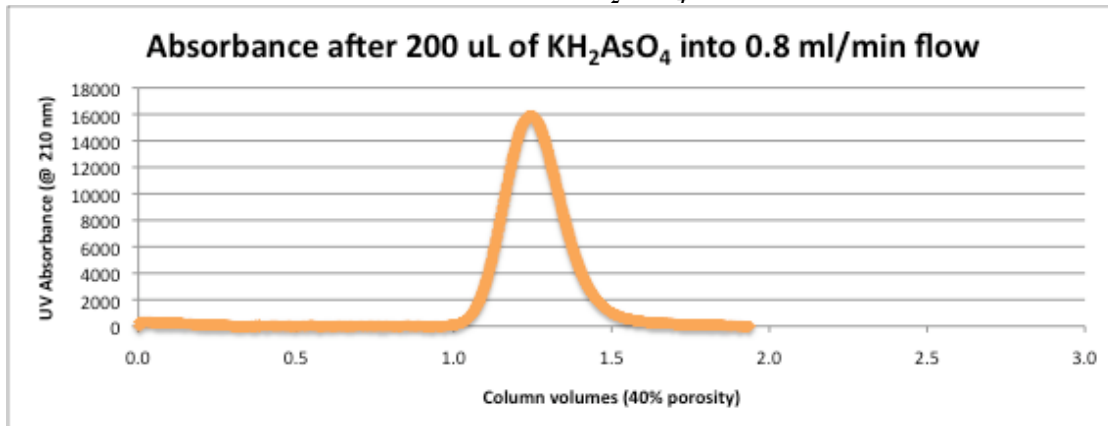
0.8 mmol KH₂AsO₄



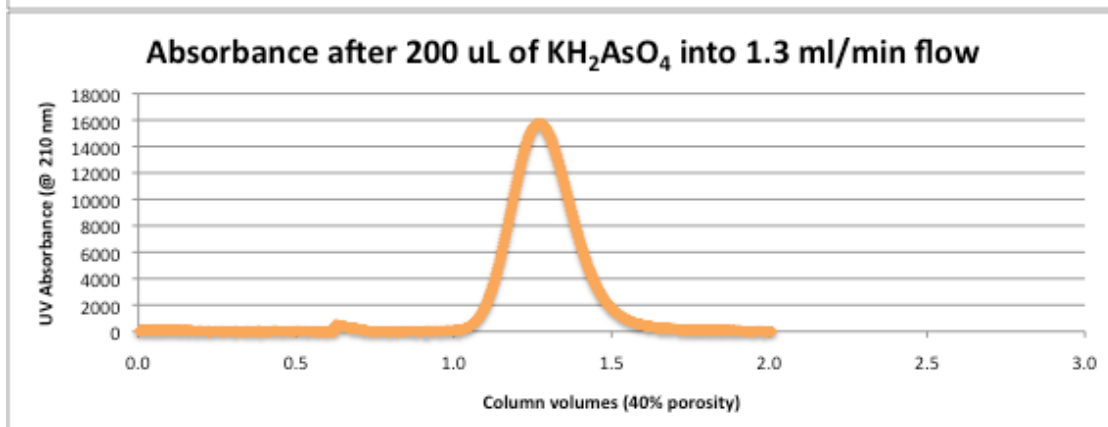
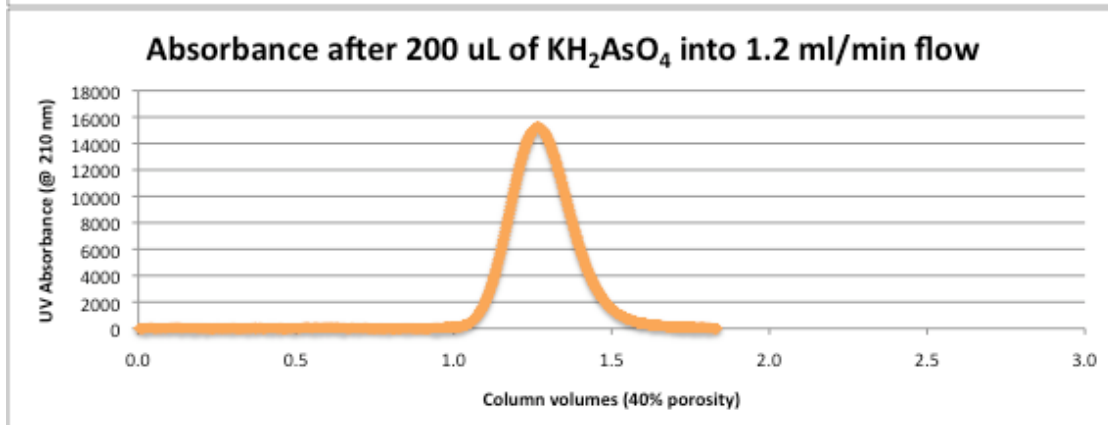
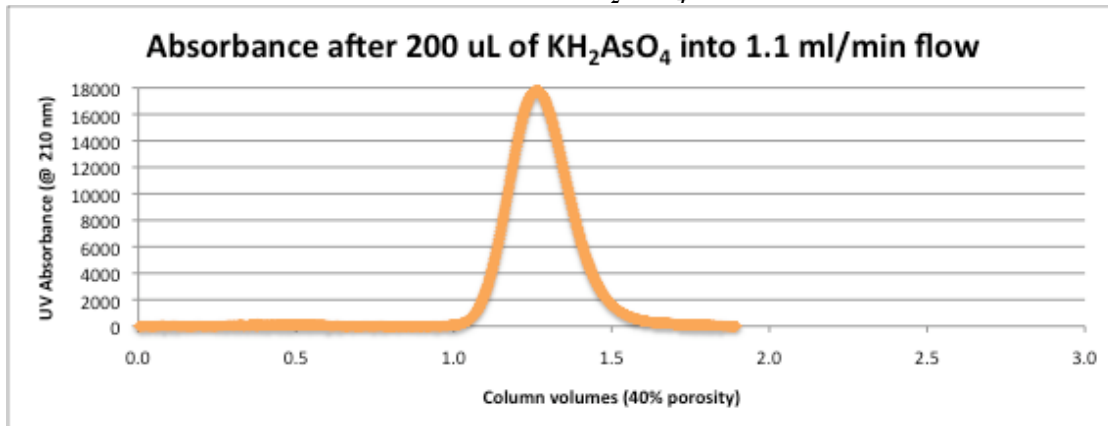
0.9 mmol KH₂AsO₄



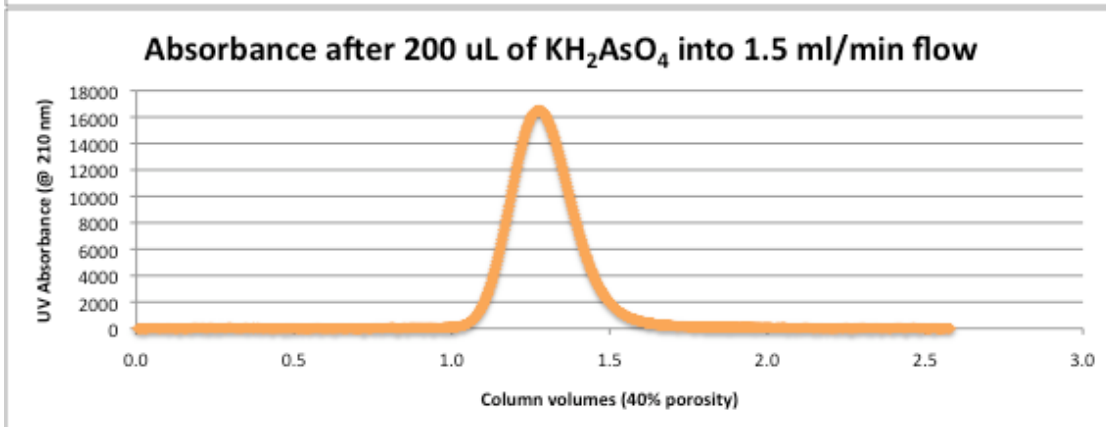
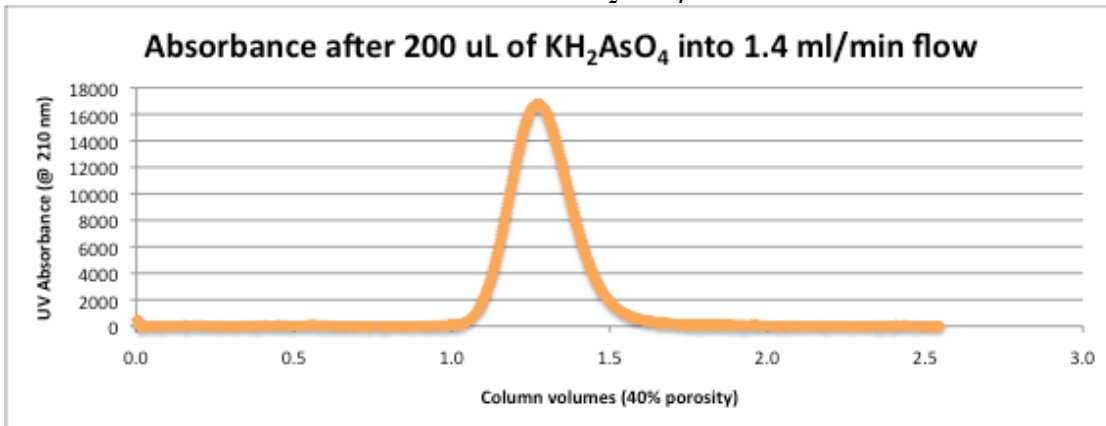
0.9 mmol KH₂AsO₄



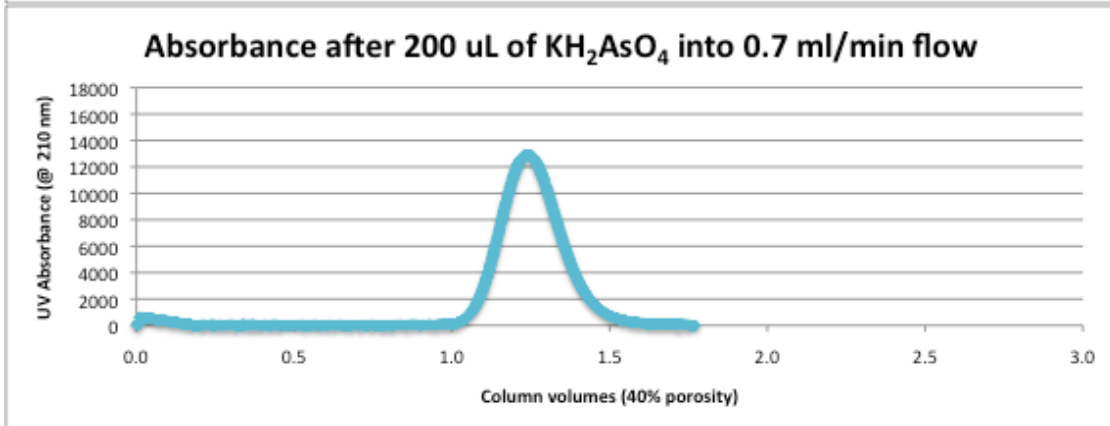
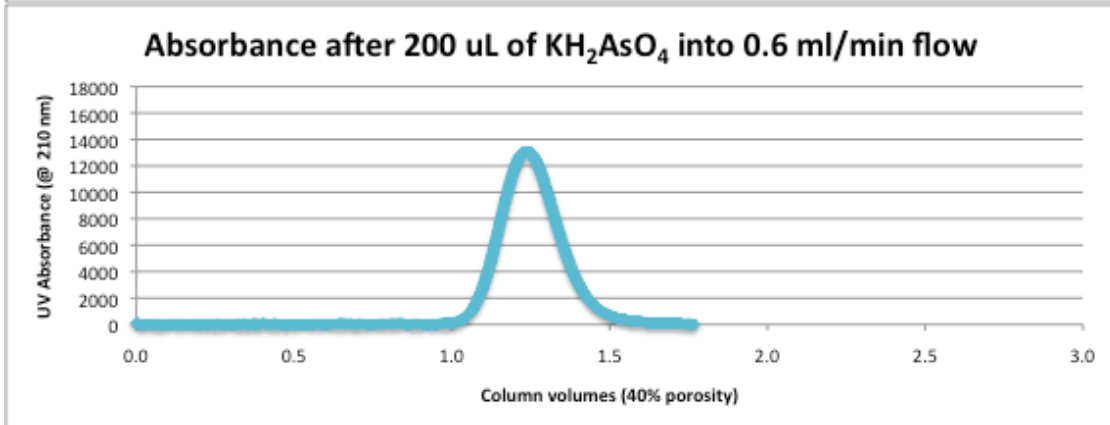
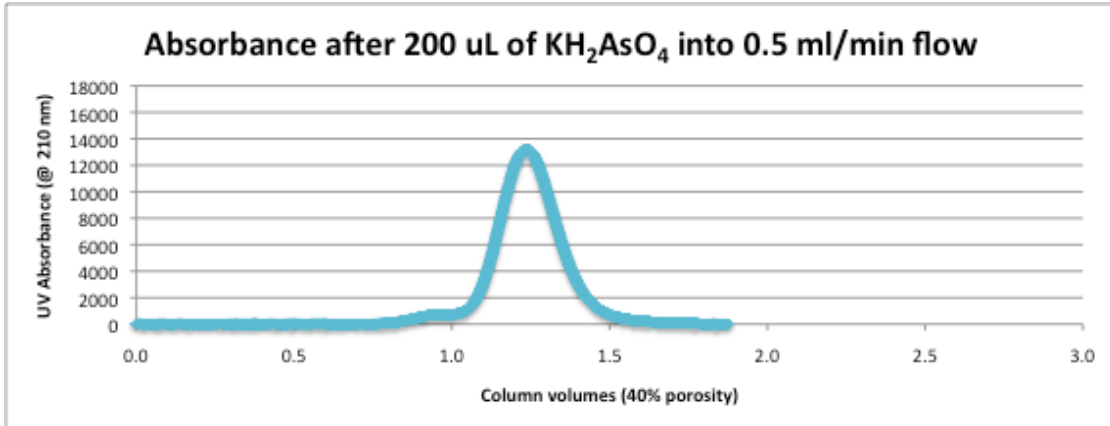
0.9 mmol KH₂AsO₄



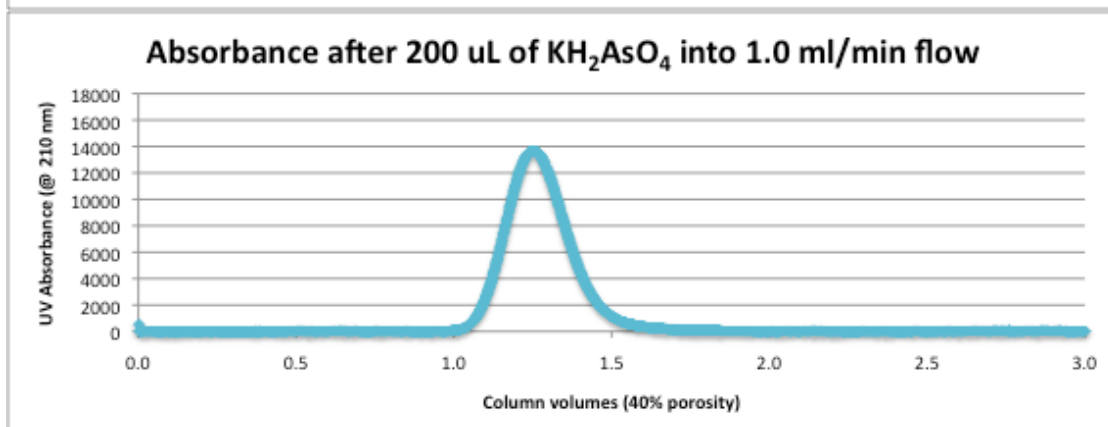
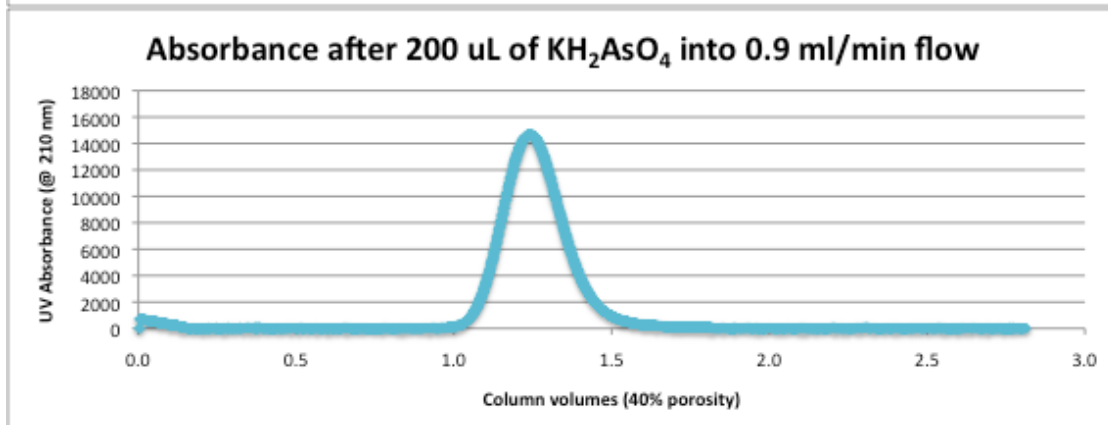
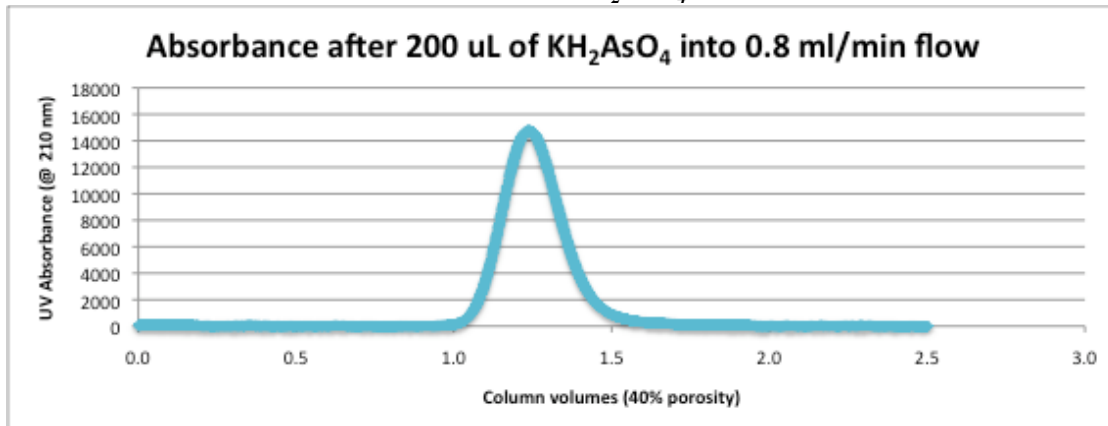
0.9 mmol KH₂AsO₄



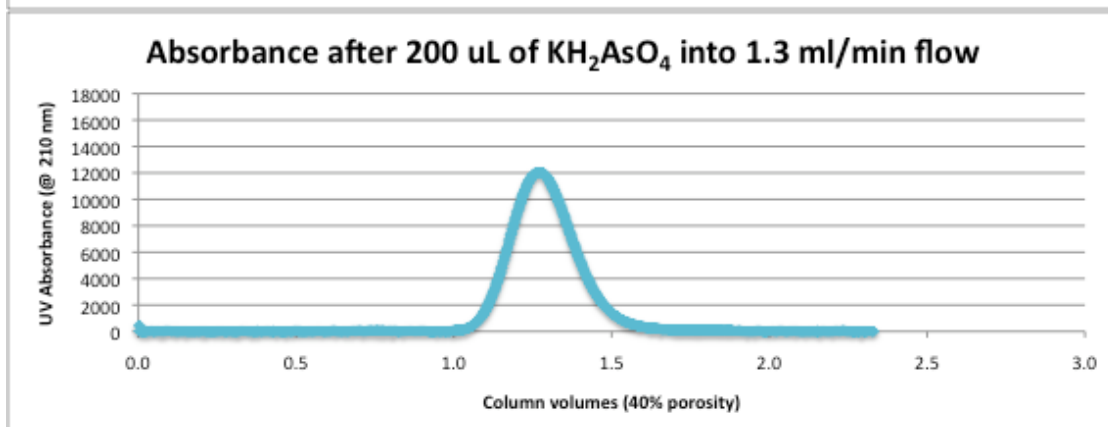
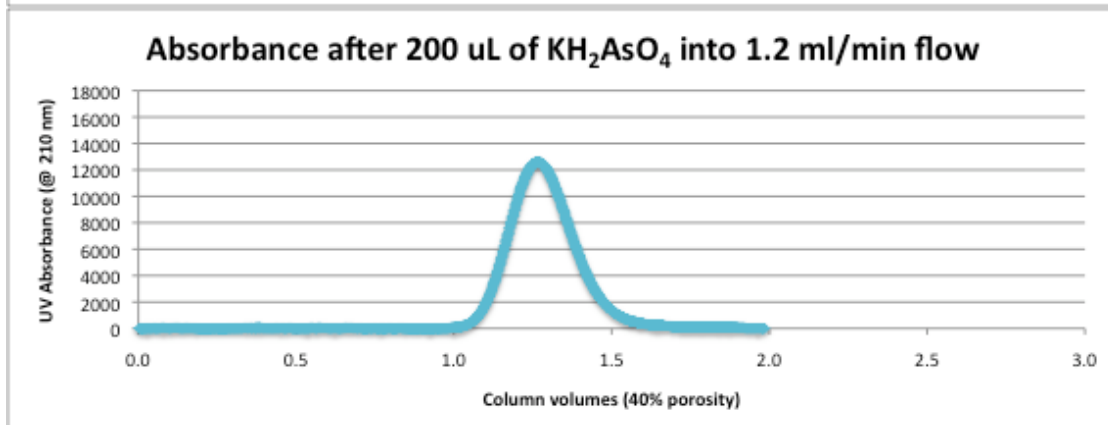
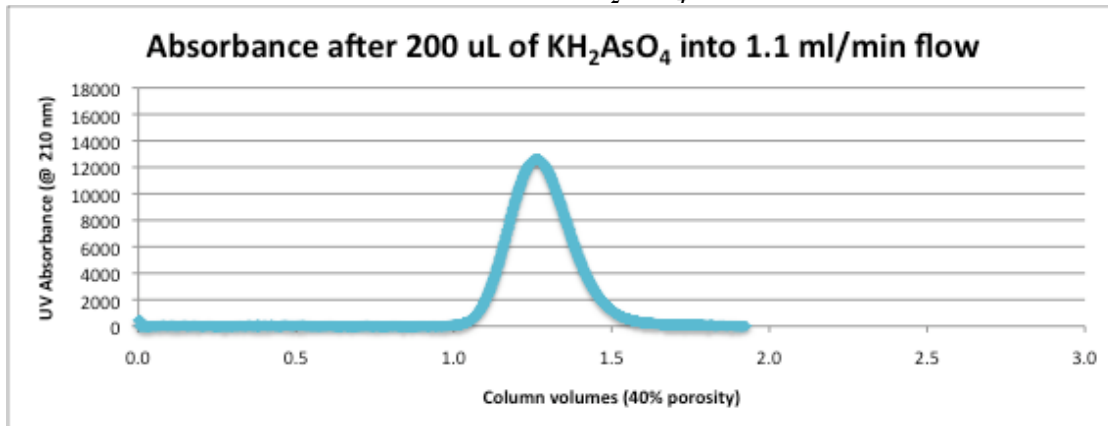
1.0 mmol KH₂AsO₄



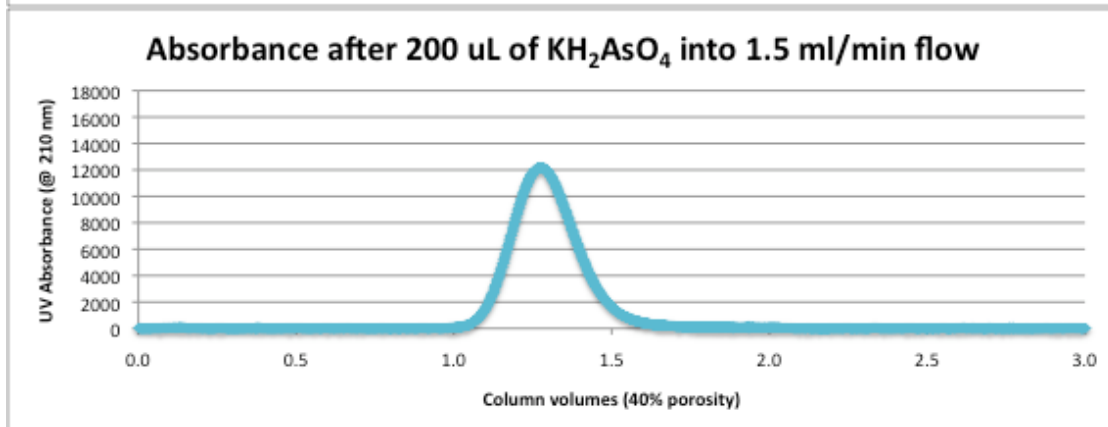
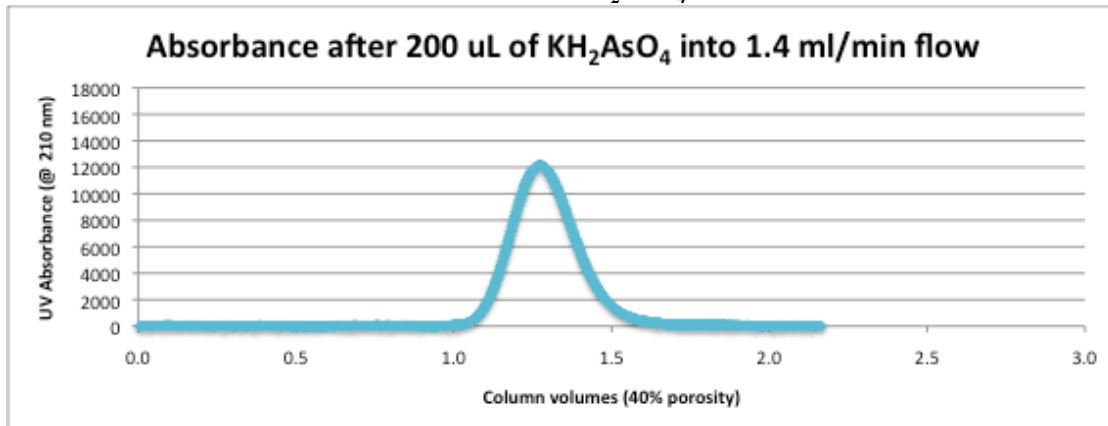
1.0 mmol KH₂AsO₄



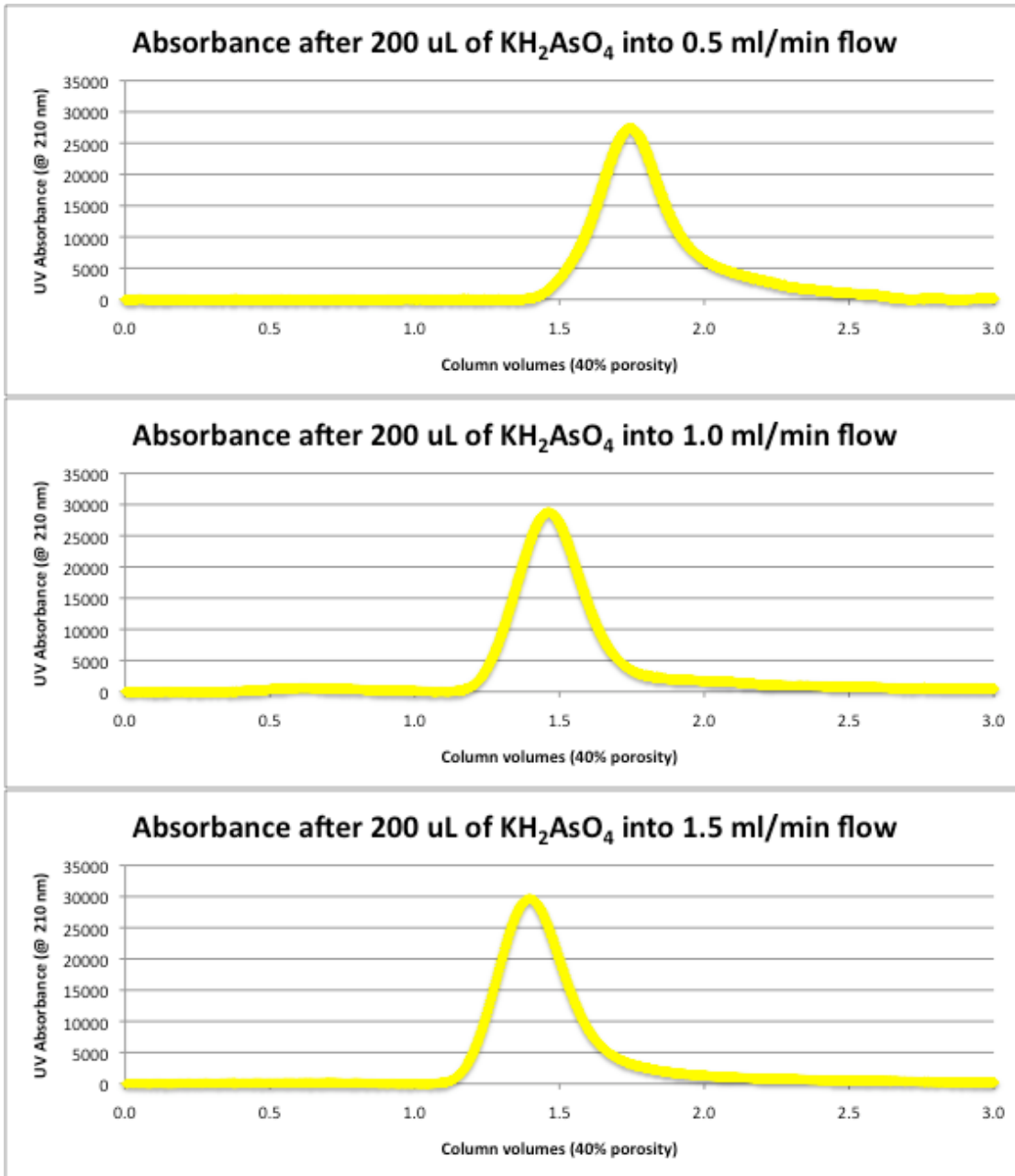
1.0 mmol KH₂AsO₄



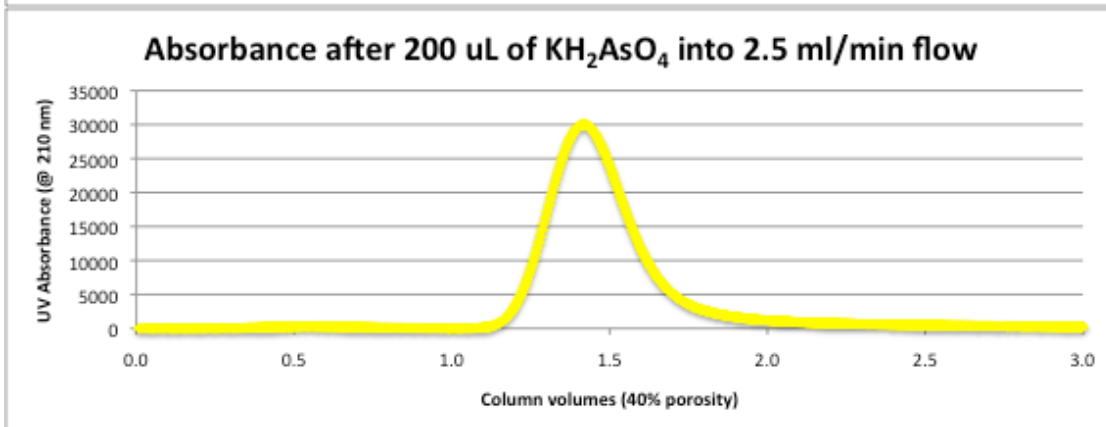
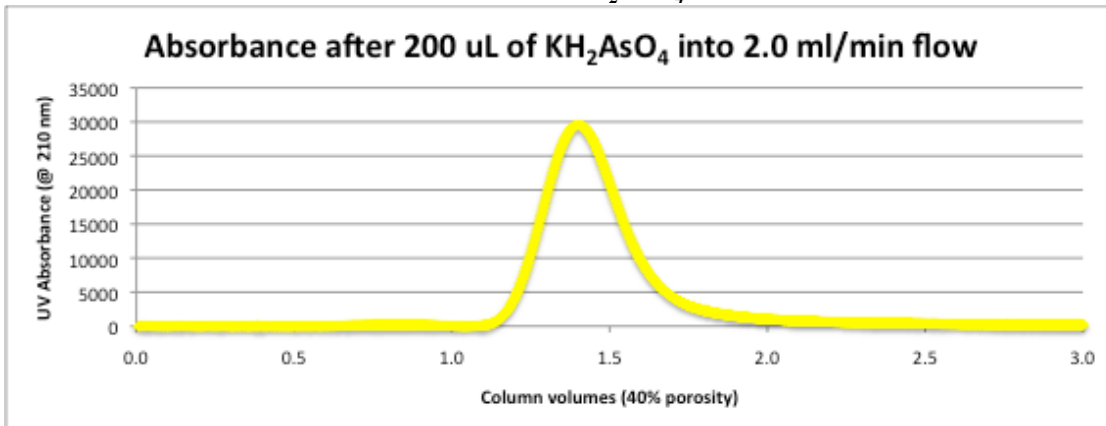
1.0 mmol KH₂AsO₄



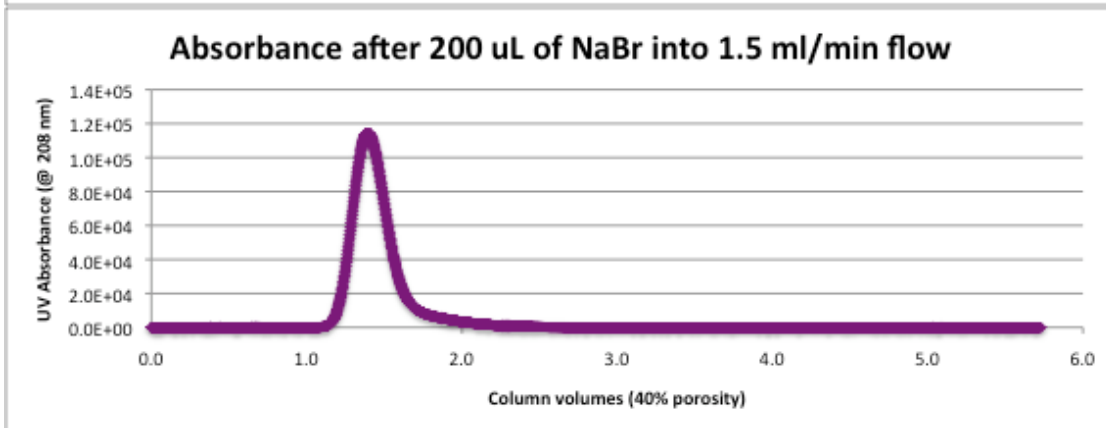
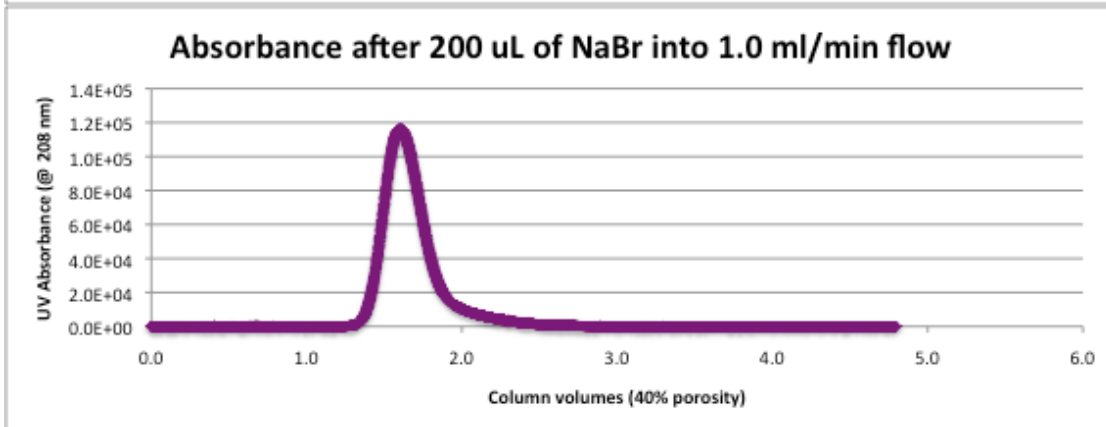
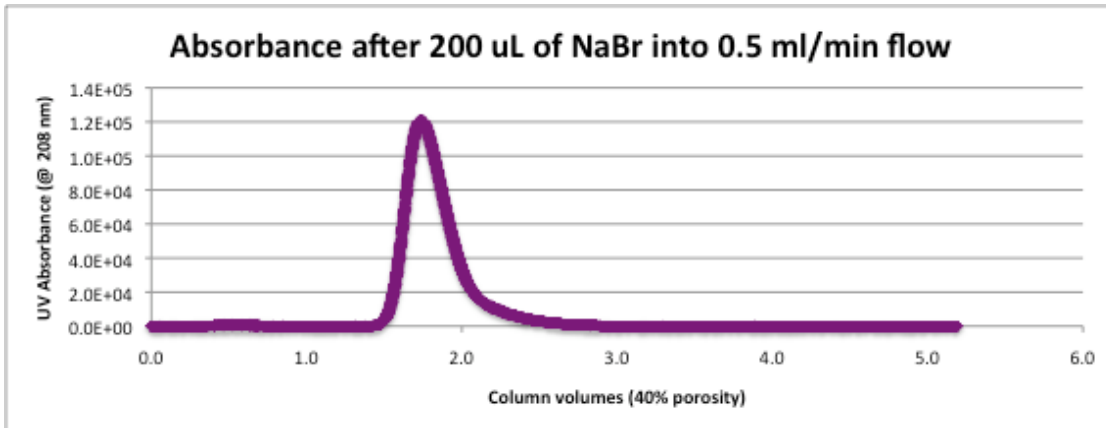
3.0 mmol KH₂AsO₄



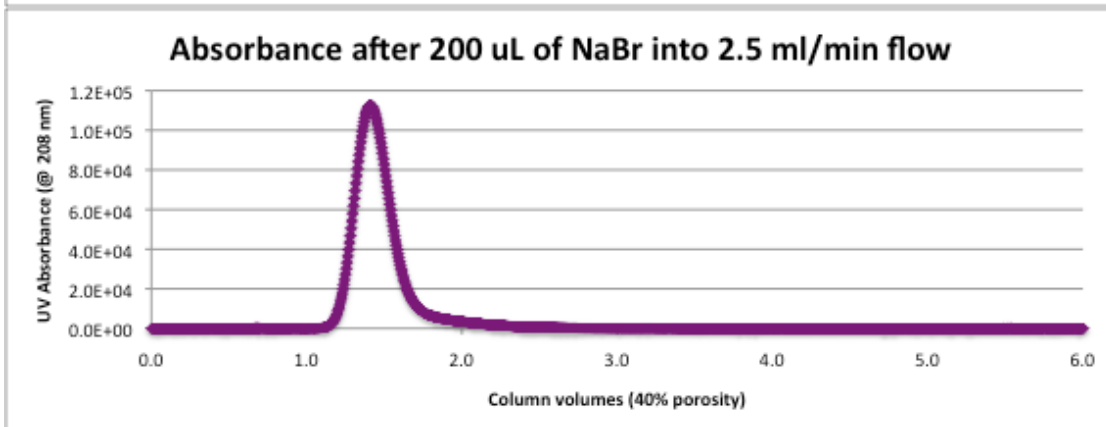
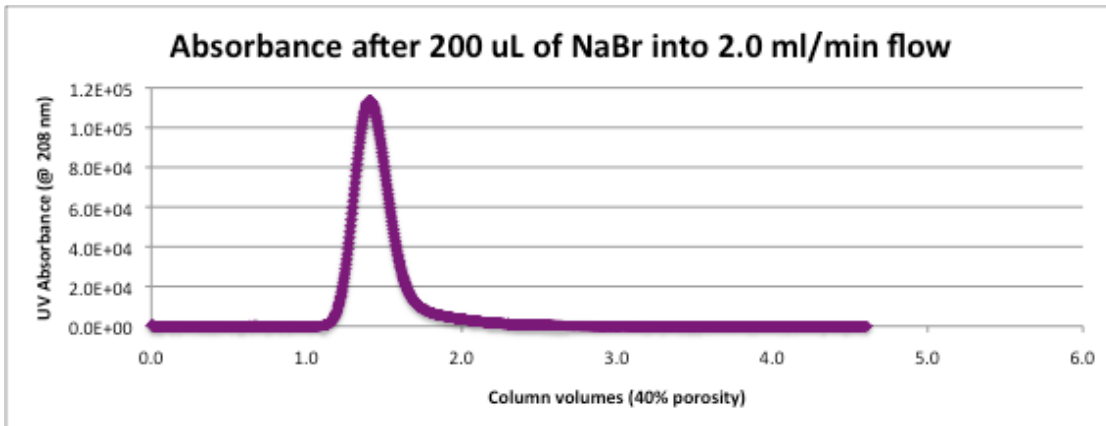
3.0 mmol KH₂AsO₄



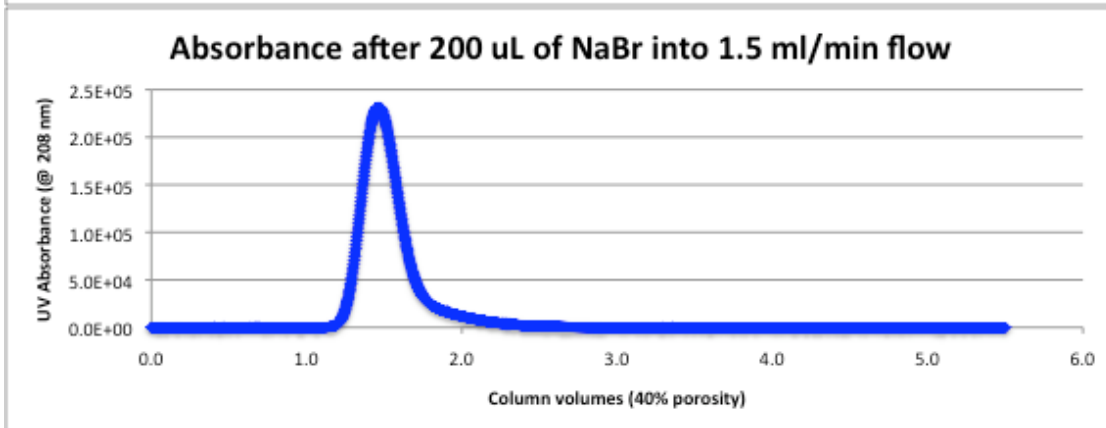
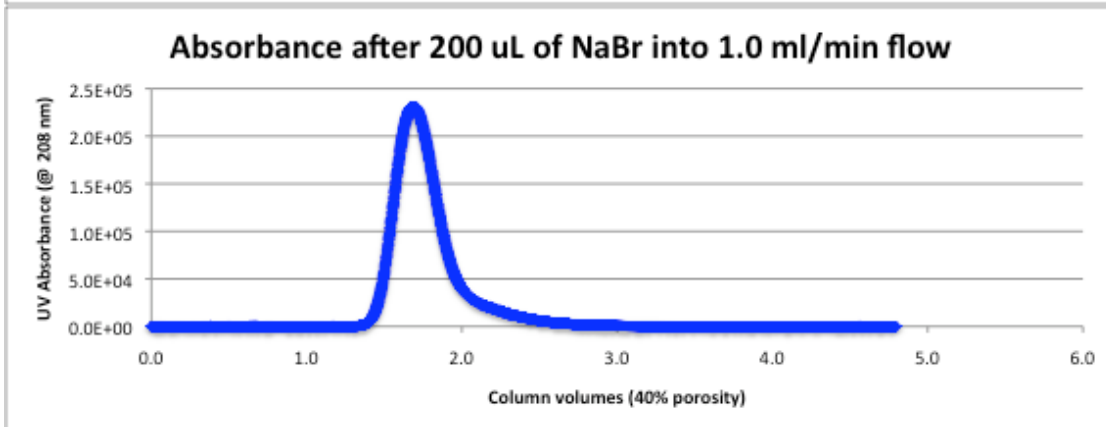
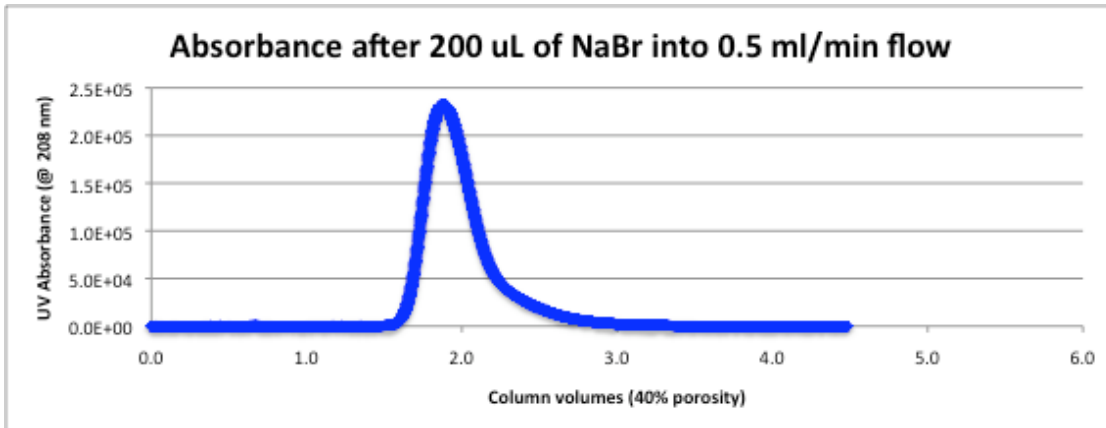
0.5 mmol NaBr



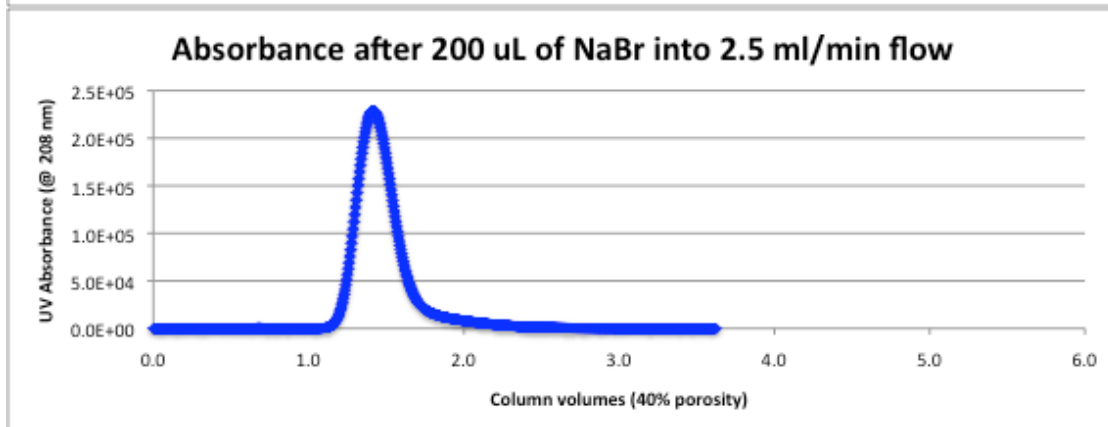
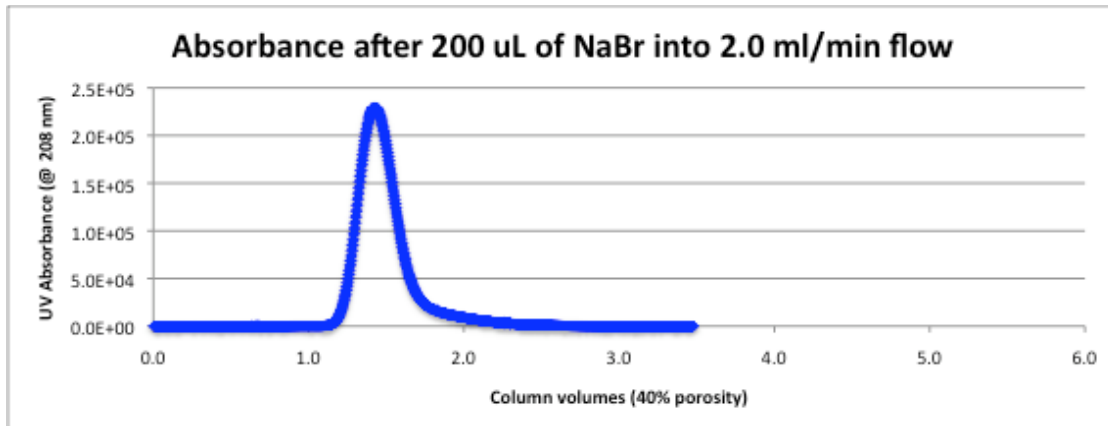
0.5 mmol NaBr



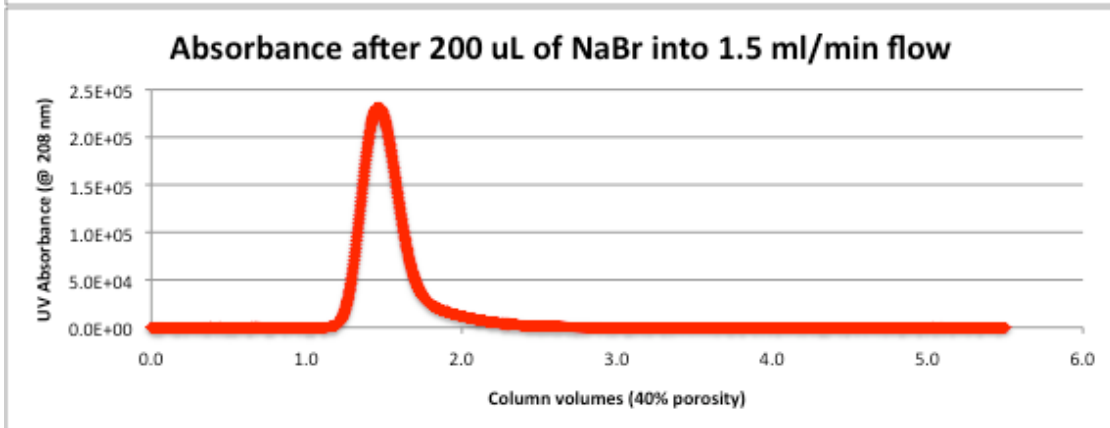
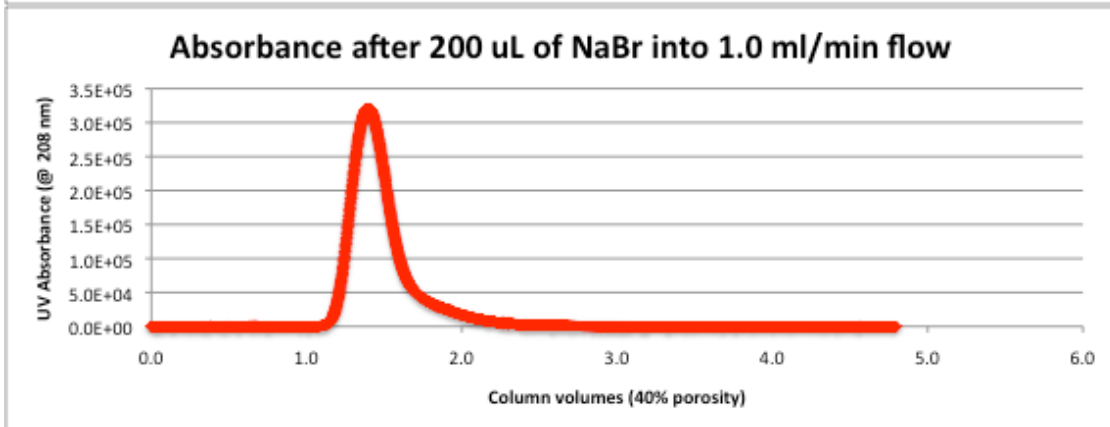
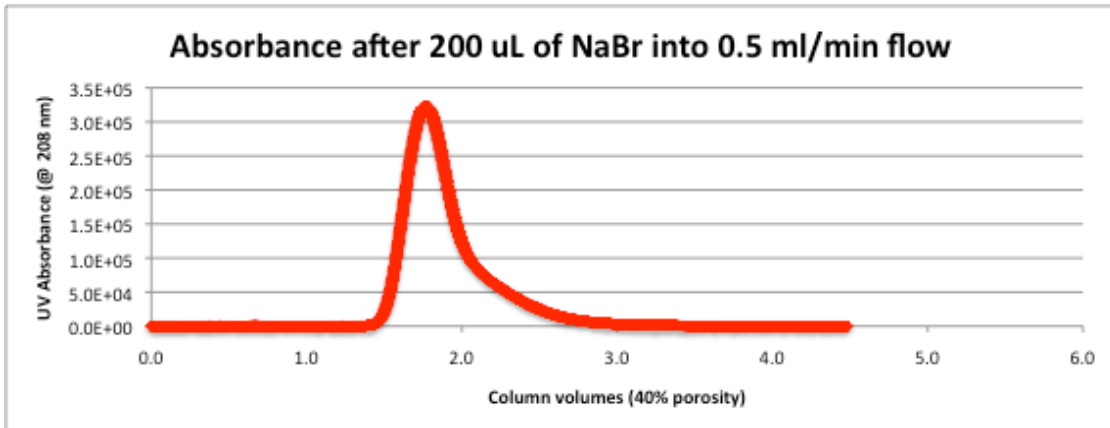
1.0 mmol NaBr



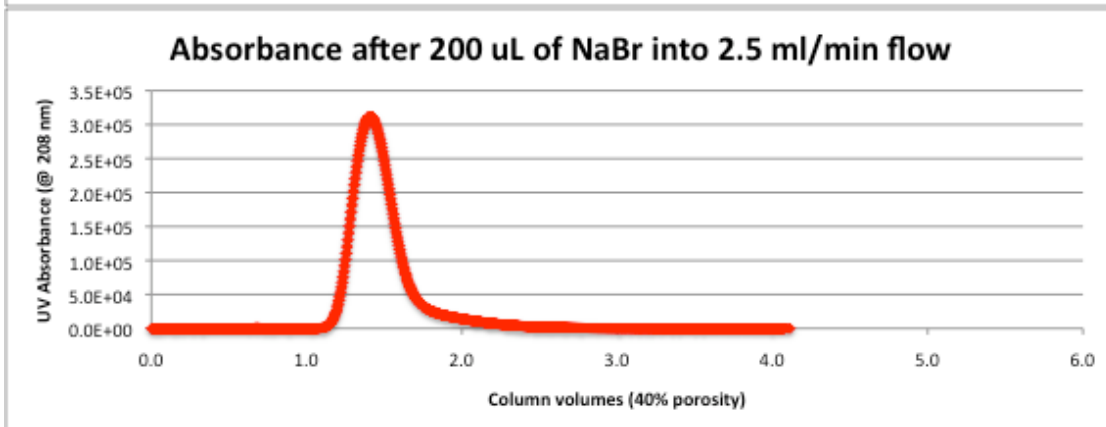
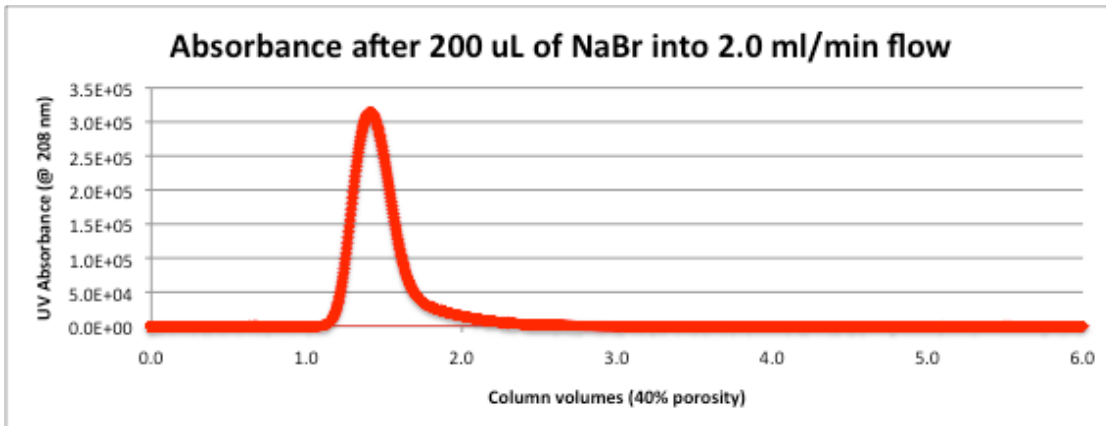
1.0 mmol NaBr



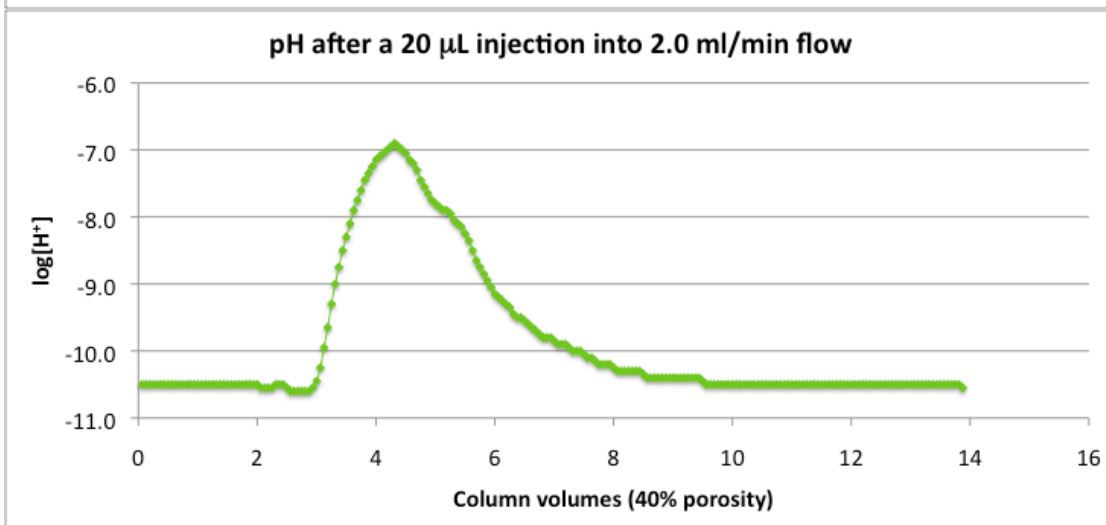
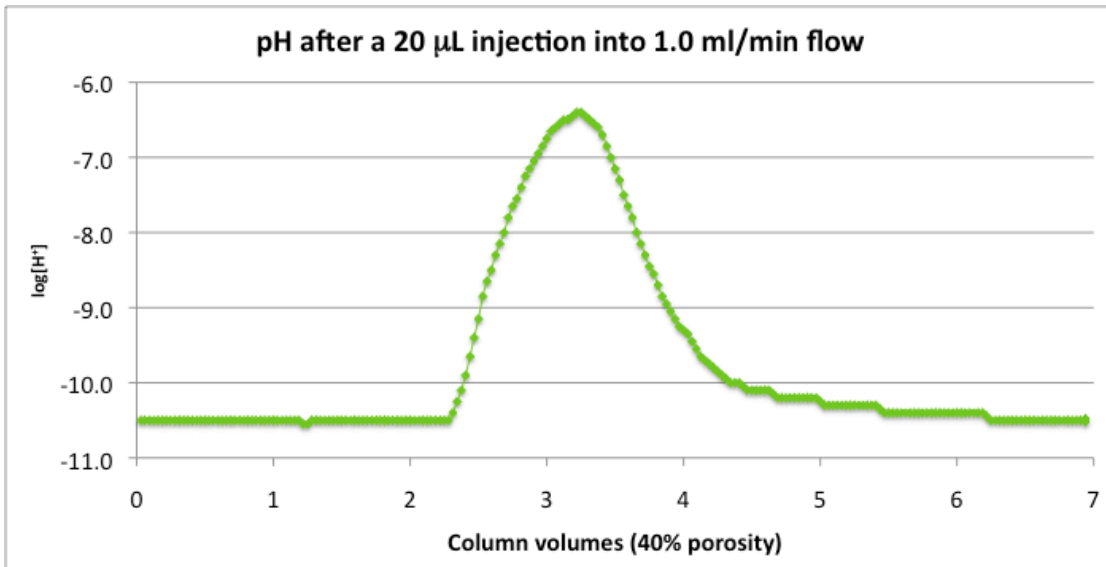
2.0 mmol NaBr



2.0 mmol NaBr

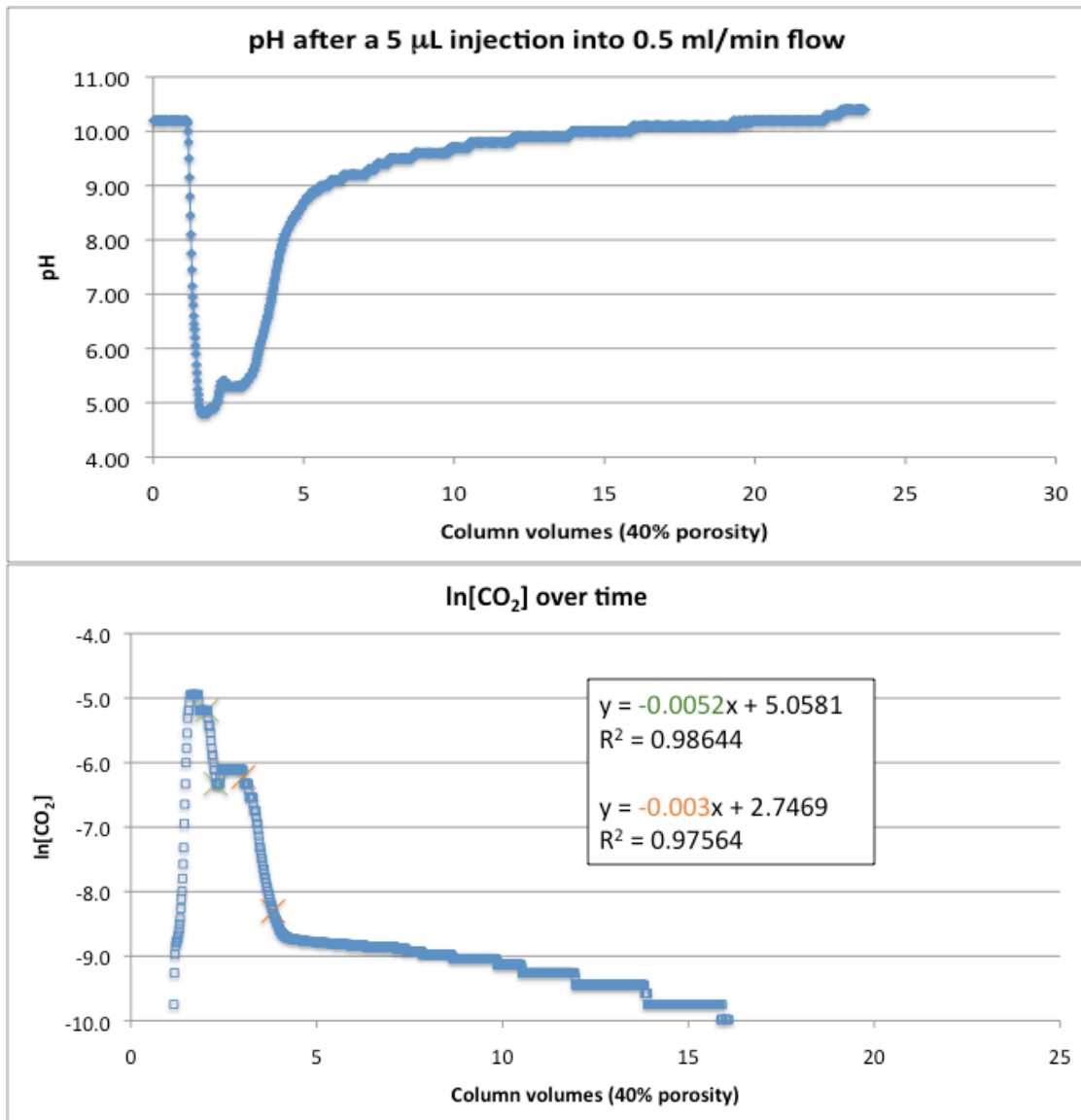


Dissolved CO₂ in 0.1 N CaCl₂

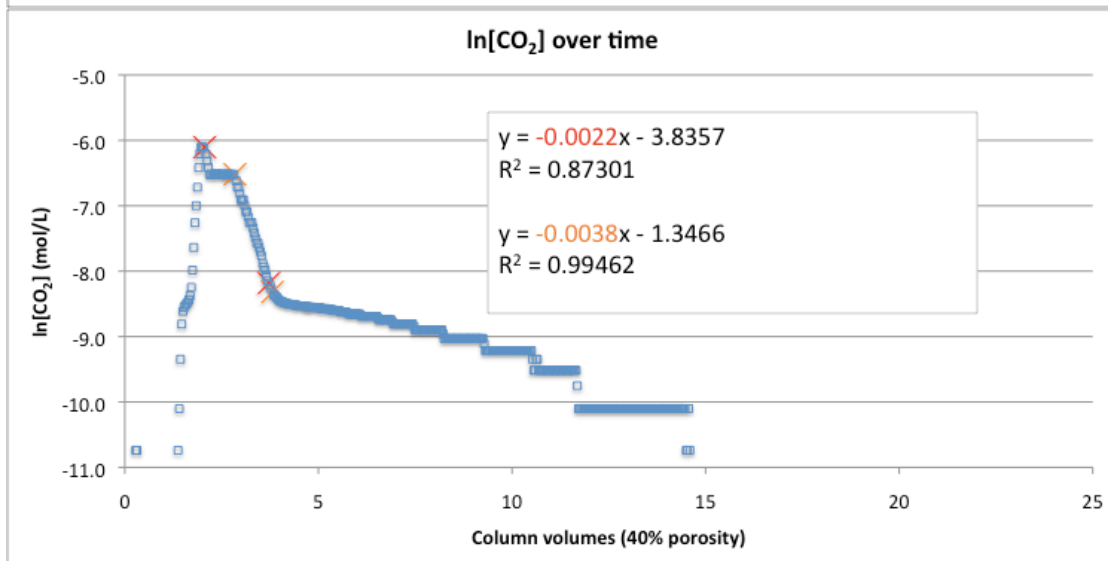
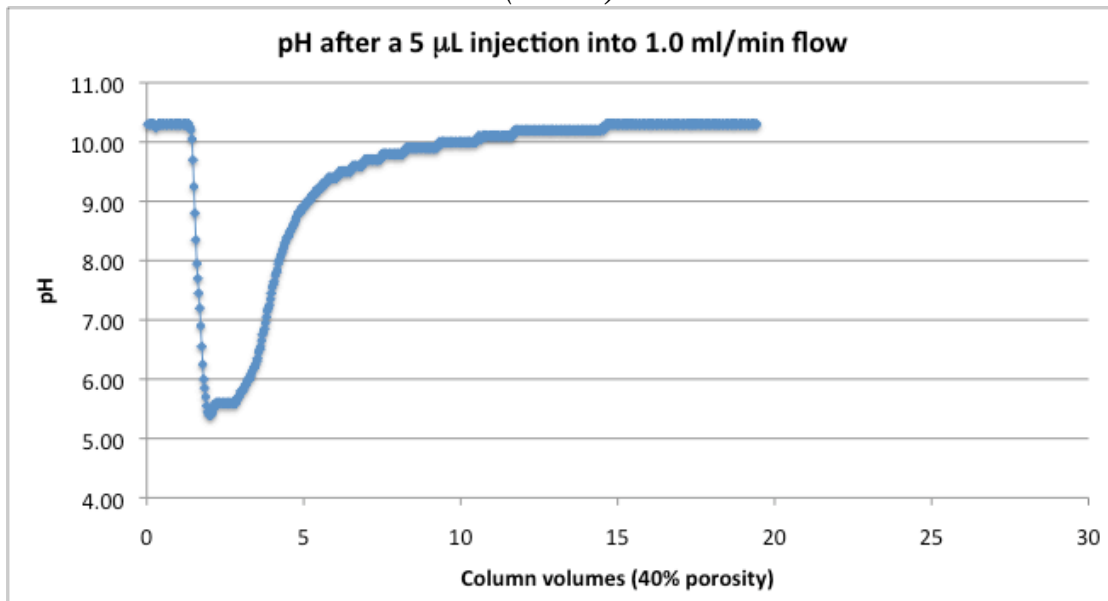


Appendix II: curves for all liquid and SC CO₂ injections

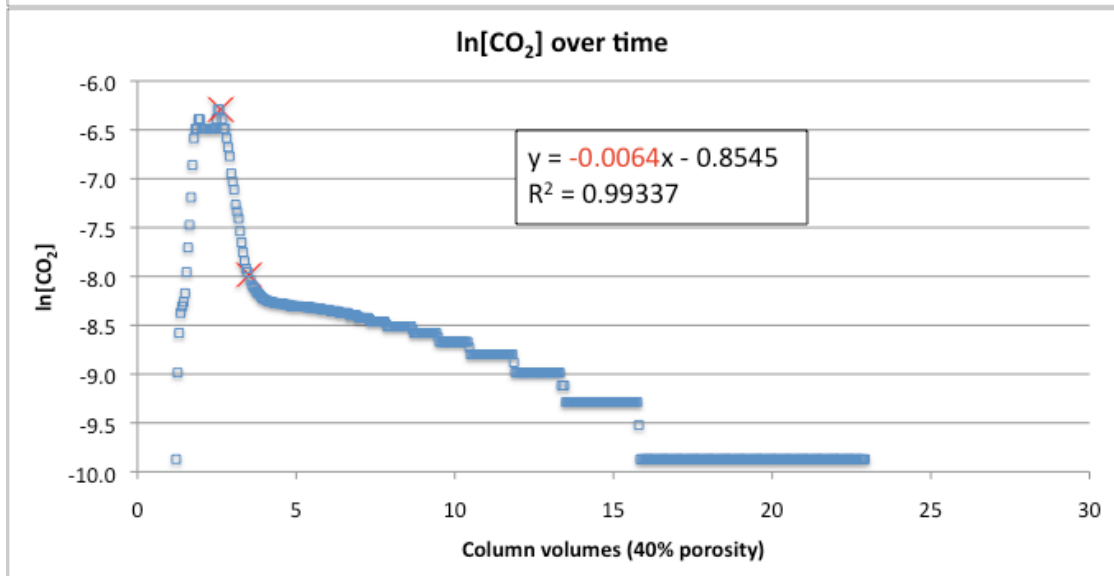
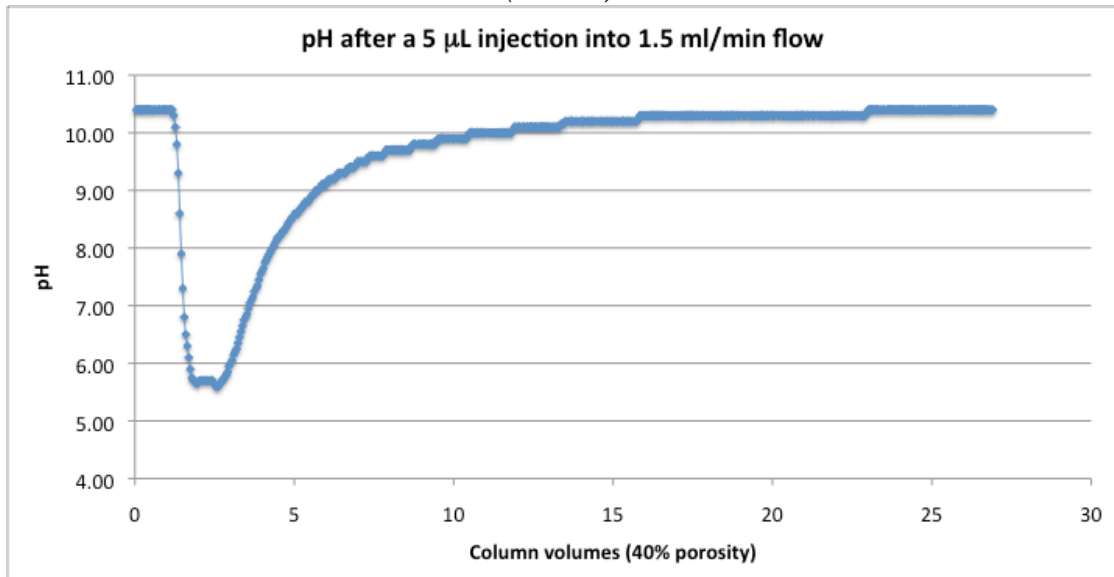
Liquid CO₂ (28.5°C), 5 μL injections



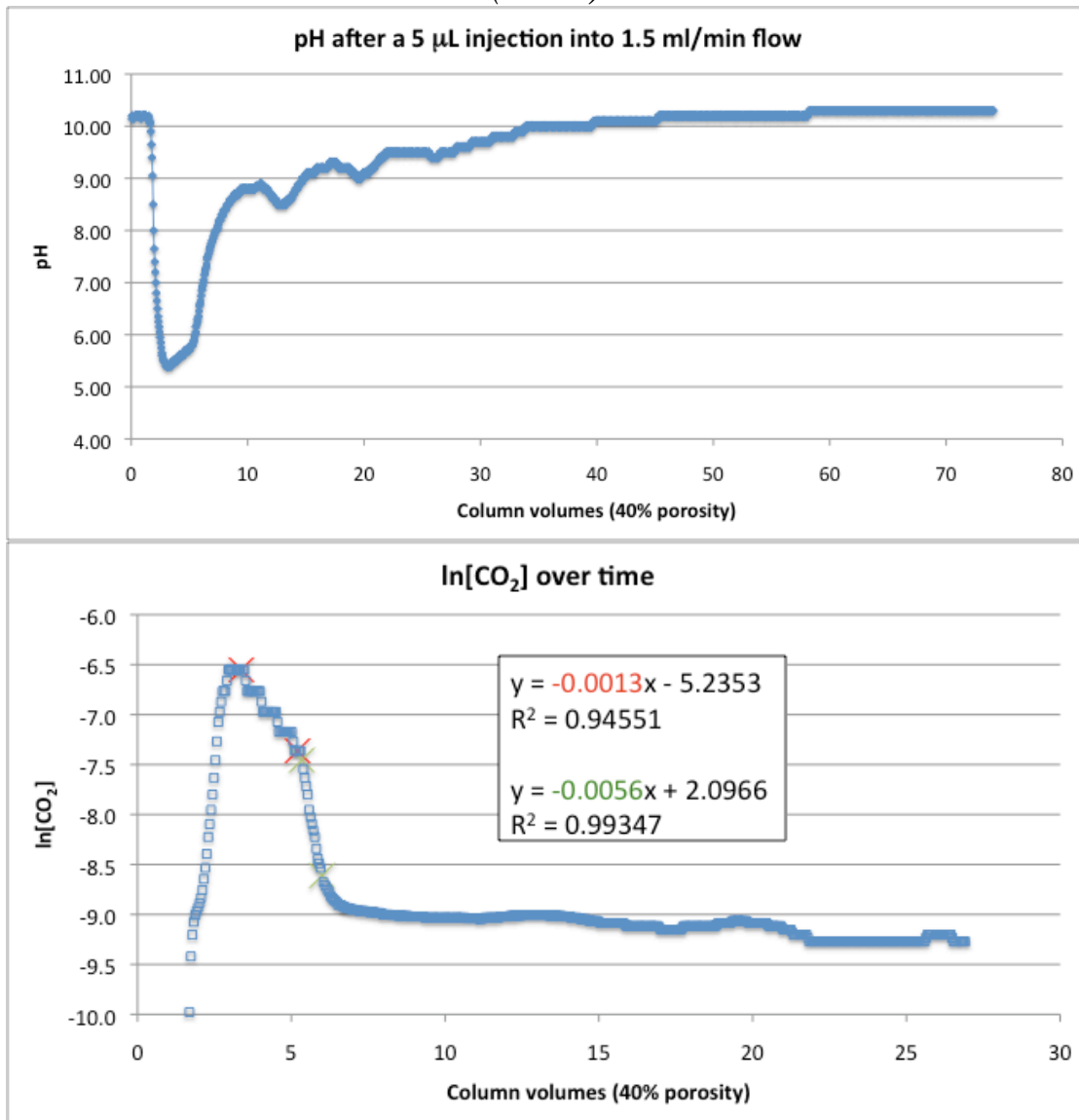
(28.5°C)



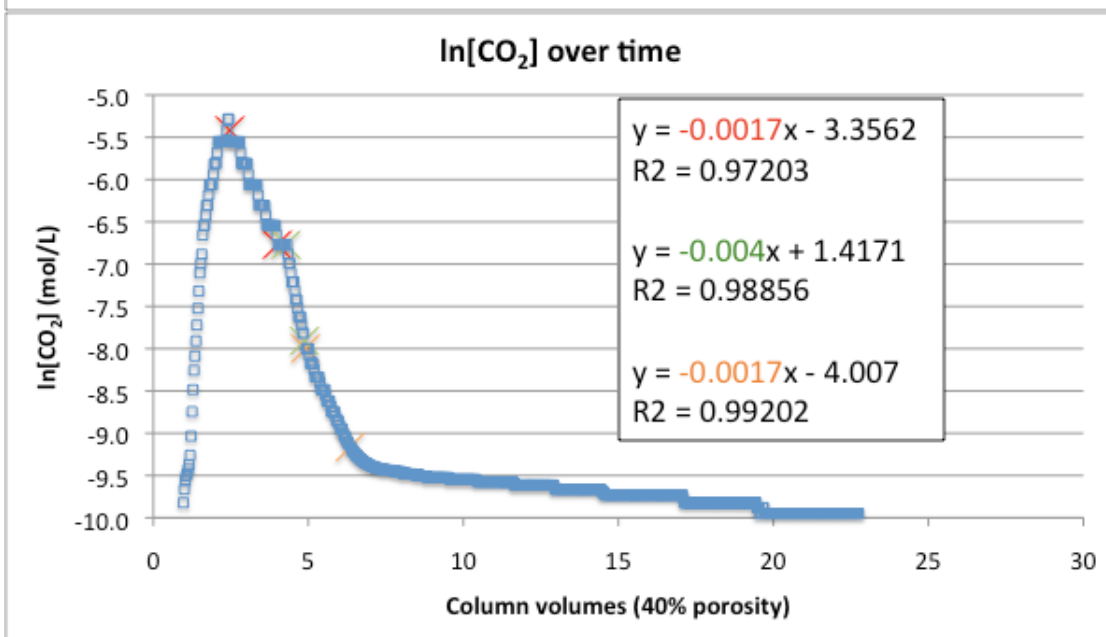
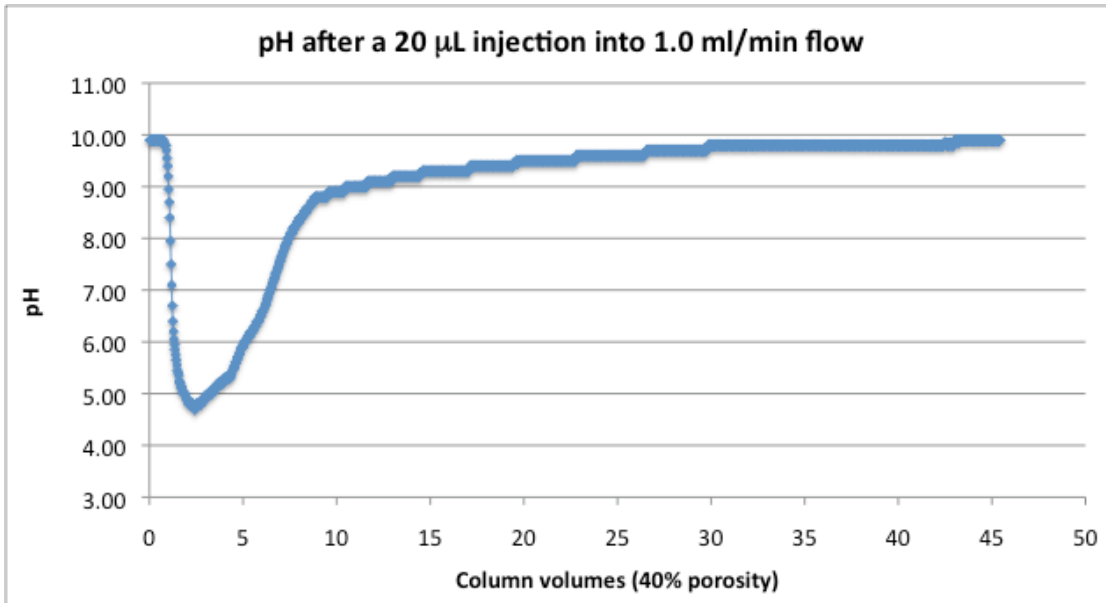
(28.5°C)



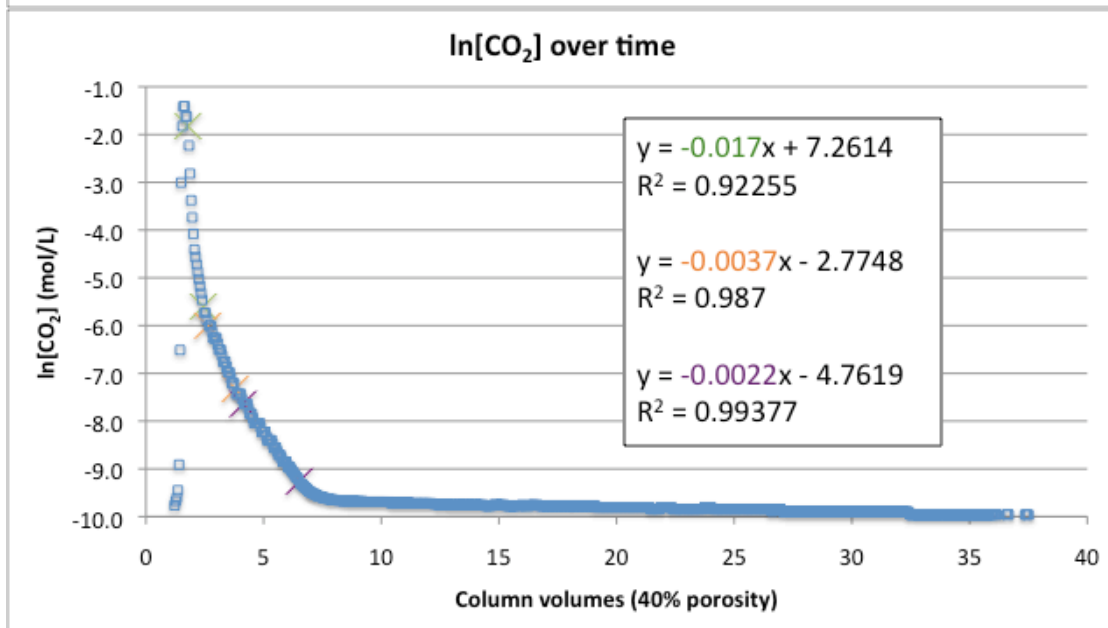
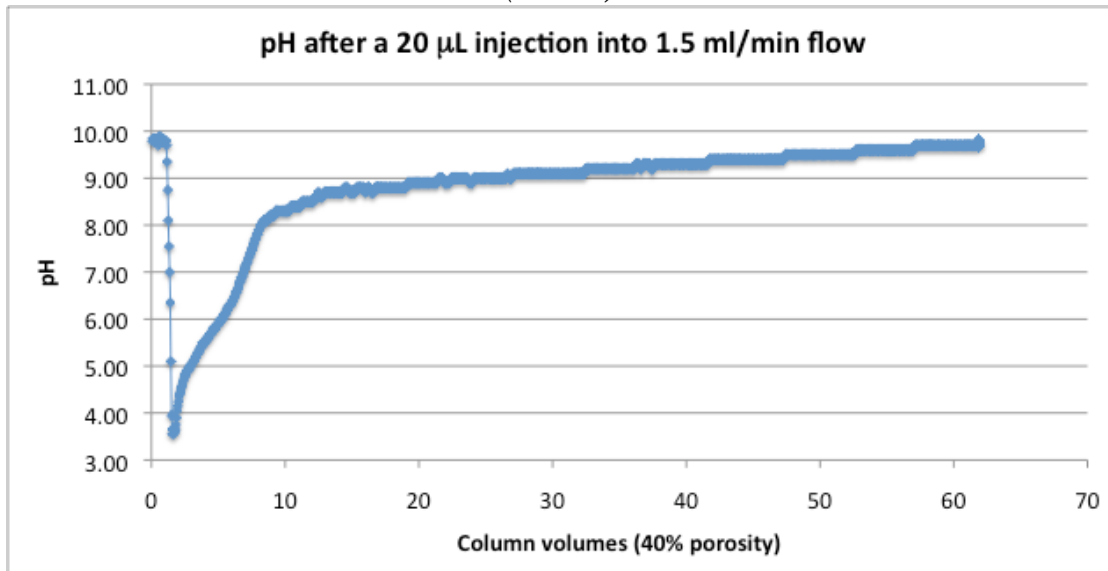
(28.5°C)



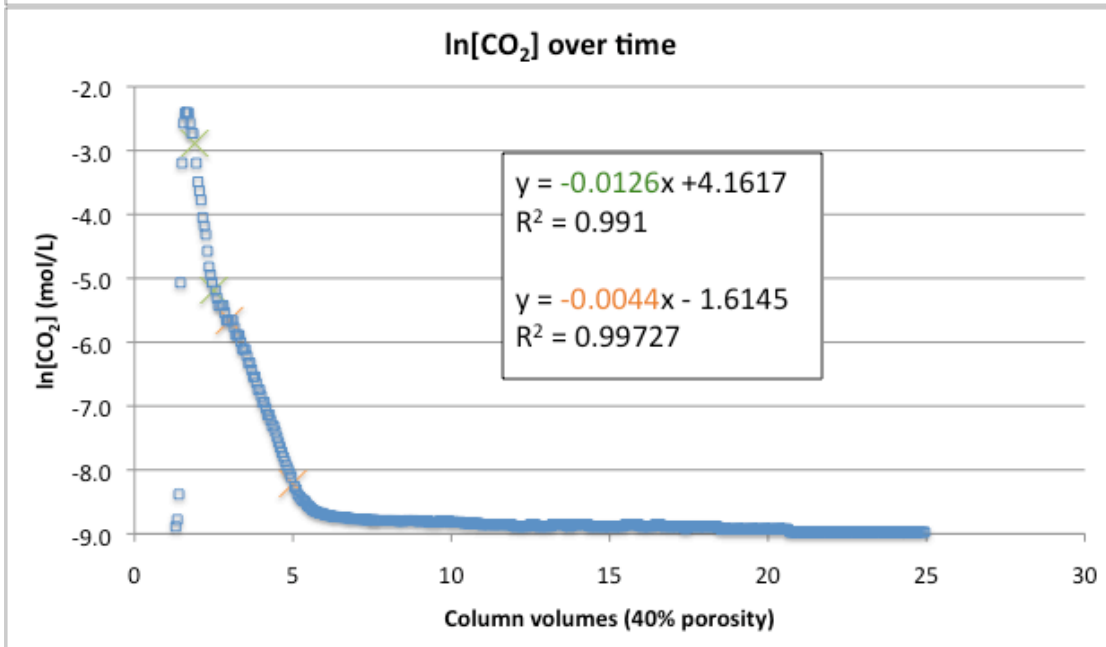
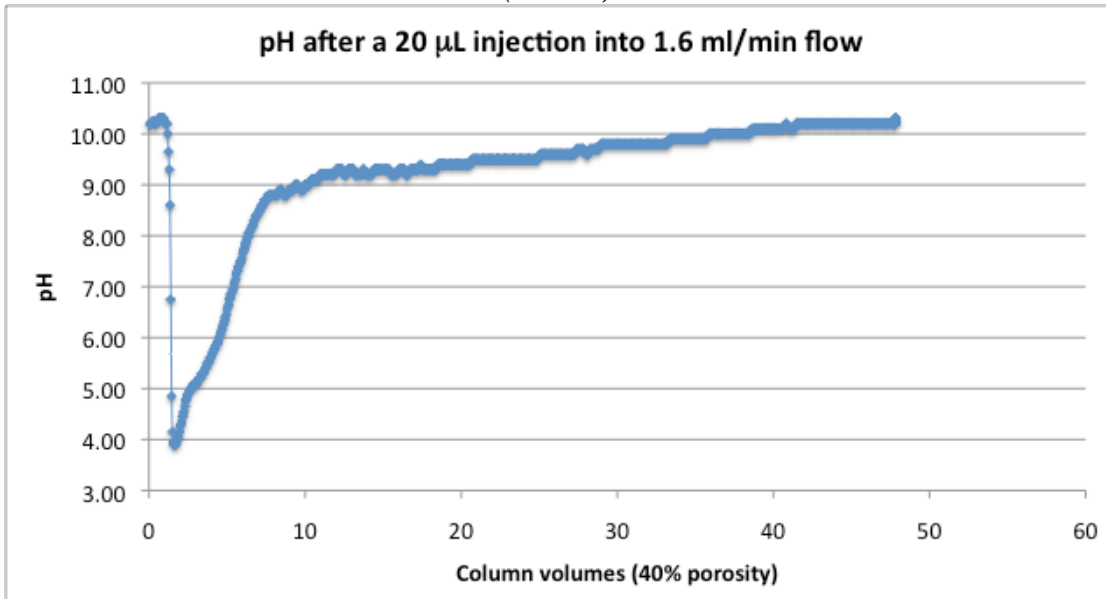
Liquid CO₂ (28.5°C), 20 μL injections



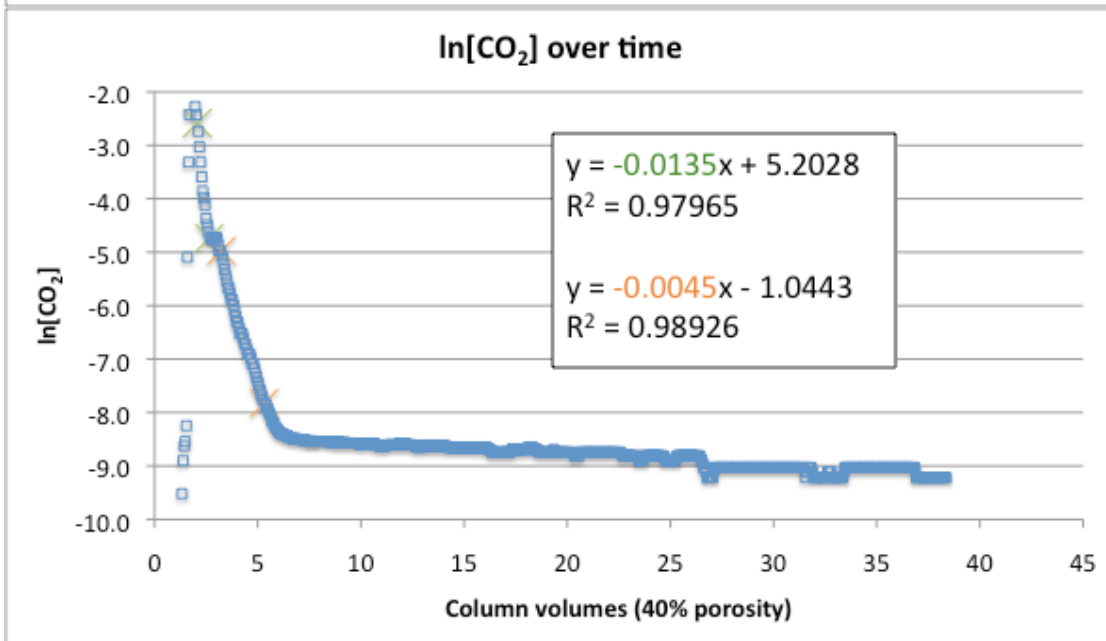
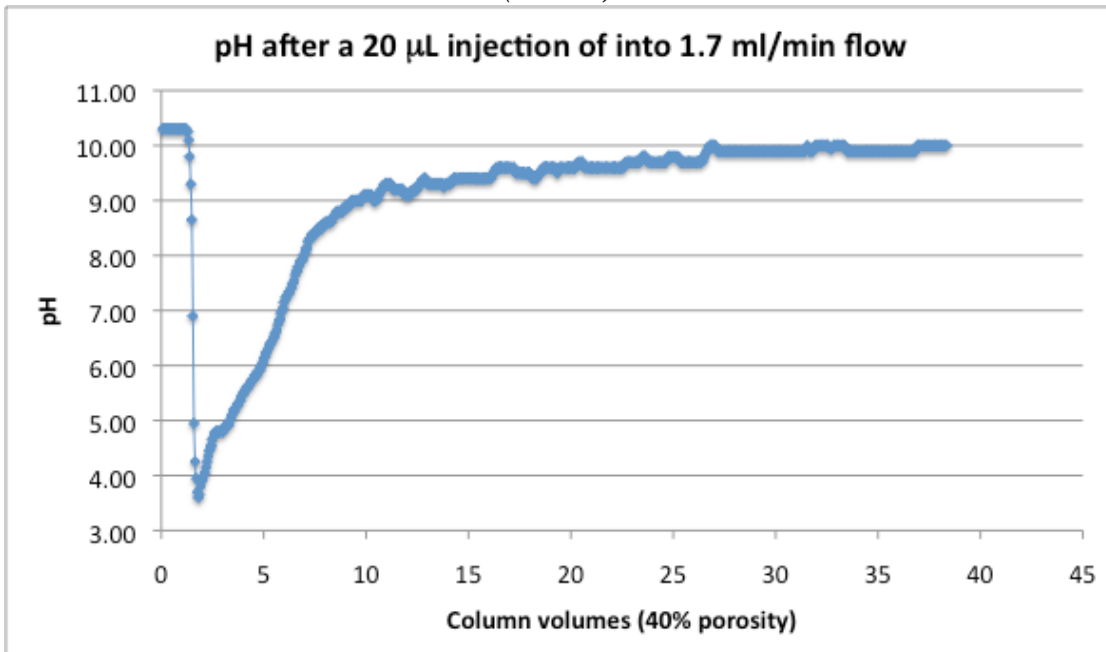
(28.5°C)



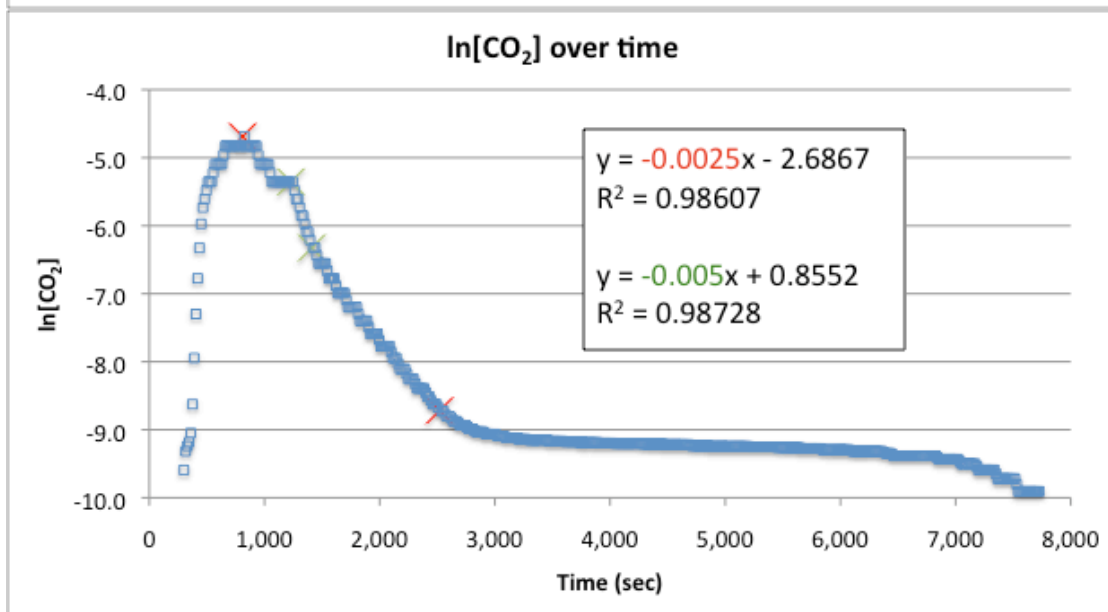
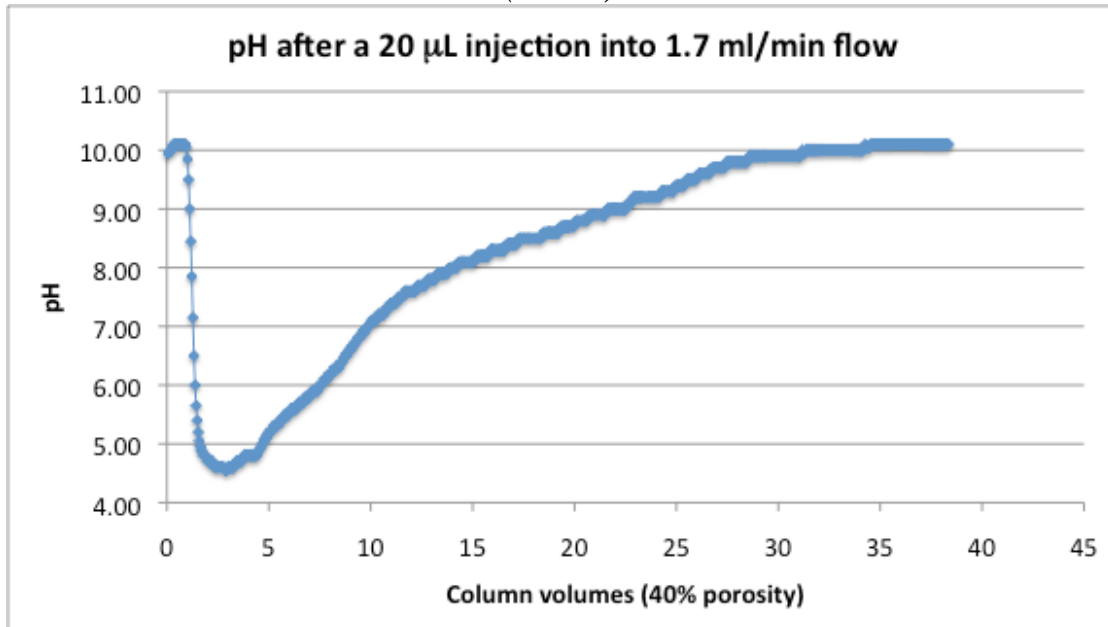
(28.5°C)



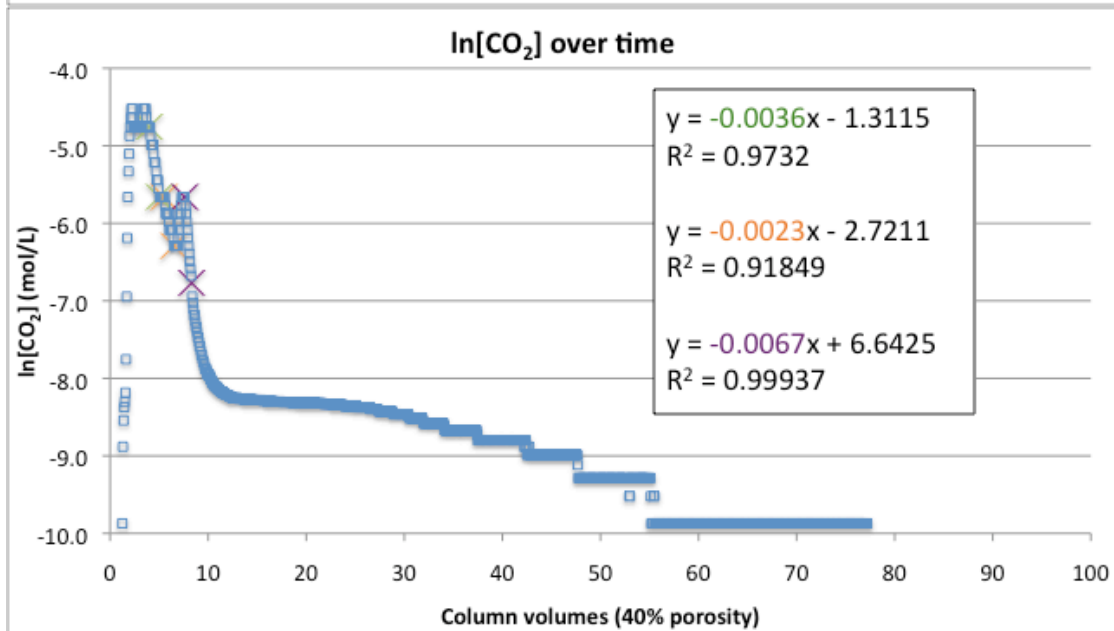
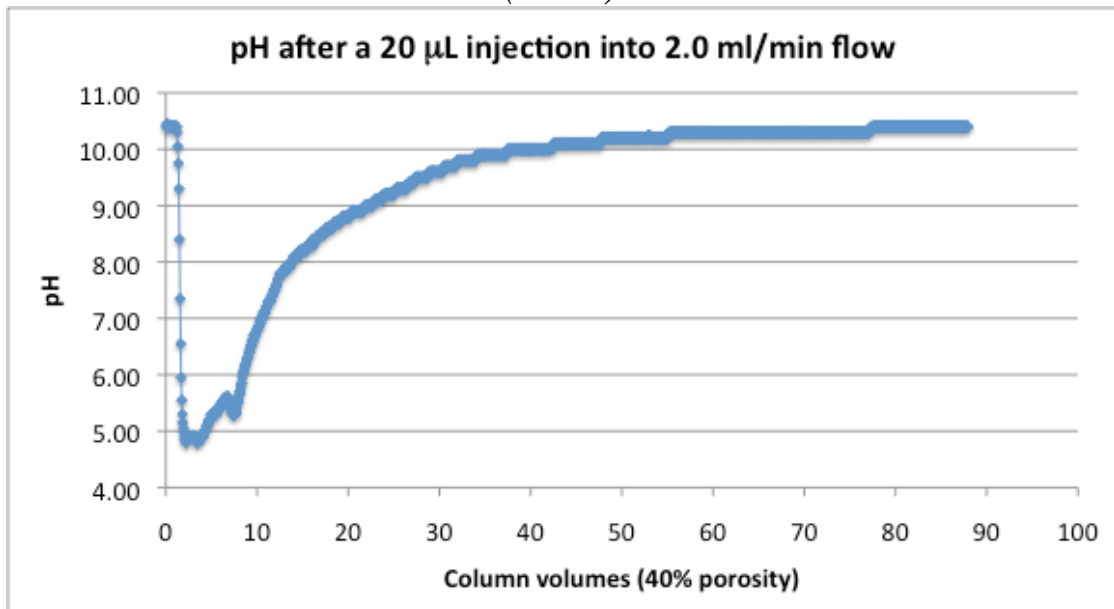
(28.5°C)



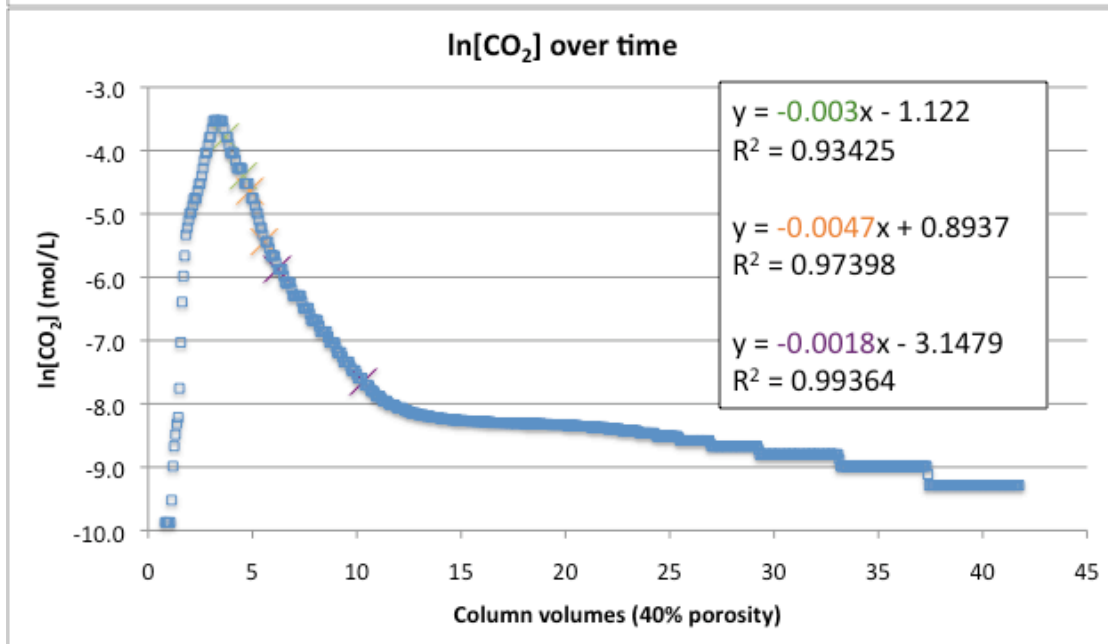
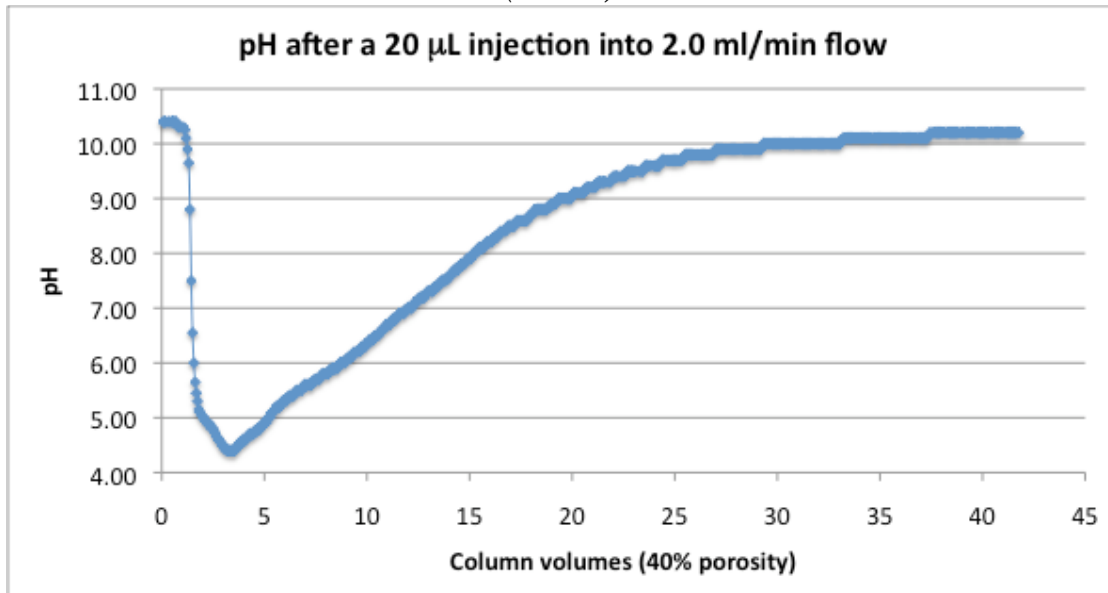
(28.5°C)



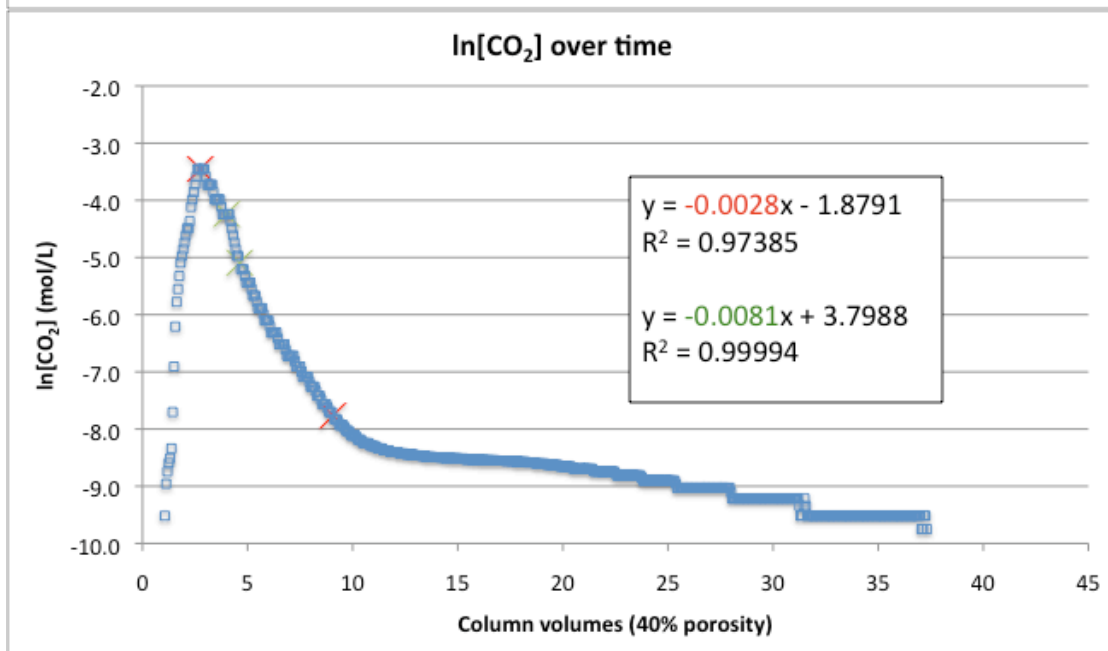
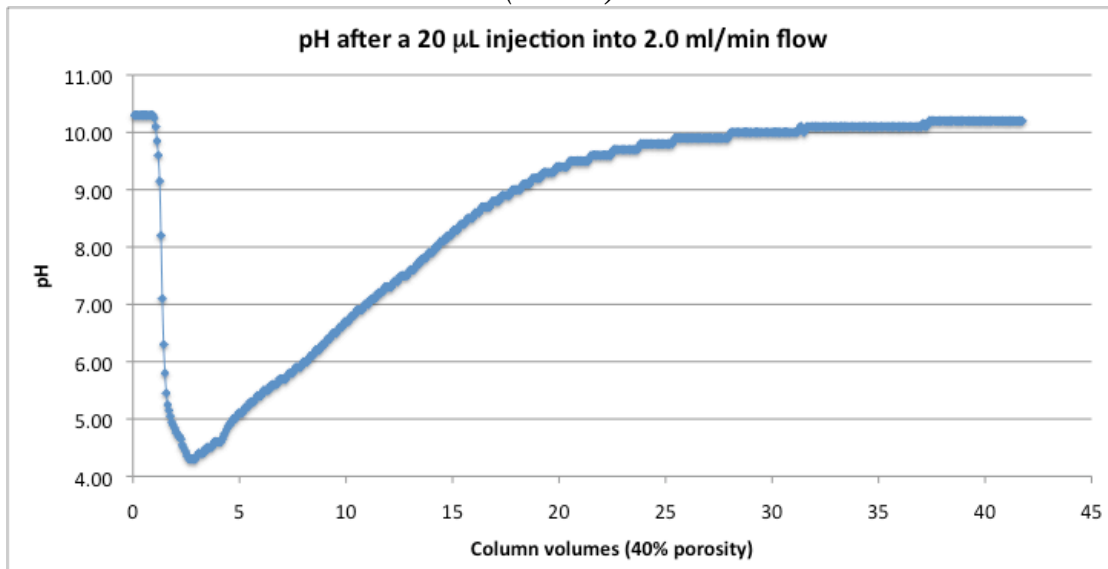
(28.5°C)



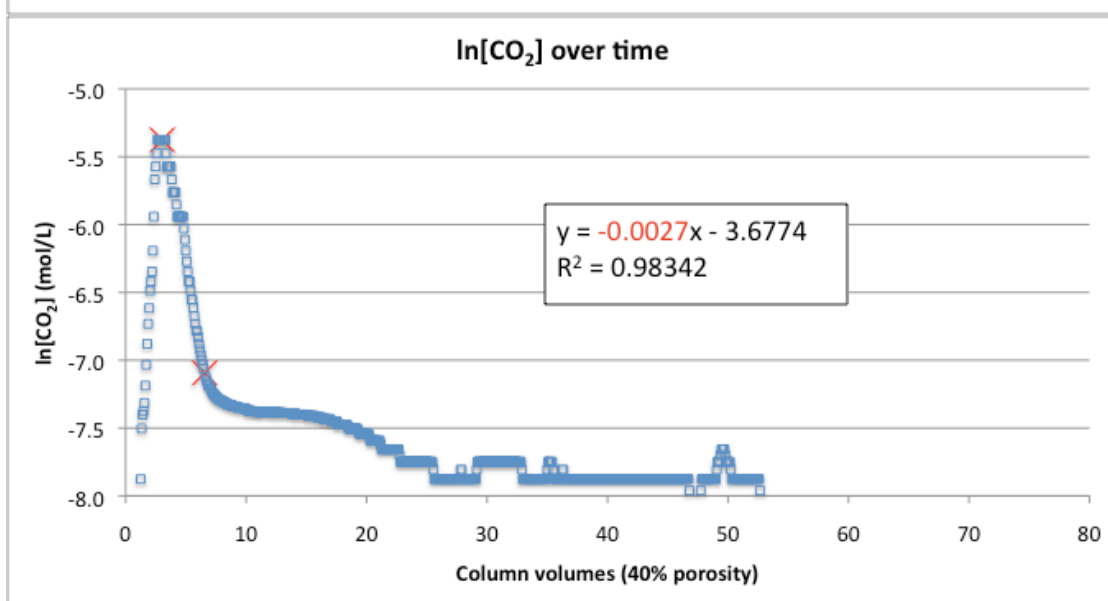
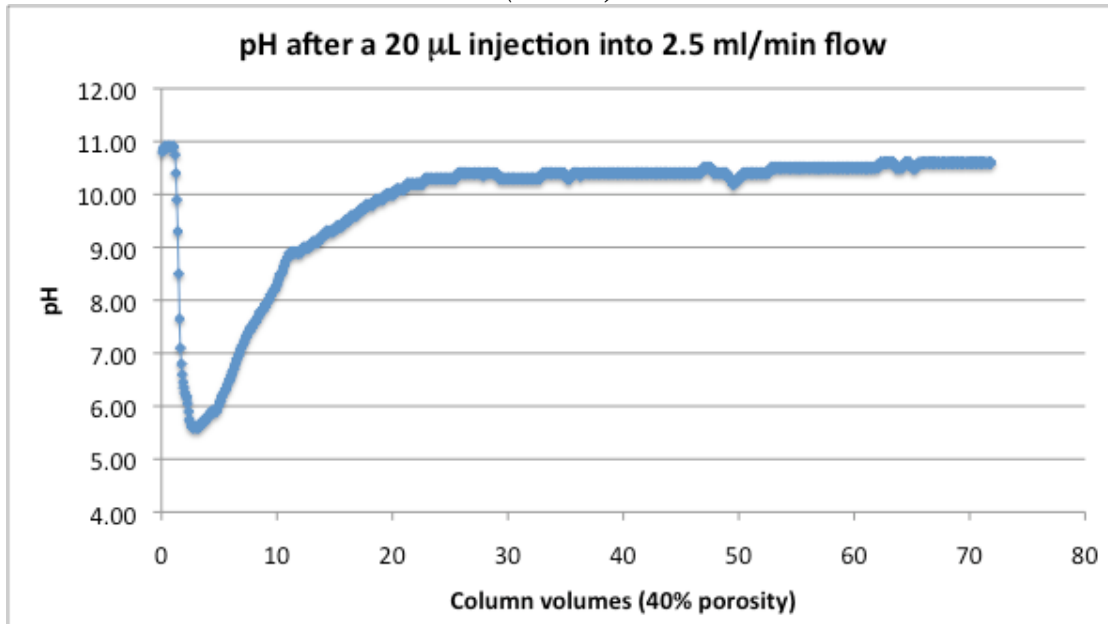
(28.5°C)



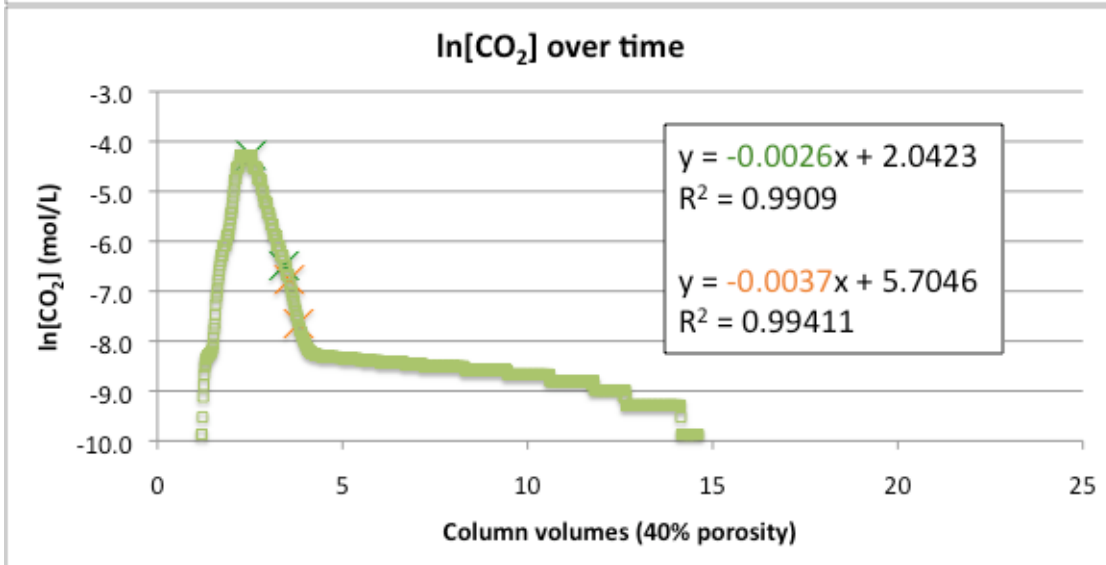
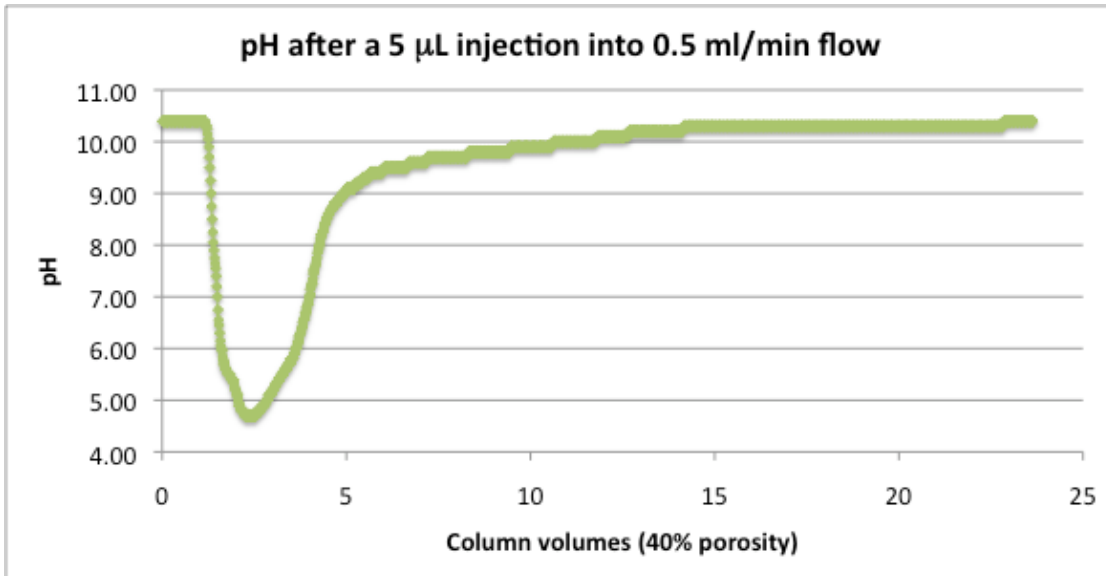
(28.5°C)



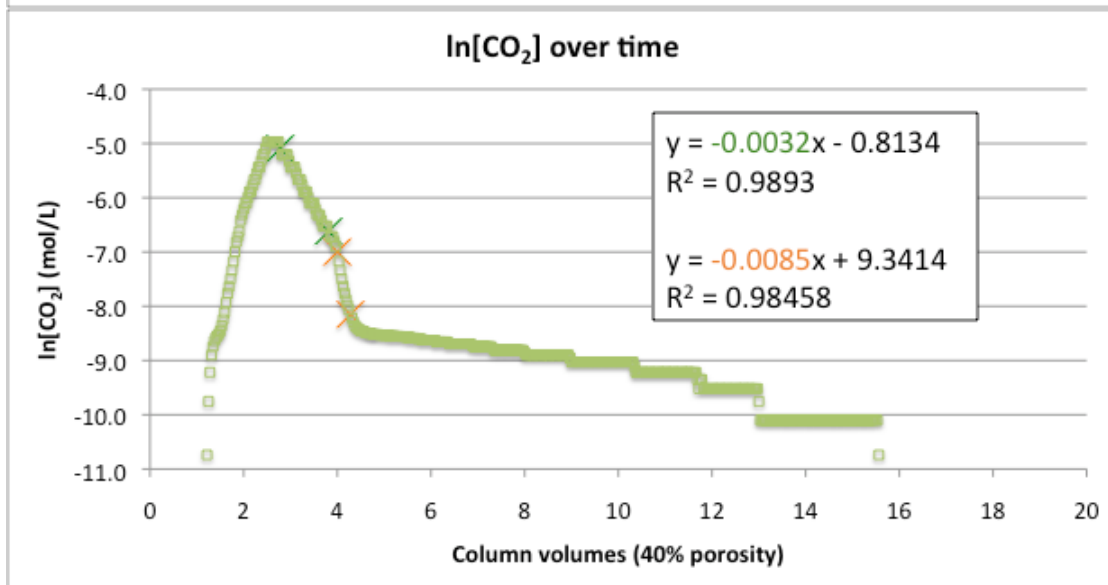
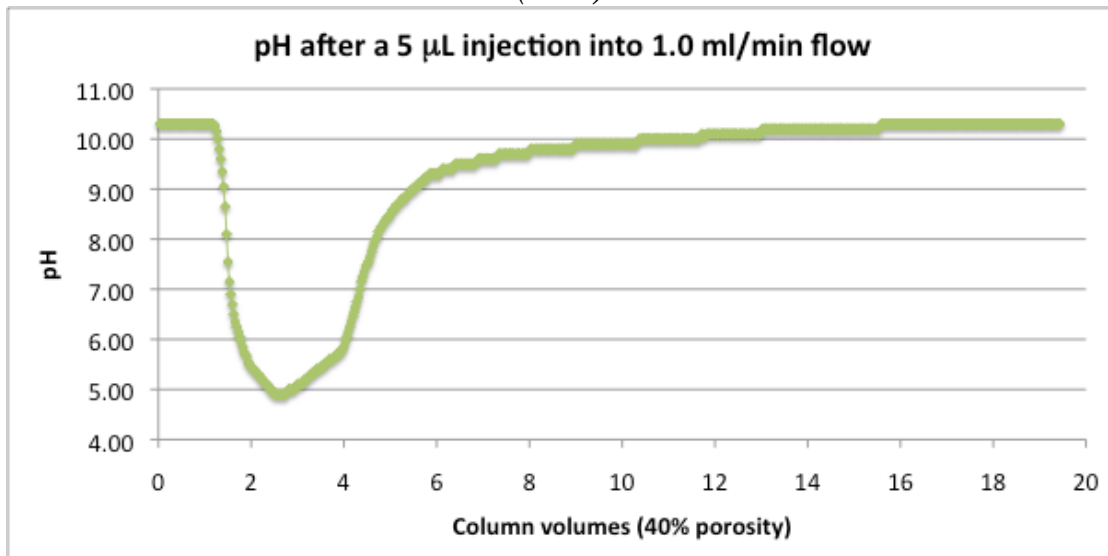
(28.5°C)



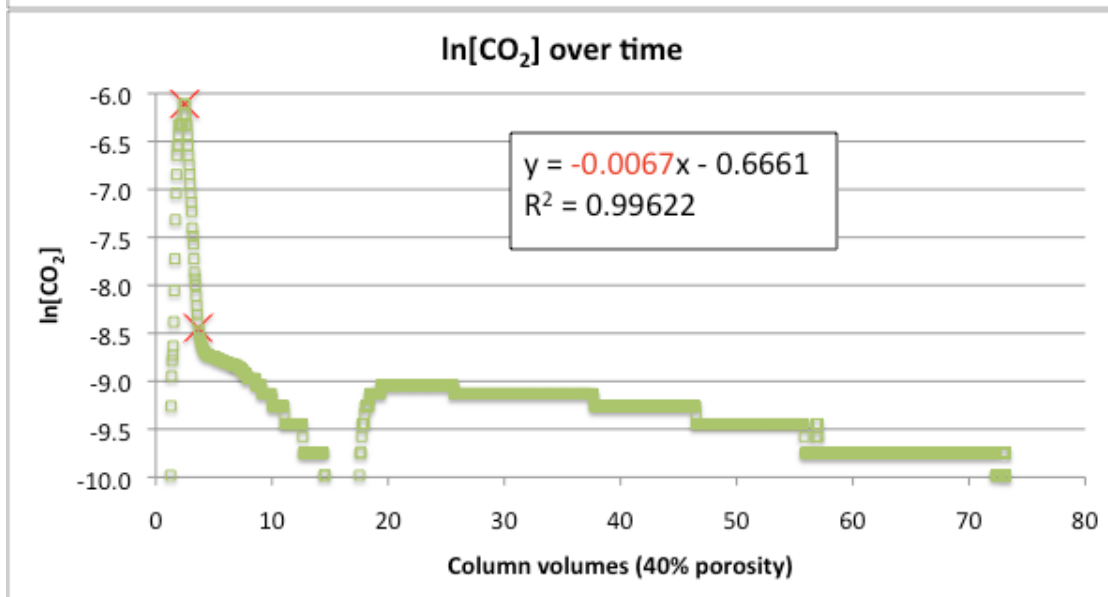
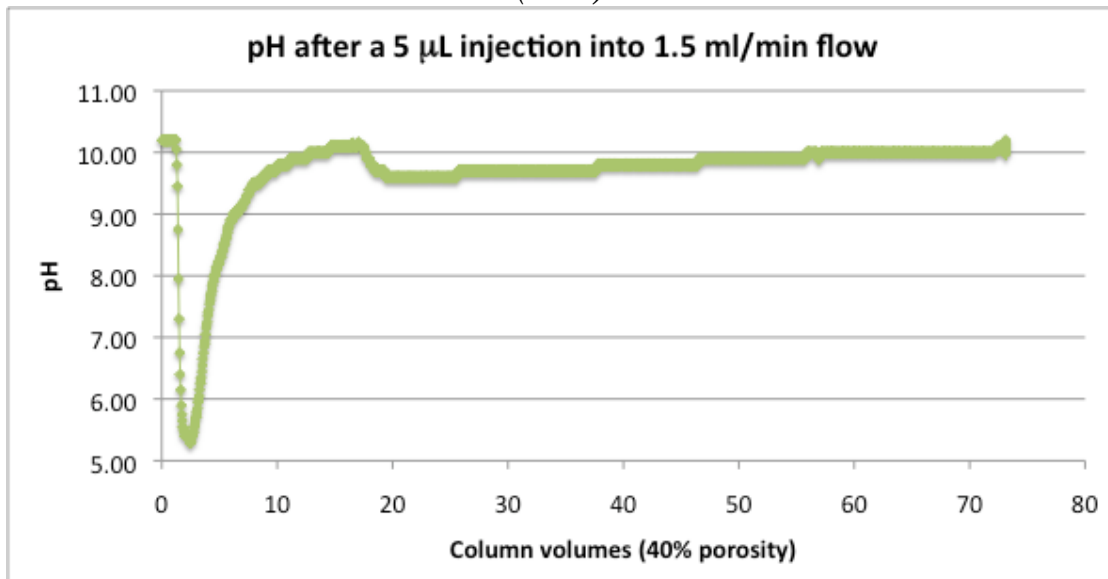
Supercritical CO₂ (35°C), 5 μL injections



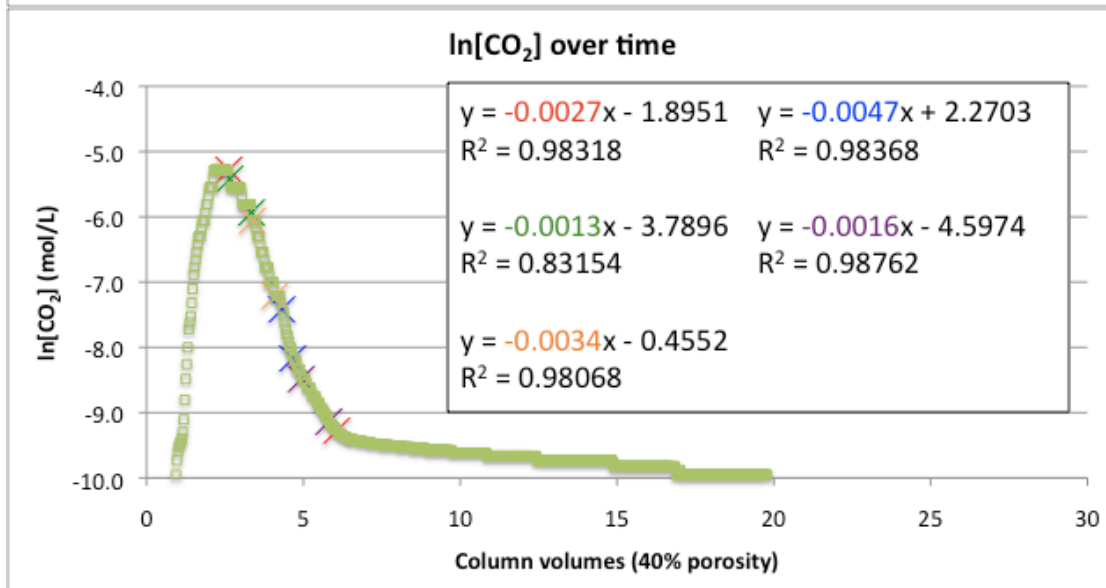
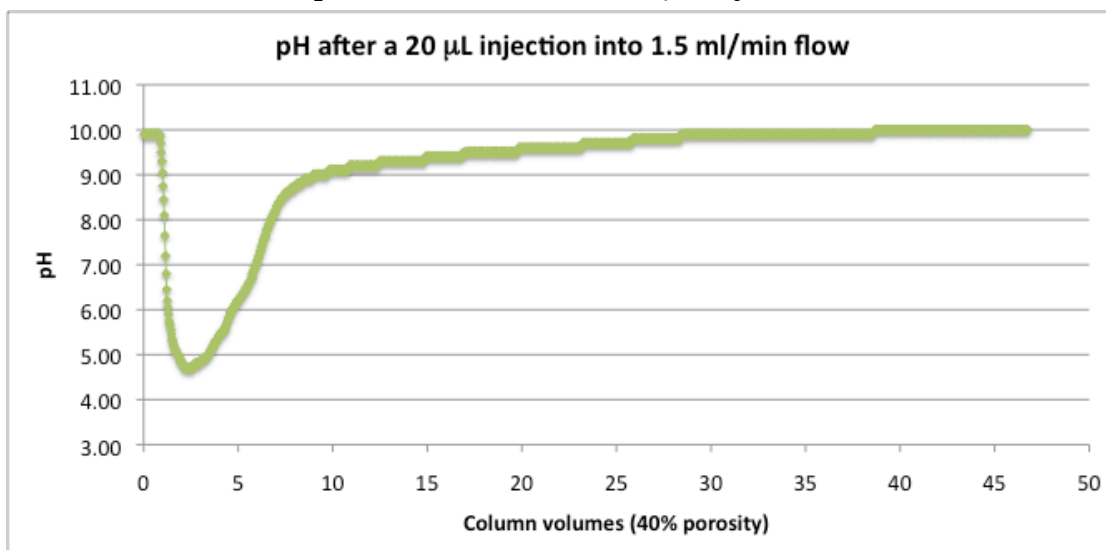
(35°C)



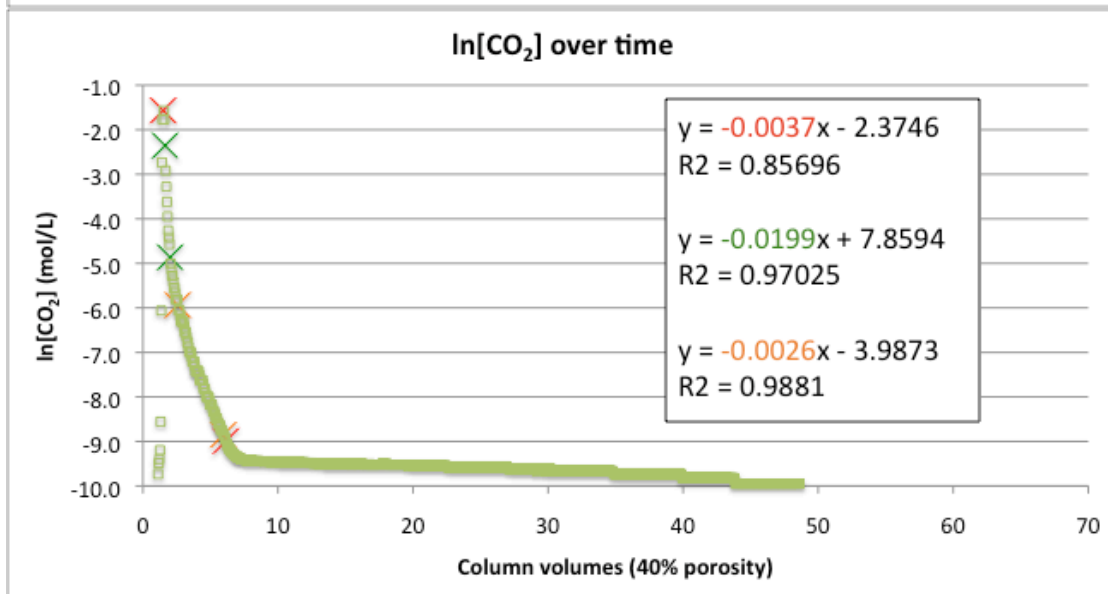
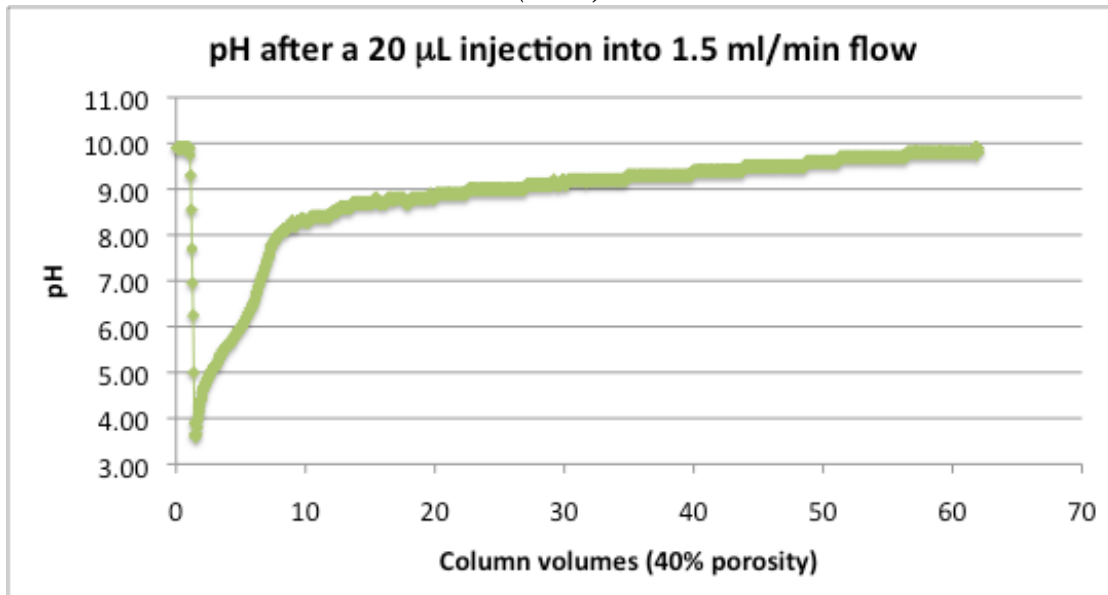
(35°C)



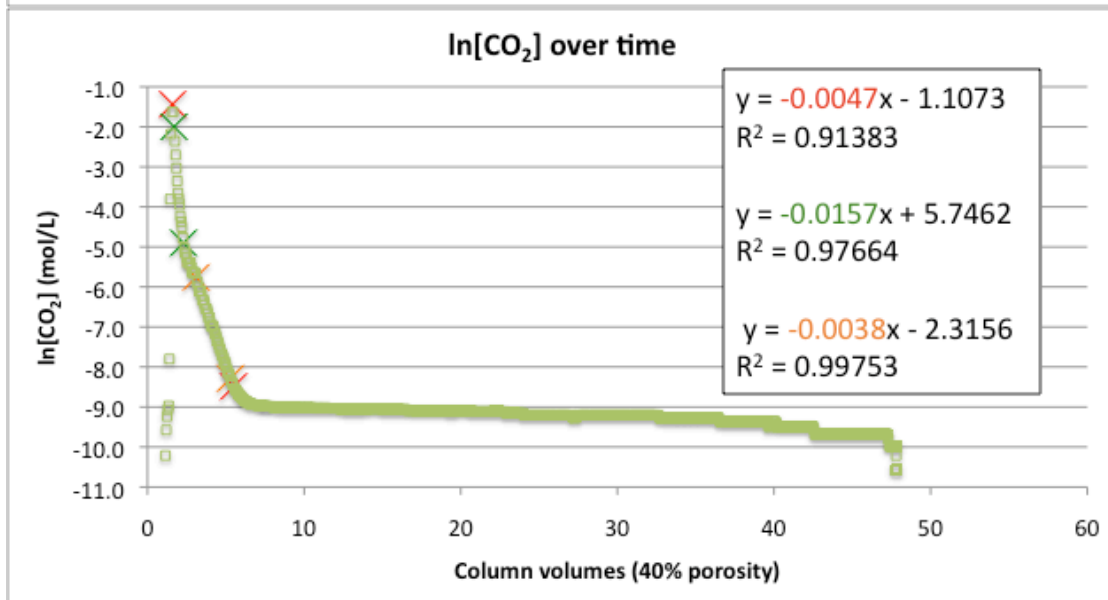
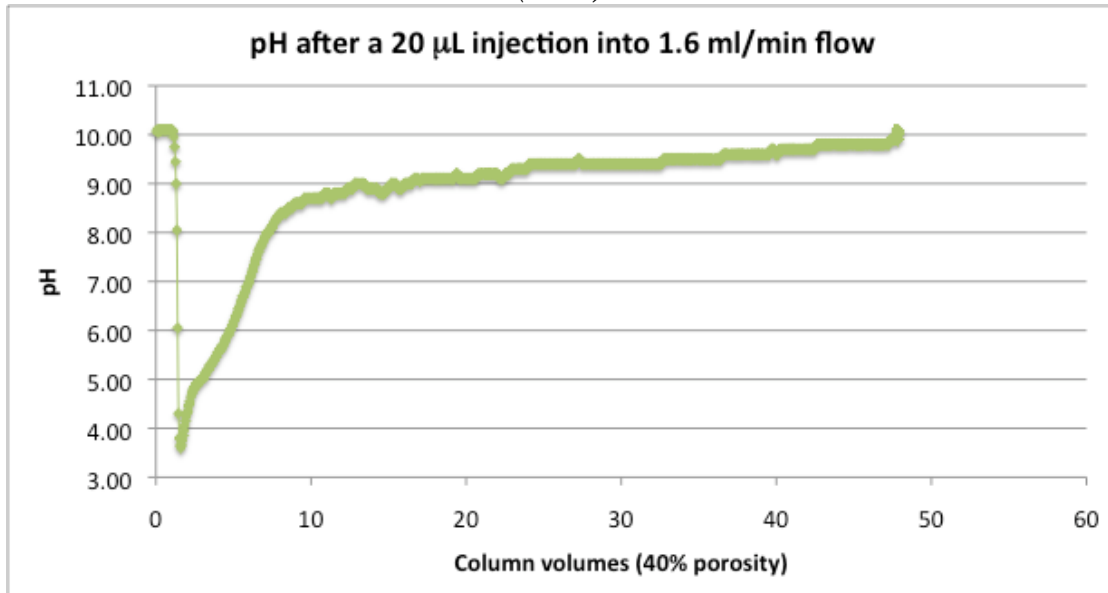
Supercritical CO₂ (35°C), 20 μL injections



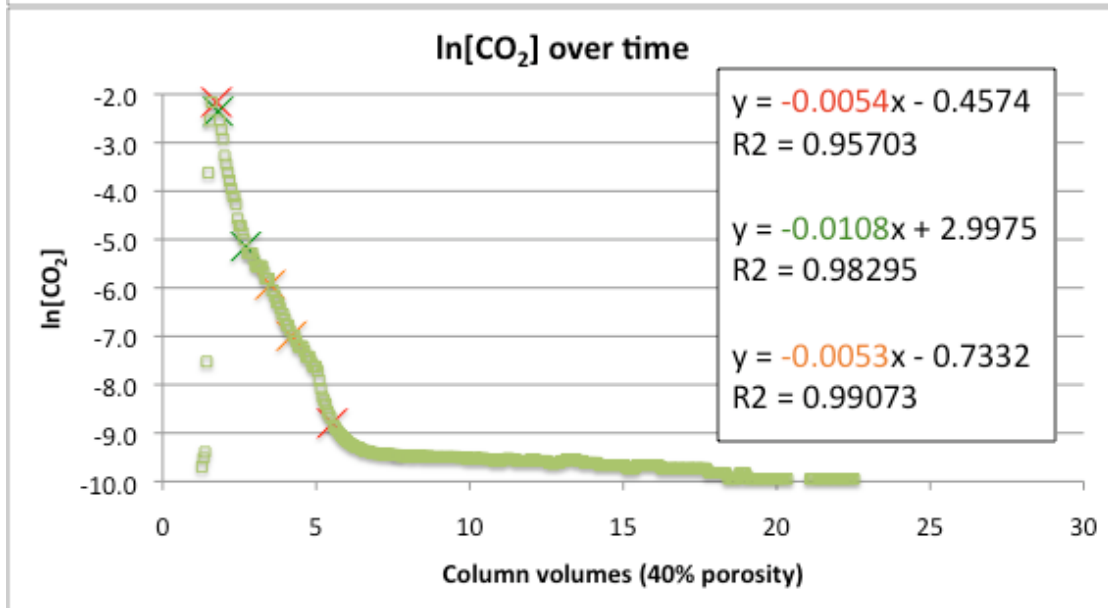
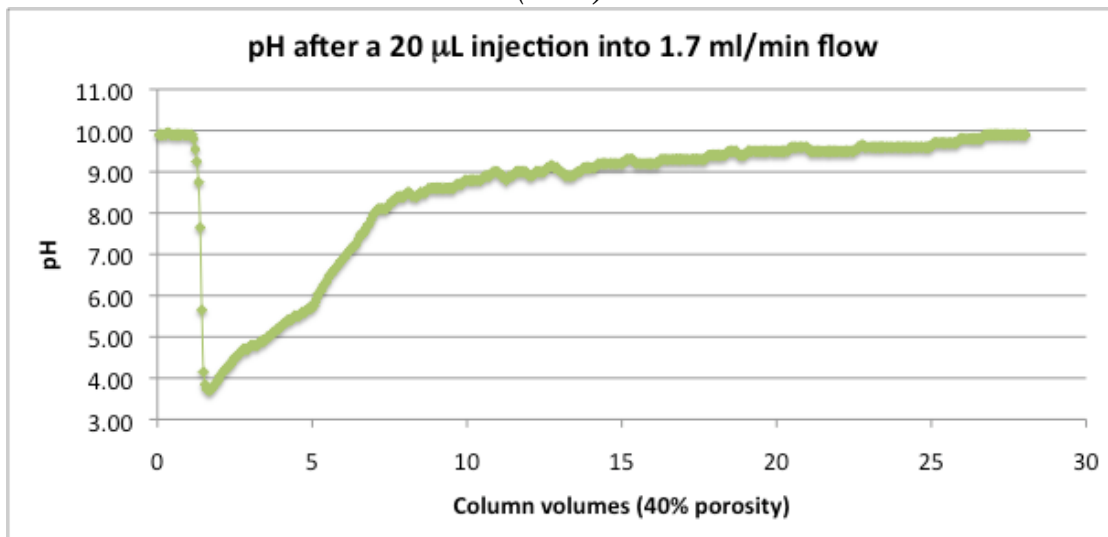
(35°C)



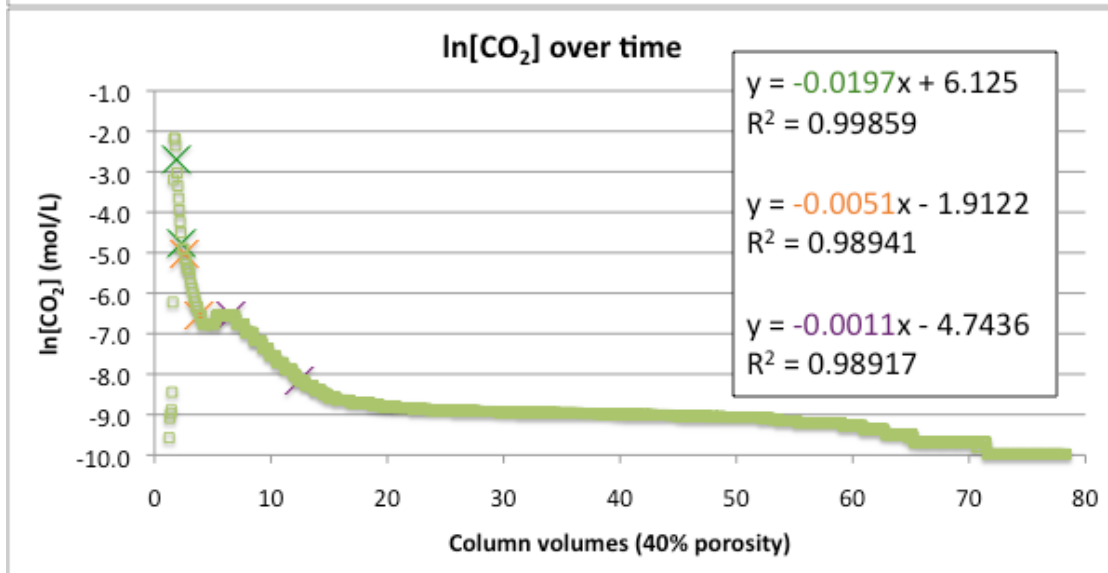
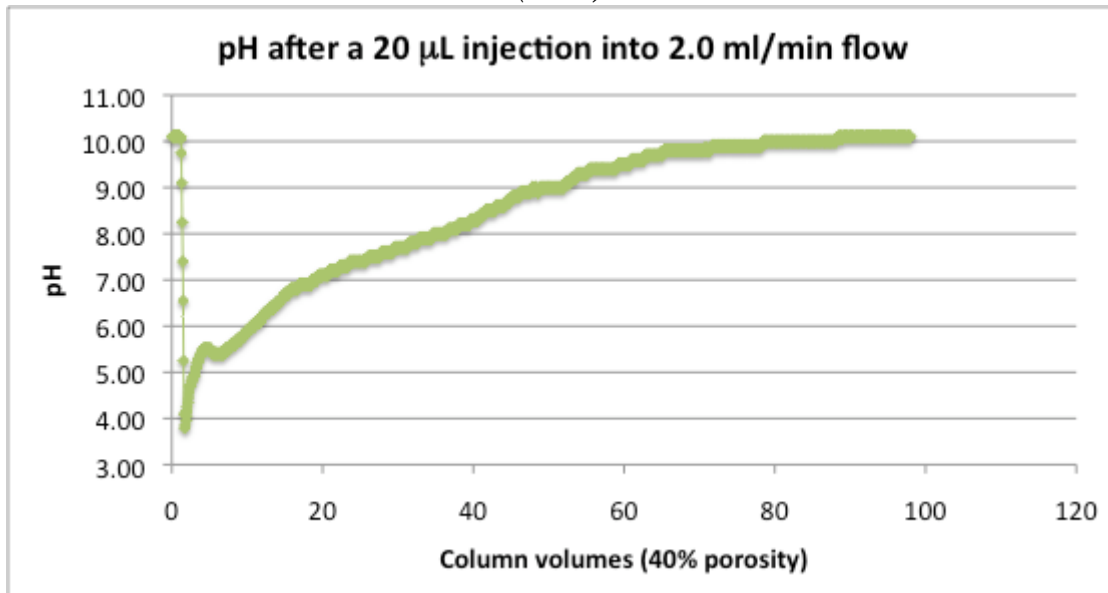
(35°C)



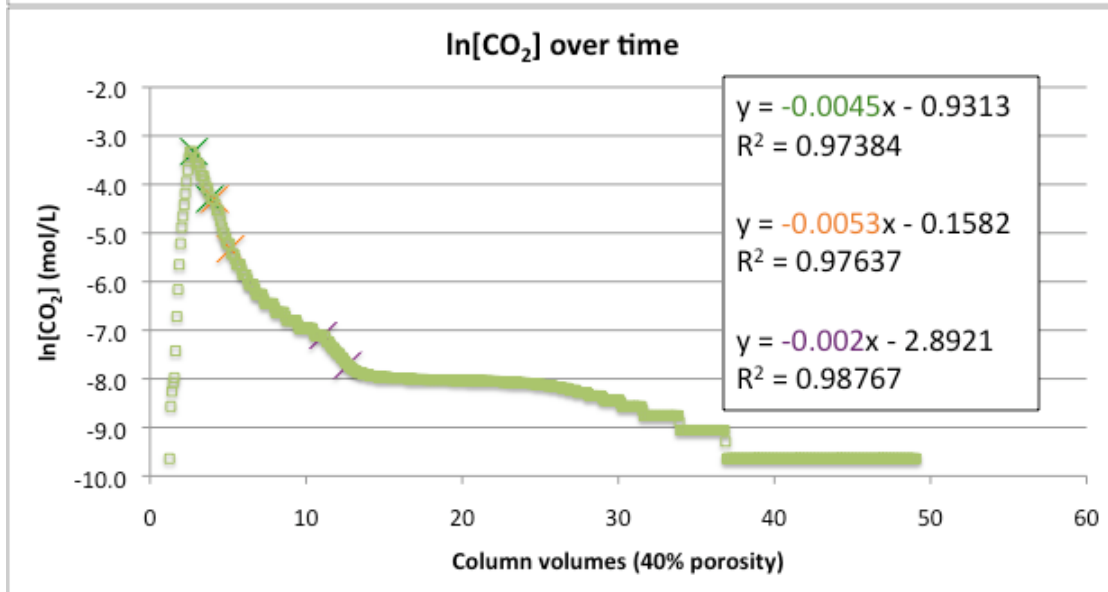
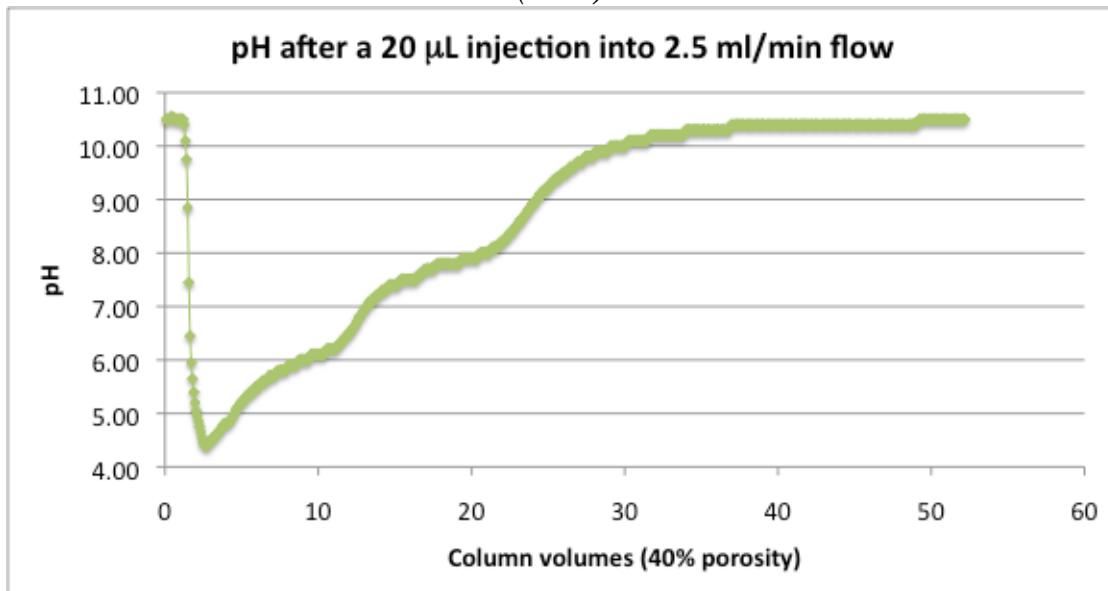
(35°C)



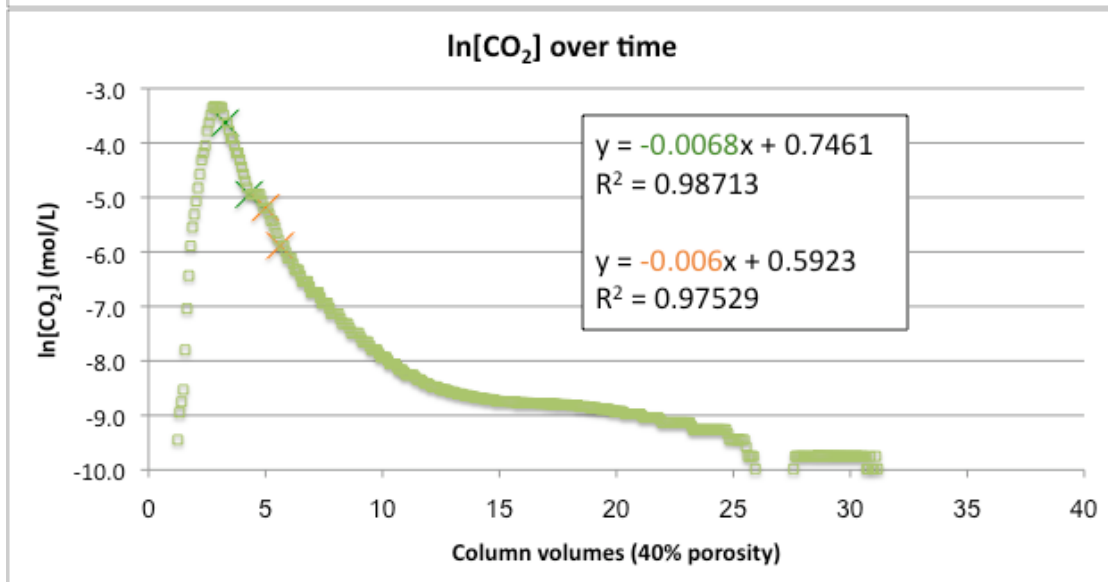
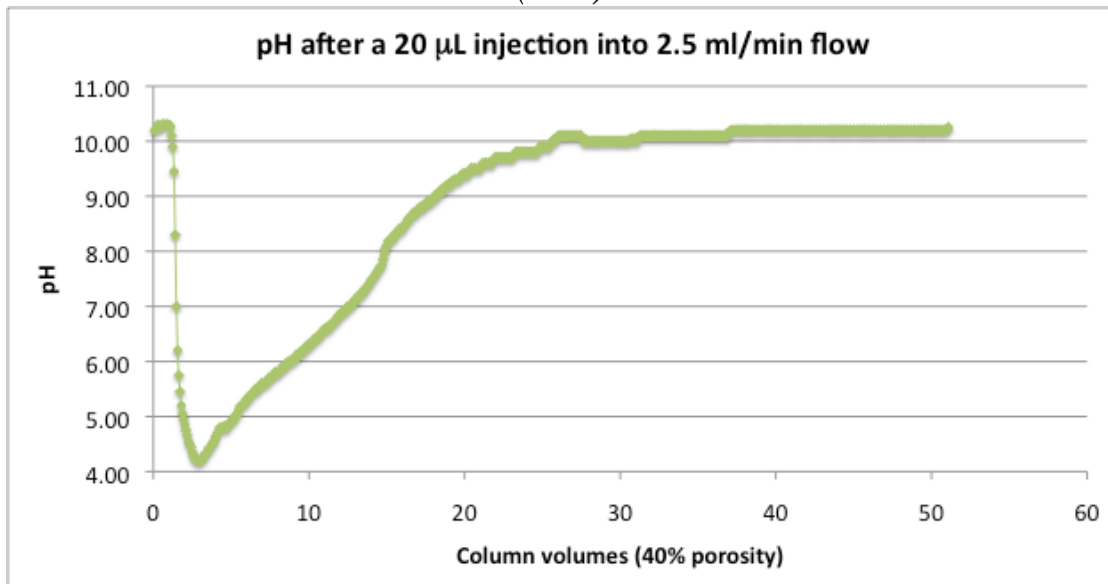
(35°C)



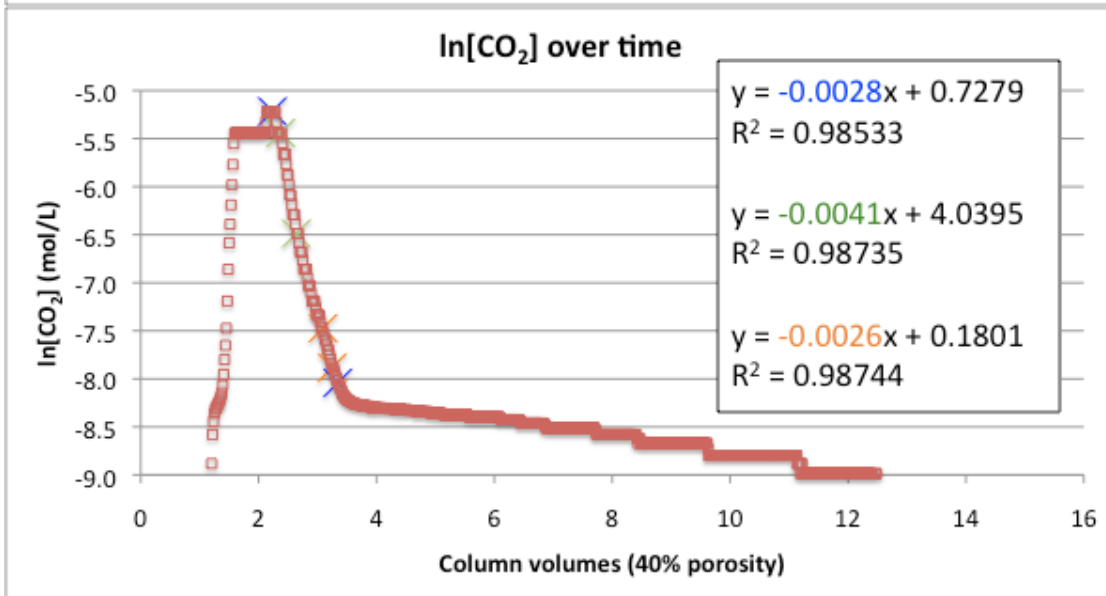
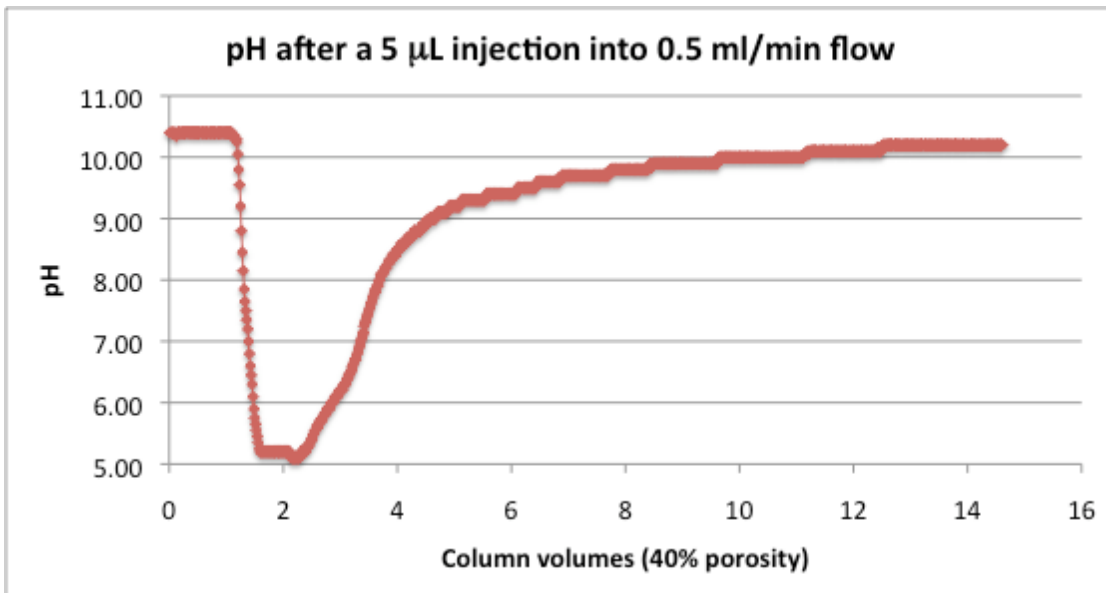
(35°C)



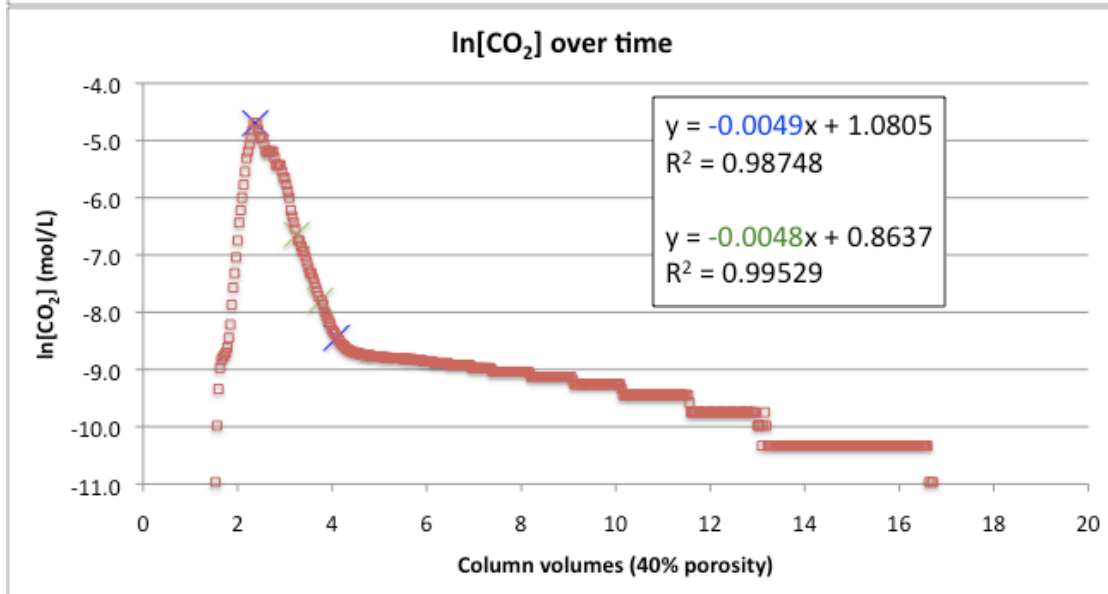
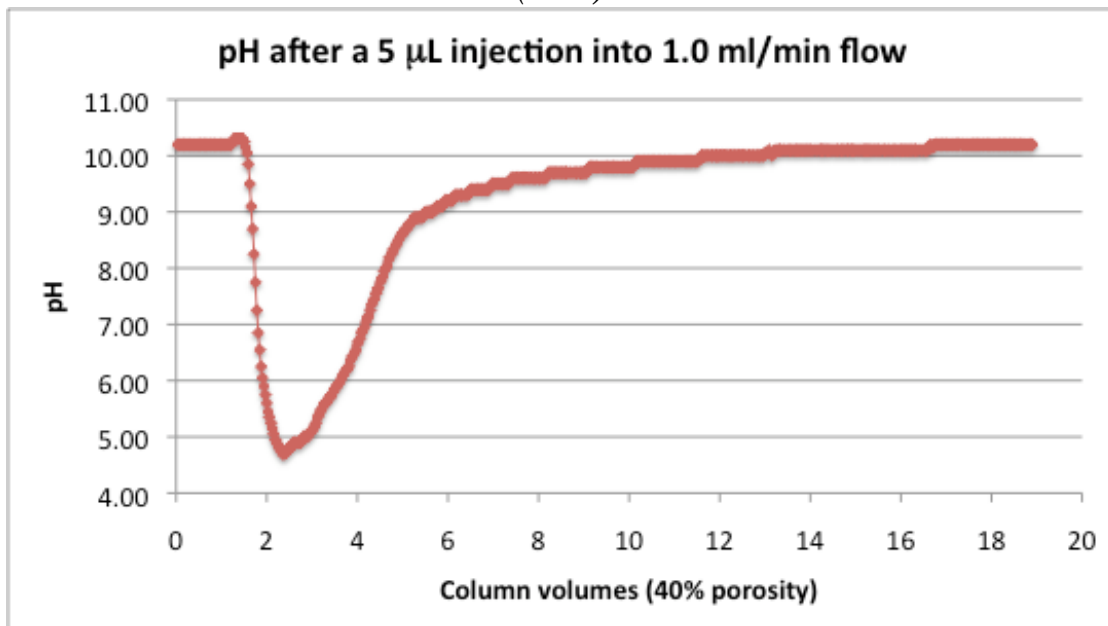
(35°C)



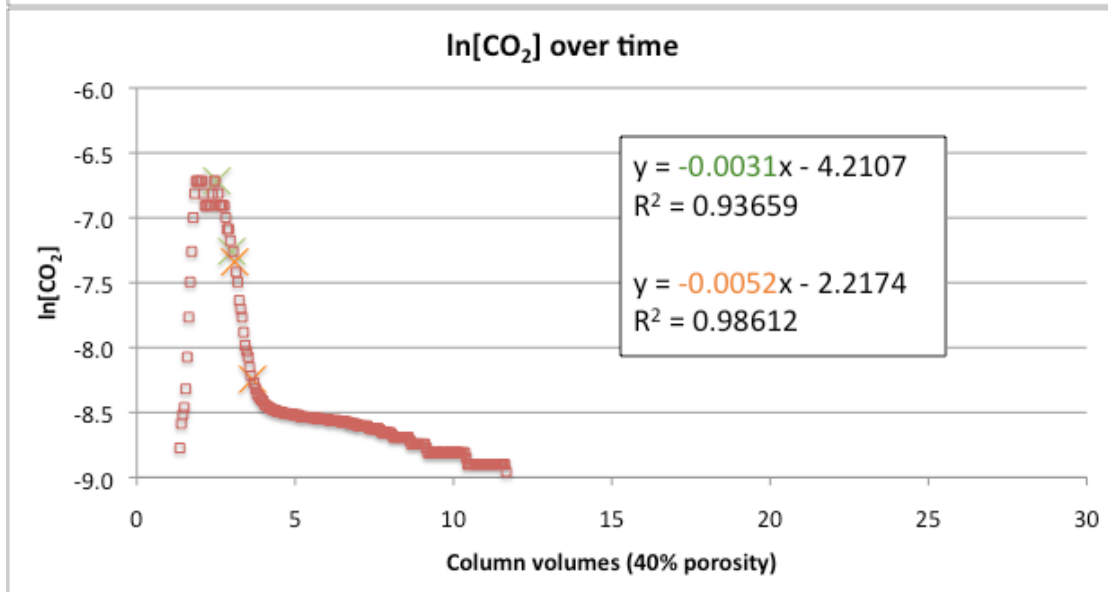
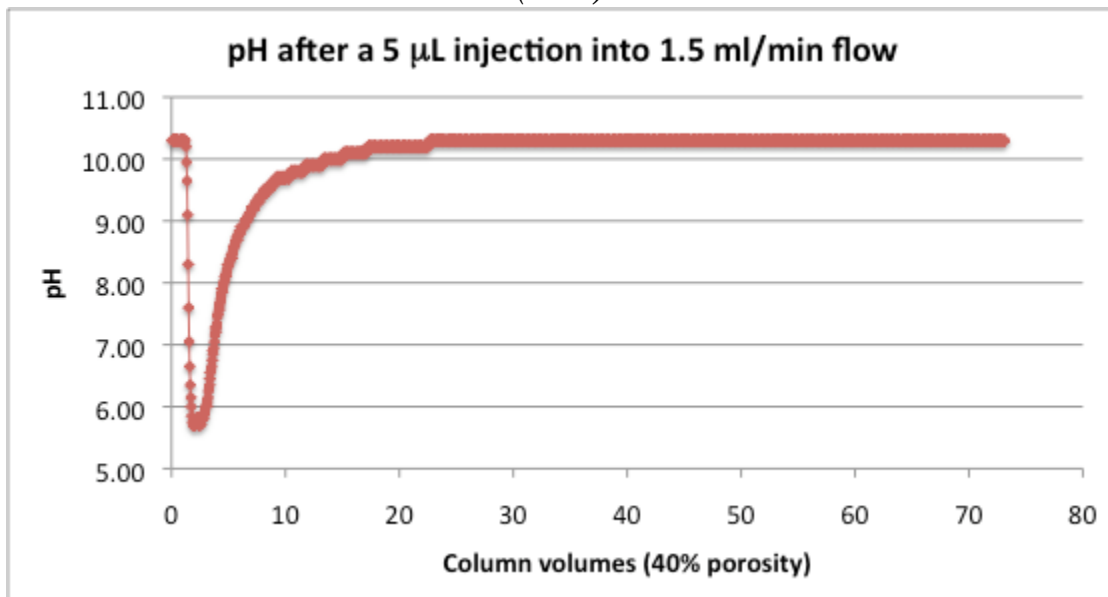
Supercritical CO₂ (45°C), 5 μL injections



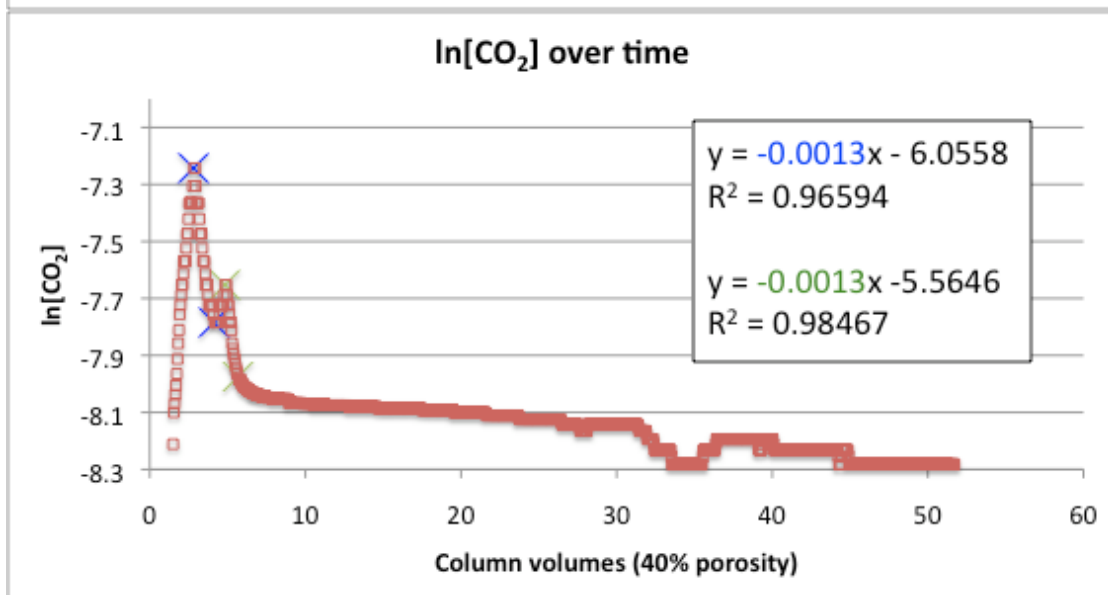
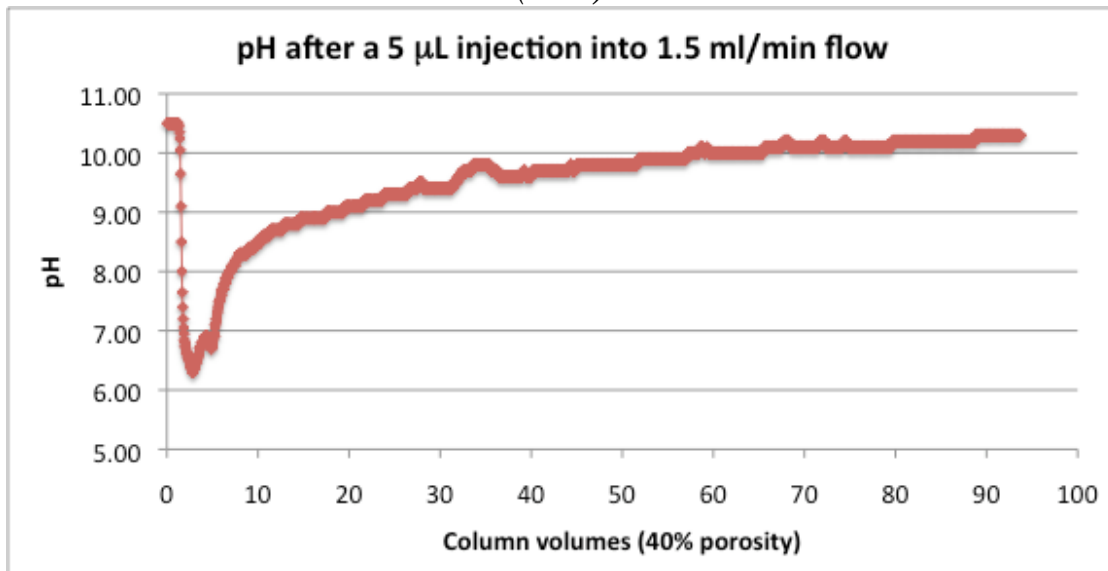
(45°C)



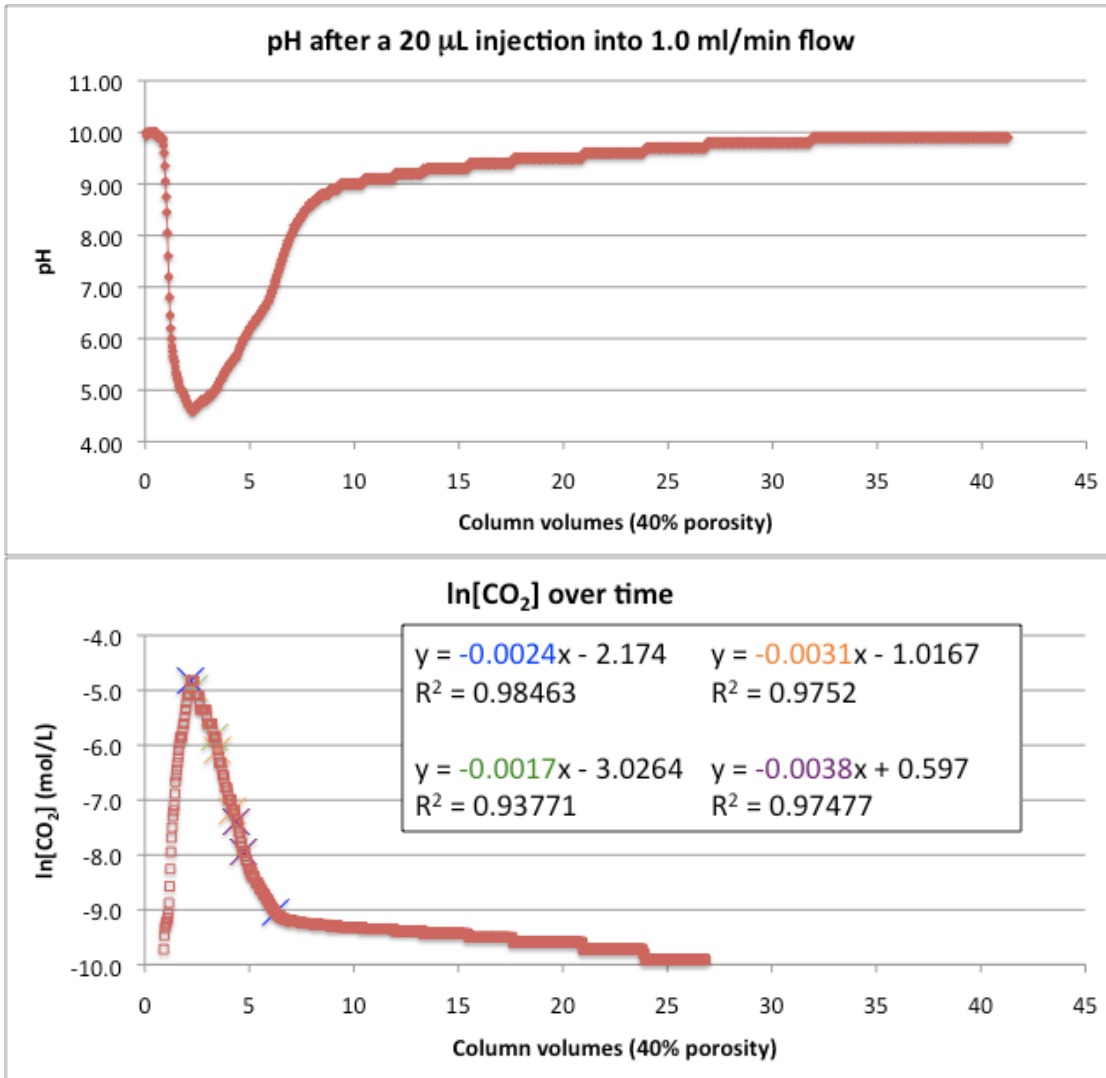
(45°C)



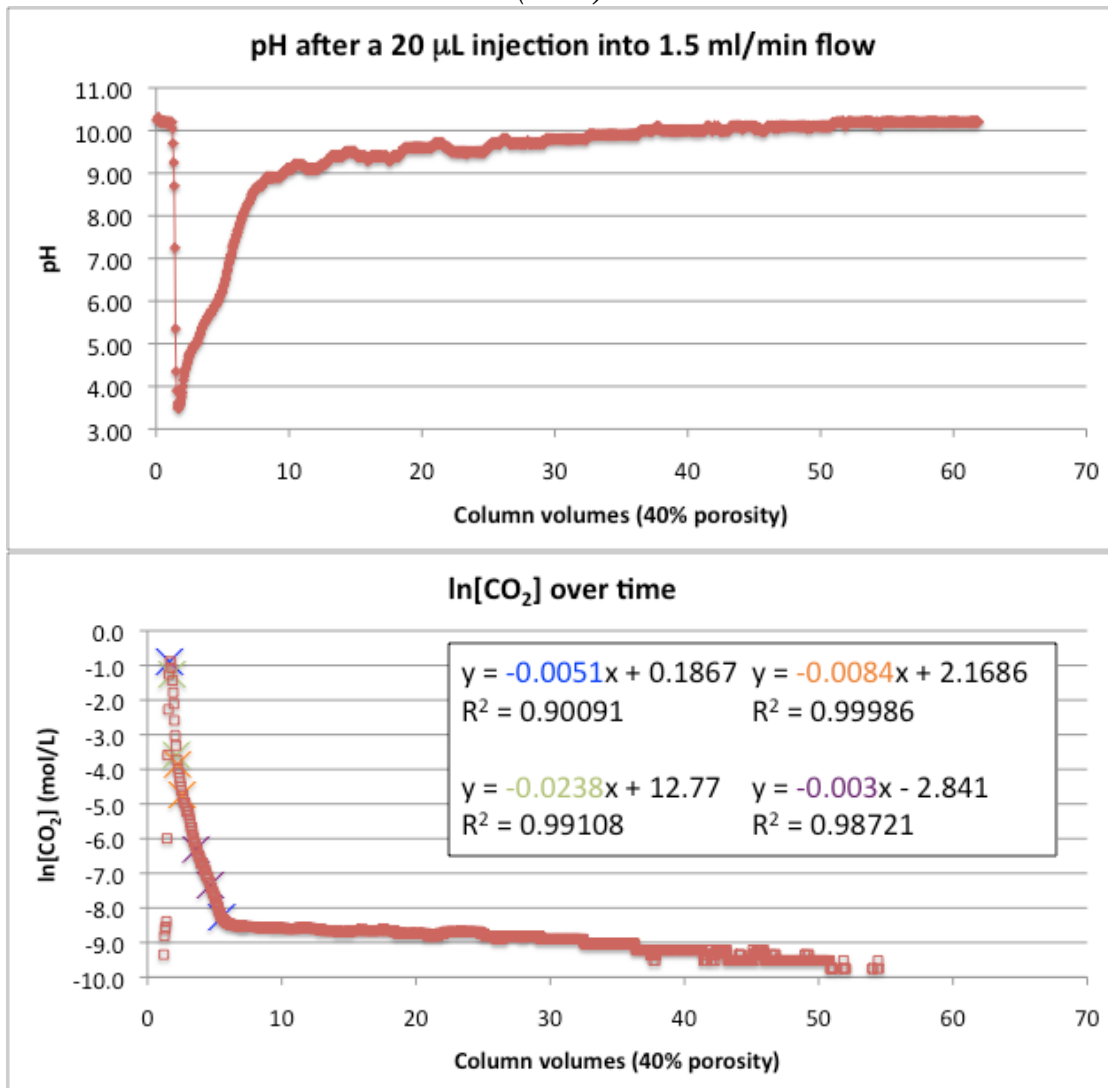
(45°C)



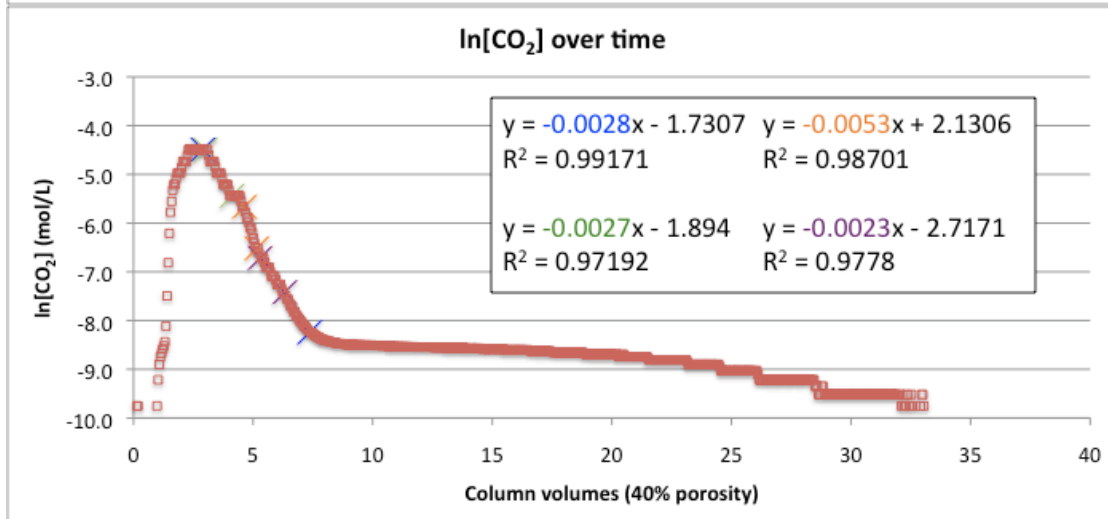
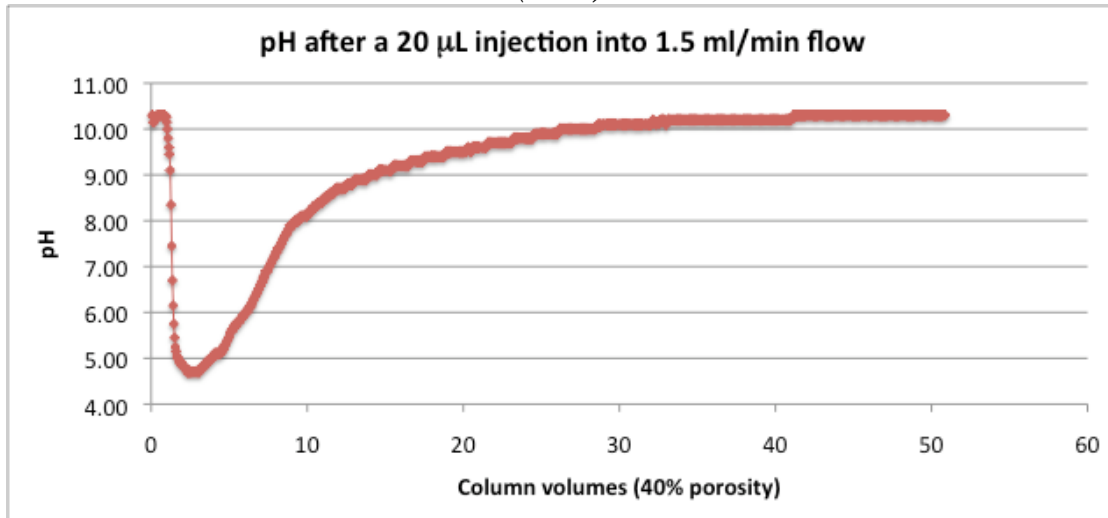
Supercritical CO₂ (45°C), 20 μL injections



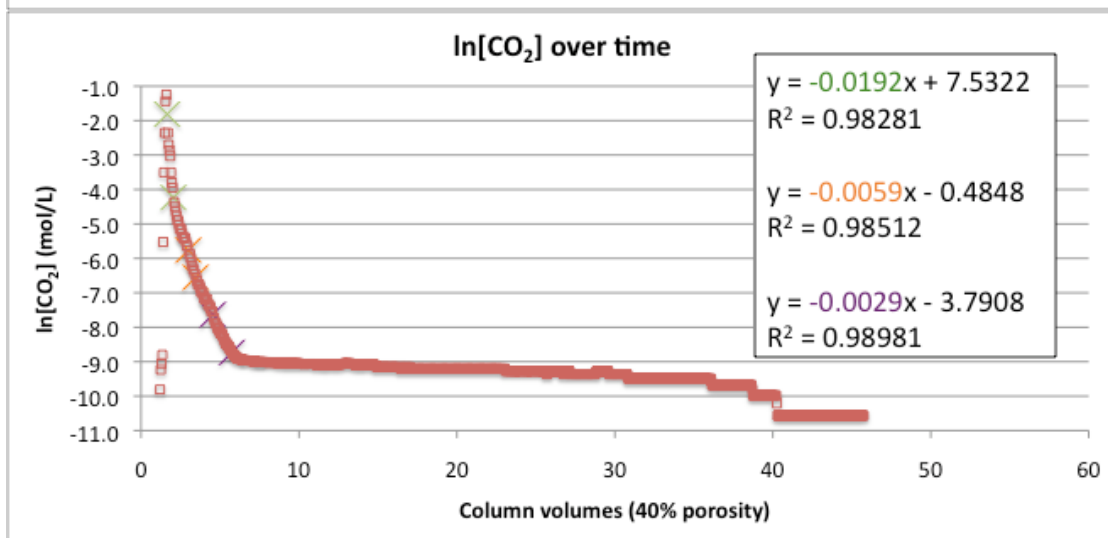
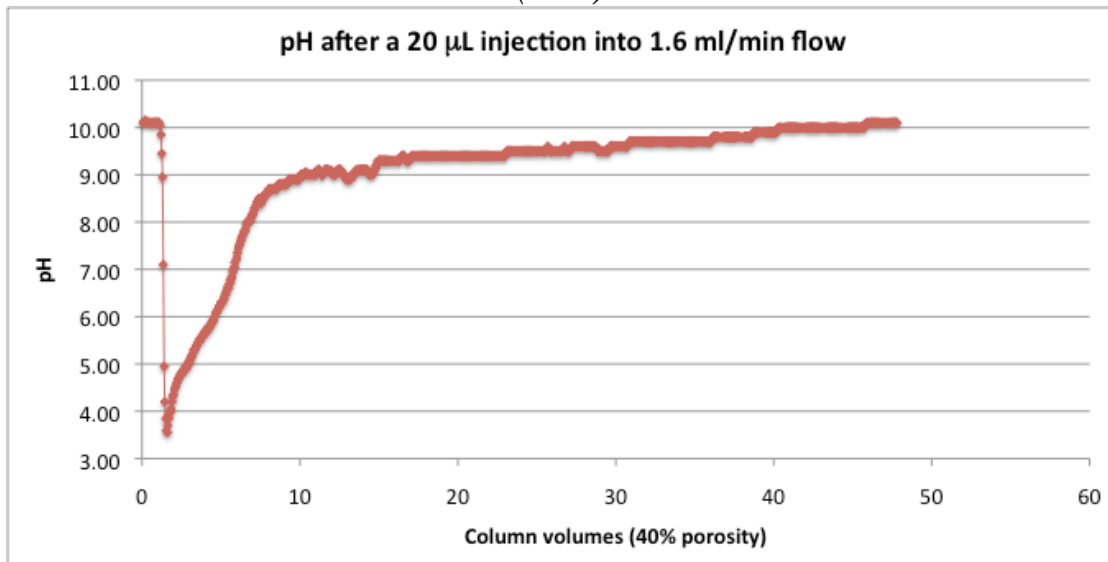
(45°C)



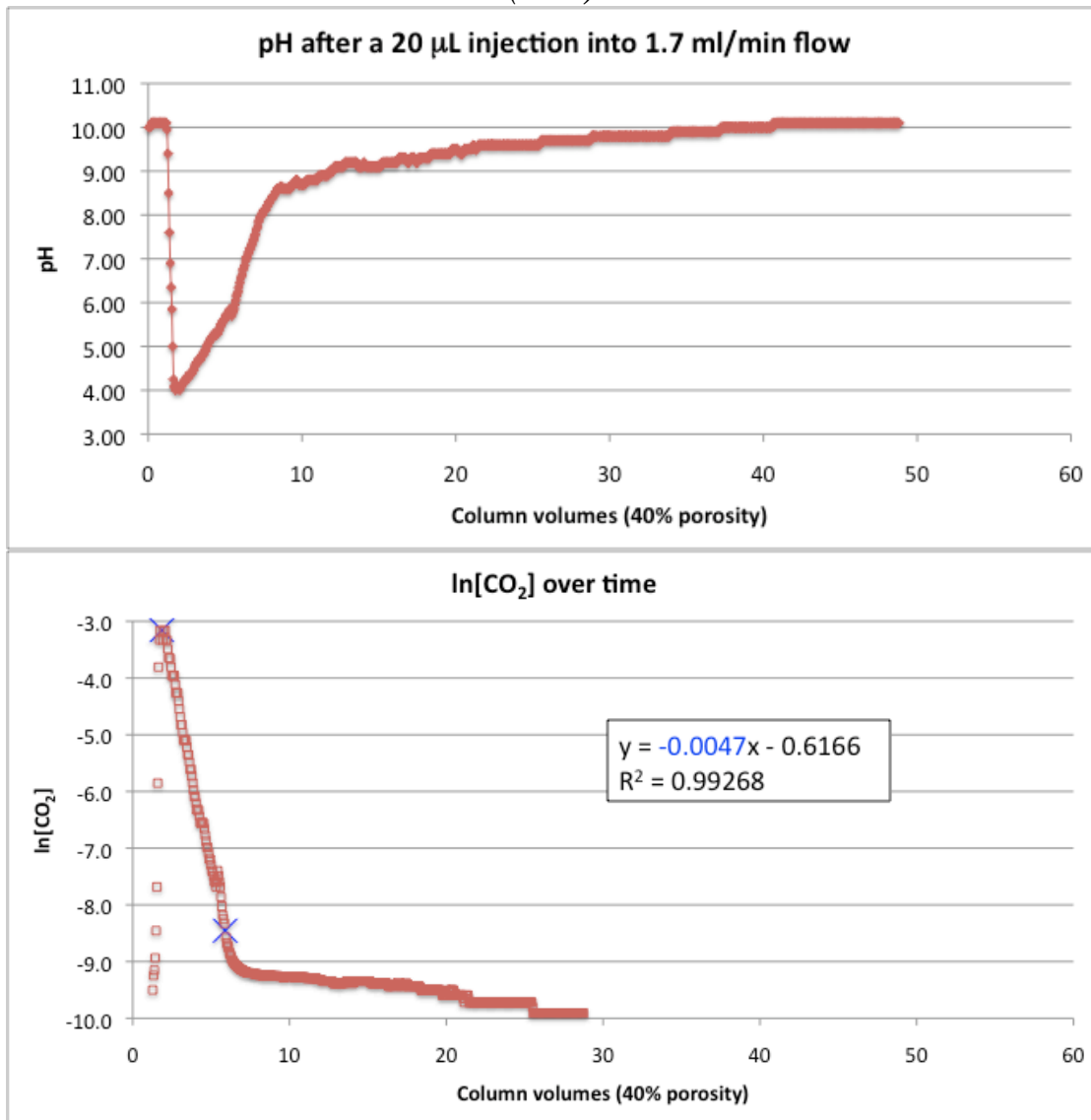
(45°C)



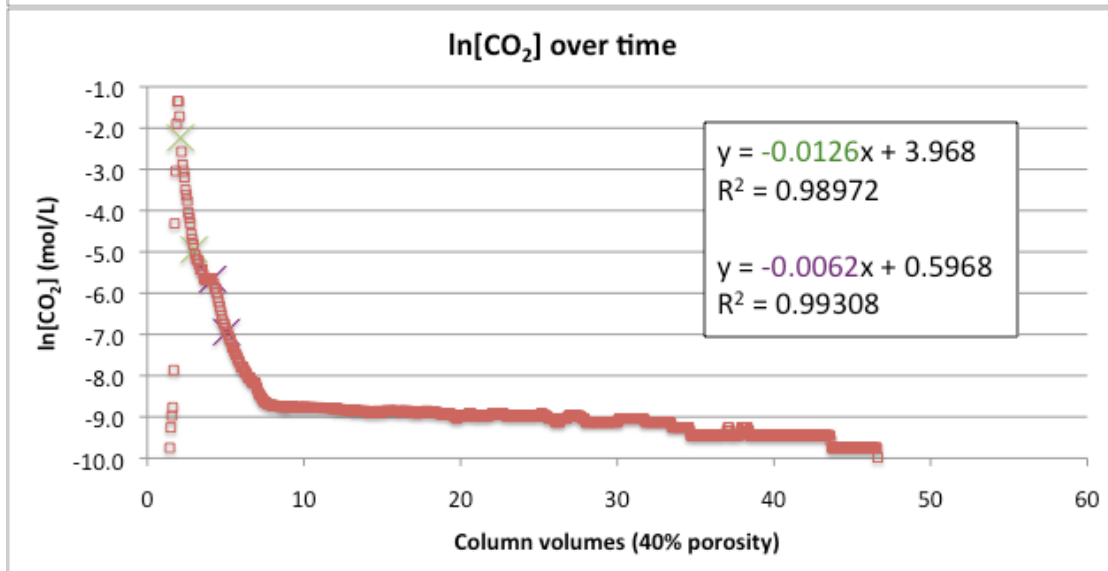
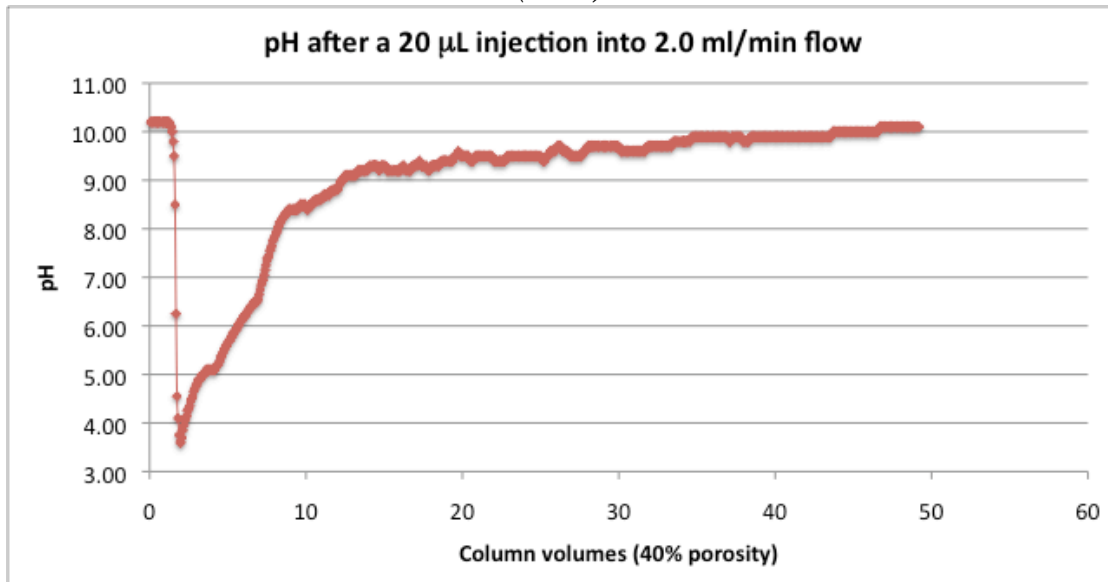
(45°C)



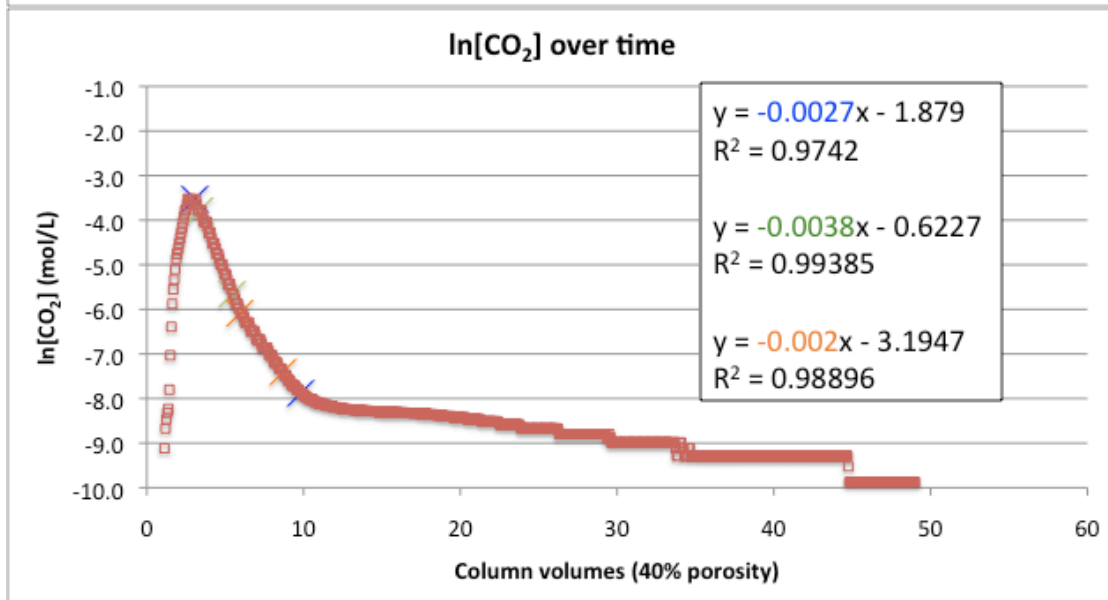
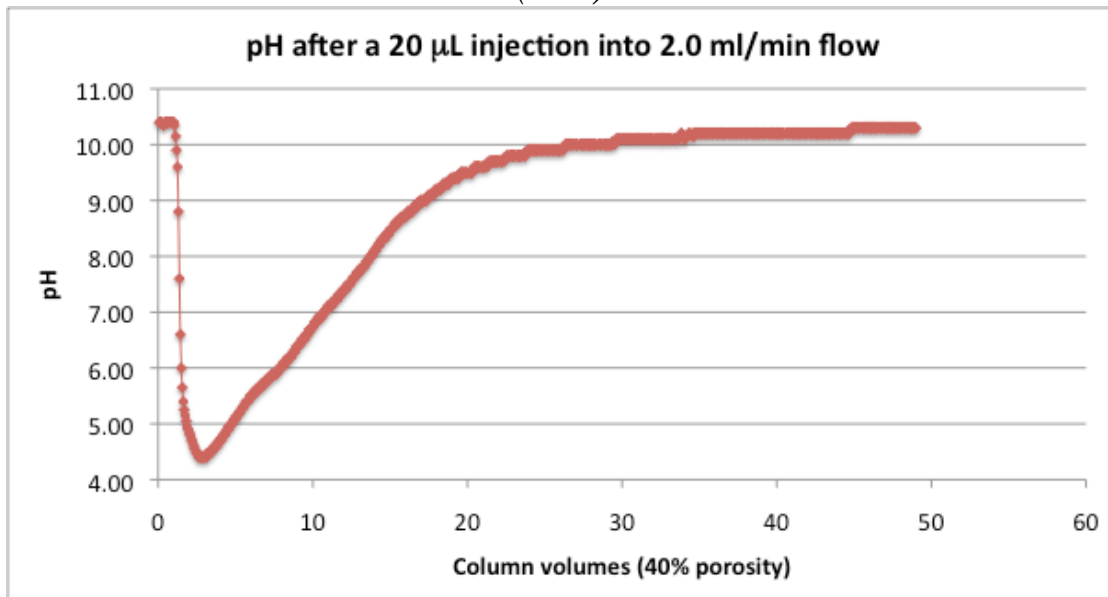
(45°C)



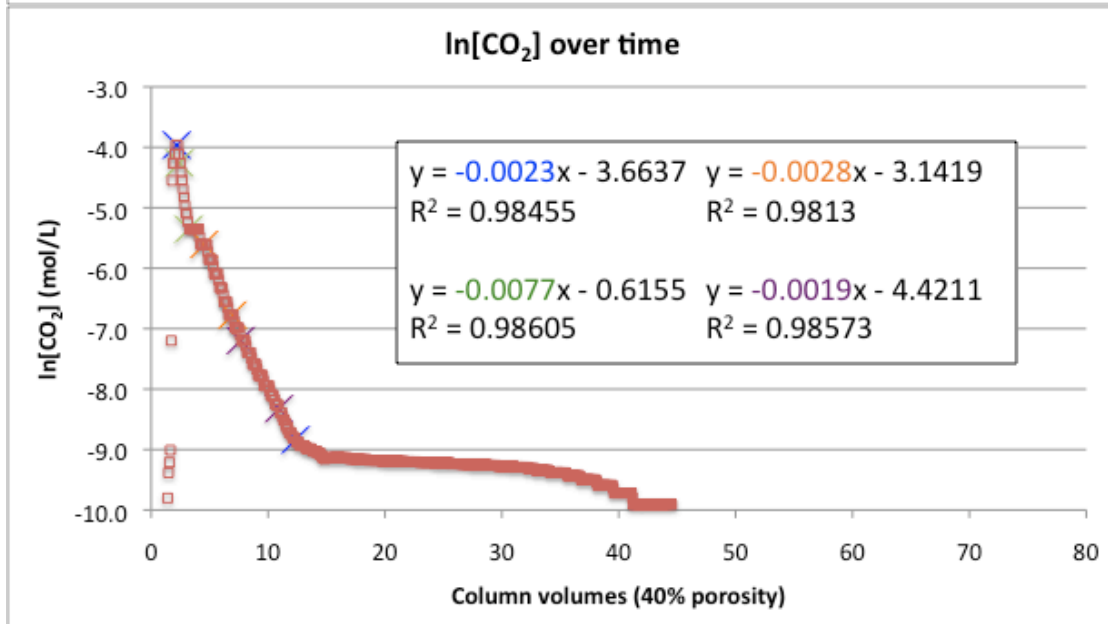
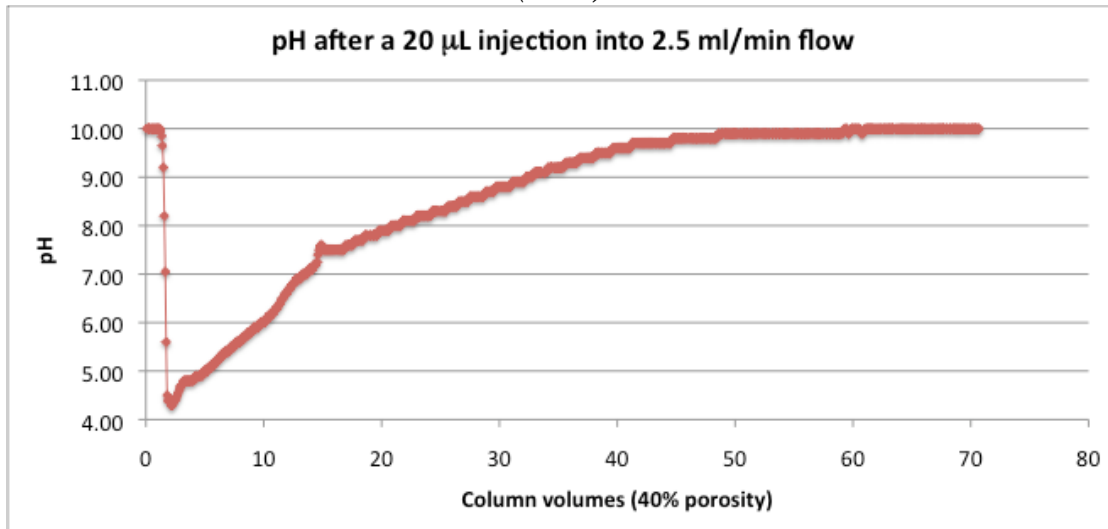
(45°C)



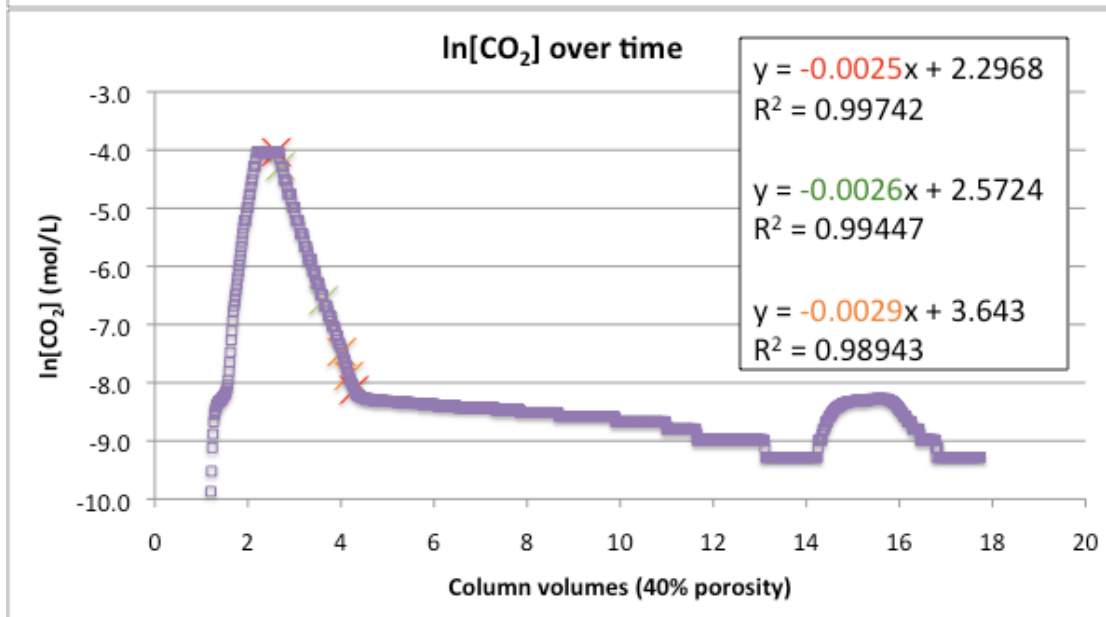
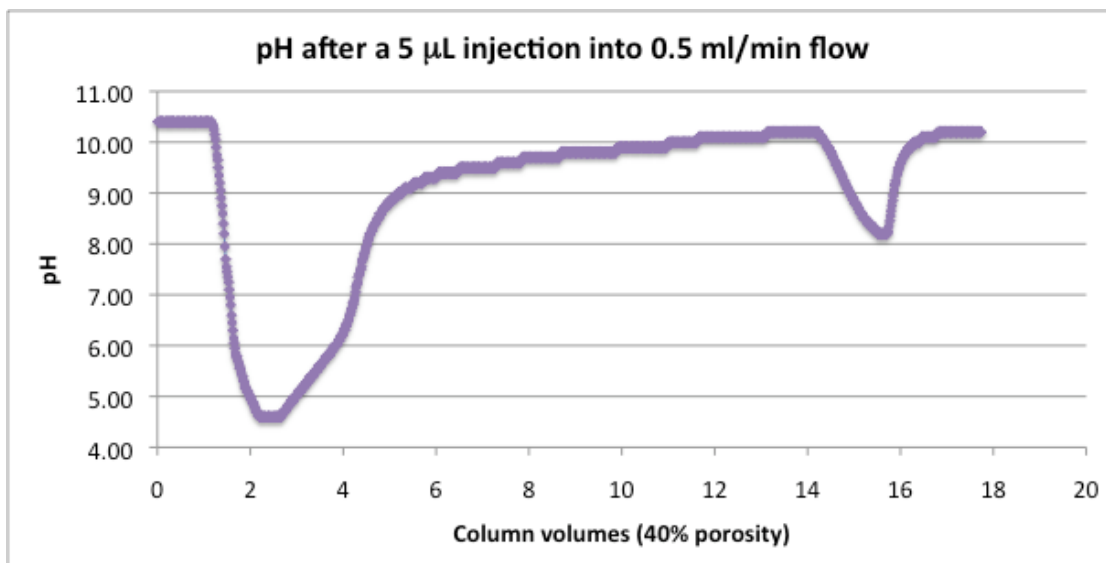
(45°C)



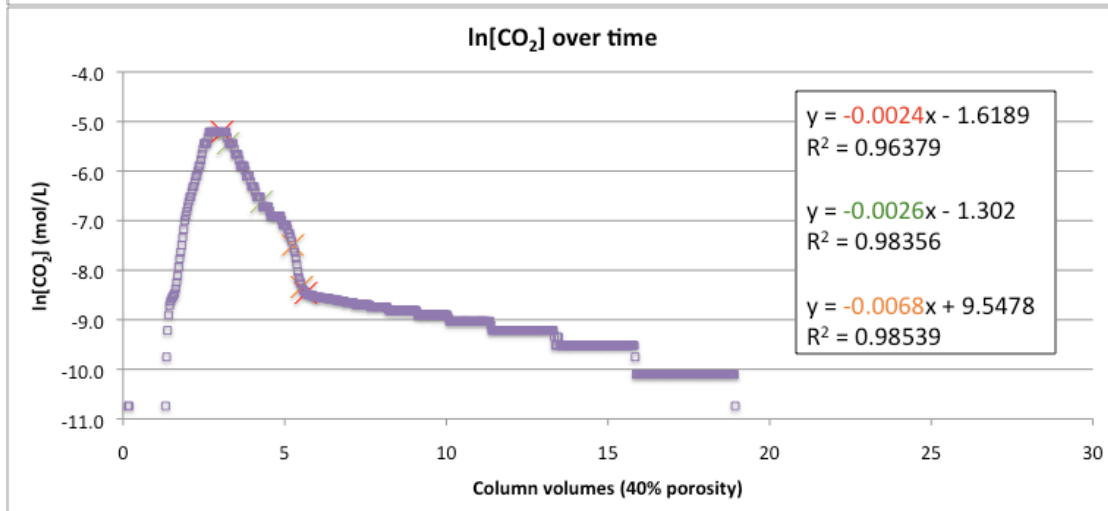
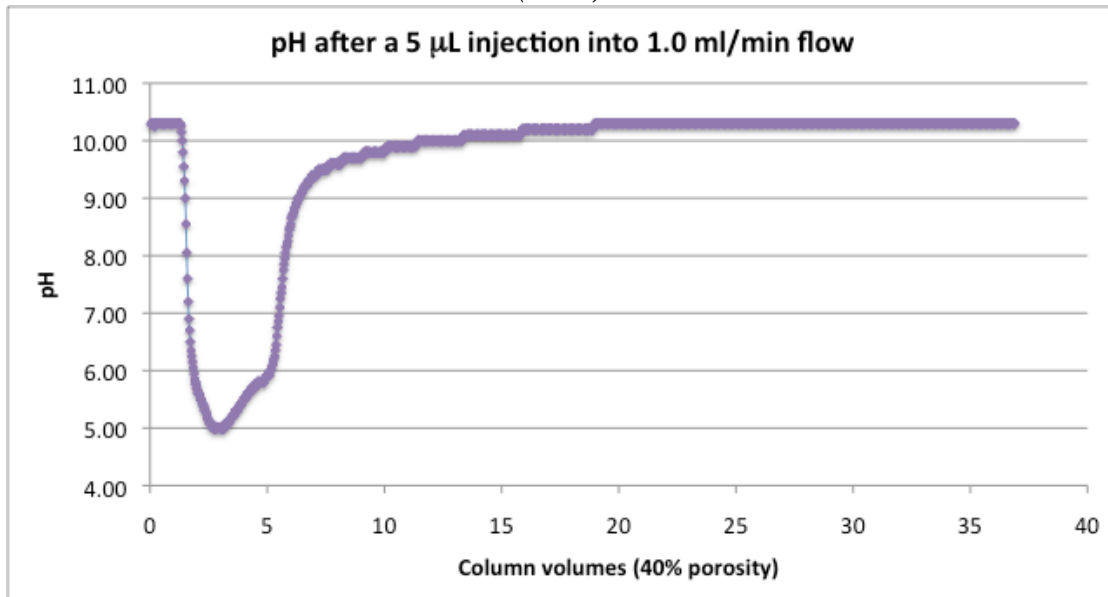
(45°C)



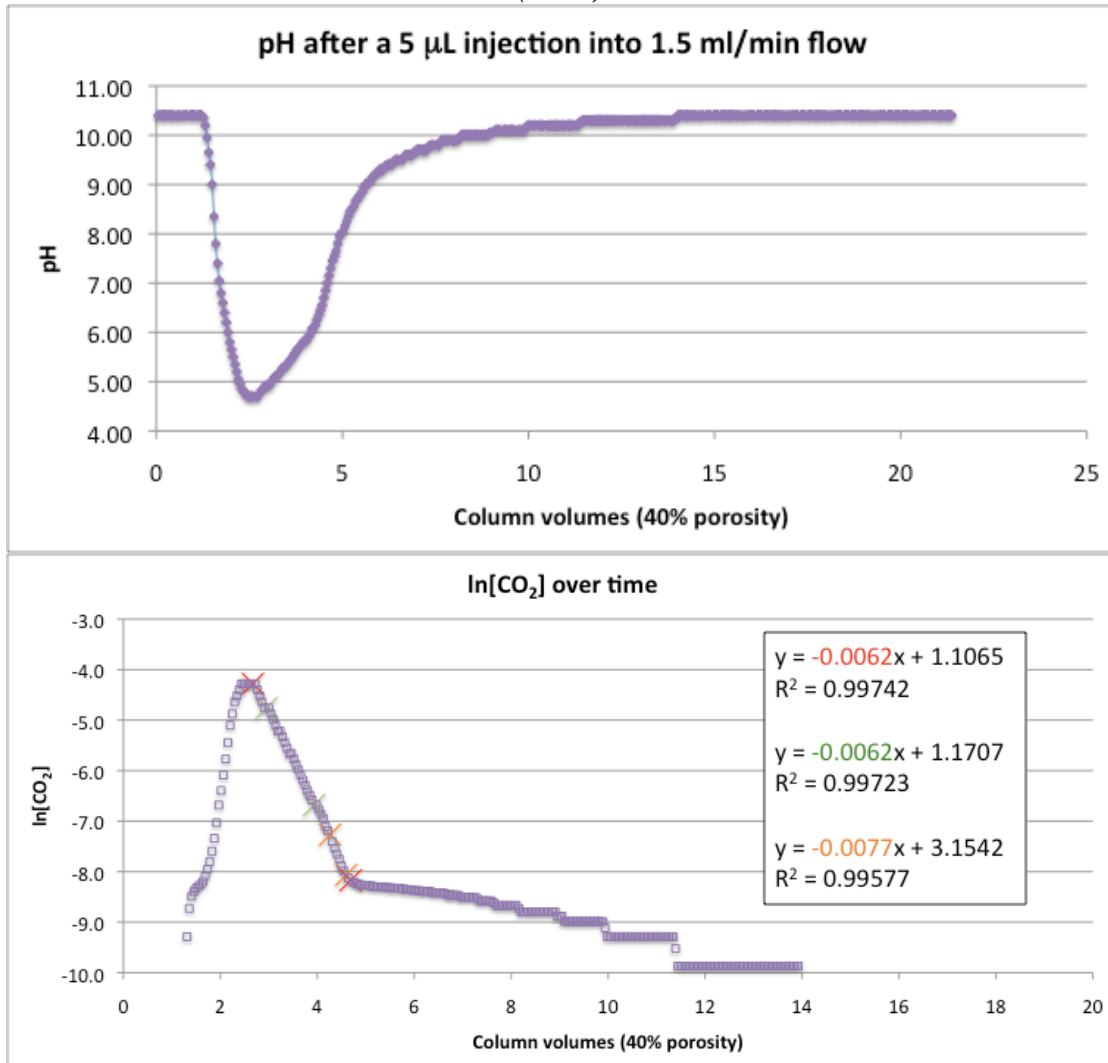
Supercritical CO₂ (60°C), 5 μL injections



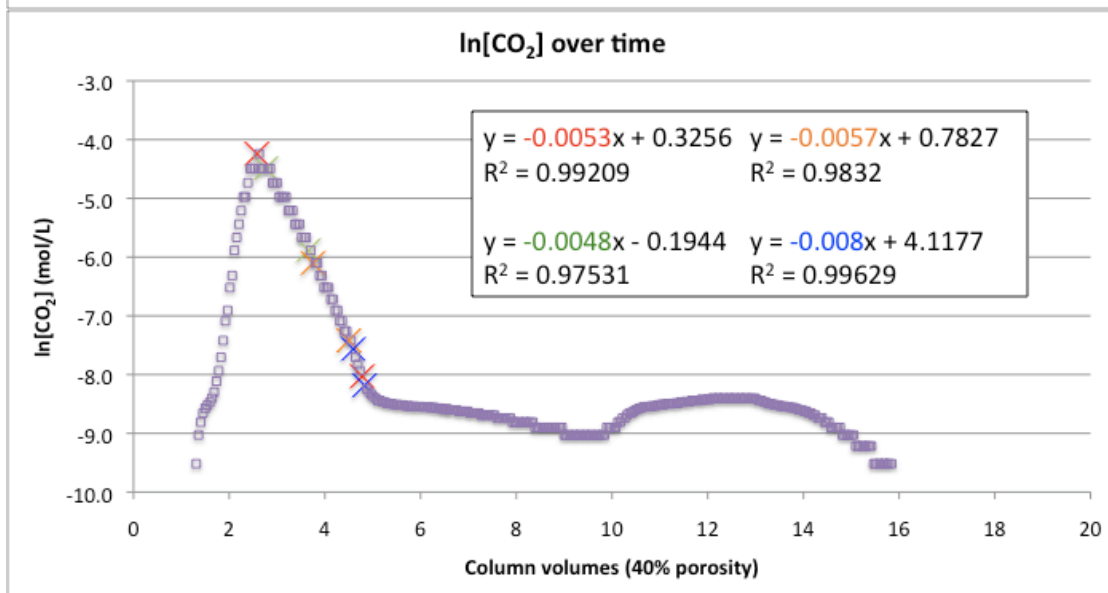
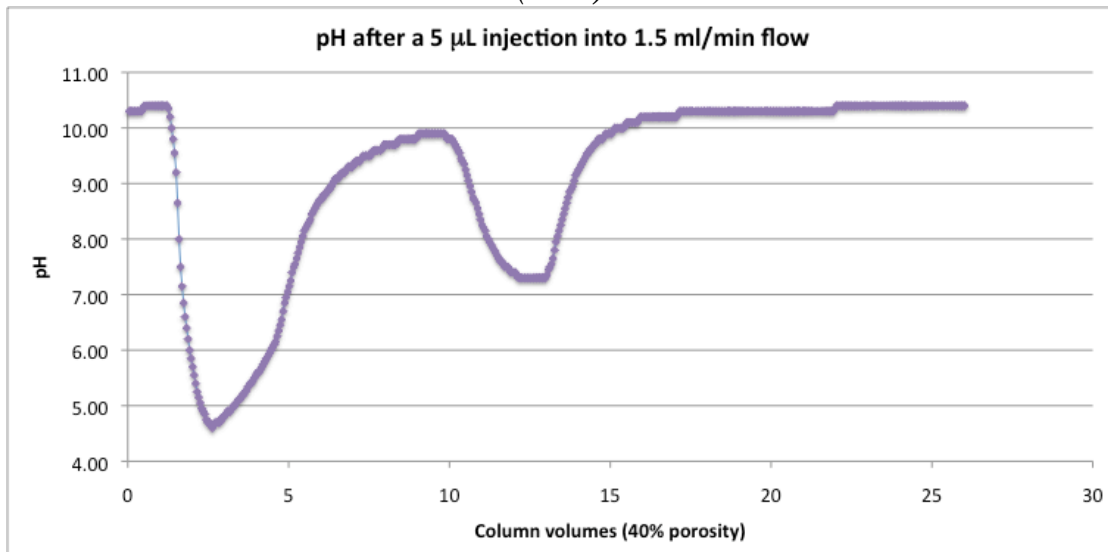
(60°C)



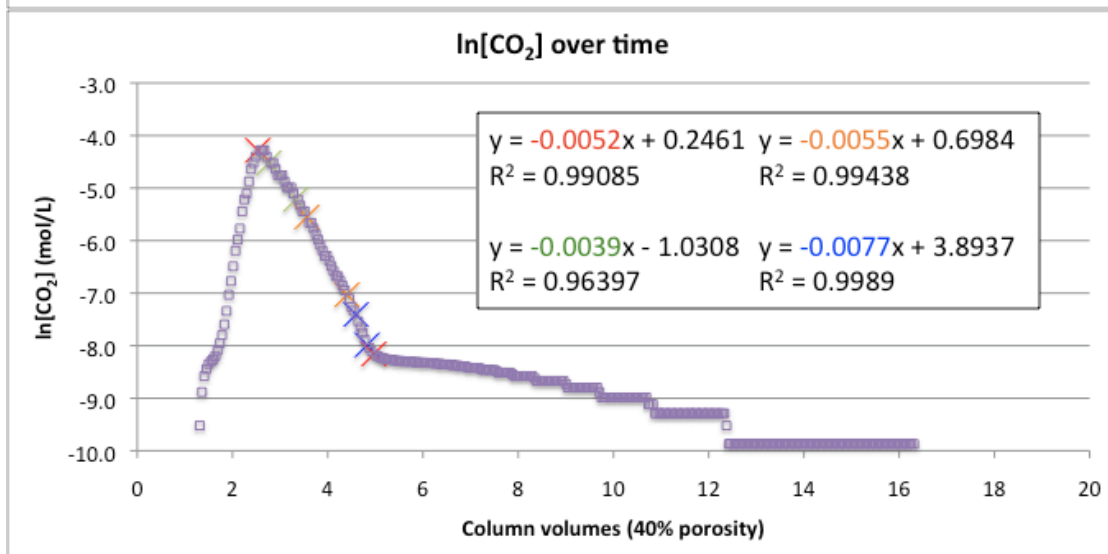
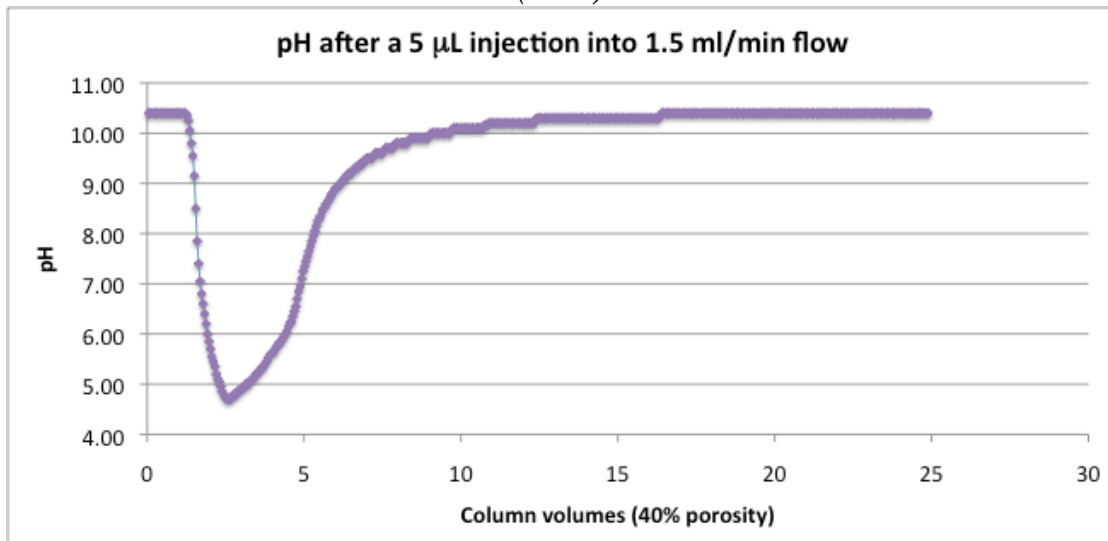
(60°C)



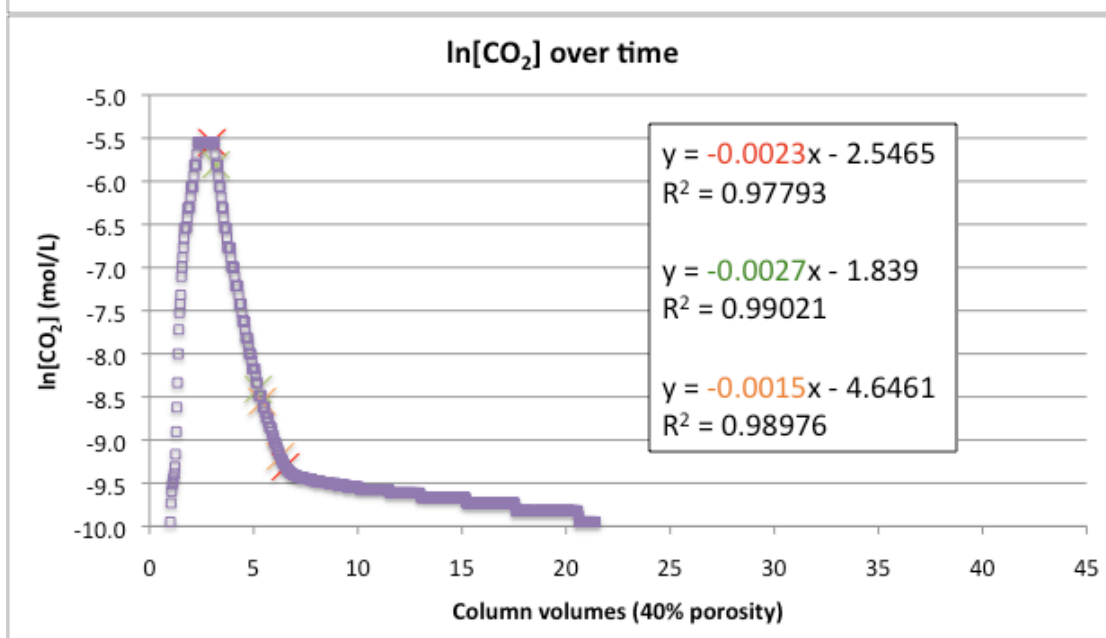
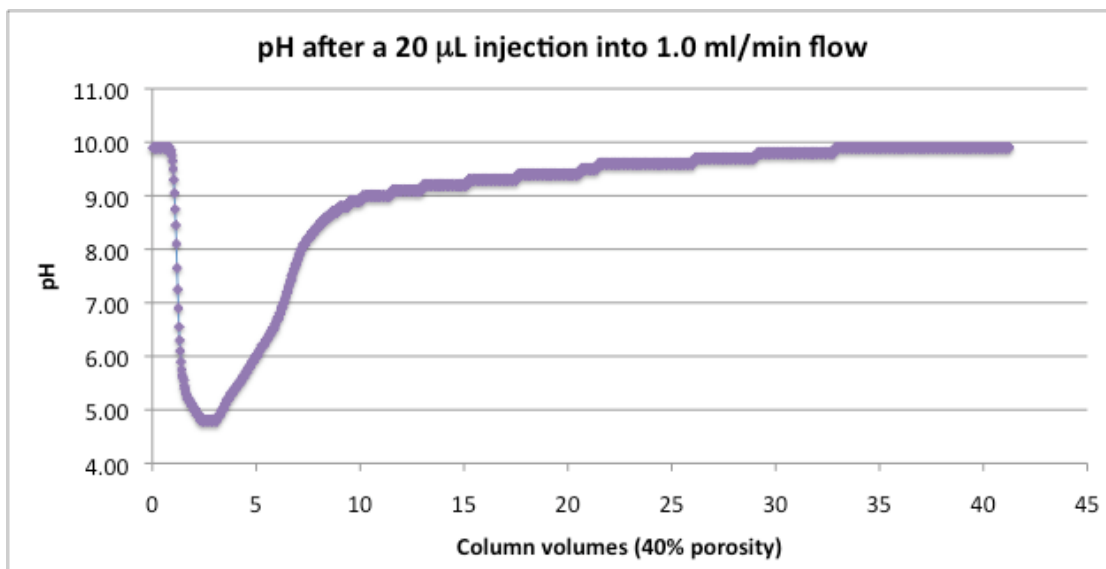
(60°C)



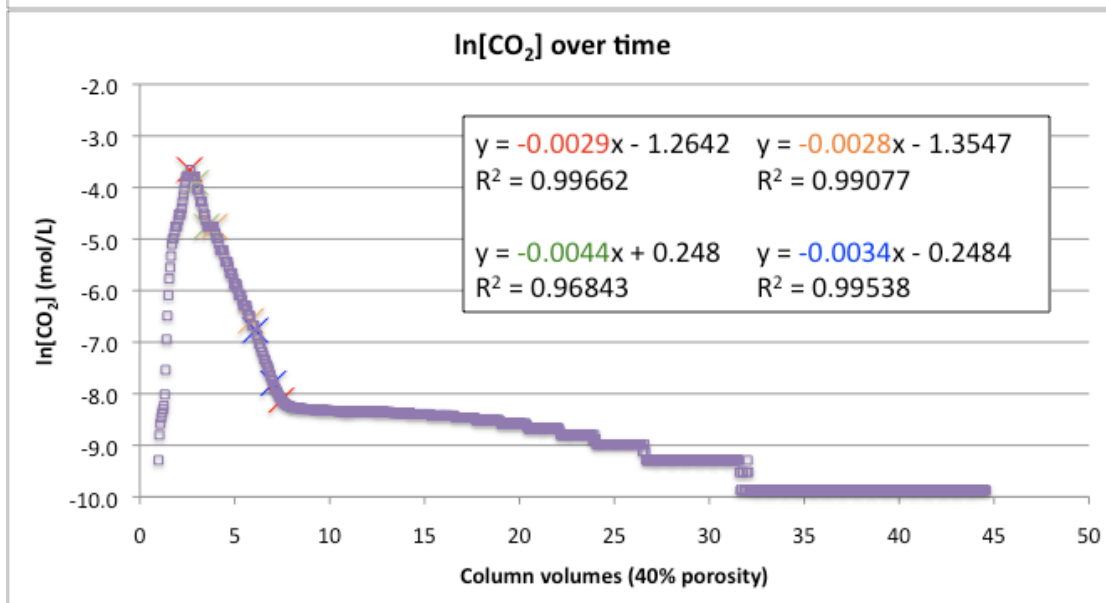
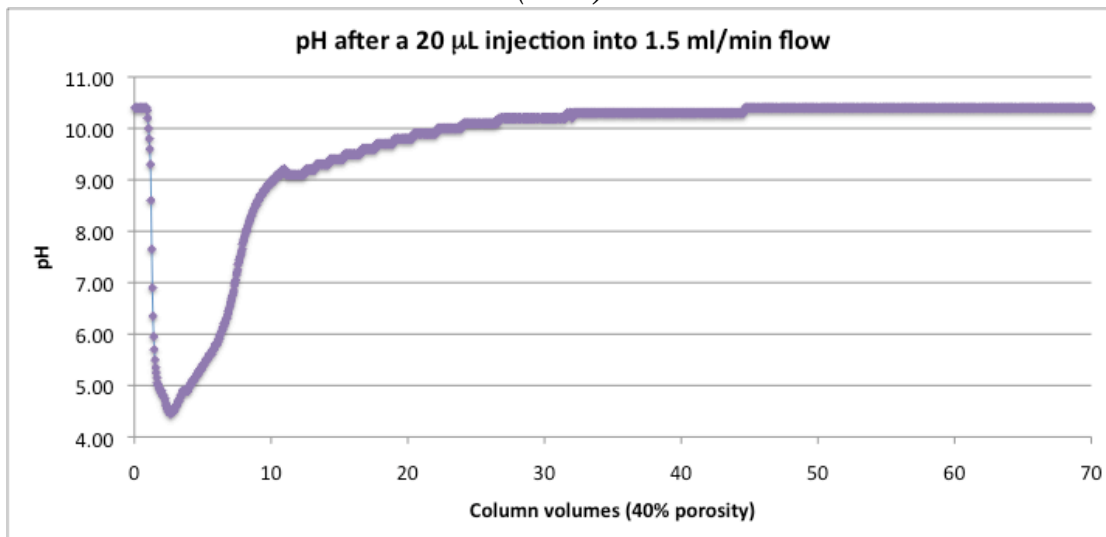
(60°C)



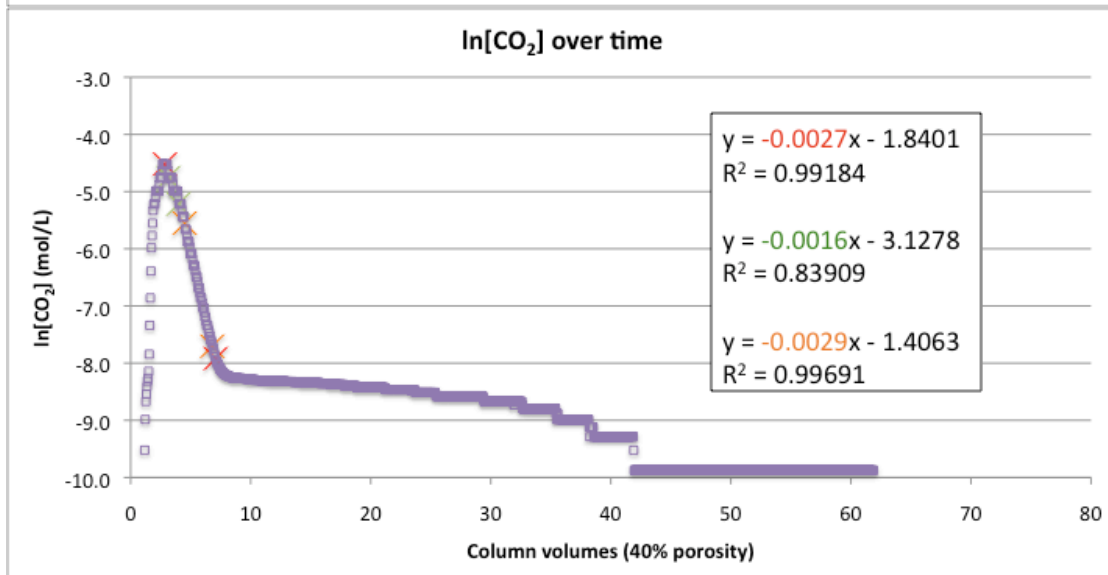
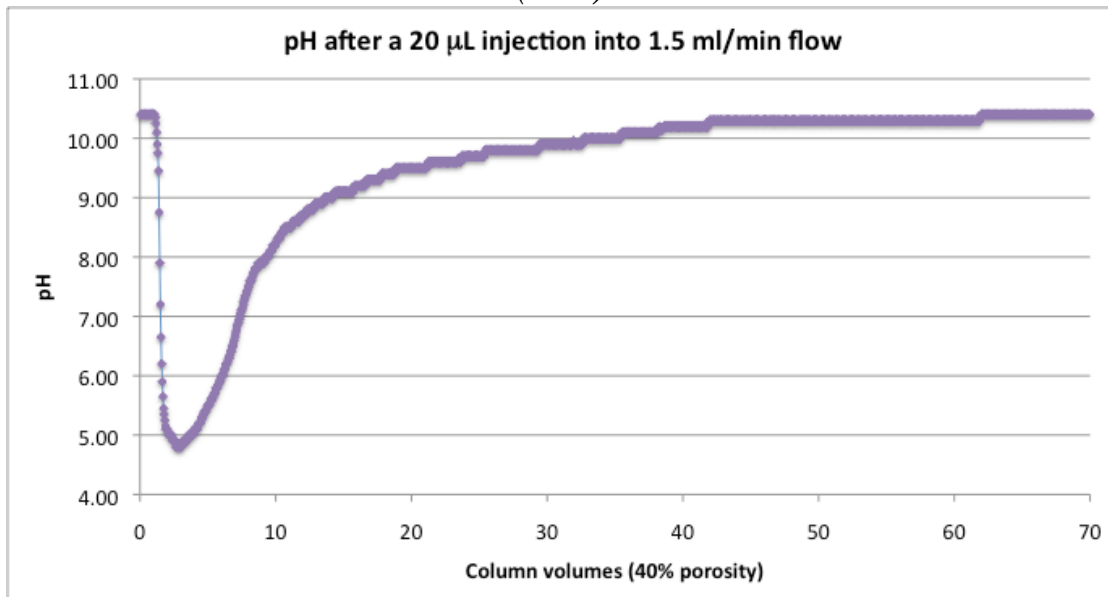
Supercritical CO₂ (60°C), 20 μL injections



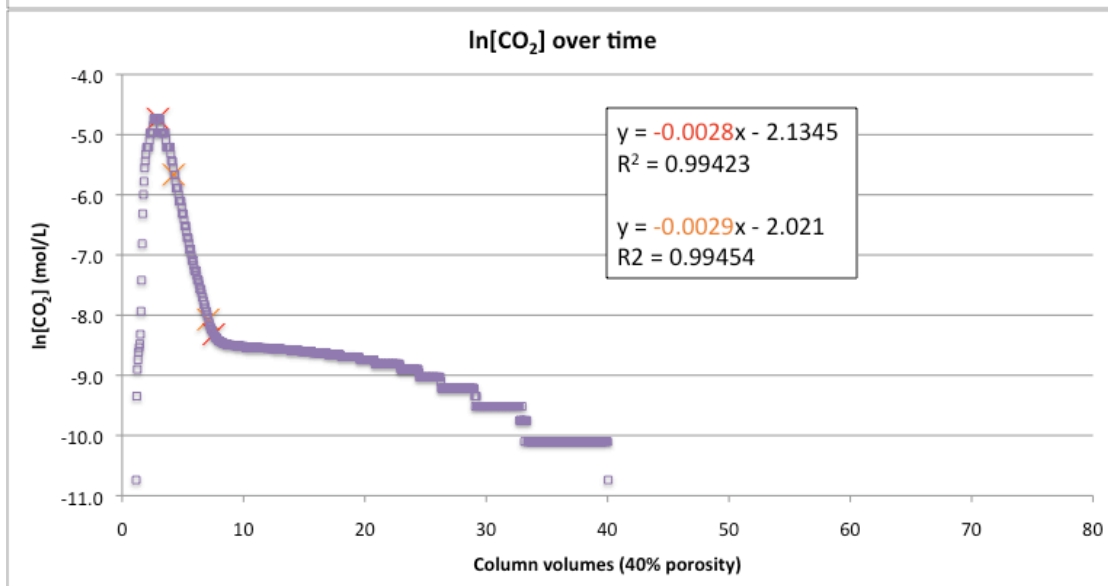
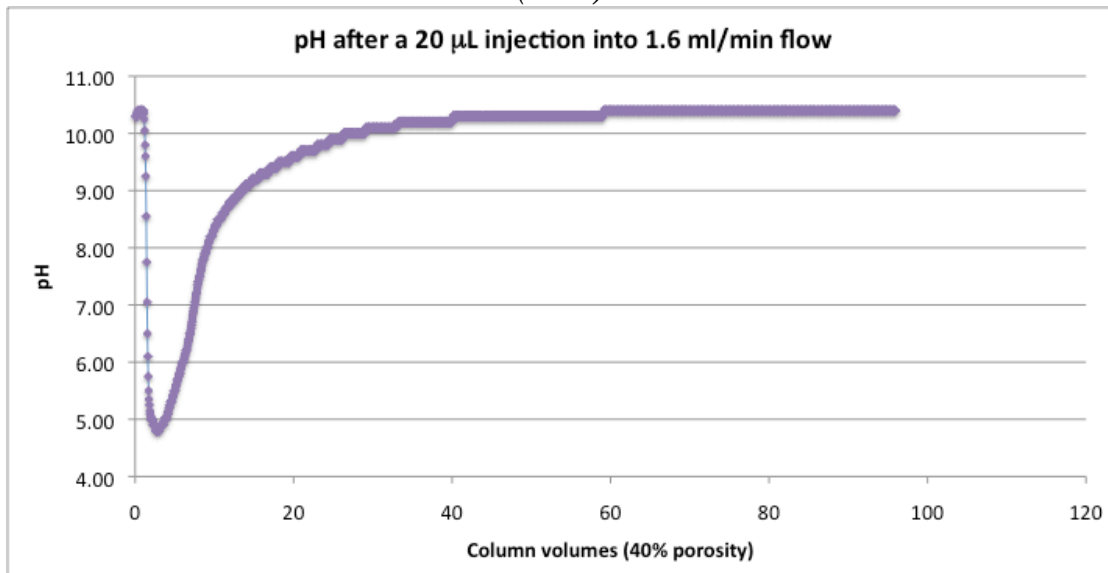
(60°C)



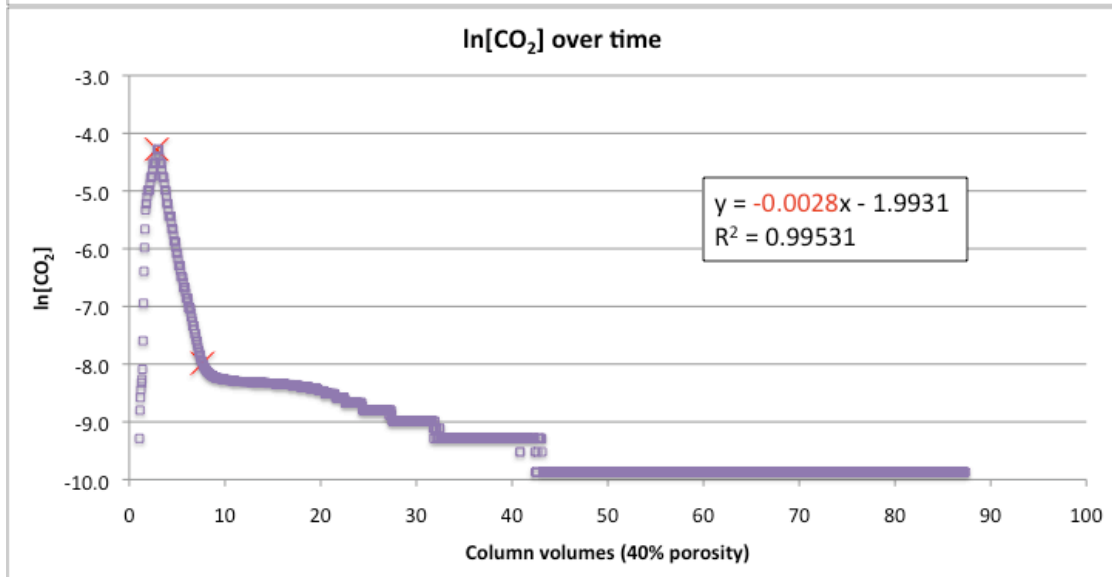
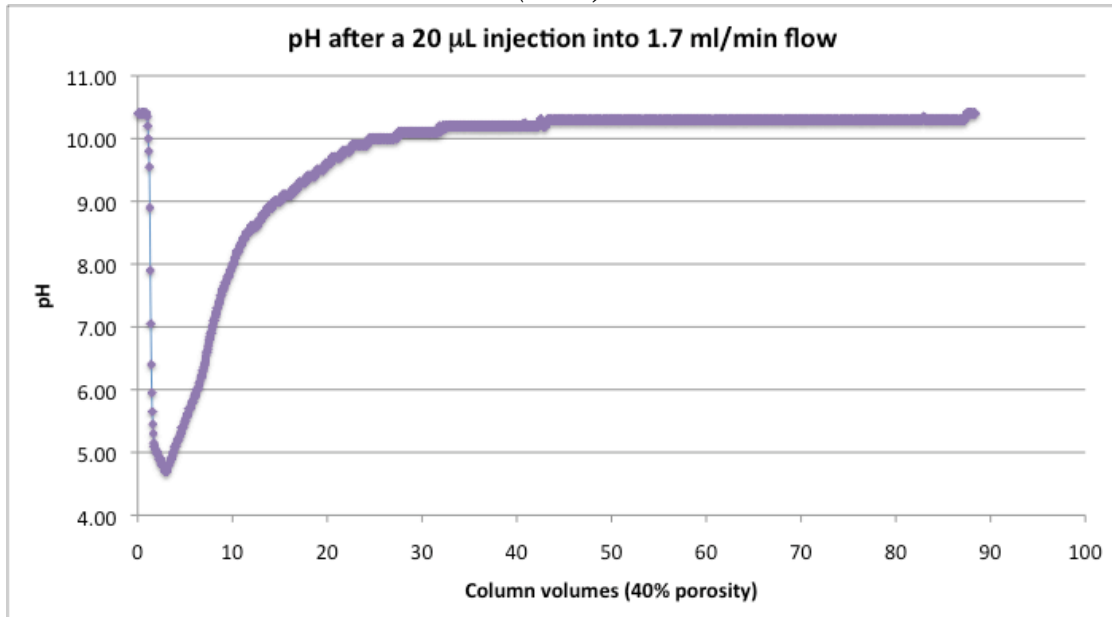
(60°C)



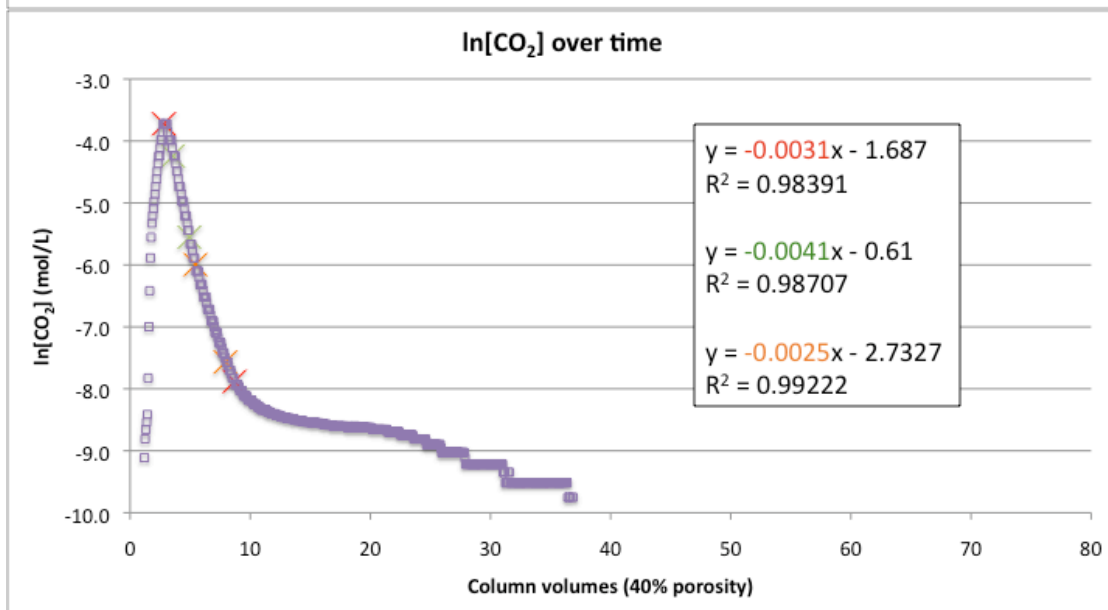
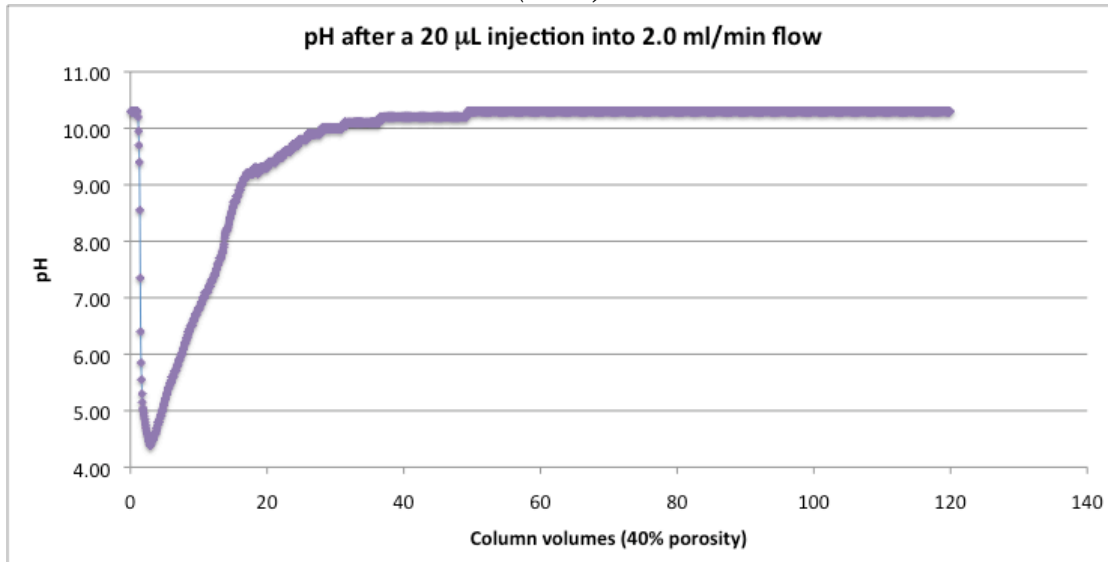
(60°C)



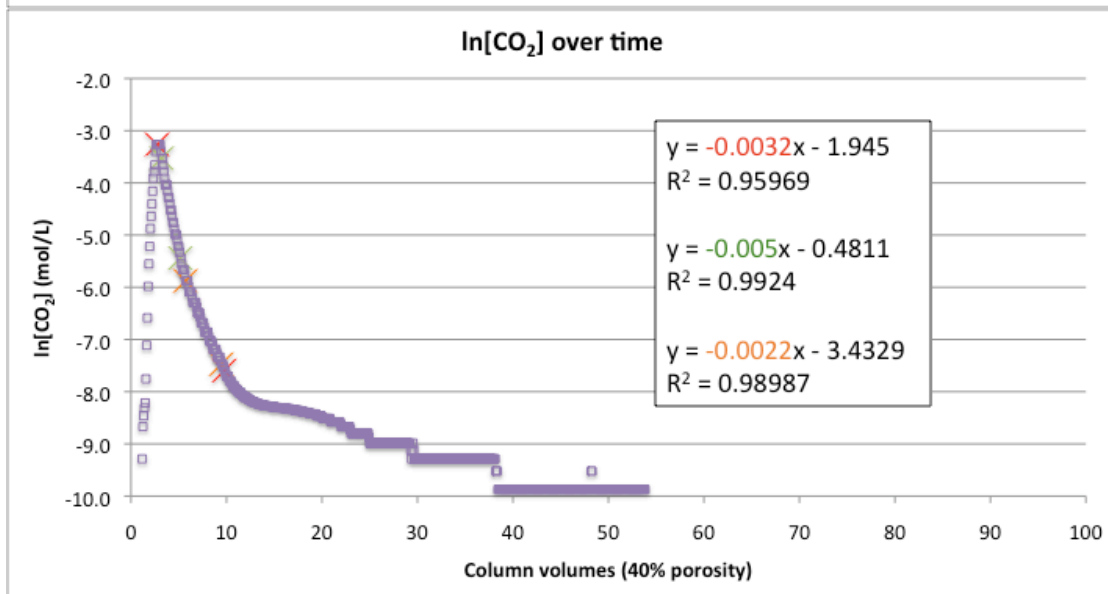
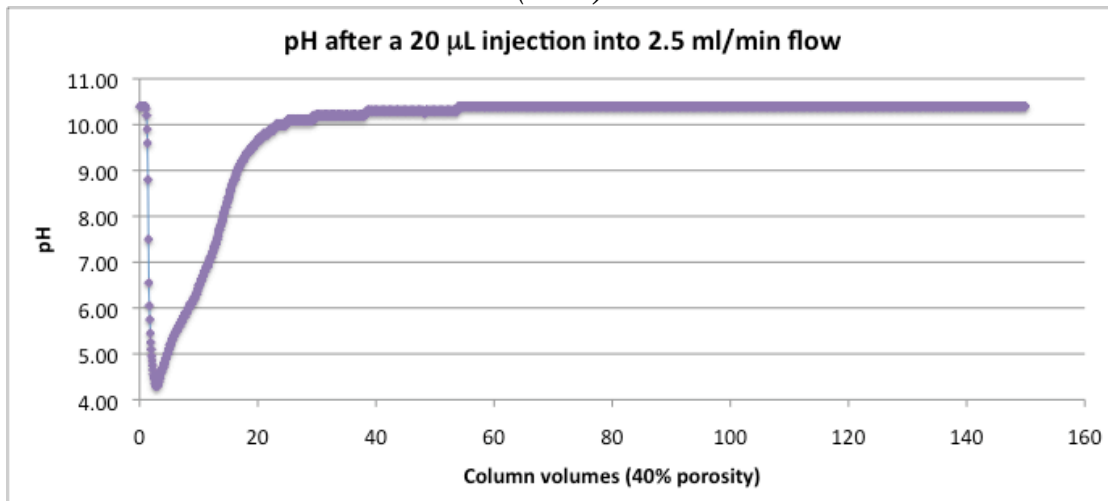
(60°C)



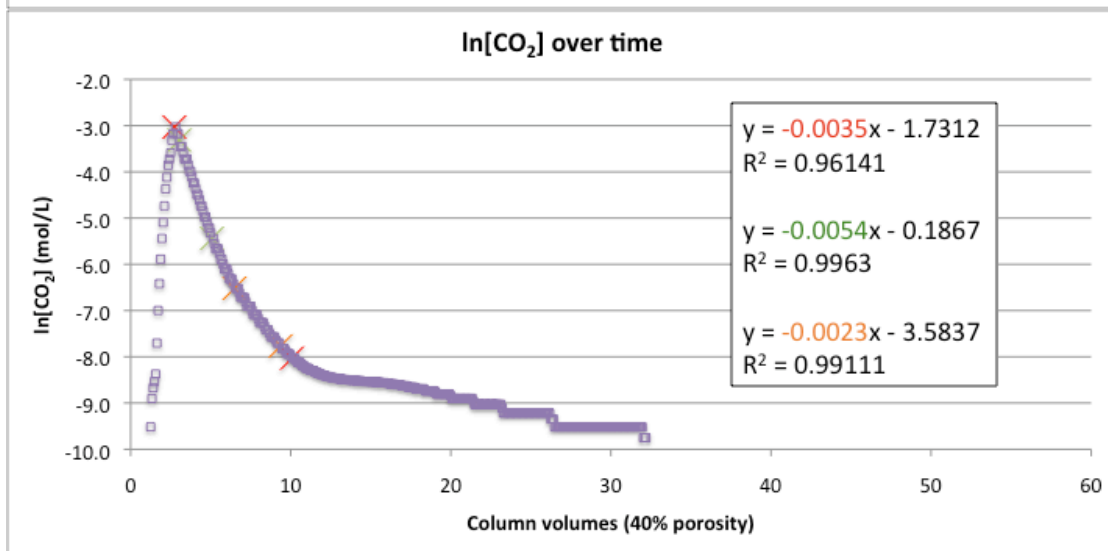
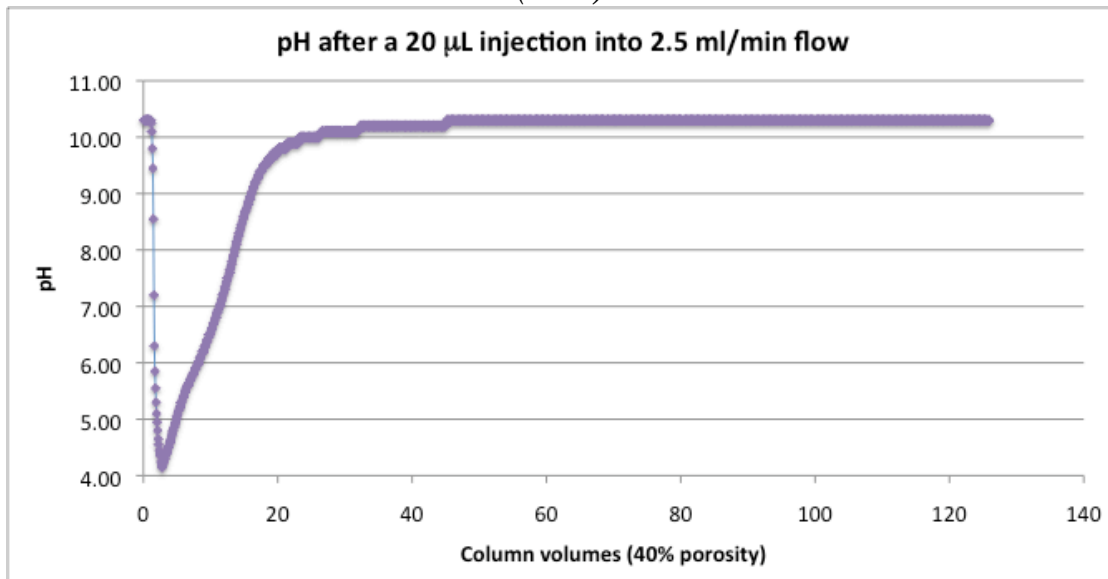
(60°C)



(60°C)



(60°C)



Appendix III: sample spreadsheet

Conditional formatting was used in pH columns to highlight separate calculation zones. Consecutive pH values were averaged to minimize bias when the total concentration of CO₂ was calculated. This appendix includes the first 25.75 minutes of data recorded for a 5 μL injection of supercritical CO₂ at 35°C, as a sample of the spreadsheets used in this research.

5 µL SC INJECTION @ 35°C					
	minus 0.1	minus 0.05	meas.	plus 0.05	plus 0.1
C_{TCO3} (mol)	1.51E-04	1.35E-04	1.21E-04	1.07E-04	9.46E-05
C_{TCO3} (µmol)	1.51E+02	1.35E+02	1.21E+02	1.07E+02	9.46E+01
% recovered	182.47%	162.97%	145.24%	128.99%	113.94%
meas-inj	6.84E-05	5.23E-05	3.75E-05	2.41E-05	1.16E-05
total flow (ml)			182.75		
vols to rec.			22.84		
max pH			10.40		
min pH			4.70		
ΔpH			5.7		
Ka1		3.98E-07			
Ka2		5.01E-11			
Kw		1.00E-14			
[NaOH]	mmol/L	2.51E-04			
Flowrate	ml/min	0.5			
Flowrate	L/min	0.0005			
Injection	µl	5			
Temp	C	35.1			
Press	psi	1527			
MIT ρ	kg/m ³	730.36			
	g/µl	0.00073			
MIT inj.	g	3.65E-03			
MIT inj.	moles	8.30E-05			
col vol	ml	20			
porosity 40%	ml	8			
1 pore	µl	0.125			
plus 50%		0.188			
minus 50%		0.063			
Flowrate	ml/min	0.5	differences	minus 0.1	182.47%
Temp	C	35.1	%	minus 0.05	162.97%
Press	psi	1527		actual	145.24%
MIT ρ	kg/m ³	730.36		plus 0.05	128.99%
MIT inj.	moles	8.30E-05		plus 0.1	113.94%
CTCO3	minus 0.1	1.51E-04	pos error		1.35E-05
CTCO3	minus 0.05	1.35E-04	neg error		1.47E-05
CTCO3	actual	1.21E-04	Vs to recover	40% porosity	22.84
CTCO3	plus 0.05	1.07E-04	t of min.	sec	2145
CTCO3	plus 0.1	9.46E-05	ΔpH		5.7
			K		0.0025

A Time after injection	col. pore volumes	L/15 sec interval	pH -0.1	pH -0.05	measured pH	pH +0.05	pH +0.1
sec							
0	0.00	1.25E-04	10.30	10.35	10.40	10.45	10.50
15	0.02	1.25E-04	10.30	10.35	10.40	10.45	10.50
30	0.03	1.25E-04	10.30	10.35	10.40	10.45	10.50
45	0.05	1.25E-04	10.30	10.35	10.40	10.45	10.50
60	0.06	1.25E-04	10.30	10.35	10.40	10.45	10.50
75	0.08	1.25E-04	10.30	10.35	10.40	10.45	10.50
90	0.09	1.25E-04	10.30	10.35	10.40	10.45	10.50
105	0.11	1.25E-04	10.30	10.35	10.40	10.45	10.50
120	0.13	1.25E-04	10.30	10.35	10.40	10.45	10.50
135	0.14	1.25E-04	10.30	10.35	10.40	10.45	10.50
150	0.16	1.25E-04	10.30	10.35	10.40	10.45	10.50
165	0.17	1.25E-04	10.30	10.35	10.40	10.45	10.50
180	0.19	1.25E-04	10.30	10.35	10.40	10.45	10.50
195	0.20	1.25E-04	10.30	10.35	10.40	10.45	10.50
210	0.22	1.25E-04	10.30	10.35	10.40	10.45	10.50
225	0.23	1.25E-04	10.30	10.35	10.40	10.45	10.50
240	0.25	1.25E-04	10.30	10.35	10.40	10.45	10.50
255	0.27	1.25E-04	10.30	10.35	10.40	10.45	10.50
270	0.28	1.25E-04	10.30	10.35	10.40	10.45	10.50
285	0.30	1.25E-04	10.30	10.35	10.40	10.45	10.50
300	0.31	1.25E-04	10.30	10.35	10.40	10.45	10.50
315	0.33	1.25E-04	10.30	10.35	10.40	10.45	10.50
330	0.34	1.25E-04	10.30	10.35	10.40	10.45	10.50
345	0.36	1.25E-04	10.30	10.35	10.40	10.45	10.50
360	0.38	1.25E-04	10.30	10.35	10.40	10.45	10.50
375	0.39	1.25E-04	10.30	10.35	10.40	10.45	10.50
390	0.41	1.25E-04	10.30	10.35	10.40	10.45	10.50
405	0.42	1.25E-04	10.30	10.35	10.40	10.45	10.50
420	0.44	1.25E-04	10.30	10.35	10.40	10.45	10.50
435	0.45	1.25E-04	10.30	10.35	10.40	10.45	10.50
450	0.47	1.25E-04	10.30	10.35	10.40	10.45	10.50
465	0.48	1.25E-04	10.30	10.35	10.40	10.45	10.50
480	0.50	1.25E-04	10.30	10.35	10.40	10.45	10.50
495	0.52	1.25E-04	10.30	10.35	10.40	10.45	10.50
510	0.53	1.25E-04	10.30	10.35	10.40	10.45	10.50
525	0.55	1.25E-04	10.30	10.35	10.40	10.45	10.50
540	0.56	1.25E-04	10.30	10.35	10.40	10.45	10.50
555	0.58	1.25E-04	10.30	10.35	10.40	10.45	10.50
570	0.59	1.25E-04	10.30	10.35	10.40	10.45	10.50
585	0.61	1.25E-04	10.30	10.35	10.40	10.45	10.50
600	0.63	1.25E-04	10.30	10.35	10.40	10.45	10.50
615	0.64	1.25E-04	10.30	10.35	10.40	10.45	10.50
630	0.66	1.25E-04	10.30	10.35	10.40	10.45	10.50
645	0.67	1.25E-04	10.30	10.35	10.40	10.45	10.50
660	0.69	1.25E-04	10.30	10.35	10.40	10.45	10.50
675	0.70	1.25E-04	10.30	10.35	10.40	10.45	10.50
690	0.72	1.25E-04	10.30	10.35	10.40	10.45	10.50
705	0.73	1.25E-04	10.30	10.35	10.40	10.45	10.50
720	0.75	1.25E-04	10.30	10.35	10.40	10.45	10.50
735	0.77	1.25E-04	10.30	10.35	10.40	10.45	10.50
750	0.78	1.25E-04	10.30	10.35	10.40	10.45	10.50

B Time after injection	col. pore volumes	L/15 sec interval	pH -0.1	pH -0.05	measured pH	pH +0.05	pH +0.1
765	0.80	1.25E-04	10.30	10.35	10.40	10.45	10.50
780	0.81	1.25E-04	10.30	10.35	10.40	10.45	10.50
795	0.83	1.25E-04	10.30	10.35	10.40	10.45	10.50
810	0.84	1.25E-04	10.30	10.35	10.40	10.45	10.50
825	0.86	1.25E-04	10.30	10.35	10.40	10.45	10.50
840	0.88	1.25E-04	10.30	10.35	10.40	10.45	10.50
855	0.89	1.25E-04	10.30	10.35	10.40	10.45	10.50
870	0.91	1.25E-04	10.30	10.35	10.40	10.45	10.50
885	0.92	1.25E-04	10.30	10.35	10.40	10.45	10.50
900	0.94	1.25E-04	10.30	10.35	10.40	10.45	10.50
915	0.95	1.25E-04	10.30	10.35	10.40	10.45	10.50
930	0.97	1.25E-04	10.30	10.35	10.40	10.45	10.50
945	0.98	1.25E-04	10.30	10.35	10.40	10.45	10.50
960	1.00	1.25E-04	10.30	10.35	10.40	10.45	10.50
975	1.02	1.25E-04	10.30	10.35	10.40	10.45	10.50
990	1.03	1.25E-04	10.30	10.35	10.40	10.45	10.50
1005	1.05	1.25E-04	10.30	10.35	10.40	10.45	10.50
1020	1.06	1.25E-04	10.30	10.35	10.40	10.45	10.50
1035	1.08	1.25E-04	10.30	10.35	10.40	10.45	10.50
1050	1.09	1.25E-04	10.30	10.35	10.40	10.45	10.50
1065	1.11	1.25E-04	10.30	10.35	10.40	10.45	10.50
1080	1.13	1.25E-04	10.30	10.35	10.40	10.45	10.50
1095	1.14	1.25E-04	10.30	10.35	10.40	10.45	10.50
1110	1.16	1.25E-04	10.30	10.35	10.40	10.45	10.50
1125	1.17	1.25E-04	10.20	10.25	10.30	10.35	10.40
1140	1.19	1.25E-04	10.20	10.25	10.30	10.35	10.40
1155	1.20	1.25E-04	10.20	10.25	10.30	10.35	10.40
1170	1.22	1.25E-04	10.10	10.15	10.20	10.25	10.30
1185	1.23	1.25E-04	10.00	10.05	10.10	10.15	10.20
1200	1.25	1.25E-04	9.90	9.95	10.00	10.05	10.10
1215	1.27	1.25E-04	9.70	9.75	9.80	9.85	9.90
1230	1.28	1.25E-04	9.50	9.55	9.60	9.65	9.70
1245	1.30	1.25E-04	9.30	9.35	9.40	9.45	9.50
1260	1.31	1.25E-04	9.00	9.05	9.10	9.15	9.20
1275	1.33	1.25E-04	8.80	8.85	8.90	8.95	9.00
1290	1.34	1.25E-04	8.50	8.55	8.60	8.65	8.70
1305	1.36	1.25E-04	8.30	8.35	8.40	8.45	8.50
1320	1.38	1.25E-04	8.00	8.05	8.10	8.15	8.20
1335	1.39	1.25E-04	7.90	7.95	8.00	8.05	8.10
1350	1.41	1.25E-04	7.70	7.75	7.80	7.85	7.90
1365	1.42	1.25E-04	7.60	7.65	7.70	7.75	7.80
1380	1.44	1.25E-04	7.50	7.55	7.60	7.65	7.70
1395	1.45	1.25E-04	7.40	7.45	7.50	7.55	7.60
1410	1.47	1.25E-04	7.20	7.25	7.30	7.35	7.40
1425	1.48	1.25E-04	7.00	7.05	7.10	7.15	7.20
1440	1.50	1.25E-04	6.80	6.85	6.90	6.95	7.00
1455	1.52	1.25E-04	6.50	6.55	6.60	6.65	6.70
1470	1.53	1.25E-04	6.40	6.45	6.50	6.55	6.60
1485	1.55	1.25E-04	6.30	6.35	6.40	6.45	6.50
1500	1.56	1.25E-04	6.10	6.15	6.20	6.25	6.30
1515	1.58	1.25E-04	6.00	6.05	6.10	6.15	6.20
1530	1.59	1.25E-04	5.90	5.95	6.00	6.05	6.10
1545	1.61	1.25E-04	5.90	5.95	6.00	6.05	6.10

References

- (1) *IPCC Special Report on Carbon Dioxide Capture and Storage*; Working Group III of the Intergovernmental Panel on Climate Change (Metz, B.; Davidson, O.; de Coninck, H. C.; Loos, M.; Meyer, L. A.; eds.); Cambridge University Press: New York, NY, 2005; http://www.ipcc.ch/pdf/special-reports/srccs/srccs_wholereport.pdf.
- (2) Krupa, S. V.; Kickert, R. N. The Greenhouse Effect: Impacts of Ultraviolet-B (UV-B) Radiation, Carbon Dioxide (CO₂), and Ozone (O₃) on Vegetation. *Environmental Pollution*. **1989**, *61*, 263-393.
- (3) Karl, T. R.; Trenberth, K. E. Modern Global Climate Change. *Science*. **2003**, *302*, 1719-1723.
- (4) Fano, G. A primer on the carbon cycle. *American Journal of Physics*. **2010**, *78* (4), 367-376.
- (5) Ruddiman, W. F. *Earth's Climate Past and Future*; W. H. Freeman and Company: New York, NY, 2001.
- (6) Figueroa, J. D.; Fout, T.; Plasynski, S.; McIlvried, H.; Srivastava, R. D. Advances in CO₂ capture technology – The U.S. Department of Energy's Carbon Sequestration Program. *International Journal of Greenhouse Gas Control*. **2008**, *2*, 9-20.
- (7) Trends in Atmospheric Carbon Dioxide; <http://www.esrl.noaa.gov/gmd/ccgg/trends/mlo.html>
- (8) Herzog, H. J. What Future for Carbon Capture and Sequestration? *Environmental Science and Technology*. **2001**, *35* (7), 148A-153A.
- (9) Lackner, K. S. A Guide to CO₂ Sequestration. *Science*. **2003**, *300*, 1677-1678.
- (10) McCoy, S. T.; Pollack, M.; Jaramillo, P. Geologic sequestration through EOR: policy and regulatory considerations for greenhouse gas accounting. *Energy Procedia*. **2011**, *4*, 5794-5801.
- (11) Orr, J. C. *et. al.* Anthropogenic ocean acidification over the twenty-first century and its impact on calcifying organisms. *Nature*. **2005**, *437*, 681-686.
- (12) Broad, W. J.; Revkin, A. C. Has the Sea Given Up Its Bounty? *New York Times*. **2003**. <http://www.nytimes.com/2003/07/29/science/290CEA.html?pagewanted=print&position=>
- (13) Energy Frontier Research Centers; <http://www.er.doe.gov/bes/EFRC/index.html>

- (14) *Center for Frontiers of Subsurface Energy Security Website*; <http://utefrc.com/>
- (15) *Pure Component Properties*; <http://www.cheric.org/research/kdb/hcprop/cmprch.php>
- (16) André, L.; Audigane, P.; Azaroual, M.; Menjot, A. Numerical modeling of fluid-rock chemical interactions at the supercritical CO₂-liquid interface during CO₂ injection into a carbonate reservoir, the Dogger aquifer (Paris Basin, France). *Energy Conversion and Management*. **2007**, *48*, 1782-1797.
- (17) Leitner, W. Green Chemistry: Designed to dissolve. *Nature*. **2000**, *405*, 129-130.
- (18) Berner, R. A. Rate Control of Mineral Dissolution Under Earth Surface Conditions. *American Journal of Science*. **1978**, *278*, 1235-1252.
- (19) Chaudhary, K. *CT scan results*, personal communication. March 1, **2011**.
- (20) Klein, C. *The Manual of Mineral Science*, 22nd ed; John Wiley & Sons: New York, NY, 2002.
- (21) Fetter, C. W. *Contaminant Hydrogeology*, 2nd ed; Prentice-Hall: Upper Saddle River, NJ, 1999.
- (22) Appelo, C. A. J.; Postma, D. *Geochemistry, groundwater and pollution*, 2nd ed.; A. A. Balkema Publishers: Leiden, The Netherlands, 2007.
- (23) CO₂ Thermophysical Property Calculator; <http://sequestration.mit.edu/tools/index.html>
- (24) Wolfe, W. *CO₂ density experiment results*, personal communication. March 8, **2011**.
- (25) Ritter, Michael E. *The Physical Environment: an Introduction to Physical Geography*. **2009**. http://www.uwsp.edu/geo/faculty/ritter/geog101/textbook/title_page.html

Vita

Molly Kent attended Carleton College in Northfield, MN, where she received a BA in Studio Art in 2006. She enrolled at the University of Texas at Austin in the fall of 2008.

kent.molly@gmail.com

This thesis was typed by the author.